



HAL
open science

Understanding the impact behavior and long-term durability of marine composites for propellers

Alban Robin

► **To cite this version:**

Alban Robin. Understanding the impact behavior and long-term durability of marine composites for propellers. Mechanical engineering [physics.class-ph]. Université de Bretagne occidentale - Brest, 2023. English. NNT: 2023BRES0032 . tel-04401000

HAL Id: tel-04401000

<https://theses.hal.science/tel-04401000v1>

Submitted on 17 Jan 2024

HAL is a multi-disciplinary open access archive for the deposit and dissemination of scientific research documents, whether they are published or not. The documents may come from teaching and research institutions in France or abroad, or from public or private research centers.

L'archive ouverte pluridisciplinaire **HAL**, est destinée au dépôt et à la diffusion de documents scientifiques de niveau recherche, publiés ou non, émanant des établissements d'enseignement et de recherche français ou étrangers, des laboratoires publics ou privés.

THESE DE DOCTORAT DE

L'UNIVERSITE DE BRETAGNE OCCIDENTALE

ECOLE DOCTORALE N° 598

Sciences de la Mer et du Littoral

*Spécialité : Mécanique, génie mécanique, mécanique des fluides et
énergétique*

Par

Alban ROBIN

Understanding the impact behavior and long-term durability of marine composites for propellers

Thèse présentée et soutenue à Plouzané, le 14/06/2023

Unité de recherche : IFREMER - Laboratoire Structures, Matériaux Avancés et Sollicitations Hyperbares

Rapporteurs avant soutenance :

Christophe BOUVET Professeur des universités, ISAE SUPAERO
Federica DAGHIA Maitre de conférences HDR, ENS Paris-Saclay

Composition du Jury :

Président : Pascal CASARI Professeur des universités, Nantes Université

Examineurs : Christophe BOUVET Professeur des universités, ISAE SUPAERO
Federica DAGHIA Maitre de conférences HDR, ENS Paris-Saclay
Nahiene HAMILA Professeur des universités, ENI Brest
Patrick ROZYCKI Professeur des universités, Ecole Centrale de Nantes
Laurent SOHIER Maitre de conférences, Université de Bretagne Occidentale

Dir. de thèse : Peter DAVIES Chercheur, IFREMER RDT/SMASH

Invité(s) :

Mael ARHANT Chercheur, IFREMER RDT/SMASH
Guillaume DOLO Ingénieur de recherche, NAVAL GROUP CESMAN
Bertrand HABERT Ingénieur de recherche, Direction Générale de l'Armement

Remerciements

Avant de vous présenter ce travail de thèse, il me semble évident de remercier l'ensemble des personnes y ayant contribué, de près ou de loin.

Je tenais tout d'abord à remercier Peter DAVIES et Mael ARHANT pour avoir dirigé mes travaux à l'IFREMER. Merci de m'avoir encouragé à réaliser ce travail. Je retiendrai vos compétences et connaissances, mais aussi votre disponibilité et votre sympathie tout au long de ces quatre années. Je remercie aussi chaleureusement Sébastien LE JEUNE pour l'ensemble du travail abattu dans la fabrication et le contrôle des plaques fabriquées, mais aussi pour son inventivité à réaliser des moules non standards. A la Team Composites de l'IFREMER, j'ai été fier de travailler avec vous.

Merci à Bertrand HABERT pour les nombreuses discussions techniques mais aussi plus personnelles. Merci d'avoir organisé la visite du CMT Sagittaire et de la base navale de Brest, un des moments forts de mon séjour Brestois. Ça a été un réel plaisir de te côtoyer, et je suis sûr qu'à l'avenir nous aurons l'opportunité d'échanger à nouveau.

Merci aussi à Thomas BONNEMAINS et Éric LOLIVE de l'IUT de Brest et Laurent SOHIER de l'UBO pour votre accompagnement et vos recommandations. J'en profite aussi pour remercier Bertrand FOREST, Damien Le VOURC'H et Alan TASSIN à l'IFREMER pour les résolutions rapides des problèmes que j'ai rencontrés.

Le projet international Durability of Composite Propellers (DCP) m'ayant amené à voyager en Australie pendant trois mois et demi, je tenais à remercier l'UNSW, notamment Ganga PRUSTY pour m'avoir accueilli, mais aussi Matt DONOUGH et Rowan CALDWELL pour les discussions que nous avons eues. Merci à la DSTG de m'avoir accueilli à Melbourne dans leurs locaux, plus particulièrement à Nigel St JOHN, Andrew PHILIPPS et Gleny CHIRIMA. Merci pour le temps que vous m'avez consacré aux horaires de travail, mais aussi en dehors.

Ensuite, je tenais à remercier les rapporteurs de cette étude, Christophe BOUVET et Federica DAGHIA, pour la qualité des discussions menées suite à vos rapports. Merci aussi à Pascal CASARI d'avoir présidé ce jury de thèse. Il me paraît évident de spécifier que c'est toi qui, le premier, m'a fait confiance dans le cadre d'un projet étudiant en DUT sur les matériaux composites. Que de chemin parcouru depuis ! Merci aussi à Patrick ROZYCKI pour son suivi dans le cadre du CSI ainsi qu'à Nahiene HAMILA.

Enfin, merci à Guillaume DOLO pour la visite du Technocampus OCEAN et pour m'avoir permis de réaliser les essais d'impact durs sur les bords d'attaque.

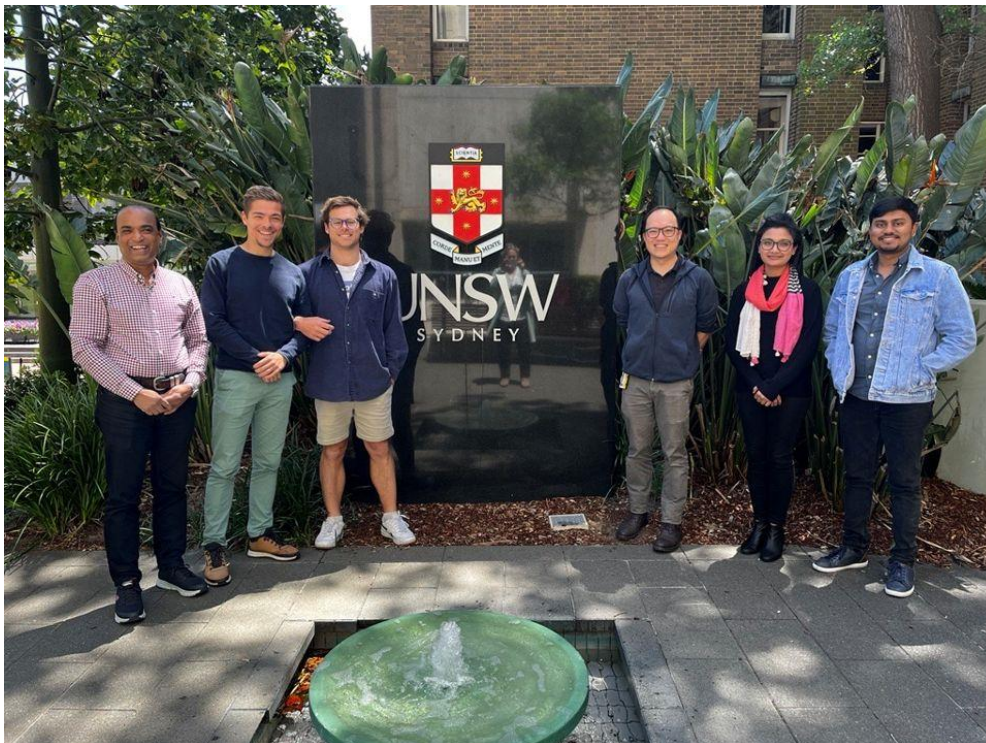
Je tenais à remercier les équipes matériaux et caissons hyperbares du laboratoire SMASH. Exhaustivement, merci à Noémie COLIN, Pierre-Yves LEOST, Christophe PEYRONNET, Mickael PREMEL-CABIC et Luc RIOU, ainsi qu'à Benoit BIGOURDAN, Nicolas DUMERGUE, Pierre-Yves Le GAC et Maelenn Le GALL pour les nombreuses discussions d'intérêt. Christian Le GALL, une pensée aussi pour toi malgré nos divergences footballistiques !

Remerciements sincères aux doctorants que j'ai pu croiser, Antoine B., Alexandre, Quentin, Florian, Robin, Louis, Antoine LGG, Gauthier et Hugo. Mention spéciale à mes ex collègues de bureau Romain puis Laure. Bon vent à vous tous !

Comment ne pas remercier aussi le PAC Futsal pour ces nombreuses victoires en R1 Futsal ! Merci à vous les gars. Une pensée particulière à Ren, Baba et Lolo pour mon introduction rapide au sein du groupe.

Enfin, je tenais à remercier ma famille pour son soutien et son accompagnement lors de cette thèse. Malgré des difficultés à certains moments, vous m'avez toujours accompagné.

Enfin, une pensée particulière pour toi Estelle, merci de faire partie de ma vie !



Membres du projet DCP à l'UNSW (Novembre 2022) : de gauche à droite Ganga PRUSTY, Alban ROBIN, Rowan CALDWELL, Matt DONOUGH, Shafaq et Faisal ISLAM

General introduction

Naval construction has a long history. The Egyptians started boat building around 4000 BC. Wood was the first material used in the shipbuilding industry, as it was easy to find and form. This material dominated shipbuilding until the industrial revolution in the 19th century, when ships began to be built from iron and steel. This was the result of improvements in the knowledge of manufacturing with metals. Sails were also replaced with steam engines and paddles with propellers. The use of metals to replace wood improved the waterproofing, safety and durability of the ship.

However, metallic materials are heavy, which increases the fuel consumption of the vessel. The massive development of marine composites began after the Second World War with the US Navy. The use of composite boats in operation gave good results in terms of durability, stiffness and repair. In addition, composite parts are lighter than metallic parts, which results in lower energy consumption: this is also a suitable material for fast sailing boats (Figure I.1) where the efficiency is a priority to improve the boat performance.



Figure I.1 – SVR LAZARTIGUE Ultim made of CFRP composite ©Thierry MARTINEZ

Today, Carbon Fiber Reinforced Polymers (CFRP) are widely used in the marine environment for high performance applications. These materials are chosen because of their high specific properties: high mechanical properties compared to the material density. Recent developments including hulls, superstructures, radomes and propellers have shown the advantages of CFRP materials. The work environment is severe: composite parts are continuously subjected to humid air or are immersed in sea water. Depending on the material system, water diffusion into the structure may lead to a loss of the mechanical properties. In addition, external parts such as propellers or hulls can be subjected to impact events, with floating solids.

This study is part of the Durability of Composite Propellers (DCP) project. A collaboration has been set up between the Direction Générale de l'Armement (DGA, France) and the Defense Science and Technology

Group (DSTG, Australia) to develop the knowledge on marine composite propellers. On one side, the French research institute for the Oceans (IFREMER) focused on long-term durability and impact behavior of a thermoset CFRP composite suited for naval applications. On the other, the University of New South Wales (UNSW) with the Centre for Automated Manufacture of Advanced Composites (AMAC) worked on a thermoplastic CFRP manufactured by Automated Fiber Placement (AFP) or with a hot press. Their activities included the AFP process parameters optimization, the numerical simulation of the AFP process, and an underwater impact study with the effects of a damage induced by an impact on the water uptake and the post-impact strength.

The aim of the present study is to investigate the effects of aging on the long-term durability and impact behavior of a CFRP composite for marine propeller. Five chapters will present the work performed in this study. The three last chapters, the technical and scientific work performed, are summarized Figure I.2.

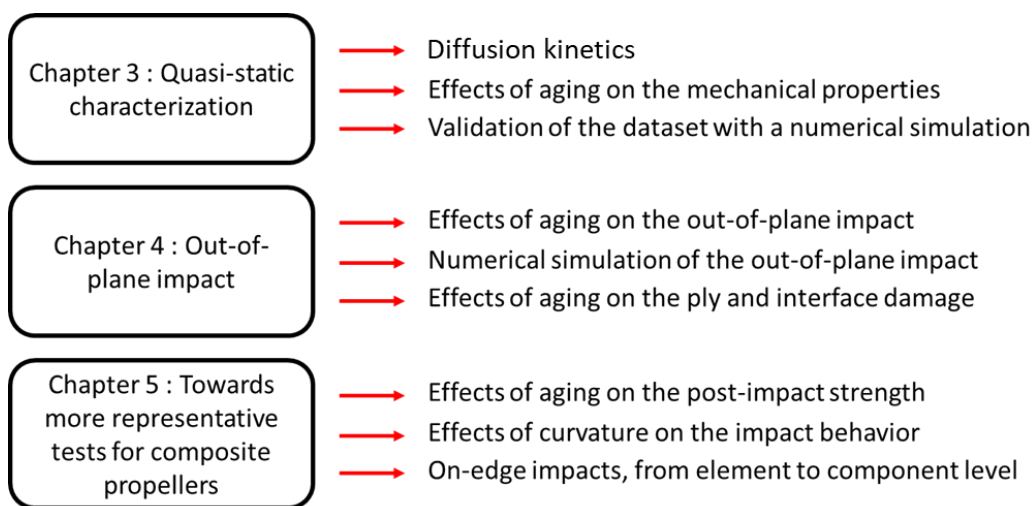


Figure I.2 – Scheme of the study performed

In the first chapter, a literature study will introduce the reader to the world of marine propellers. Historical materials and current problem areas will be discussed. Then, scientific studies of impact events will be presented. Finally, a section will be devoted to the aging process and durability of FRP composites.

In the second chapter, the scientific approach chosen for this project, and the methods associated, will be introduced. All the mechanical tests, whether standardized or custom will be presented.

In the third chapter, a first section dedicated to seawater aging results and modeling the water diffusion in a blade leading-edge will be presented. Then, the quasi-static characterization and the influence of the aging on the mechanical properties will be addressed. The complete dataset obtained experimentally will be used to simulate a complex four-point bending test that was experimentally performed.

In the fourth chapter, the influence of aging on the impact behavior will be described. A standardized out-of-plane impact test has been performed on quasi-isotropic coupons, and results are compared with a numerical simulation. A finite element model has been developed, and experimental mechanical properties obtained in Chapter 3 are used to simulate the composite behavior.

In the fifth chapter, the post-impact strength will be discussed. Then, preliminary studies on tests that are more relevant to characterize the impact behavior of a marine propeller will be presented. The first concern the effects of curvature on the impact behavior. Then, on-edge impact tests at the element and component levels will be presented and compared.

Finally, a conclusion on the work achieved and some perspectives will be presented.

Contents

CHAPTER 1 – STATE OF THE ART	12
1.1. PROPELLERS IN INDUSTRY	14
1.2. IMPACT TESTING ON COMPOSITE MATERIALS AND MODELLING	29
1.3. FRP AGING AND DURABILITY	50
1.4. CONCLUSION	62
CHAPTER 2 – MATERIALS AND METHODS	64
2.1. MATERIALS	66
2.2. MANUFACTURING C/EPOXY PANELS.....	66
2.3. AGING OF PURE EPOXY AND C/EPOXY COUPONS.....	67
2.4. PHYSICOCHEMICAL CHARACTERIZATION	70
2.5. IMAGING TECHNIQUES	70
2.6. SCIENTIFIC APPROACH.....	72
2.7. CHARACTERIZATION AT COUPON SCALE	74
2.8. CHARACTERIZATION AT ELEMENT SCALE.....	83
2.9. CHARACTERIZATION AT COMPONENT SCALE	87
2.10. NUMERICAL SIMULATION OF COMPOSITES	87
CHAPTER 3 – INFLUENCE OF AGING ON QUASI-STATIC MECHANICAL PROPERTIES.....	94
3.1. SEAWATER AGING	96
3.2. PLY PROPERTIES.....	104
3.3. INTERFACE PROPERTIES	113
3.4. NORMALIZATION OF THE PROPERTIES CHANGE.....	121
3.5. APPLICATION OF AGED PROPERTIES TO A STRUCTURAL TEST	123
3.6. CONCLUSION	128
CHAPTER 4 – INFLUENCE OF AGING ON C/EPOXY IMPACT BEHAVIOR	130
4.1. INTRODUCTION	132
4.2. INFLUENCE OF THE LOADING-RATE ON THE MECHANICAL PROPERTIES OF THE C/EPOXY	132
4.3. DEVELOPMENT OF A NEW DROP WEIGHT IMPACT TOWER.....	137
4.4. EXPERIMENTAL IMPACT BEHAVIOR IN THE UNAGED STATE	140
4.5. NUMERICAL SIMULATION FOR UNAGED STATE	146
4.6. EFFECT OF AGING ON THE IMPACT BEHAVIOR.....	156
4.7. CONCLUSION	168
CHAPTER 5 – TOWARDS MORE REPRESENTATIVE TESTS FOR COMPOSITE PROPELLERS	170
5.1. INTRODUCTION	172

5.2. INFLUENCE OF AGING ON THE CAI STRENGTH	172
5.3. INFLUENCE OF CURVATURE ON THE OUT-OF-PLANE IMPACT BEHAVIOR.....	179
5.4. IN-PLANE IMPACT: FROM ELEMENT LEVEL TO COMPONENT LEVEL.....	186
5.5. CONCLUSION	194
CONCLUSIONS & PERSPECTIVES	196
CONCLUSIONS	197
PERSPECTIVES.....	199
LIST OF FIGURES	201
LIST OF TABLES	209
APPENDIX 1 – C-SCANS OF AGED C/EPOXY COUPON IMPACTED FROM 5J TO 80J.....	211
APPENDIX 2 – COMPARISON EXP/SIM FOR UNAGED COUPONS.....	212
APPENDIX 3 – COMPARISON EXP/SIM FOR PHYSICALLY AGED COUPONS	214
APPENDIX 4 – COMPARISON EXP/SIM FOR SEAWATER SATURATED COUPONS.....	216
APPENDIX 5 – EXTENDED FRENCH ABSTRACT	218
APPENDIX 6 – SCIENTIFIC CONTRIBUTIONS	232
REFERENCES	233

Chapter 1

—

State of the art

Chapter 1 – State of the art

1.1. PROPELLERS IN INDUSTRY	14
1.1.1. INTRODUCTION TO MARINE PROPELLERS	14
1.1.2. PROPELLERS IN A MARINE ENVIRONMENT	18
1.1.3. COMPOSITES PROPELLERS.....	24
1.1.4. CONCLUSION	29
1.2. IMPACT TESTING ON COMPOSITE MATERIALS AND MODELLING.....	29
1.2.1. MARINE IMPACTS	29
1.2.2. OUT-OF-PLANE IMPACT AND MATERIAL PARAMETERS	35
1.2.3. EXPERIMENTAL AND SIMULATION METHODOLOGY FOR LVI ON COMPOSITE LAMINATES	42
1.2.4. SIMULATION OF LVI AND CAI	45
1.2.5. TESTING AND MODELING OF IMPACT ON COMPOSITE BLADES	46
1.2.6. ON-EDGE IMPACT TESTS.....	49
1.2.7. CONCLUSION	50
1.3. FRP AGING AND DURABILITY	50
1.3.1. FRP AGING AND DURABILITY	51
1.3.2. POLYMERIC COMPOSITES IN MARINE ENVIRONMENT	54
1.4. CONCLUSION	62

1.1. Propellers in industry

1.1.1. Introduction to marine propellers

1.1.1.1. History

Historically the first propellers employed were screw propellers. They started with Archimedes, who used a screw propeller to lift water for irrigation and bailing boats.

The beginning of the motorization of the naval industry was a turning point and the SS Archimedes, built in 1838 by Wimhurst of London, was the first steamship to be driven by a screw propeller.

Gradually, the Royal Navy adopted more screw propulsion systems for their vessels. Trials continued with HMS Rattler in 1845 and SS Great Britain in 1843, the first screw propelled steamship to cross the Atlantic Ocean in August 1845.

The design of screw propellers stabilized in the 1880s, due to the development of several theories. First, the momentum theory, or disk actuator theory was created by Rankine (1865), Greenhill (1888) and Froude (1889). It describes the propeller as a simple actuator disk accelerating the flow in the axial direction by creating a pressure jump in the propeller plane [1]. Second, the Blade Element Theory (BET) was proposed by Froude (1878), Taylor (1893) and Drzewiecki (1892). It refers to a mathematical process allowing the behavior of propellers to be calculated. It estimates the thrust of a propeller by dividing each blade into several segments, called blade elements. The propeller properties are evaluated after the hydrodynamic force calculation. This technique ignores the presence of induced flow inside the propeller stream tube resulting in an over-prediction of the calculated thrust compared to the value obtained experimentally [2].

In 1907, the steam turbine driven liner Mauritania generated 70 000 shaft horsepower (shp) using four propellers rotating at 180 rpm and achieved a speed of 26.3 knots. Some years later, the Queen Mary, powered by four single reduction geared turbine sets aggregating 160 000 shp on four propellers, achieved speeds of 30-32 knots. The main differences between the Queen Mary and the Mauritania were the propeller blade surface area ratios and the weights of the propellers: 18.7 tons for the Mauritania and 35 tons for the Queen Mary.

The arrival of propellers with increased blade area ratios led to cavitation erosion and induced cavitation excited vibration in the ship. This issue was solved by new approaches, such as redesign of propellers, with respect to blade shape and section form [3].

1.1.1.2. Current applications

Today, propellers are used in several domains: aeronautical, industrial and in the marine environment. The constraints induced by the environment can be severe.

In the aeronautical industry, airscrews are used for propulsion of aircraft. They convert rotary motion from an engine into a swirling slipstream which pushes the propeller forwards or backwards. They generally consist

of at least two blades having an aerodynamic profile. The rotation of a propeller acts on the mass of air that passes through it and is projected backwards at great speed. According to the principle of momentum theory, a reaction force is applied to the propeller and propels the aircraft forward. Due to a speed too close to the speed of sound near the blade tip, propellers are only suitable for use at subsonic airspeeds, below about 770 km/h.

In the marine environment, propellers are used for vessel propulsion and renewable marine energy (tidal turbines). Theoretically, aircraft and marine propellers operate in a similar way, producing thrust/lift by rotating blades in a manner analogous to rotating a screw through a solid. However, there are more limitations on marine propellers. Aircraft propellers operate in relatively uniform flow and through a nearly inviscid medium when compared with marine propellers. In addition, geometric constraints have much more influence on propeller performance in marine environment, such as the proximity of the hull to the propeller or the inclination of the shaft. Fluid parameters are also very different, since air is less viscous than seawater, and air density is 0.1 – 0.15% of the density of seawater. The consequence is much higher hydrodynamic loads on marine propellers than on aircraft propellers, for a given rotation speed. Figure 1.1 shows examples of marine propellers.



Figure 1.1 – CFRP marine propellers commercialized by Nakashima (from Nakashima website) – In the order : i) Fixed Pitch Propeller (FPP) ii) Controllable Pitch Propeller (CPP) iii) Side thruster

Seas and oceans are endowed with vast reserves of renewable energy. Due to increasing concerns about environmental issues and depletion of fossil resources, technologies to produce more clean energy from renewable sources in marine environment are being developed, and countries and territories that have extensive maritime areas can make a significant contribution to low-carbon electricity production in the energy mix.

This energy takes the form of kinetic energy from currents or winds, potential energy, mechanical energy, thermal potential or osmotic pressure [4]. The machines being developed to recover wind and current energy use composite blades and are thus of interest here and will be briefly described below.

1.1.1.2.1. Wind turbine blades

Wind turbines have been developed to produce energy from the wind. For island territories, transport costs of oil and gas are expensive. Due to the proximity of the oceans, costly investments in offshore wind turbines are profitable.

In 2017, the cost of producing offshore wind power in Europe was estimated at around 160€/MWh, compared to 80€/MWh for onshore wind power. Even if the cost for offshore wind power is twice the cost for onshore wind turbines, the gap is decreasing.

Compared to onshore wind, offshore wind turbines can capture more regular wind and the variation in production is easier to predict, thus it is easier to manage production intermittence. Despite expensive maintenance costs because of limited accessibility for inspection of offshore wind turbines, they generate fewer conflicts with residents, limiting the legal risks and costs of operation. However, new issues have appeared in touristic areas, as offshore wind turbines close to the shore may alter the landscape.

The offshore wind turbine market is divided in two categories, depending on water depth. Down to around 50m depths, the turbine is attached to a support fixed to the seabed. Beyond 50m depth, technical and economic constraints limit this technique. In this case, wind turbines are fixed to a floating support, itself anchored to the seabed.

Due to the application and the need to reduce the weight to take the maximal benefit from the wind loading, blades are manufactured in composite materials while generator and tower are manufactured from metals. Blades consist of two faces, the suction side and the pressure side. They are joined together and stiffened either by one or several integral (shear) webs, linking the upper and the lower parts of the blade shell or by a box beam (Figure 1.2). The flapwise load is caused by the wind pressure, and the edgewise load is caused by gravitational forces and torque load. The flapwise bending is resisted by the spar, internal webs or spar inside the blade, while the edges of the profile carry the edgewise bending. The laminates at the leading and trailing edges that carry the bending moments associated with the gravitational loads are subjected to tension–compression loads. The aeroshells, which are made of sandwich structures, are primarily designed against elastic buckling.

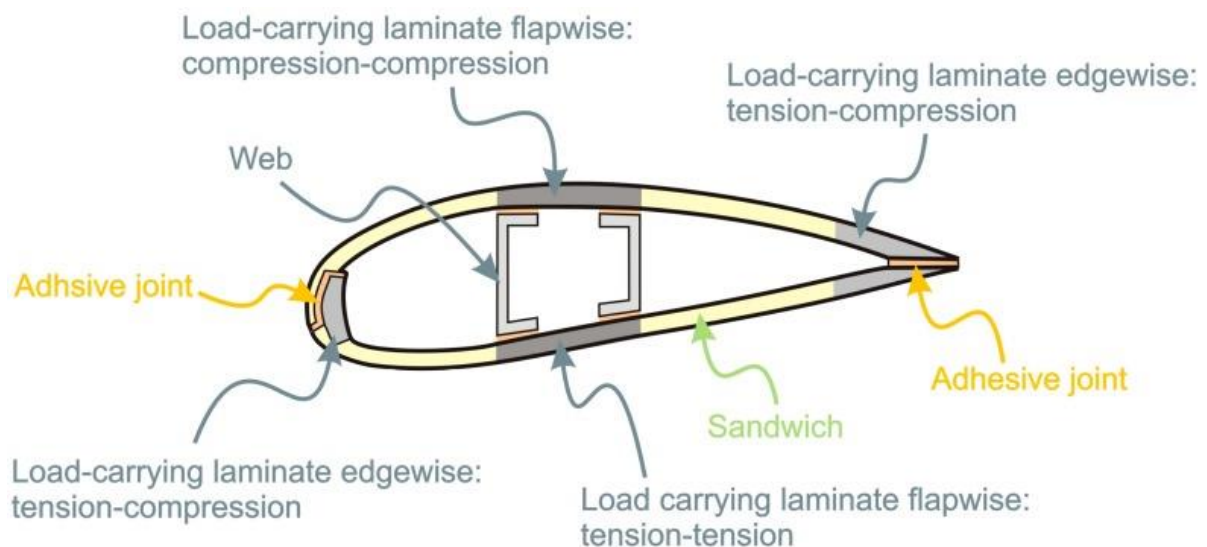


Figure 1.2 – Schematic diagram of the section of the wind turbine blade [5]

Turbine developments are focused on the increase in size and offshore placements. Increasing size is motivated by the desire to reduce the leveraged cost of energy. However, with size increased, the weight of

the rotor blades also increases, which includes high gravitational loads. In addition, longer blades deflect more, and it is important to improve the structural stiffness to keep an interesting efficiency. A major advantage of composite materials is their high-cycle fatigue behavior, as more than 100 million load cycles may be applied during 25 years in operation.

1.1.1.2.2. Tidal turbine blades

The first studies on the use of tidal currents to produce electricity began in 1990. Today, an estimation of a profitability threshold recommends using this technology in areas where currents during high tide are more than 2 m/s. There are relatively few areas which satisfy this condition, so today tidal turbines are a niche market. However, this technology is interesting for islands and isolated systems and is of interest here as tidal turbine blades are mostly large composite structures.

The global exploitable marine current energy is estimated to be 75 GW, including 11 GW in Europe. UK and France have the highest marine current potential in Europe (6GW and 3.4 GW respectively) [6]. One of the advantages of tidal current energy is the high predictability of the tidal current resource: the prediction accuracy is about 98% for several decades [7]. There are two ways to harness the power from marine tidal resources: by building a tidal barrage across an estuary or a bay, or by extracting the kinetic energy directly from flowing tidal currents [8].

The main advantage of a tidal barrage is that it allows GW to be produced, compared to a few MW for tidal current turbines. However, the hydrology and local ecosystem can be changed because of the large barrage system [9], and the cost of that type of infrastructure is very high compared to other technologies.

In comparison, tidal current turbines are more flexible and can be grouped in farms. In that case, the production of electricity can be modulated. A recent example is Ushant, an island separated from France by 18.5 km of sea. A French government project (PHARES) aims to produce 80% of the energy demand of the 850 annual inhabitants of the island by the production of electricity from two Sabella tidal turbines (diameter of 12m, 500kW per turbine), one wind turbine (0.9 MW) and a solar panel farm of 500 kW. The ambition of the project is to replace the use of 2 million liters of fuel per year.

During the last few decades, various research projects on tidal current turbines have been performed. Different technologies have been studied and discussed in recent papers [10]. They conclude that both vertically and horizontally oriented cross flow turbines are well suited to this application since they have relatively high–power density.

Some industrial projects have also been developed and explained [11]. The main disadvantages associated with vertical axis turbines are relative low self-starting capability, high torque fluctuation and generally lower efficiency than horizontal axis turbine design. For large scale marine current turbines with power capacity over 500 kW, horizontal axis marine current tidal appear to be the most technologically and economically viable solution. Table 1.1 gives some examples of industrial tidal turbine projects.

Table 1.1 – Development sites and procurement of the EU funded Tidal Stream Industry Energiser project (TIGER)

Site	Key partners	Location	Capacity to be installed	Technology to be installed	Timescale for deployment
Ramsey Sound	Cambrian Offshore SW	Pembrokeshire, UK	Up to 1MW	TBC	2021-22
Yarmouth Harbour	QED Naval	Isle of Wight, UK	up to 300kW	Community scale SubHub with 3x Tocardo T1 turbines	2021-22
Perpetuus Tidal Energy Centre	Orbital Marine Power, EMEC	Isle of Wight, UK	30MW	Orbital O2 TBC	Deployment outside scope of TIGER (2025)
Le Raz Blanchard	Normandie Hydroliennes	Normandy, FR	12MW	TBC likely SIMEC AR2000 series variant	Deployment outside of scope of TIGER (2024-25)
	Hydroquest	Normandy, FR	17 MW	Oceanquest next generation turbine	Deployment outside of scope of TIGER (2024-25)
Paimpol-Bréhat	EDF, SEEEOH, Hydroquest & EMEC	Brittany, FR	1MW	Oceanquest 1 MW	Deployed (retrieval summer 2021)
	EDF, SEEEOH, BDI & Minesto	Brittany, FR	100kW	DG100	2022
	EDF, SEEEOH & BDI	Brittany, FR	Various	TBC	TBC
Morbihan Gulf	Morbihan Hydro Energies SAS	Brittany, FR	500kW	Sabella turbines 2x D08 250kW	2022

The ocean climate is particularly harsh and variable, with a corrosive seawater environment. Rotor blades must be extremely strong to survive in seawater and novel materials with improved strength, fatigue and anti-corrosion properties are already developed [12]. Advanced composites seem to be ideal candidates, and recent studies have shown potential cost reductions and increased durability compared with metallic solutions [13]. However, and because of a turbulent hydrodynamic flow, turbines are subjected to solid projections which can damage the structure. One of the aims of this thesis is to improve the understanding of the effect of impact on composite blades, when, for example, a rock carried away by the flow hits the blade.

1.1.2. Propellers in a marine environment

1.1.2.1. Applications in marine environment

In the marine environment, most propellers are used for propulsion. Depending on their application, the geometries, materials used and propeller types are different. A marine propeller is a complex 3D structure. The shape and the material used are chosen according to the performance required. The design process must consider both material properties (strength, flexibility) and manufacturing possibilities.

For propulsion, propellers are designed to operate at a constant ratio of axial to rotational velocity, at which point the torque thrust and efficiency are optimal for the propulsion system. Designing a propeller is limited

by operating laws, since the originally designed torque, thrust and efficiency at the designed axial velocity must be maintained. In the case where a diesel engine is used, an optimum can be reached between engine revolutions and engine power. If the pitch is incorrectly selected, the propeller will be either over-pitched (curve A in Figure 1.3) or under-pitched (curve B in Figure 1.3). The consequence is that the maximum power of the engine is not reached, because in the case of over pitching, limitations will be induced by engine torque limit (point X), and in the case of under-pitching, limitations will be induced by engine speed limit (point Y) [14] (Figure 1.3).

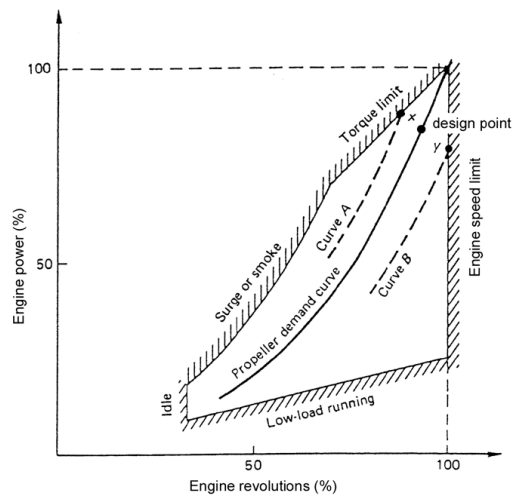


Figure 1.3 – Engine power (%) vs. Engine revolutions (%) : under-pitch and over-pitched propeller blade comparison [14].

The marine environment is severe for immersed structures. Seawater temperature is between 0°C and 30°C, and hydrostatic pressure increases by 1 bar every 10 meters. In addition, chemical and biological species can result in corrosion.

1.1.2.2. Specifications

According to the type of application, the design specifications vary. For civil vessels, specifications require stiffness. Durability is characterized in terms of the cyclic mechanical loading on the material chosen to work in marine conditions. Corrosion mechanisms are now well known, following some failures in service [15]. Impact resistance and low vibrations are also required.

For military vessels or submarines, specifications are more complex. Due to the purpose of that type of vehicle, stealth (low acoustic and electromagnetic signature) is essential [16].

For tidal turbines, durability is the most important requirement. During operation, the profitability of the infrastructure is dependent on maintenance, which must be reduced to a minimum. Structural degradation such as erosion or mechanical impact events must be reduced, so materials which reduce the consequences of damage on the structure must be used.

1.1.2.3. Types of propellers: FPP and CPP

Different propulsion technologies exist, some old and others innovative [17]. Historically, propellers were fixed pitch (FPP), which have formed the basis of propeller production over the years. Two kinds of FPP exist:

monoblock or built-up. Monoblock is the most common type of propeller today, embracing a large spectrum of design types and sizes; from propellers weighing a few kilograms for small boats to those which may weigh upwards of 100 tons, and are destined for large container ships. Manufacturing of large monoblock propellers creates issues, because it requires the simultaneous casting of more metal than can be accommodated in one ladle to produce the casting. In addition, facing the inherent problems of machining and quality required, built-up FPP was considered as more interesting. In this case, blades are cast separately from the central boss, and then are bolted or fixed after machining. Today, with improvements in large casting quality and machining, built-up FPP is limited to a few niche markets.

Historically, propellers were designed for efficiency [18]. Today, associated with energy conservation, other parameters have been included in the design requirements. Some aspects have been studied by torpedo propeller and naval ship designers, and concern reduction of vibration excitation and radiated noise from the propeller. Cavitation issues are underlying these aspects: they will produce undesired noise which can produce unexpected consequences.

The second type of propeller is the Controllable Pitch Propeller (CPP), also known as Variable Pitch Propeller (VPP). It can allow each blade to rotate around its spindle axis. The advantage of CPP is to provide an extra degree of freedom with the ability to change blade pitch. It represents 35% of the market share when compared to FPP systems, and is popular for ferries, general cargo, tug, and trawling markets. A pitch adjustment can result in better thrust control, and better efficiency leading to fuel saving. CPP also improves maneuverability of a vessel, which is important for docking tugs.

CPP is not suited to all kinds of vessels. For example, vessels that make long trips at constant service speed such as tankers, with much more energy produced than they need, are not designed to use CPP. Globally, the range of CPP available offers a maximum output of 44MW (60.000 hp) [16].

1.1.2.4. Materials used

As was noted in part 1.2.1., propellers operate in a harsh environment. Today, the main interest for composites is that they avoid issues inherent to metal casting and machining. However, an important mechanical characteristic is the fatigue resistance curve. For a civil propeller rotating at 120rpm, and operating 250 days per year, the accumulation of stress cycles over a 20-year life will exceed 8.6×10^8 . Table 1.2 shows an example of the first order fatigue cycles on a propeller blade, as a function of operating time. Herein, the first order corresponds to loading and blade motions, while second order corresponds to vibrations.

Table 1.2 – Build up of first-order fatigue cycles on a blade of propeller [19]

Time	1st hour	1st day	1st month	1st year	2nd year	10th year	20th year
Number of first order fatigue cycles	7.2×10^3	1.7×10^5	3.6×10^6	4.3×10^7	8.6×10^7	4.3×10^8	8.6×10^8

1.1.2.4.1. Metallic propellers

Historically, propellers were manufactured in metals. The most desirable set of properties which a metal propeller should possess are (from [19]) : high corrosion fatigue resistance in sea water, a high resistance to cavitation erosion, a good resistance to general corrosion, a high resistance to impingement attack and crevice corrosion, a high strength to weight ratio, good repair characteristics including weldability and freedom from subsequent cracking and good casting characteristics.

Metal composition will have a direct influence on the performance of metals used in a marine environment. Corrosion rate and mechanical properties are influenced by alloy element contents [20]. Choosing a propeller material is complex because of the large number of requirements. The manufacturing process will also influence material properties. Most propellers are made by casting, a process which leads to inhomogeneity in the thickness of large parts.

Today, most marine propellers are made with Nickel–Aluminium–Bronze (NAB or NiBrAl). There are several reasons for this, including good corrosion characteristics and anti–biofouling qualities. The yield strength of NAB is much more than design stress, giving a comfortable factor of safety above two [21]. In addition, the corrosion for this material is galvanic, cathodically controlled. The anode, in most cases the steel hull and sacrificial anodes, will begin to rust away. The primary cathode in the marine environment surrounding the hull is the NAB propeller, which does not itself corrode. However, it will cause significant steel plating rust and wastage of the sacrificial anodes. The corrosion costs can be high, so avoiding this is beneficial.

Another main issue using NAB is the machining cost due to complex blade shape geometries. In addition, NAB propellers are prone to fatigue–induced cracking and have relatively poor acoustic damping properties that can lead to noise problems from vibrations [22].

Other metallic materials are or have been used for propellers, such as stainless steel and titanium alloys.

1.1.2.4.2. Composite propellers

To overcome the disadvantages of metallic propellers, composite materials are now being investigated for use as a propeller material. These materials are made from high strength fibers impregnated by a polymer resin, which give to the piece the shape and volume and provide toughness and impact strength.

The benefits of these materials have been shown in the literature [23][24]: reduced fabrication costs if a large number of blades are manufactured, reduced through–life maintenance costs, reduced wear on gearbox/shaft, weight savings, improved vibration damping properties, improved fatigue performance,

superior corrosion and chemical resistance, increased cavitation inception speeds by using thick and flexible blades, and for military applications, lower electromagnetic and noise signatures. In addition, they suffer less from leading-edge erosion in water made abrasive by suspended grit (Figure 1.4).

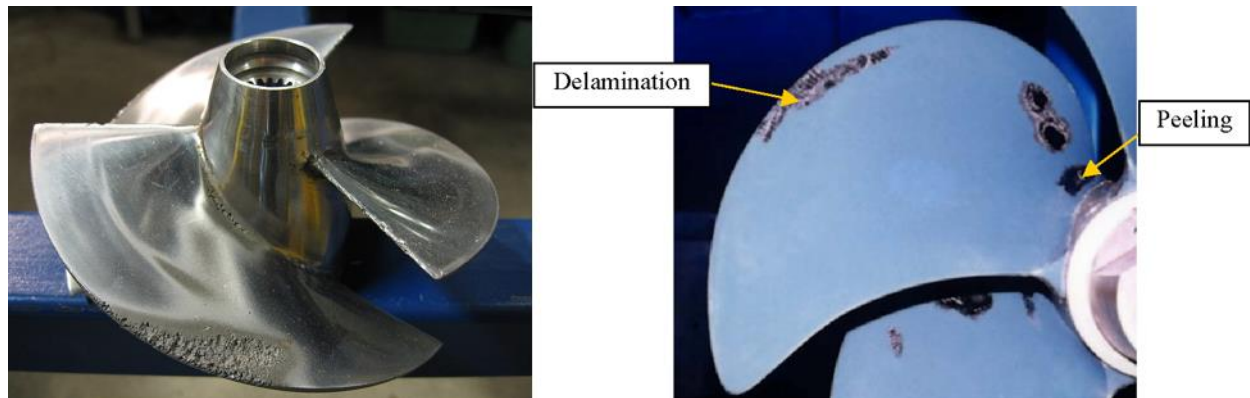


Figure 1.4 – Comparison of cavitation effects on metallic propeller (left) and composite propeller (right) [25]

Recent examples have shown the interest of composite propellers. Starting from small composite propellers for fishing boats, several companies have tried to design larger propellers. However, scaling up small units to larger propeller is a challenge. Research and industrial examples are presented in the literature [16].

Small scale composite propellers:

In Sweden, *ProPulse* designs composite propellers and blades in a fiberglass–reinforced polyamide, which is well suited to the market for outboards in the range of 20–300 hp [26]. Blades can be replaced one by one, and the pitch can be adjusted during installation to one of five settings. The company states that composites are tough and resilient compared to their aluminum counterparts, stronger and weigh 40% less.

In the USA, *Piranha* manufactured the world’s first modular composite propeller [27]–[28]. They developed long glass fiber reinforced polyamide thermoplastic composite propellers made by injection molding. These propellers are reported to be 10–15% stronger than traditional die–cast aluminum. *Pirhana* composite propellers are suitable for motors of 120–190 hp.

Also in the USA, *Composite Marine Propeller* developed its “Comprop” composite propeller that are single–piece four–blade propellers, up to 55 cm in diameter [29]. In their concept, the blades are designed to flex slightly or break off should they hit an obstruction, so the boat structure remains undamaged.

Large scale composite propellers:

In Germany, *AIR Fertigung–Technologie GmbH* worked with the University of Rostock to develop a Carbon Fiber–based composite propeller, dedicated to super yachts and ships [16]. Diameters were in the range 50 cm – 5 m. The company stated that the weight of its propellers was only a third of conventional NAB equivalents. They designed thinner blades at the tip, and they found this geometry reduced propeller noise by 5 dB compared to the metallic counterpart. They also studied a smart propeller, made with carbon, aramid

and polyethylene fibers that are distributed within the composite in such a way as to provide hydroelasticity. Blades were manufactured in closed molds by a RTM-like process. Full scale tests were conducted to compare the composite propeller to conventional NAB propellers. Results showed fuel reductions of almost 10% at full speed and 17.5% at mid-range. Acceleration was enhanced and noise in the wheelhouse was cut by up to 4%.

In the UK, *QinetiQ*, in collaboration with *Dowty Propellers* and *Wartsila Propulsion* designed, built and carried out sea trials on a 2.9 m diameter, five-blade composite propeller assembled on a bronze hub [30]. The blades were designed and assembled to respect warship standards, using a hybrid glass/carbon composite. The propeller was assembled on the RV Triton triple hull warship. The design resulted in thicker blades that offer improved cavitation performance, while reducing vibrations and underwater signature. This propeller design provided weight savings of about 20% compared with bronze blades.

In Germany, the Navy has used composites propellers for several months for submarine applications (German 206A and 212A) [16]. A study performed in that project involved three different kinds of composite propellers. Researchers indicated that more research is necessary, on both design and material engineering. They concluded that one of the major issues with large composite propellers is the tendency for cavitation erosion that is much worse than with metallic propellers. A coating material such as polyurethane was recommended to decrease cavitation erosion. The first composite propeller was installed in 2002, with the same geometry as a metallic propeller but with carbon fibers. The propulsion committee [31] reported that at the time of their report, the composite propeller had been in operation for over two years and approximately 20 000 nautical miles without any damage or malfunction. The study also reported the installation of a highly damped composite propeller using Aramid fiber (Kevlar). Acoustic trials “exceeded all expectation”.

In the Netherlands, Airborne Composites (La Hague, The Netherlands) has developed (since 2004) a prototype composite naval propeller for the Alkmaar-class minehunter vessels [32]. The propeller diameter is 2.5m, with a power output of 1.4MW. Collaboration with the Maritime Research Institute Netherlands (MARIN, Wageningen, The Netherlands) included FEA analysis on a particular blade design, then evaluation of the performance in water using MARIN knowledge in fluid mechanics. The propeller was manufactured in carbon, glass and epoxy resin.

In 2020, the only company to sell large scale composite propellers is NAKASHIMA PROPELLER CO., LTD. CFRP propellers have been developed there since 2007, and installed for the first time in 2014 on a domestic merchant vessel [33]. The four-blade propeller was manufactured by VARTM. A composite hub was also developed allowing propulsive force to be increased.

In France, a consortium between Loiretech, Naval Group and Méca, and funded by a DGA RAPID project, designed and manufactured a five-blade composite propeller with a diameter of 1.1m in 2018. The CFRP propeller “Fabheli” [34] was installed on a transportation vessel “Le Palais” and tested in real conditions in the Atlantic Ocean. The project reported a lower fuel consumption. In addition, they designed an innovative

junction between blades and root, which can be dismantled and was adapted to the Resin Transfer Moulding (RTM) process. They also added carbon textile at the leading and trailing edge for added impact resistance. This propeller was exhibited at the JEC Asia 2018 and won an innovation award (Figure 1.5).

Other developments have been reported in the literature [21], but it should be noted that much work within naval projects is sensitive and confidential.



Figure 1.5 – Fabheli composite propeller at JEC Asia 2018

1.1.3. Composites propellers

The previous section showed advantages and disadvantages of composites propellers, and some industrial examples. Since the propeller material is different, it is necessary to develop specific design, manufacturing, and experimentation tools to verify the durability of the propeller, and to correlate experimental results with data from numerical models.

In the marine industry, two types of propellers have been studied: rigid and flexible (pitch adaptive). The rigid composite propeller acts like a metallic propeller [35]. As a rigid propeller operates in a non-uniform (circumferentially varying) flow field, the blade deforms very little (bending) with almost no change in response to the hydrodynamic loading. However, the flexible composite propeller utilizes composite material with orientation-dependent stiffness in the blade to operate very differently. As the flexible composite propeller rotates in the non-uniform flow field, the blade deforms (bending and twisting), the pitch and rake change, reducing the loading and resulting in reduced cavitation and hull vibration (numerical studies : [36]–[38]). The lay-up of the fibers and the way they are combined in the matrix will give different deflection properties in each of the radial and chordal directions of the blade. The blade can be designed to deflect in different ways, which can be beneficial from a power absorption or cavitation inception and control perspective as the rotational speed is increased. This implies that the design process must be based on a fully

hydroelastic Finite Element Method, capable of accommodating orthotropic materials [39]. Fluid–structure interaction modelling is obligatory. Under the hydrodynamic loading, the propeller shape will change, which will imply a hydrodynamic loading difference between two steps of calculation.

1.1.3.1. Design of composite propellers

Designing a composite material propeller with orientation–dependent stiffness is complex. Different methods have been explained in the literature, and reviewed recently [40]. This section is based on that reference.

1.1.3.1.1. FEM & PSF–2 programs

The first method presented is the finite–element method and the Propeller Steady Flow 2 program (PSF-2) [40]. This approach was developed for analyzing a thick–shell composite blade [41]. The propeller is considered as a partial-composite structure. The thick–laminate method is applied to consider 3D features of composite blades. The composite material is considered as layers of orthotropic materials, and the skin composite layer and shear–web are treated as several sub–laminates. Effective moduli are obtained by integrating the constituent lamina properties through the thickness of the sub–laminate.

The aim of this method is to determine stress and elastic deflections, and to compare values obtained with values for an isotropic propeller. The blade loading is obtained by predicting the pressure coefficient difference using the PSF–2 program, which allows the blade loading to be obtained under hypothetical operating conditions. Finally, the calculated cross–sectional pressure load differences are applied to the pressure side of the blade, and elastic stress and deflection are obtained by numerical analysis, from commercial FEM software, Abaqus™ in this case.

1.1.3.1.2. Coupled 3D FEM/VLM

A second method presented is the 3D finite–element method / vortex–lattice method. It was presented in 1996 [42], and is dedicated to the hydro–elastic analysis of composite marine propellers in steady, non–cavitating flow.

Recent research has used FEM/VLM methods to investigate the response of a composite blade under hydrodynamic loading. The influence of stacking sequence on the hydro–elastic behavior of composite material propeller blades has been discussed [43]. This model was improved by introduction of the Hashin failure criteria [44], strength of the composite material propeller was evaluated, and stress distributions have been smoothed [45]. For the structural analysis, recent papers discussed the vibration characteristics of composite propeller [46], and described experimental tests to evaluate optimized designs [14].

1.1.3.1.3. Coupled FEM/CFD

The last method presented in the literature is a finite element model (FEM) coupled with a computational fluid dynamics model (CFD). The aim of this approach is to analyze the hydro-elastic performance of composite marine propellers in steady and unsteady flows. In contrast to VLM and BEM, the CFD model

considers the viscosity of the flow. The CFD method used in [47] was based on the Reynolds Averaged Navier–Stokes (RANS) equation, and a non–conforming layered solid element was used to build the finite element model of composite propeller blades.

The hydrodynamic performances of the composite propeller can be solved by applying a CFD method based on the RANS equation. A Semi-Implicit Method for Pressure Linked Equations (SIMPLE) algorithm was used for completing the coupling of pressure and velocity and solving the equations of incompressible fluids [48].

1.1.3.1.4. Performance optimization

The design of propellers includes both fluid dynamics studies and structural studies, which depend on both structure and material properties. Designers can have two approaches. Either, they consider more important functional requirements, such as propulsion efficiency, cavitation probability or noise. Or they consider structural requirements to be more important, such as lighter weight, higher strength, and lower vibration. Several researchers have published work on improving composite propeller performance. For example, a genetic algorithm was combined with a pre–deformed composite propeller in order to determine the best stacking sequence [43]. Herein, two optimization requirements were satisfied. Genetic algorithms also allowed the optimization of a composite marine propeller efficiency under different inflow velocities and an optimization of design parameters in [49]. This study was completed by the optimization of hydrodynamic load coefficients and the vibratory hub loads, which were directly function of ply angles and stacking sequences [50]. More recently, a genetic algorithm was combined with Cell–based Smoothed Finite Element Method (CS–FEM) creating an innovating optimization scheme [51]. The variation of propeller pitch was considered, as well as the hygrothermal effects of composites under thermal and moisture expansion. The hydrodynamic load was considered as a homogeneous pressure on the blade surface, but a more recent study took into account the hydrodynamic load by a CFD study [52]. Layup optimization combining Non–Uniform Rotational B–Splines (NURBS)–based FEM and genetic algorithms was also described [53], taking into account hygrothermal effects, leading to non–symmetric layup optimization.

In conclusion, there are several tools and methodologies available to the designer of composite propellers, with varying assumptions and degrees of complexity. However, all these models require material data and composite material properties are strongly dependent on the manufacturing process, so this will be discussed next.

1.1.3.2. Manufacturing of composite propellers

Finite element studies are interesting because they allow the influence of geometry and ply and angle stacking sequences to be examined numerically. However, the manufacturing process may limit the options available for composite blades. Different techniques have been discussed in the literature, and numerical optimization solutions are not always possible in the real case.

Historically, the first composite propellers were manufactured using a wet lay-up process [54]. This enabled a four-blade propeller to be produced, with a diameter of 800 mm, from a mix of Carbon and E-Glass fibers.

Reinforcements were cut and laid-up by hand, so that the blade wall thickness tapered gradually from root to tip. The composite was produced in aluminum moulds, and the two halves of the split mould were clamped together until the resin had cured.

Other processes have been presented, such as Resin Transfer Molding (RTM), in which resin is injected into a mould containing reinforcement [24]. An examination of the feasibility of manufacturing small marine propellers with RTM was discussed, which allowed reduced void content and material waste, while having better handling, ability to mould complex shapes, and good control of mechanical properties. Three industrial projects were presented, using different process and materials. Hand lay-up was also used for the fabrication of CFRP blades destined for the US Navy [21], with the aim to build a propeller equivalent to the one from QinetiQ [16]. A multi-step process is described in [55], based on the Air fabrication process, from a German company which manufactured a CFRP propeller named “Contur”. The first step is mould fabrication, based on an equivalent metallic propeller. The second step is the cutting of carbon fiber layers based on the material design using a numerically controlled (NC) cutting machine. The third step is the stacking of carbon fiber layers with resin, in a gel-coated mould. Compression and heating are applied, followed by the suppression of excess material. The last step corresponds to the insertion of the blades into the slots of a metallic hub. Hand lay-up was used in other recent studies [14][56], but today the processes used in the aeronautical industry are emerging, due to the high added value of these composite structures. An example is the use of carbon fiber prepreg to manufacture a five-blade propeller with a diameter of 250 mm, adopting the compression moulding process [57]. Automated Fiber Placement (AFP) is another promising alternative, allowing greater freedom in fibre orientation, which can result in optimal mechanical properties of composite hydrofoils [58][59]; studies on thermoplastic matrix composite blades are now possible using this process. In the wind turbine industry, which has been established for a longer time, blades are now produced using either Vacuum Assisted Resin Transfer Moulding (VARTM) or prepreg. VARTM is often preferred as it is less expensive, but prepreg offers optimized and consistent resin ratios [60]. The blade surfaces are covered by a gelcoat layer, providing a smooth surface to enhance hydrodynamic properties. Within the blade, a box-section includes an embedded core material to limit buckling. New developments using one-shot processes [61] have been recently discussed, where 13m blades are manufactured using powder epoxy materials that have comparable strength to traditional glass fiber/epoxy [13]. The process, which avoids the thermochemical constraints of a traditional epoxy resin, must be maintained at 180°C, and for this reason, an integrally heated composite ceramic tooling has been developed.

1.1.3.3. Hydrodynamic and mechanical testing

Designing and manufacturing are the two first steps of the study on composite propellers. However, experimental testing and correlation with numerical models are essential before industrial production, and standardization of composite propellers can be achieved.

First tests were performed in 1993 [24]. Regular utilization of composite propellers showed interesting performances, but low resistance to impact events. In that study after three weeks of utilization, the hub joint showed no signs of degradation, but one leading edge had been slightly scuffed, due to an impact event. Other practical tests led to the definitive failure of the propeller, due to impact. A shorter study showed the importance of the manufacturing process in order to increase propeller durability [21]. Other studies compared results from numerical simulations and experimental data. In a 36m water–tunnel, thrust, torque, cavitation inception and blade deflection were measured on three different composite propellers [55]. Among these three, two were designed to be flexible (one with reduced blade thickness and the other with a modified blade section shape), and one was rigid. For all values of relative inflow velocity, the measured pitch change, torque and thrust were larger than predictions. The advantage of a flexible propeller was its efficiency, which was improved by up to 5%. The main difference between the propellers tested was their cavitation performances. Another study [14] showed that measured displacements were smaller than the calculated values. An optimization of the composite lay-up was performed, and it was shown that pitch decreased as the ship speed decreased, reducing torque but increasing efficiency. In addition, pitch automatically changed with the inflow angle.

A new measurement technique has been developed in the Netherlands to measure the deflection of a propeller made by an isotropic ABS thermoplastic material [62]. A propeller was designed with a thickness distribution to achieve significant deflection of the blade. The authors concluded that the measurement technique based on 3D–Digital Image Correlation can be used to validate the results of hydro–elastic calculation. Increasing flow velocity was shown to induce an increase of blade deflection (Figure 1.6).

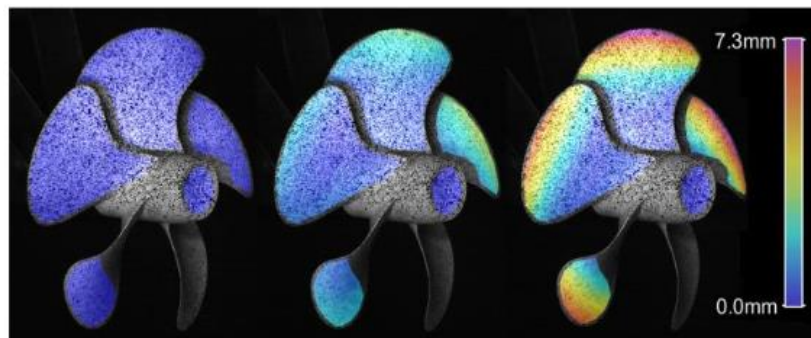


Figure 1.6 – Measured propeller deflection at increasing RPM for bollard pull condition [62]

For static tests, studies are more numerous in the wind turbine industry. As noted previously hydrodynamic loading is more severe for structures compared to aerodynamic loading, because of water viscosity, which induces higher stress at a given rotating velocity. It is therefore necessary to perform tests in marine environment. Full scale static tests were performed on a 13m glass–fiber epoxy composite wind turbine blade [63]. Results were coupled with an optimization algorithm (GA), allowing both the mass of the optimized blade and of the products used during manufacturing to be reduced. Bigger wind turbine blades have been tested under flap–wise loading to collapse [64], and showed complex interactions between materials leading to the failure of the blade.

For dynamic tests, there have been few results published on composite blades designed for either propulsion in a marine environment or for tidal turbines. There have been many general studies of impact testing of composites reported in the literature, especially by the aerospace industry where impacts on commercial or military rotor engine blades can have important consequences [65]. Impact will be discussed in the next section of this chapter. A recent paper [66] studied consequences of edge and frontal impact on composite blades for helicopters, and compared results with numerical values obtained with FEA.

1.1.4. Conclusion

To conclude this first section, a composite propeller is a complex structure, but knowledge on its mechanical behavior under hydrodynamic loading can lead to a better efficiency, and improved thrust. There are also significant economic interests involved, not only with respect to fuel savings but also where manufacturing processes can be optimized, and moulds are re-used. The long-term durability of marine propellers is a determining factor and needs to be studied under realistic conditions.

Different design techniques have been described. Lay-up optimization can be coupled to hydrodynamic and mechanical models with algorithms to obtain improved stacking sequences and fiber angles. However, the ideal composite is not always achievable due to manufacturing limitations, and choices must be made between different requirements.

The last section concerns experimental testing. The literature reports static tests on wind turbine blades, and dynamic tests on blades designed for aeronautical applications. However, dynamic, fatigue and impact tests on blades designed for the marine environment have so far received little attention.

1.2. Impact testing on composite materials and modelling

Composite materials can be difficult to analyze, particularly under dynamic loading: due to the interactions between reinforcement and matrix, complex phenomena appear during an impact event. This thesis will focus on transverse loading because of the designs involved in marine structures. In this section, the literature on impact events in a marine environment will be examined. A first section will focus on the impact on marine structures. A second section will focus on parameters affecting impact test results, such as impactor parameters and material constituents. A third section will focus on residual properties after impact, and possible ways to monitor damage induced during testing. Finally, the last section will be devoted to modelling of impacts on composites.

1.2.1. Marine impacts

The marine industry uses composite materials in a large range of applications, from pleasure boats to racing vessels, from naval and coastguard patrol craft to the offshore oil and gas industry [67]. There are numerous reasons: corrosion resistance, high specific mechanical properties, or easier forming of complex shapes. The main issue with these materials is their low resistance to out-of-plane loading, and particularly to impact

events, leading to a complex interaction between the structure and the material. For most marine applications, impact of objects involves a limited range of low velocities between the impactor and the target. To investigate the consequences of an impact event on composite structures, tests can be performed, but the loading and boundary conditions must be carefully controlled.

1.2.1.1. Impact events on composite materials

1.2.1.1.1. Type of impact

To simulate an impact event which is representative of the service environment, different tests are available, depending on the velocity and on the mass of the impactor and the stiffness of the surrounding structure. Generally, there are four types of impact with respect to velocity: low-, high-, ballistic- and hyper-velocity [68] (Table 1.3). However, there is no clear transition between categories and their definition is controversial. Some studies define LVI as a relative velocity between the impactor and the target as up to 10 m/s [69]–[71] while other define LVI as a relative velocity in the range 1–100 m/s [72].

The consequences of the test are directly linked to the response of the structure, as shown in Figure 1.7. If the contact time is of the order of the transition time for elastic waves, the behavior will be controlled by transverse waves (ballistic impact, Figure 1.7–a). For a longer time period, the behavior will be controlled by flexure and shear waves, consecutive to an Intermediate Velocity Impact (IVI) (Figure 1.7–b). If the impact duration is greater than the time for the elastic waves to arrive at target edges, the consequential behavior will be quasi-static, corresponding to Low Velocity Impact (LVI) (Figure 1.7–c).

Table 1.3 – Type of impacts depending on velocity range [73]

Type of impact	Velocity range (m/s)	Test equipment	Applications
Low Velocity Impact (LVI)	< 10	– Drop Hammer – Pneumatic accelerator	– Tool drops
Intermediate Velocity Impact (IVI)	10 – 500	– Compressed air gun – Gas gun	– Blast debris – Hurricane and tornado debris – Foreign objects debris on roads and runways
High Velocity (ballistic) Impact	> 500	– Compressed air gun – Gas gun	– Arm fire – Explosive warhead fragments
Hyper Velocity Impact	> 2000	– Powder gun – Two stage light gas gun	– Micrometeorites

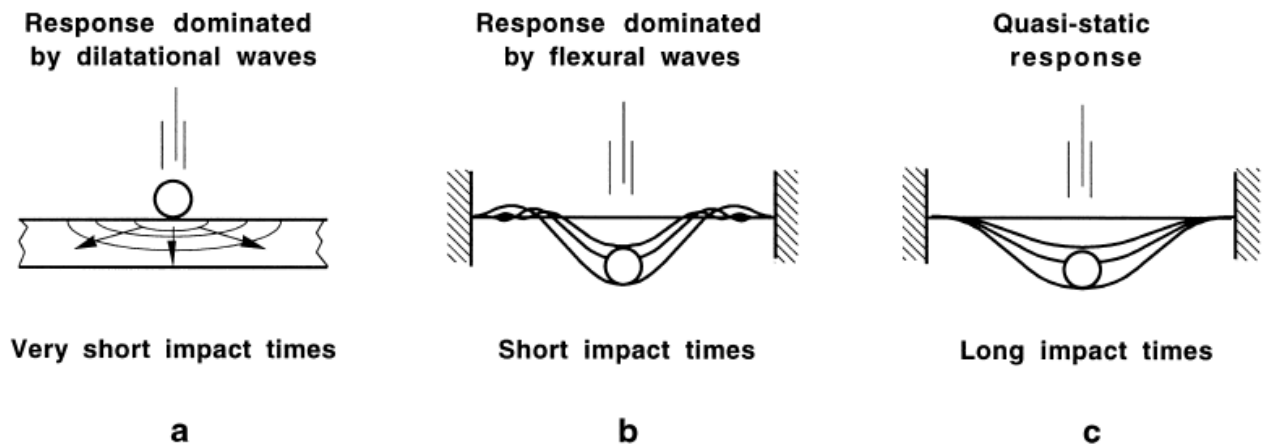


Figure 1.7 – Impact regimes on structures (adapted from [74])

In the marine environment, common impact events include collisions with floating debris, with other craft, docks, grounding, and handling issues. All these impacts are considered as Low Velocity Impacts (LVI) [75] so this thesis will focus on LVI. This impact type is generally simulated in the laboratory using a falling weight or a swinging pendulum. In this case, the contact period is such that the whole structure has time to respond to the loading [76].

1.2.1.1.2. Direction of impact

The direction of impact is also critical. Depending on the application, impact events happen parallel or perpendicular to the fibers. Events are then called respectively in-plane or out-of-plane impact.

In automotive, aeronautical, and aerospace applications, high energy impacts are possible. To face the problem, studies have been performed on absorbers, which is defined as a system that converts, totally or partially, kinetic energy into another form of energy [77]. Metallic absorbers have been studied, then composites, because of their high strength-to-weight ratio and their high specific energy absorption characteristics (SEA) [78]. Energy absorption induces macroscopic damage, which can lead to the complete failure of the system. A recent study was performed to understand the energy absorption during the progressive crush of CFRP structures [79].

In applications where lower energy impacts are possible, it is necessary to characterize the resistance of composite panels. Introduction of core material can improve the structural resistance, and the properties of each composite component affect the global response of the panel [80].

Because normal impacts rarely occur in real engineering situations, it is important to study oblique impact. For example, a low-velocity oblique impact study on composite sandwich structures, consisting of carbon/epoxy skin and Nomex honeycomb core, was performed under four different impact angles (0°, 5°, 10° and 15°) [81]. The authors concluded that the damage area decreased with increasing impact angle, as the contact area between impactor and upper face-sheet decreased with the angle of obliquity. In addition, it was observed that the maximum contact force (peak force) and absorbed energy decreased with increasing impact angle. However, the contact time and maximum impactor deflection were independent of this

parameter. Other studies showed a high influence of the angle between the firing axis and the fiber orientation on the shape of the fracture surface and on the tearing energy threshold [82]. The damage mechanisms for the glass/epoxy woven fabric studied were shown to be highly dependent on the orientation of the impact axis.

1.2.1.1.3. Scale effects

Impact testing on full-scale composite structures is complex and expensive, and is seldom carried out [83]. To limit costs, tests are performed on small samples, but respecting the conditions in which the composite structure will work. To this end, scaling laws have to be developed, to ensure that the laboratory sample tested is representative of the composite structure, and allow extrapolations of results to a larger scale [84]. In the case of composite materials, the main issue is to scale a sample representative of the interactions with the structure. Ideally, impact test fixtures should be designed to simulate the loading conditions to which a composite component is subjected in operational service and then reproduce the failure modes and mechanisms likely to occur. As recalled in a recent review [84], the concepts of similitude and dimensional analysis can be used to develop scaling laws [85]. A scaling factor λ is generated as a function of the ratio between different variables. This approach has been followed to scale low fiber-volume glass-polyester laminate samples intended for impact testing [86]. The author concluded that the simplified model was coherent compared with experimental results, but some “size effects” appeared, particularly for the damage response.

Other approaches have been developed, such as analytical or numerical scaling models. Assuming that the impact delamination is shear controlled, an equivalence model function of impactor properties and thickness of composite panel has been proposed (Eq. 1.1) [83] :

$$\frac{(m \cdot V^2)_2}{(m \cdot V^2)_1} = \frac{t_2}{t_1} \quad \text{Eq. 1.1}$$

Here m and V represent respectively the mass and velocity of the impactor, t is the thickness of the sample, and 1 and 2 represent the sample or the full-scale structure.

However, this technique has limits, and does not work when the scale difference is too high between the full-scale structure and the laboratory sample. Additional mechanisms such as edge delamination may occur for example, and great care is needed in avoiding differences in material meso-structure and manufacturing defects.

Another model has been proposed (Eq. 1.2) [83], to determine the critical load above which delamination occurs. This model considers material parameters (Young’s modulus E , Mode-II strain energy release rate G_{IIc} and Poisson’s ratio ν) and structural parameters with the thickness h .

$$P_c = \frac{2\sqrt{2\pi}}{3} \cdot \left(\frac{EG_{IIc}}{1-\nu^2} \right)^{1/2} \cdot h^{3/2} \quad \text{Eq. 1.2}$$

This model was applied in [86] and the authors showed a good correlation with experimental results.

Other numerical approaches have been proposed [87], such as FEA to predict the scaling of low-velocity impact on composite panels (E-Glass/Vinyl ester).

1.2.1.2. Impact on marine composites

Since environmental effects are directly linked to the durability of structures, marine type laminate materials and in-service impact events need to be characterized to understand the influence of impacts on composite materials.

1.2.1.2.1. Marine laminates

Different types of composite materials are used in a marine environment, such as sandwich laminates, single skin laminates, filament-wound tubes, or pultruded laminates. For laminates, composites are composed of two components: a matrix and a reinforcement.

➤ Composite matrix polymers

The matrix can be thermoset (cross-linked polymer) or thermoplastic (linear polymer). They are defined by characteristic temperatures. For thermoplastics, in the normal ascending order, these are the glass transition temperature (T_g), the peak crystallization temperature (T_c) and the crystalline melting point (T_m), the latter two are not applicable to fully amorphous polymers. For both types of matrix, thermo-mechanical behavior is dependent on the T_g . Below this temperature, in very general terms the matrix is normally elastic and brittle, while above this temperature the matrix is normally viscoelastic and tough.

The most common thermoset resins are epoxies, unsaturated polyesters, phenolics, and vinyl esters. In the present study all thermoset composites were made with an epoxy resin.

For thermoplastic polymers, the most common are polypropylenes (PP), polyamides (PA), polyesters (PET) or high temperature thermoplastics such as PEEK (polyetheretherketone) and PPS (polyphenylene sulfide). In the present project, PEEK will be studied as a substitute for epoxy resin.

Table 1.4 presents advantages and drawbacks of both matrix types.

➤ Composites reinforcement

Composite structures are reinforced by fibers, which can be aramid, carbon, glass, polymeric or natural fibers. The reinforcement can be arranged in a variety of different ways and this results in ranges for both the achievable fiber volume fraction and the reinforcing efficiency. Reinforcement can be woven fabrics, stitched or knitted fabrics, braids, 3D woven fabrics or preimpregnated reinforcements. Only continuous fibers will be considered here.

➤ Sandwich structures

Because of their specific properties (high bending stiffness with low overall density), sandwich laminates have been adopted for many marine structures, such as racing boat hulls. They consist of stiff, strong skins on either side of a lightweight core [88]. This configuration moves the reinforcement materials away from the neutral axis of a beam or plate, conferring higher stiffness without a significant increase in weight. Skin

materials follow the approach of monolithic composites, while the core may be a natural material, polymeric foam, corrugated structure, or honeycomb.

Table 1.4 – Advantages and drawbacks of TS and TP composites [89]

	Thermoset composites	Thermoplastic composites
Advantages	Low viscosity Suitable for high temperatures Low processing temperatures Well-established properties Excellent bonding with fibers	Infinite shelf life Recyclable/reparable Impact resistance No emissions
Drawbacks	Limited shelf life Difficult to manufacture thick composite parts Mostly non-recyclable, (though some recyclable epoxies are now being tested for wind blades).	High viscosity High manufacturing temperatures Limited marine experience Generally more expensive

1.2.1.2.2. In service impact events

In service impact events are extremely dangerous for composite structures (Figure 1.8) and are difficult to study and to reproduce in laboratory environment. There are many types of impact, linked with the large range of marine structures. From small boats to frigates and fast ferries, from marine jetties to offshore production platforms, the corresponding loading conditions are very different. The impact tolerance required will depend on the usage of the structure, for example pleasure boats need tolerance to accidental damage, while ocean-racing yachts need additional wave slamming and floating object resistance [90].



Figure 1.8 – Examples of structural damage on vessels due to marine impacts [91]

There is a complex relation between laboratory tests and real marine events. The critical point is to evaluate the impact resistance, which should model the collision with debris fairly accurately, with local stress levels close to the reality. Impact criteria have been proposed and separated into three categories: collision with a floating or submerged object, objects dropped onto a deck, or low-speed berthing impacts.

In order to replicate a floating object hitting a vessel in operation, drop test were performed on single skin GRP panels at an oblique angle of 24° [92], which was considered as representative. The results were

different compared with an angle of 90° , highlighting the influence of impact angle. In addition, oblique impacts at angles from 0° to 30° were considered for chopped strand mat (CSM) laminates [93]; the authors concluded that delamination area and permanent indentation depth were lower at more oblique angles, leading to the observation that residual tensile strength was at minimum for perpendicular impacts, especially at higher impact energies.

In several geographic regions, another possible impact is with floating ice. This has been studied recently, and results showed a complex problem, due to extremely variable size, shape and consistency of ice, which limits the possibilities to perform equivalent tests to real cases in the laboratory [94].

However, to the knowledge of the author no research results are available in the open literature for impact events on composite marine propellers.

1.2.2. Out-of-plane impact and material parameters

An impact event on composite material is complex because of the heterogeneity of the anisotropic material. Damage is a function of the loading level, of the geometrical parameters of the impactor, and of the composite constituents. Because of the range of impact types in marine environment, only out-of-plane impacts have been reviewed here. Some other possibilities will be discussed in the final chapter of the manuscript.

1.2.2.1. Types of damage induced by impact

In composite materials, high stress levels can induce irreversible damage in the material, leading to deterioration or, in the worst case, to the destruction of the material. During transverse LVI, four major modes of failure are discussed in the literature, due to the heterogeneous and anisotropic nature of fiber-reinforced polymer laminates [76].

1.2.2.1.1. Matrix damage

The first damage is the matrix mode. Cracks appear parallel to the fibers, due to tension, compression or shear stresses, with sometimes debonding between fiber and matrix. This is due to a mismatch between the mechanical properties of each constituent, leading to singularities in the material. Cracks are usually oriented in planes parallel to the fibers direction in unidirectional layers [95].

During transverse impact on composite laminates, the contact force and contact area lead to high transverse shear stresses, which cause shear cracks inclined at approximately 45° . The matrix cracks in the upper layer (Figure 1.9–a) and the middle layer (Figure 1.9–b) start under the edges of the impactor. The crack on the bottom layer of Figure 1.9-a is named a bending crack because it is induced by high tensile stress and is characteristically vertical. This stress initiates damage, which will be maximal near the back face. For composites, bending matrix cracks are

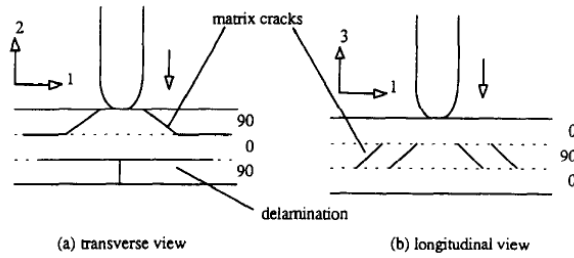


Figure 1.9 – Initial damage in an impacted 0/90/0 composite plate [76]

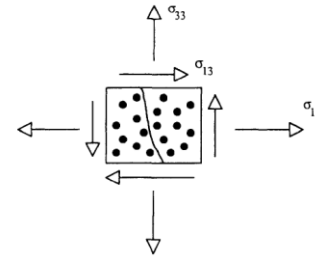


Figure 1.10 – Diagram of the stress components contributing to a bending matrix crack in a transverse layer

The literature showed that bending stresses are closely related to the flexural deformation of the laminate [96][97]. Bending cracks in the 90° layer are caused by a combination of σ_{11} , σ_{33} and σ_{13} (Figure 1.10) for line-loading impact damage. It appears that σ_{33} is very small relative to σ_{11} and σ_{13} throughout the impact event, and that there is a critical energy below which no damage occurs [98].

1.2.2.1.2. Delamination

The second damage type is delamination, which occurs when a crack runs in the resin-rich area between plies of different fiber orientation. A major cause of delamination is a bending induced stress, due to a bending stiffness mismatch between adjacent layers, which depends on fiber stiffness and orientation [99]. The delamination area is generally rectangular with the major axis being coincident with the fiber orientation of the layer below the interface. Depending on stiffness mismatch parameters, four different patterns have been characterized in the literature [100]. Circular is the most basic and widely used, but the twin ellipse pattern, the peanut or lemniscate, and the split peanut exist.

A bending mismatch coefficient M between the two adjacent laminates which includes bending stiffness terms and predicts the peanut shape [99] was defined (Eq. 1.3). The greater the mismatch, the greater the delamination area will be. However, other parameters influence the delamination area: material properties, stacking sequence and laminate thickness.

$$M = \frac{D_{11}(\theta b) - D_{11}(\theta t)}{D_{11}(0^\circ) - D_{11}(90^\circ)} \quad \text{Eq. 1.3}$$

where θb and θt represent the fiber angles in the two adjacent layers considered, b for bottom layer and t for top layer. The difference in the bending stiffness is normalized by the difference in the bending stiffness between 0° and 90° directions.

Delamination is a two-step process. The first step is initiation, which occurs when the stress at the interface exceeds the polymer capability. Delamination is initiated as a mode I fracture process due to out-of-plane normal stresses caused by the presence of matrix cracks and high interlaminar shear stress along the interface [98].

The second step is delamination growth, or propagation. Most studies focus on interlaminar mode I (opening mode) and mode II (shear or sliding mode) fracture toughness. Critical strain energy rates G_{Ic} and G_{IIc} are often higher for GRP than for CFRPs, and strain energy rates are loading rate dependent for GRP, while for CFRPs they can remain relatively constant [101]. However, it is difficult to generalize as the type of matrix has also an influence: several thermoplastics have higher strain energy release rates than thermosets, which results in a lower delaminated surface at the same stress level.

1.2.2.1.3. Fiber failure

Another failure possibility is fiber failure. This usually appears much later in the fracture process than matrix cracking and delamination. Due to high local stresses and indentation effects, fibers break either under the impactor or on the non-impacted face because of high bending stresses. Fiber failure is generally an indication of catastrophic structure failure and can lead to a penetration mode.

An equation has been given in [76] to determine the energy E needed for fiber failure due to back surface flexure (Eq. 1.4).

$$E = \frac{\sigma^2 w t L}{18 E_f} \quad \text{Eq. 1.4}$$

Where σ is the flexural stress, E_f is the flexural modulus, w is the width, L represents the unsupported length and t represents the specimen thickness.

1.2.2.1.4. Penetration

The last damage type is penetration. It represents a macroscopic mode of failure and occurs when the fiber failure reaches a critical extent, enabling the impactor to penetrate the material. Most studies performed on this mode involve ballistic impact. However, this phenomenon can appear during LVI. It has been shown that the impact energy threshold rises rapidly with specimen thickness for CFRP [71]. An analytical expression (Eq. 1.5) has been proposed [76] to give the energy E absorbed during penetration:

$$E = \pi \gamma t d \quad \text{Eq. 1.5}$$

Where γ is the fracture energy, d is the diameter of the impactor and t is the plate thickness.

1.2.2.2. Impact testing parameters

During an impact test the response, such as deflection, damage or penetration, depends on different parameters. The fixture parameters (boundary conditions) are among the most important, and it is necessary to find laboratory testing conditions equivalent to impact events in service conditions.

1.2.2.2.1. Influence of the impactor

The first parameter to consider is the impactor. Impact test behavior is directly linked to the impactor/indenter geometry. There are various potential impactor objects, and the impactor should be the

one which reproduces real impact events. The main issue when studying the impactor geometry influence on composite damage is the interactions with the material.

In the literature, different impactors have been compared. An impactor shape influence study [102] showed that the energy absorbed by the composite laminate is highest when the impactor tip is sharp (Figure 1.11), while the peak force and the damage threshold load (DTL) are greater for blunt impactors which also provide the shortest contact duration. Similar conclusions were proposed in [103], and the authors found that the contact area is the key parameter which affects the energy absorption of the composite. Impactors with larger contact surface produce higher initial peak, higher maximum force, larger delamination between hybrid layers and shorter contact duration.

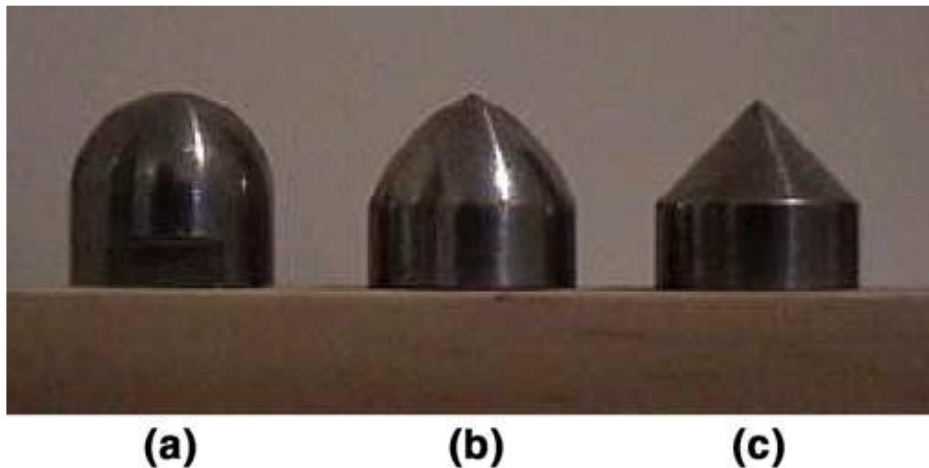


Figure 1.11 – Impactors used to characterize the influence of shape and tip on composite damage [102]

A LVI study performed on woven glass epoxy composite plates with variable impactor diameters showed that increasing impactor diameter leads to an increase of penetration and perforation thresholds, and an increase of the maximum contact force for the same impact energy [104].

1.2.2.2. Influence of the target

The role of the target can be divided into two parts. The first correspond to the thickness, the second to the curvature.

The target thickness is considered as a vital parameter, since it alters the energy absorption mode and the area of failure of the composite [105]. From a structural study (bending under LVI), the increase of span-to-depth ratio can change the response from structural (bending under LVI) to material [106], with local damage of composite material during LVI. In addition, a large span-to-depth ratio increases the deformation needed to break fibers, which leads to better penetration properties [107] and a decrease of the shear mode of deformation under impact loading [108]. A study of the influence of the thickness on the energy absorbed by woven carbon epoxy under LVI showed that the failure threshold shifts to larger impact energies as the laminate thickness increases [109]. Coupled with finite element modelling, experimental testing showed that above a span-to-depth ratio of 30, 2D FEM techniques could be applied to study damage patterns of composite laminates [110].

The curvature of the composite part is also important, as it adds a structural parameter to the material response. Both experimental and numerical studies have been performed, though numerical studies are more common. As an example of the former, impact testing was performed on AS4/3502 composite laminates with different thicknesses ($[+45/0/-45/90]_{ns}$; $n=1,2,3$), curvature radii (0.381m or 1.524m) and boundary conditions [111]. The authors found that flatter panels responded to impact with larger peak forces than more curved panels, as well as showing smaller peak displacements and contact durations. In a more recent study a test fixture was developed to impact curved plates extracted from tubes [112], in respect of full-scale structure boundary conditions (no free edges on tubes). Results showed good correlation for damage between impacted structures and impacted samples. In addition, the effects of a compressive load on the impact response of curved composite panels has been studied. LVI was performed on buckled composite laminates and it was concluded that compressive loads stiffen the global structure, but the tensioned part on the tension side promotes crack propagation [113]. Boundary conditions have been studied [114], and the authors concluded that they can significantly influence the susceptibility to damage by eliminating the back face delamination damage mechanism.

1.2.2.3. Material parameters

In addition to the two major constituents (fiber and matrix) composites also contain an interphase region, which is the area of bonding between fiber and matrix. This area includes the fiber coating, or sizing and is highly confidential for fiber manufacturers. The properties of each of these three constituents affect the threshold energies or stresses required to initiate the different failure modes induced by impact.

1.2.2.3.1. Influence of the reinforcement

In a composite material, fibers provide most of the strength and stiffness. Major fibers are glass (GF), carbon (CF) or aramid (AF). CF is more brittle with a strain at failure between 0.5 and 2.4%, while GF is more ductile, with a strain at failure about 3.2%. Aramid fibers have properties between CF and GF.

➤ Influence of the fiber type

During a LVI event, the ability of fibers to store energy elastically is the fundamental parameter [71]. It corresponds to the area under the stress-strain curve, which depends on two parameters: the Young's modulus E and the strain at failure ϵ_{xx}^R . Property optimization is also possible by using two types of fibers in the same composite [115][116]: this is referred to as hybridization. This technique can allow improved impact resistance, but moduli mismatching between the fibers has to be taken in account and may introduce additional complexity.

➤ Effect of fiber architecture

Another factor is the fiber architecture. UD composites are poor under transverse loadings and undergo large delamination, interface failure and matrix damage [71]. To address limitations of UD composites, 2D woven/bidirectional composites have been developed which show better impact resistance due to waviness of yarns in the fabric architecture (Figure 1.12). The main issue of these textiles is their in-plane properties

which are lower, due to stress concentration caused by the crimping of yarns. To avoid this issue, non-crimp fabrics (NCF) have been developed, which improve impact and delamination resistance [117].

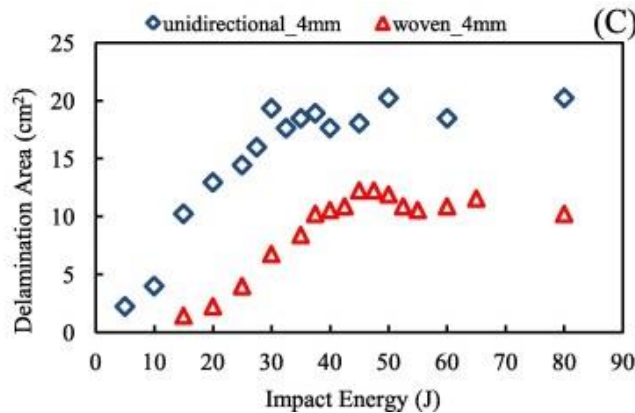


Figure 1.12 – Delamination area measured after LVI for two fiber architectures [105]

In addition, different technologies have been developed to decrease delamination probability, such as stitching which improves through-thickness properties such as interlaminar fracture toughness [118], z-pinning or 3-D weaving, which consist of introducing fibres in the z-direction. Z-pinning can improve transverse properties of laminates, such as delamination and interlaminar fracture toughness in both modes (I and II) [119]–[121], despite a reduction in the in-plane properties [122].

The development of 3D composites results in composite resistance improvements during LVI events. With these materials, impact performance is dominated by fabric architecture and the arrangement of yarns. Comparison between 2D and 3D architecture shows a better energy absorption capability of 3D composites [123], and better LVI properties due to the increased structural integrity of the fabrics [124].

➤ Influence of the stacking sequence

The last factor is the stacking sequence. The damage tolerance of laminated composite is also a function of the stacking sequence, and this has been characterized in the literature. Studies have shown that the stacking sequence affects delamination and plastic deformation [125], as well as the damaged area [126]. The coupling effects of stacking sequences on damage tolerance have been characterized [127] on benchmarking configurations developed in a previous study [128]. The authors concluded that anti-symmetric laminates give the highest damage tolerance, a little better than non-symmetrical laminates, while symmetrical laminates give the lowest. In addition, studies were performed to characterize the influence of stacking sequence on the Mode-I [129] and Mode-II [130] fracture toughness. Simulations were performed and showed large variations in the values of G_{IC} and G_{IIC} , due to coupling effects (bending/extension, extension/twisting or shearing/bending coupling).

1.2.2.3.2. Influence of the matrix

In a composite material, the matrix system can align and stabilize the reinforcements, allowing the load to be distributed uniformly across the cross section. Reviews in the literature ([80][131][132]) present comparisons between TP and TS resin systems, and the influence of the matrix on impact damage.

The main composite material parameter during an impact event is the fracture toughness of the resin system. According to the mechanical properties of the resin, cracking then delamination are more or less rapid. A brittle resin system has lower resistance to fracture onset and propagation compared to ductile resin systems. Improvements in the matrix fracture toughness lead to increasing resistance to fracture propagation, which raises the tolerance of the composite to interlaminar delamination onset generated by resin cracking [133].

In a transverse impact event a two-step delamination process begins via a crack opening (Mode-I) mechanism and continues via propagation which often occurs due to shear (Mode-II) induced by bending. Thus, the mechanical properties G_{IC} and G_{IIC} are of the utmost importance. A study on the interconnectivity of cracks and delamination [134] proposed a mixed-mode approach to study multiple delaminations during impact testing, which requires values of $G_{I/II}$. These coefficients are necessary to model progressive damage mechanisms, and the more accurate values of interlaminar and intralaminar fracture toughness are, the more realistic the finite element model results will be [135].

To obtain these mechanical properties, various tests have been proposed [136]. Studies performed showed the fracture toughness of many thermoplastics is higher than that of standard thermosets [137]–[139], resulting in an enhancement of structural toughness: the energy at failure is higher. In addition, the damage area is generally higher for thermoset matrix composites (Figure 1.13). It should be noted that these are general remarks, some rubber toughened epoxy composites show very high toughness while a thermoplastic matrix with a poor fiber/matrix interface will damage very easily.

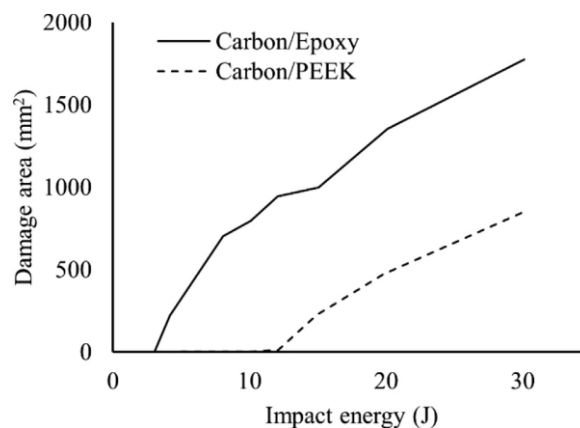


Figure 1.13 – Damage area (mm²) vs. Impact energy (J) : comparison between TS and TP resin system [140]

1.2.2.3.3. Influence of the manufacturing process

Manufacturing parameters have also been studied. For thermoplastics, cooling rate is the main factor. It was shown that fast cooled CF/PEEK was less damaged after LVI than slow cooled CF/PEEK [140] during LVI, due to a change of the degree and morphology of the crystallinity. Fast cooling (more amorphous microstructure) enhances systematically the ductility of PEEK matrix, which lead to high interlaminar fracture toughness and impact damage resistance of composite, while a slow cooling improves both the fiber/matrix interface bond

strength and strength/stiffness, resulting in high strength and modulus of the composite. A compromise between these parameters is needed to optimize the structural mechanical properties.

For thermosets, the effects of post curing on C/Epoxy properties have been studied [141]. In that study it was shown that increasing post curing temperature led to increased residual stresses. If compressive residual stresses are generated, an improvement in fracture toughness can result.

1.2.3. Experimental and simulation methodology for LVI on composite laminates

In-service impact events on composite structures are complex to understand and simulate. Qualification of new materials begins at the coupon scale to obtain the mechanical properties from simple loads. Then, impacts tests are performed and simulated from the data obtained at coupon scale. This section focuses on the impact tests and the simulation.

1.2.3.1. LVI impact experiments

Standard tests exist for low velocity impacts. In most cases, coupons are supported by the fixture and then clamped to avoid sliding during the test. A window allows the coupon deflection, leading sometimes to delamination. Impactor velocity prior to the contact is measured and the impact kinetic energy is determined from the impactor mass. In addition, a high-speed laser sensor is often used to measure the out-of-plane displacement of the coupon.

1.2.3.2. Damage assessment using destructive (NE) and non-destructive evaluation (NDE)

Different techniques exist to characterize the damage extent in a composite laminate after an impact event. These techniques can be either destructive or non-destructive.

1.2.3.2.1. Microscopy

One of the most common techniques is microscopic observation. The coupon is cut then polished with micron-graded abrasives. Observations at different magnifications (by optical or scanning electron microscopy) allow the characterization of the type of damage involved during the impact. Figure 1.14 shows an example of an impacted coupon observed with a microscope. This technique can be coupled with penetrant impregnation to highlight the damage pattern [142]. Macroscopic porosities can also be measured with this technique.

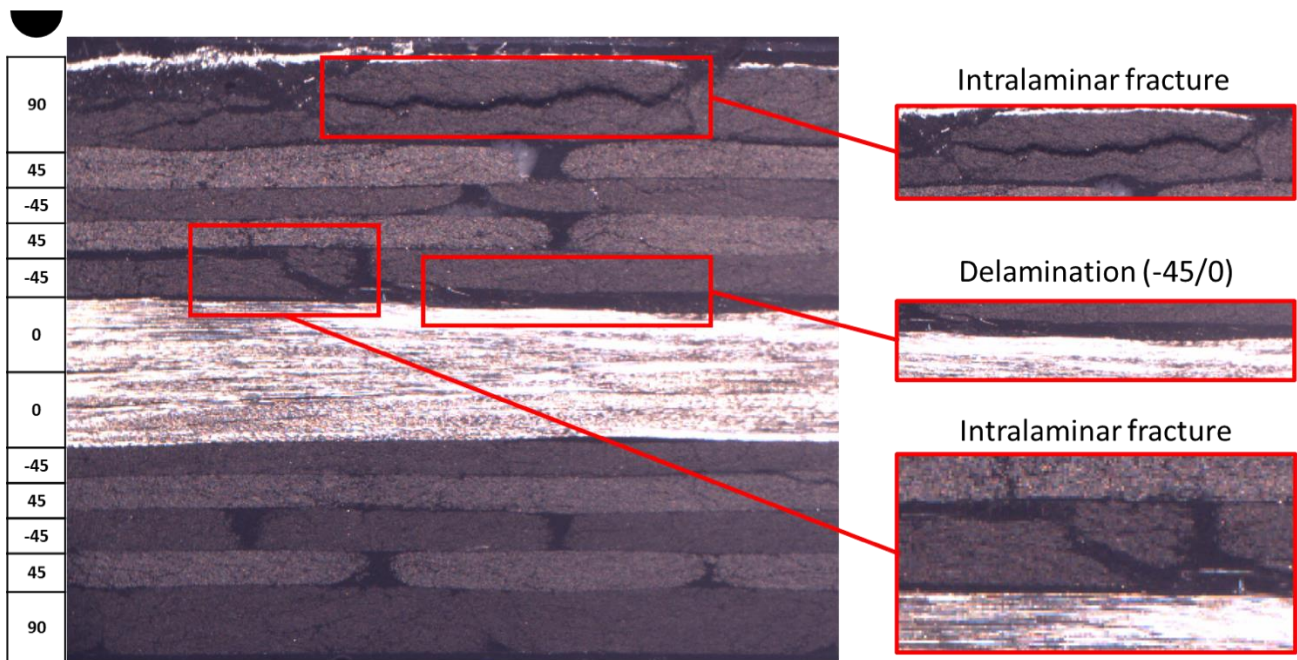


Figure 1.14 – Example of a micrograph on C/Epoxy coupon impacted at 80J

1.2.3.2.2. Infrared thermography

Another technique is infrared thermography (IR). This technique assumes that energy is released in the material when a damage occurs. Experimentally, an IR camera records the thermal changes on the coupon surface during the test. This technique has been used to track the crack tip during a pure mode II cracking test [143] at a high loading rate. It can be used during an impact test to reconstruct the damage scenario [144].

This technique can also be used after a test for damage monitoring, but a thermal excitation is then necessary. In this case, damaged parts of the coupon are supposed to locally modify the thermal diffusion. On the thermal image, the damage will be observed as a singularity [145].

1.2.3.2.3. Ultrasonic mapping

One of the most widely used NDE techniques is ultrasonic mapping (Figure 1.15). The basic principles of ultrasonic inspection are well-established [146]. Ultrasonic waves are generated by piezoelectric transducers which convert an oscillating applied voltage into mechanical vibrations. This technique is often performed in a water tank where the composite coupon is immersed, but it can also be performed in air if a couplant is used. The latter ensures that ultrasonic waves propagate from the transducers to the composite coupon. Once the waves reach the coupon surface, a part is reflected due to the water/composite interface. The transducer receives the reflected signal and allows the detection of the gate entrance in the material. For the rest of the signal, the wave crosses the laminate thickness and is reflected by a metallic sheet positioned a few millimeters from the coupon lower surface. The signal then received by the transducer is defined as the way-out gate. However, if damage is present within the sample thickness, part of the wave will be

reflected toward the transducer. The obtained output is an array of ultrasonic wave attenuation signals in dB.

One of the most useful post processing methods is known as C-Scan. A map is built from the attenuation signals measured and the displacement of the transducer on a plane parallel to the coupon upper surface.

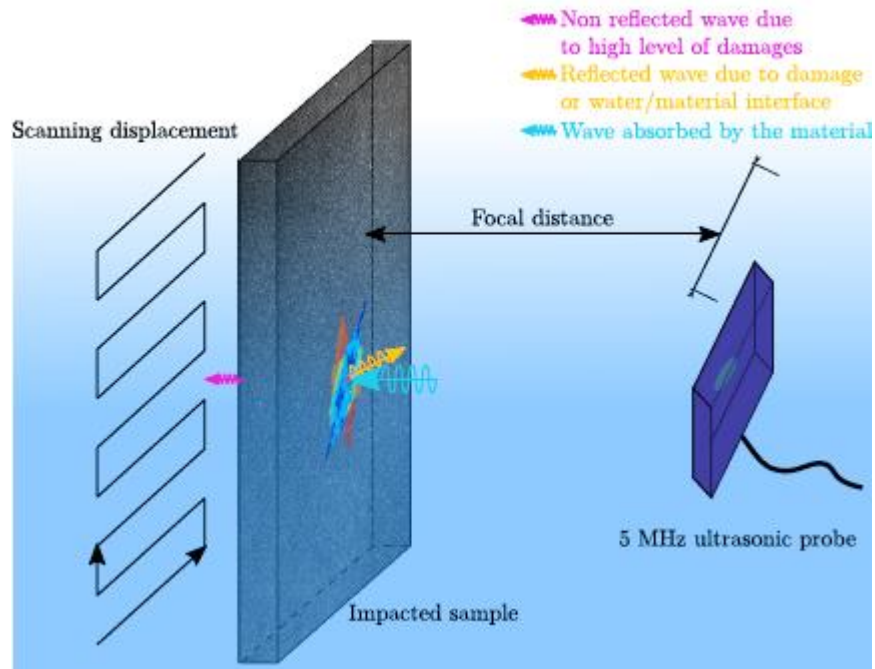


Figure 1.15 – Schematic diagram of the non-destructive evaluation of an impacted coupon (from [144])

1.2.3.2.4. X-ray computed tomography

The recent development of X-ray tomography provides a powerful technique to investigate damage within composite specimens and is being increasingly applied to impact studies [123][147]. During a scan, the damaged coupon is rotated within an X-ray beam. A large number of 2-D radiographs are taken, which are then assembled to provide a 3-D image. As the material absorbs X-ray radiation, the presence of damage results in voids, which do not absorb radiation. Therefore, the X-ray detector captures the X-ray radiation escaped from the material due to damage and a map of density variations can be constructed.

The limiting factor of this technique is that the resolution depends on the sample dimensions. The closer to the source the coupon is, the better the resolution. However, a minimum safety distance is required to avoid a collision when the composite panel is rotating.

1.2.3.3. Residual strength after LVI

The damage tolerance is defined as the capability of a composite structure to maintain its undamaged or initial properties after the introduction of damage. For composites, damage tolerance is determined by measuring the residual strength. The most common method to determine damage tolerance is to produce barely visible impact damage (BVID), and then to perform mechanical testing to measure residual strength, e.g. compression after impact (CAI) or flexure after impact (FAI).

1.2.3.3.1. Compression after impact (CAI)

To evaluate compression strength after impact, a standard approach has been proposed [148] and is defined by three steps. The first corresponds to inspection of the specimen with a nondestructive evaluation technique (NDE). The second corresponds to the impact with measurement of the event. Then, an in-plane quasi-static compression test is performed in a CAI support to prevent global buckling. Studies performed on thick monolithic GRP laminates have shown that the residual compressive strength can be greatly reduced [149] by impact damage due to delamination and changes of local fiber curvature in the contact area [150].

1.2.3.3.2. Flexure after impact (FAI)

Interlaminar shear stress (ILSS) and flexural strength have been measured after repeated impacts on GRP in [151]. The authors concluded that a single impact loading leads to a slight reduction in flexural strength but a large reduction in ILSS. This was explained by the fact that a single impact creates the main types of damage necessary for shear failure, while repeated impact propagates damage throughout the structure. In addition, three-point-bending is not recommended because the loading roller presses onto the center of the damage area. A study performed on GRP after impact showed that greatest loss of flexural strength occurred because damage reached the edges of the beam [152], so specimens must be of appropriate size with respect to damage.

1.2.3.3.3. Tolerance to other loadings

Under operating conditions, loadings are not limited to compression or flexure. A study performed on thick GRP tubes showed that low impact energy resulted in a large drop in subsequent implosion pressure resistance [153]. The authors concluded that this corresponded to the appearance of intralaminar cracks rather than delamination. For fatigue behavior, a post impact fatigue (PIF) study performed after marine ageing then LVI compared the mechanical behavior of plain woven and multiaxial knitted fibers [154]. The authors concluded that for plain-woven reinforcements the effects of water absorption were small, while for multiaxial knitted fibers, PIF properties were drastically decreased.

1.2.4. Simulation of LVI and CAI

The Building Block Approach (BBA) is a progressive qualification process in which each step needs both experiments and numerical simulations to be validated. The LVI impact test (ASTM D7136) and the CAI test (ASTM D7137) have been developed to evaluate the tolerance to damage of composite coupons and characterize the drop of residual strength due to the impact. The simulation of both these tests is necessary to validate the mechanical properties obtained at coupon scale. The results of the simulation can validate a complete dataset, which will be used to simulate an impact on a more complex structure.

The most common approach is at the meso-scale. Each ply of the composite is described with one element through the thickness. The mesh density is chosen to reduce the computation time while keeping a good

accuracy. It can be thin close to the impactor contact area, and coarse further away. Recent reviews of modeling techniques at the element scale have been proposed [144][155].

1.2.4.1. Impact models using stacked shell elements

The use of continuum shell elements (SC8R) is a possibility offered when using Abaqus™. Compared to conventional shell elements such as S4R, they capture more accurately the through–thickness response for composite laminate structures. These elements are reduced (low-order) and are often used with their first–order (linear) version for composites to reduce the computation time. An hourglass control is therefore necessary. For delamination prediction, both cohesive surfaces and cohesive elements (COH3D8) can be used. Even if cohesive elements are known to give better results, especially for mixed–mode bending, given the computation cost cohesive surfaces are often considered to be sufficient. Another advantage of the cohesive surfaces is their ability to connect two regions with different mesh sizes.

A continuum damage mechanics model based on the Hashin criterion [44] is implemented and ready to use in Abaqus™. Once the damage criterion is reached, a degradation procedure can be applied. SC8R elements have been used recently in [156]. The authors have shown a good prediction of both the stiffness and the maximum force. The contact time has been found to be longer numerically than experimentally.

1.2.4.2. Impact models using stacked solid elements

Another approach is to use elements with 3D formulations (3 degrees of freedom per node). The approach works in a similar way to a stacked shell model. However, due to the element’s formulation, all the stress components are computed and in particular σ_{23} which is mainly responsible for matrix damage. With respect to the mesh, a coarser mesh far from the impactor contact area allows the computation cost to be limited [157]. A recent model uses cohesive elements both for delamination prediction and inter fiber failure [158]. This model is more complex to build since both cohesive surfaces and cohesive contacts need to be placed between ply elements oriented in the fiber direction. It has shown accurate results and can predict the final indentation of the coupon.

1.2.5. Testing and modeling of impact on composite blades

Experimental testing and numerical analysis of composite blades must be performed in parallel if the models developed are to be validated. Blades are manufactured using foam, composites and sometimes metallic shields to reduce damage caused by impact (Figure 1.16). Because of the experimental cost of manufacturing, impact testing on composite blades has been more studied numerically than experimentally. However, two kinds of impact can occur: frontal impacts on the leading edge, and oblique impacts on the lower skin of the blade. The relevant impact angle depends on the blade inclination when the propeller is rotating.

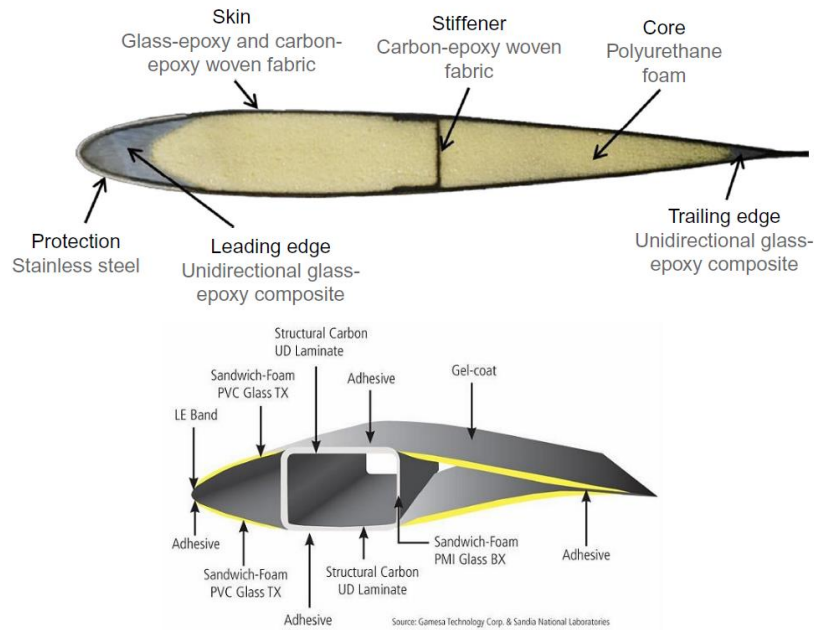


Figure 1.16 – Helicopter section blade [159] and wind turbine section (Sandia National Laboratories)

1.2.5.1. Experimental testing

Several experimental tests can be performed to characterize the behavior under impact of composite blades. Wind turbine blades are also subjected to environmental effects, which lead to material degradation [160]. This type of degradation induces progressive structural damage, whereas impact testing can lead to destruction of a blade. The influence of reinforced foam core has been studied [161], as well as the obliquity [162] where authors concluded that elastic response is largely dependent on the curvature: when the curvature increases, the stiffness decreases. On helicopter blades, front edge impact testing (Figure 1.17) has been performed at different energies [66]. The authors concluded that the front edge is the first element that undergoes damage, and then a rise of the impact energy level causes a plastic deformation of the stainless-steel protection, which leads to the skin-foam delamination of the structure. UD glass-epoxy behind the steel protection was affected by the impact, with damage observed in the rovings. Slipping of the bundles of fibers on both sides of the impacted zone was observed, due to resin cracks. This study was performed using non-standard impact tests.

It is also important to note that impact energy during the LVI is not a sufficient parameter to characterize the impact response: it needs to be uncoupled, between impactor velocity and mass. Previous research has found that at the same impact energies, failure modes can be different, due to the influence of these two parameters [163].

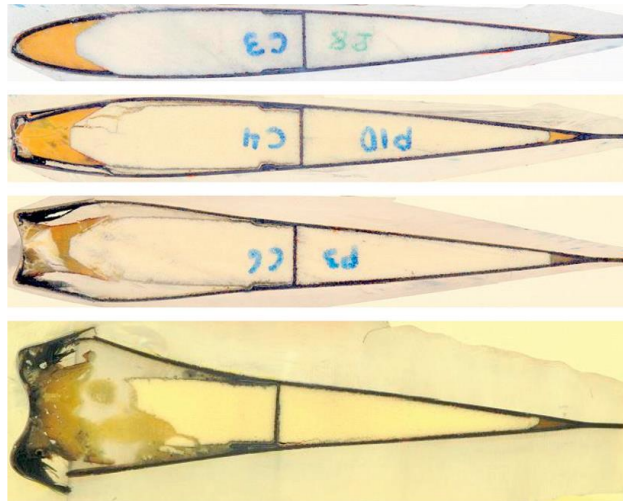


Figure 1.17 – Blade cross section in the plane of impact [66] for different energy levels.

1.2.5.2. Numerical analysis

To limit experimental campaigns, numerical studies have been performed to understand the behavior of composite blades under impact. In the wind turbine industry, results from different numerical modeling methods have been compared for a composite blade [164] subjected to leading edge impact. The authors mentioned that a realistic composite structure, such as the DTU 10 MW blade they studied, has larger flexibility with complex boundary conditions compared to its coupon scale–representation. Three existing techniques were studied using Abaqus™: (1) the pure shell technique, and global–local methods based on (2) shell–to–solid coupling, and (3) sub–modelling. In this study, a reference model based on shell elements was chosen. Advantages and drawbacks of each method are presented in Table 1.5.

Some papers have also described results for helicopter blades subjected to impact. A modeling strategy which consisted of separating the functions of the fiber bundles from those of the resin was proposed [165]. This strategy gave a good representation of the kinematics of the skin damage, and was validated by representing several load cases, such as static normal indentation, low velocity normal impact and high velocity oblique impact (Figure 1.18).

Table 1.5 – Advantages and drawbacks given for three numerical analysis techniques [164]

Indicator	Pure-shell-based modelling technique (1)	Shell-to-solid coupling technique (2)	Submodelling method (3)
Impact response	<ul style="list-style-type: none"> – Stiffer response to the impact exhibited – Higher maximum contact force – Smaller contact duration – Underestimation of the out-of-plane displacement of the impactor and of the permanently absorbed energy levels 	<ul style="list-style-type: none"> – Similar results for the contact forces, displacements, and energies – Predict a softer response 	
Energy results	<ul style="list-style-type: none"> – Same results for all the three techniques: due to flexural ability of composites, the largest part of impact energy is stored then restored as elastic strain energy. The remainder of energy (2–30%) is dissipated by permanent damage and inelastic deformations. 		
Impact-induced damage evolution	<ul style="list-style-type: none"> – Limitations to predict failure modes due to impact on the blade at its leading edge. – Good prediction of the flexural failure mode in the laminate face sheet upon impact – Damage due to local deformations is not captured – Simulation type does not consider lay-up, and damage associated is not represented 	<ul style="list-style-type: none"> – Methods can model and predict all major impact-induced failure modes – Results are similar to expected 	
Calculation time and cost	<ul style="list-style-type: none"> – Cheapest technique 	<ul style="list-style-type: none"> – Equivalent to (3) – 2 times calculation duration of (3) 	<ul style="list-style-type: none"> – Most efficient analysis technique – Providing closer impact response and damage evolution than other techniques

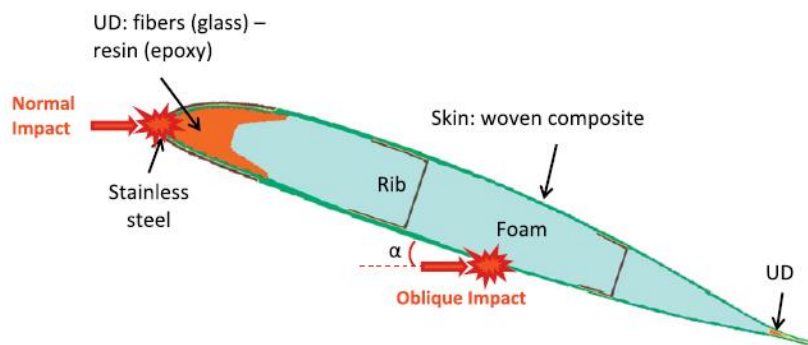


Figure 1.18 – Section of the blade studied in [165]

For the wind turbine industry, bird impacts have also been studied, because of the probability of these events and potential damage they can generate [166].

1.2.6. On-edge impact tests

Few studies published have focused on the in-plane/edge impact. This test is known to be locally more severe. In [167], the author applied the Discrete Ply Model [168] to simulate the edge impact test. They found

that if the fibers were oriented in the impact direction, then kink-bands were created. In addition, regardless of the energy level and stacking sequence, a specific crushing plateau phenomenon appeared. This was modeled by multiplying an average crushing stress of 250 MPa by an average projected area of impact of 25 mm². Finally, the force-displacement curves have been found to have the same initial stiffness, and the authors concluded that is due to the fibers properties.

Another study [169] compared edge-on impacts with two incident angles, 0° and 45°. Authors found

1.2.7. Conclusion

Impacts on composite structures are complex to understand because of the heterogeneity of the structure. They are also very important, because in a marine environment they reduce durability with consequences both for the economy and safety.

In the framework of this thesis study, some areas of work not hitherto reported in the literature will be investigated. The main objective will be to perform impact tests on coupons representing composite marine propeller blades. These tests will be performed using a thermoset CFRP composite made with an epoxy resin by vacuum infusion, and studied in a previous thesis [170].

A second objective is to examine the influence of specific marine aging parameters on quasi-static and impact performance, and this will be discussed in Chapter 3 and Chapter 4.

Finally, compared to out-of-plane impact, it is important to ask how the damage produced by in-plane-impact will affect the residual mechanical properties and service life of the composite part, this will be considered in Chapter 5

1.3. FRP aging and durability

Two types of ageing can induce mechanical property modifications during the lifetime of a polymeric structure in marine environment. This third section will be devoted to a review of these ageing mechanisms. Long term immersion in seawater will modify mechanical properties: this phenomenon is named seawater ageing and may or may not be reversible after drying. The effects of manufacturing and storage conditions also influence the material behavior: this effect is defined as physical ageing and is reversible if temperature is raised above T_g .

In the case of this thesis, a material studied in a previous study [171] will be considered. This material is a carbon/epoxy composite, with hygromechanical properties depending on the physical ageing.

1.3.1. FRP aging and durability

1.3.1.1. Molecular structure and physical aging

1.3.1.1.1. Molecular structure of epoxies and configurational changes

An epoxy is a resin formed from two constituents: a monomer and a hardener. Mixing these constituents leads to a cross-linked system with interesting mechanical properties. The molecular structure of a cured epoxy is amorphous. Manufacturing with epoxies starts in the liquid state, sometimes at elevated temperature to decrease the viscosity and to improve the wettability of the reinforcement. When the crosslinking process starts, the amorphous cross-linked structure is continuously stiffened by the presence of newly formed rigid crosslinks.

When a polymer is cooled, the molecular mobility decreases. The macromolecular network configuration changes required to reach the thermodynamic equilibrium become too slow to be reached in the time scale imposed by the cooling-rate. The polymeric material then freezes in a metastable state [172].

1.3.1.1.2. Configurational change

At the operating temperature, the polymeric material is not at equilibrium, which induces residual mobility to move slowly towards the equilibrium. This phenomenon, named ageing by structural relaxation, can be divided in three types. The first type is the orientation relaxation, when the material has been frozen in an oriented state, the main consequences will be dimensional, such as anisotropic shrinkage. The second type is the post-crystallization, when a material has been frozen before its crystallization was completed. In that case, consequences are both dimensional and mechanical, with an increase of the moduli and the stress threshold. Finally, the third type is the isotropic structural relaxation, which is common for all glassy materials.

For a glassy polymer, such as epoxy, structural relaxation at the molecular level can be described as progressive transformations from the least stable conformation to the most stable. It results in a densification of the molecular chains inducing a decrease of the free volume which strongly contributes to the molecular mobility: variations of the properties depending on the volume are then observed.

In polymers, the literature considers different characteristic temperatures [173]. The best known is the glass transition temperature T_g , which is characterized by a large decrease in modulus when temperature exceeds it. However, in the region of the transition, the material changes gradually from glassy to rubbery. This transition is accompanied by a high loss peak, the maximum of $\tan \delta$ generally lying between 1 and 3. This peak is called the α -peak. A second peak, T_β can be found at lower temperatures, related to other molecular movements.

Physical ageing kinetics vary. Ageing only occurs in a range of temperature between T_β and T_g , and the range $[T_\beta - T_g]$ can be either narrow (PS, PMMA, unsaturated polyester) or very wide (epoxy). In addition, this structural relaxation ageing is highly dependent on temperature, since the larger the distance from the

thermodynamic equilibrium, the more the phenomenon is accelerated. Finally, ageing can be “erased” because of the thermo–reversibility of the material. This phenomenon is named rejuvenation, and exposing the material to above- T_g temperature allows a total recovery of the initial state and properties of epoxy [174].

Minor transitions also occur in the glassy state for which the modulus decreases. They may have effects on mechanical properties, such as on the conservation modulus E' (Figure 1.19).

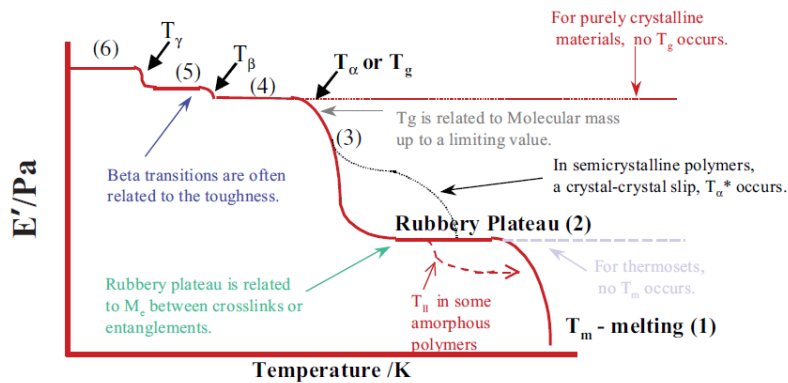


Figure 1.19 – Idealized DMA scan showing the types of transitions (PerkinElmer) – (1) chain slippage (2) large scale chain (3) gradual main chain (4) side groups (5) bend and stretch (6) local motion

Physical ageing induces mechanical property modifications, such as a decrease of the creep compliance (and an increase of the relaxation modulus) and an increase of the plasticity stress threshold which lead to an embrittlement of the polymer. In other words, the polymer embrittles during sub- T_g annealing, but with an aging history erasure above T_g , the ductile behavior can be restored.

It is possible to measure the effects of physical ageing using differential scanning calorimetry (DSC). Two phenomena appear: a T_g overshoot and an endothermic peak, such as presented on Figure 1.20.

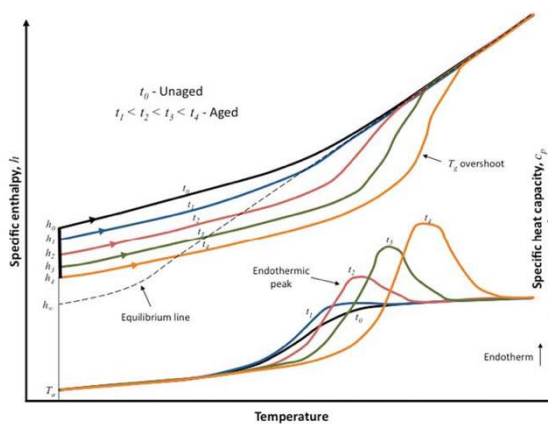


Figure 1.20 – Schematic diagram of enthalpy evolution during cycles corresponding to various aging times (top) and the heat capacity during the corresponding heating cycles (bottom) [175] (adapted from [176]).

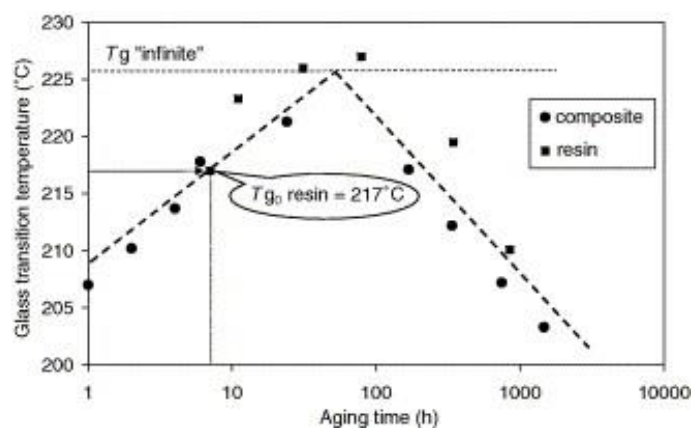


Figure 1.21 – Variation of a T_g on resin and composite after ageing at 210°C [177]

When testing unaged epoxies, there is a significant increase in the measured heat capacity near the glass transition region. This increase is caused by the rubbery-phase molecular motions, which are characteristic of the glass transition temperature. These motions require an increase in energy to be initiated. When testing aged epoxies, more energy is required to initiate the same rubbery-phase molecular motions, resulting in endothermic peaks of increasing magnitude centred at increasing temperatures (Figure 1.20). At increased physical ageing levels, endothermic peaks are more centred, due to T_g overshoot. However, chain ruptures can occur, leading to a degradation of the material; after reaching an optimum, T_g decreases (Figure 1.21).

1.3.1.1.3. Thermal rejuvenation

Effects of physical ageing can be reversed through thermal rejuvenation. Several mechanisms are presented in the literature. The most effective mechanism is the super- T_g thermal rejuvenation. When an aged epoxy is heated above its T_g for an appreciable time, the physical ageing history is lost. Different studies have been performed to determine the influence of super- T_g rejuvenation temperature and duration on the physical aging loss. One study concluded that heating the polymer at T , with $T > T_g + 40^\circ\text{C}$ for 10–15 minutes is more than adequate [178]. However, the rejuvenation can also occur at specific temperatures below T_g : this is named sub- T_g thermal rejuvenation. Studies performed have concluded that it occurs at fixed temperatures above T_α and below T_g [179]–[181]. The cause is the heterogeneity of the polymer structure, and when a sub- T_g temperature corresponds to a specific transition in the structure, the effects of physical ageing are locally erased.

1.3.1.2. Mechanical behavior of physically aged epoxies

1.3.1.2.1. Quasi-static testing

Many studies involving tension [182], compression [183] and 3-point bending [176] have been performed, allowing the measurement of the Young's modulus of epoxies at different physical ageing states. Conclusions from these studies diverge; some authors reported that the modulus is not affected by physical ageing while other saw a modest increase of elastic modulus of epoxy and epoxy composites with ageing.

Tension tests demonstrated that the ultimate tensile strain of epoxies decreased with increasing ageing time [171][174] and the different failure trends for different failure modes are caused by changes in microscopic failure mechanisms. An unaged epoxy is more ductile than an aged epoxy, and ageing embrittles the material, which results in lower loads for the growth of microcracks (Figure 1.22, Figure 1.23).

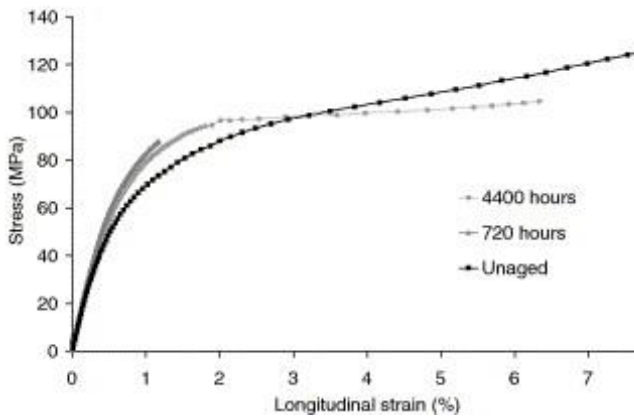


Figure 1.22 – Stress (MPa) – Strain (%) curves of tension testing on $[\pm 45]_{4s}$ IMS/977-2 laminate : influence of physical ageing [177]

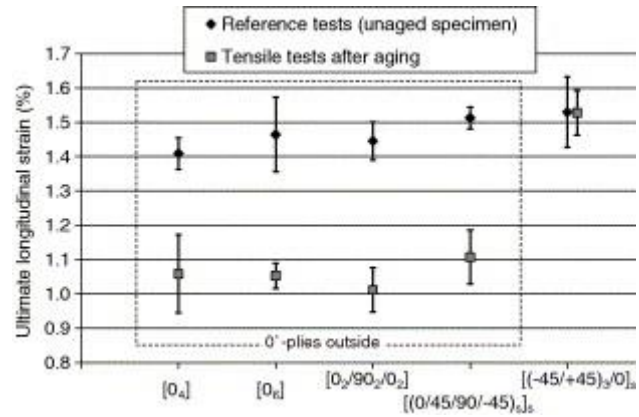


Figure 1.23 – Comparison of ultimate axial strain of different laminate lay-ups before and after physical aging [177]

A model derived from the Kohlrausch–Williams–Watts (KWW) model has been proposed to link the physical ageing to maximal stress Eq. 1.6 [171]:

$$\sigma_m(t) = \sigma_0 + \Delta\sigma \cdot \left(1 - e^{-\left(\frac{t}{\tau}\right)^\beta}\right) \quad \text{Eq. 1.6}$$

With $\sigma_m(t)$ the maximal stress function of t the ageing time, σ_0 the initial maximal stress without any ageing, β the damping factor and τ the characteristic relaxation time.

Fracture toughness studies were performed on epoxies [184][185]. It was shown that physical ageing of a DGEBA/DDS epoxy system reduced the critical energy release rate for initial crack growth $G_{i,c}$, but had little influence on the arrest energy release rate $G_{a,c}$. According to the authors, the decreases in fracture toughness and stick–slip behavior in aged epoxies were due to an increase of the yield point of the material, thus suppressing the crack–blunting mechanisms (toughening) associated with unaged epoxies.

1.3.1.2.2. Impact testing

Studies where impact testing has been performed on physical aged materials are rare. However, a recent study [186] compared the impact strength during LVI of carbon fiber / epoxy laminates, before and after physical ageing. The authors concluded that impact strength was increased by 12.5% after physical ageing. However, no other published studies were found either for thermoset or thermoplastic composites.

1.3.2. Polymeric composites in marine environment

The marine environment is severe for polymeric composites and can lead to the deterioration of mechanical properties. When polymers are exposed to fluids or vapor, the highly mobile and generally small molecules of the ambient phase penetrate the polymer. This process continues until equilibrium is reached.

The ingress of water is associated with increased separation of polymer chains, thereby inducing expansion strains. This thermodynamically reversible phenomenon is called plasticization. It increases chain mobility in

the same manner as increasing temperature [187]. However, another phenomenon appears due to water absorption: swelling. Published reviews [188][189] discuss a wide range of water uptake causes and their influence on durability of these materials.

The type and quantity of fibers has an influence on the maximal weight gain [190], in addition to the matrix type and fibre/matrix interface quality. The kinetics of sorption are also dependent on the solvent [191].

1.3.2.1. Diffusion of water in polymers and polymeric composites

Diffusion of water into polymers needs to be characterized, since it can induce mechanical property degradation. Different models are proposed in the literature, depending on the material chemistry.

In the case of ceramic fibers (glass, carbon), water diffusion is mainly located in the resin: the maximal moisture content and the transverse diffusivity of a composite can be estimated from resin studies, provided that resin and composites were processed in the same manner [191].

1.3.2.1.1. Water uptake in polymers and composites

The water uptake is largely dependent on the resin used as the matrix. A recent review presents the consequences of using thermoplastics or thermosets in different environments [187].

Epoxyes are hydrophilic thermoset resins, which can take up a large amount of water (5% by weight or more). The maximal uptake depends on the resin components (hardener and mix ratio), manufacturing process (post-curing), physical ageing and hygroscopic ageing conditions [192]. The absorption is due to the epoxy resin structure, which can accommodate two different types of water. The first is free water molecules, based on a physical approach: we consider that spaces between resin chains can be assimilated to “free volumes”, which enhance migration of water in the polymer. The second is bonded water molecules, based on a chemical approach: water is a polarized molecule which can create bonds with polarized sites of the epoxy chain ($-O=C-OH$, $-OH$, $NH-$, ...). In this case, we can consider two kinds of bonded molecules: water with simple hydrogen bonds or multiple H-bonds.

In composites, water uptake depends on additional parameters, such as fiber type, fiber volume ratio, and interface region properties [193]. For thicker composites (10 mm or more), the equilibrium may never be obtained and a through-thickness distribution of moisture varying with time is the more common condition.

1.3.2.1.2. Diffusion mechanisms

Polymers take up water through surfaces in contact with a wet environment by transient diffusion mechanisms until reaching an equilibrium water content. Two types of diffusion can take place, depending on the nature of the water uptake (free or bonded) [194].

The first diffusion is induced by free water in the polymer (Figure 1.24). Epoxy chain structures have high- and low-density regions. Low density parts include voids within polymer resins, and depend on morphological properties such as chain length, cross-link density or crystalline ratio. These voids are located between molecular entanglements or at the interface between matrix and fiber.

In this case, water molecules are located in these cavities and diffuse from one free volume to another. This results in a water uptake mechanism depending on the free volume ratio, and the attraction forces with the polymer. The influence of these parameters on diffusion is represented by an activation energy (E_a) needed to transfer a molecule from one void to another.

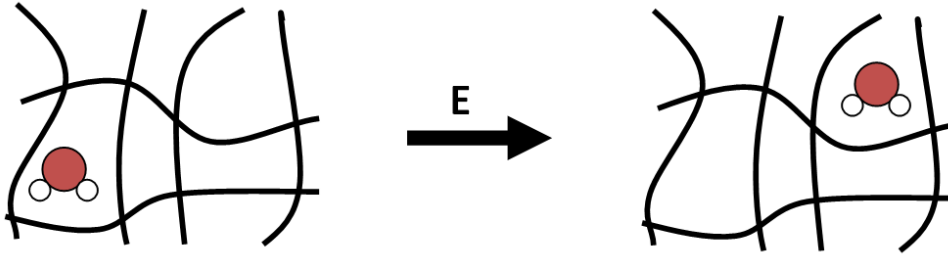


Figure 1.24 – Mechanism of the free volume diffusion of water in a polymer network

The water can also diffuse in polymers as bonded molecules due to their polarization. This property induces an attraction with charged chemical groups of the polymer chain, designated as hydrophilic groups. The diffusion is created by water retention at these hydrophilic sites and their displacement takes place when a sufficient energy ($>E_a$) is applied. This energy depends on the bond type between polymer chains and water molecules.

1.3.2.1.3. Fickian kinetics

The most widely used model to predict water uptake in a polymer is Fick's law. Fick established his model in 1855, based on Fourier's law for heat transfer. Fick's first theory can be summarized by defining the diffusive flux $\vec{\varphi}$ as the opposite of moisture concentration gradient C multiplied by the diffusion coefficient of the diffused molecule in the surrounding material D (Eq. 1.7) [194].

$$\vec{\varphi} = -D \cdot \overrightarrow{\text{grad}} C \quad \text{Eq. 1.7}$$

Fick's second law established the time derivative of moisture concentration as the divergence of the diffusion flux. In Cartesian coordinates, the divergence and gradient operators are expressed Eq. 1.8, with D_x , D_y and D_z the diffusion coefficients along the x , y and z axes respectively.

$$\frac{\partial C}{\partial t} = D_x \cdot \frac{\partial^2 C}{\partial x^2} + D_y \cdot \frac{\partial^2 C}{\partial y^2} + D_z \cdot \frac{\partial^2 C}{\partial z^2} \quad \text{Eq. 1.8}$$

In numerous cases, supposing an isotropic diffusion in polymer, it is possible to simplify the problem by the expression Eq. 1.9 given in [195], for plates.

$$\frac{M(t)}{M_\infty} = 1 - \frac{8}{\pi^2} \sum_i \frac{1}{(2i+1)^2} \cdot \exp\left(-\frac{D(2i+1)^2\pi^2 t}{h^2}\right) \quad \text{Eq. 1.9}$$

Where h is the plate thickness in mm and t is the immersion time in s. The diffusion coefficient D can be calculated from the initial linear part of the sorption curve where $\frac{M(t)}{M_\infty} \leq 0,5$ (Eq. 1.10).

$$D = \frac{\pi}{16} \cdot \frac{h^2}{t} \cdot \left(\frac{M(t)}{M_\infty} \right)^2 \quad \text{Eq. 1.10}$$

Temperature has a significant effect on the water diffusion, and the higher the temperature, the faster the water diffusion (Figure 1.25).

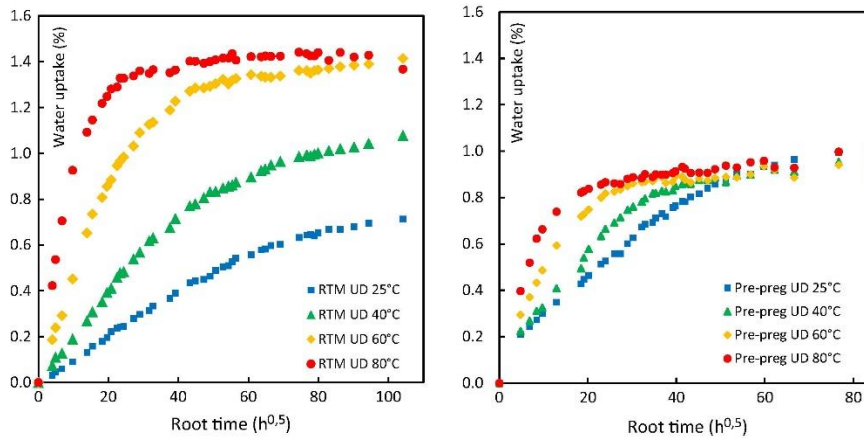


Figure 1.25 – Effect of the process and temperature ageing on water uptake [196]

1.3.2.1.4. Other diffusion mechanisms

It is possible to obtain other diffusion kinetics, depending on the material and on the ageing conditions.

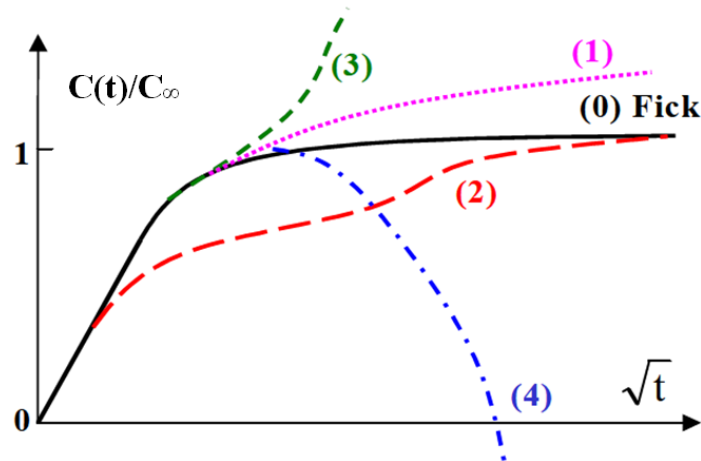


Figure 1.26 – Different diffusion kinetics [197]

In Figure 1.26, the curve noted (0) represents the Linear Fickian behaviour which was presented earlier. The curve noted (1) corresponds to a continuous increase of water content and is usually linked to the Langmuir water diffusion model. The curve (2) corresponds to a “Dual Fick” mechanism in which two different Fickian kinetics can take place at the same time. The curve (3) is associated with a rapid increase of the water diffusion that can be linked to a degradation of the material (damage). The curve (4) corresponds to a decrease of the water content and can also be associated with a degradation of the polymer, due to hydrolysis or oxidation for instance.

1.3.2.2. Effects of seawater on physico–chemical properties of polymeric composites

The two main consequences of seawater absorption on polymers are plasticization and swelling. Their consequences on mechanical behavior can be significant, and it is necessary to characterize them [172].

1.3.2.2.1. Plasticization

Solvents are characterized by a glass transition temperature T_{gS} generally lower than those of polymers T_{gp} . The diffusion of solvent into the polymer during sorption leads to a decrease of polymer T_g , respecting Eq. 1.11 :

$$T_{gS} \leq T_g \leq T_{gp} \quad \text{Eq. 1.11}$$

While different approaches are presented in the literature, the main one used is based on two hypotheses. First, the free volume fraction at $T > T_g$ is an additive function of free volume of each constituent. Second, the free volume ratio at $T = T_g$ is a constant ($f_g = 0.025$). These two hypotheses lead to an expression to determine the T_g ([198][199]) using Eq. 1.12 :

$$T_{gw} = \frac{\alpha_p(1-v)T_{gp} + \alpha_s v T_{gs}}{\alpha_p(1-v) + \alpha_s v} \quad \text{Eq. 1.12}$$

With α_p and α_s , coefficients of free volume expansion, respectively of polymer and solvent, given the formula $\alpha = \alpha_r - \alpha_g$, with r and g representing the thermal expansion coefficients in the rubbery and glassy states. With respect to the empirical formulation which considers αT_g as a constant [200], we obtain Eq. 1.13, with A the plasticization coefficient defined by $A = \frac{1}{T_{gs}} - \frac{1}{T_{gp}}$:

$$\frac{1}{T_g} = \frac{1}{T_{gp}} + Av \quad \text{Eq. 1.13}$$

This empirical relation allows structure–property relations to be predicted easily. Different cases lead to enhanced plasticization effects: an increase of solvent concentration in the polymer, a small value of T_{gS} or a high value of T_g .

Considering the solvent temperature T_u , we can consider four different cases (Table 1.6).

Table 1.6 – Temperature range of solvent ageing and impact on polymer properties

Temperature range	Impact on polymer properties
$T_{gp} < T_u$	Decrease of T_g which will not affect polymer properties
$T_{gp} > T_g > T_u + 100K :$	Polymer in glassy state remains in this state, and solvent penetration leads to a decrease in terms of mechanical properties (rigidity and stress at failure).
$T_{gp} > T_u + 100K > T_g > T_u$	Polymer in glassy state remains in this state, but the range of ageing leads to a relationship between the yield stress σ_y and the T_g given by the Kambour relation [201] : $\sigma_y = C \cdot (T_g - T_u)$ Where C represents a constant (MPa.k ⁻¹)
$T_{gp} > T_u > T_g$	Solvent absorption leads to a state change: from the glassy state, the polymer goes to a rubbery state, which induces a loss in terms of mechanical properties.

1.3.2.2.2. Swelling

When a solvent penetrates into a polymer, the polymer tends to expand, leading to swelling. Solvent molecules integrate the polymer molecular network. The physical event includes 2 cases.

In the first, the polymer initially in the glassy state remains in this state. This case represents water absorption in polymeric composites. It is possible to determine the volume difference which is induced by water diffusion, using Eq. 1.14 :

$$V = V_p + V_s + \Delta V \quad \text{Eq. 1.14}$$

Where V, V_p and V_s represent respectively the total volume, the polymer volume and the solvent volume. It is possible to determine the volume variation ΔV in the saturated state knowing the mass uptake ($m=m_\infty$), using Eq. 1.15 :

$$\frac{1 + m}{\rho} = \frac{1}{\rho_p} + \frac{m}{\rho_s} + \Delta V \quad \text{Eq. 1.15}$$

For semi-crystalline thermoplastics, only the amorphous phase absorbs solvent. Increasing the crystalline phase is interesting for applications which require low moisture absorption.

In the second case, the polymer is in a rubbery state at saturation. Swelling is induced by chain stretching, which is balanced by an opposite entropic restoring force. The relation at equilibrium is given by the Flory–Rehner equation (Eq. 1.16) [202].

$$-\ln(1 - v_p) - v_p - \chi \cdot v_p^2 = \rho \cdot v_s \cdot M_c^{-1} \cdot \left(v_p^{1/3} - \frac{v_p}{2} \right) \quad \text{Eq. 1.16}$$

Where v_p represents the volume ratio of polymer swelled, χ the polymer–solvent interaction coefficient, v_s the solvent molar volume, ρ the density of swelled sample, and M_c the chain length between branches.

In composite materials, swelling is more complicated to understand. A recent study performed on the thermal and moisture expansion behavior of vacuum infused UD laminates made with a range of tow sizes and fiber types has found that thermal expansion is fairly well understood but not moisture absorption [203]. The authors concluded that the moisture expansion was markedly greater than would be predicted from the constituents, and that the through-thickness expansion was significantly greater than the transverse expansion.

1.3.2.3. Effect of seawater on mechanical properties of polymeric composites

1.3.2.3.1. Static testing

Seawater ageing affects static mechanical properties of composites to a greater or lesser extent, depending on chemistry, immersion time and on ageing parameters.

For example, tension tests performed on UD GF/Epoxy showed a decrease of the stress at failure when increasing the ageing, while the elastic modulus was only slightly affected [204]. Similar conclusions were reached after 90 days of immersion in seawater, and the authors defined tensile and flexural strength loss to be respectively –25% and –35% [205]. For compression, another study defined a loss of 28% of the strength due to ageing [206]. For interlaminar fracture strength, seawater ageing resulted in a loss of 25% under quasi–static loading, which was irreversible in mode I and partially reversible in mode II [207]. For interlaminar shear strength, glass/silk hybrid textile fabric reinforced epoxy hand lay–up specimen ageing in natural seawater at 28°C for up to 16 days reduced the ILSS by up to 70%.

1.3.2.3.2. Impact testing

For impact testing, several studies have shown a decrease in strength after ageing. Two parameters tend to be characterized: an impact energy threshold, to give an indication of first damage, and an energy absorbing capacity at failure [208].

In one study [125], GRP with both standard and rubber–toughened epoxy resins was immersed in synthetic seawater. Matrix plasticization gave a significant increase in damage threshold energy for the standard epoxy after seawater immersion, but the energy absorbed to maximum load and the total energy absorbed were both substantially reduced due to moisture degradation of the fibers and the fiber–matrix interface for both GRP systems. In another study, C/VE laminates were conditioned in different environments (seawater at room temperature and at 40°C, environment chamber at 85% HR and 50°C) for up to 400 days. The authors concluded that impact forces recorded were not significantly affected after ageing. In addition, two different aramid/glass fibers epoxy laminates were aged [206], and the authors concluded that changes in

microstructural integrity occurred. Impact damage area was slightly less extensive in wet composites, and the compression strength after impact decreased by 42%.

Deionized water ageing at different temperatures on E-glass/polyester panels manufactured by VARTM has also been performed, to understand the influence of ageing on impact strength [209]. While impact damage on plates immersed in water did not significantly differentiate their absorption characteristics at any immersion temperature, neat resin plates showed significantly higher initial absorption rates and temporary plateaux when compared to their respective composite plates. In addition, water immersion considerably lowered peak impact force over time of immersion (Figure 1.27), while energy absorption increased with ageing time.

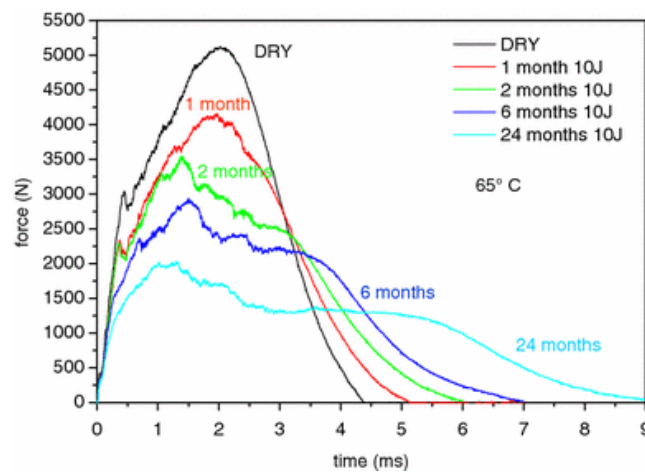


Figure 1.27 – Force – time plot for plates with a lay-up $(\pm 45^\circ, 0^\circ), (\pm 45^\circ)_2, (0^\circ, \pm 45^\circ)$ impacted at 10J both dry and after water immersion at 65°C for different ageing durations (Fig. 13 in [209]).

The authors proposed a model to link the energy absorption to the ageing time, assuming that within the range of impact energies tested, a linear monotonic increase relationship exists between the energy absorbed and the impact energy. Plots are of the form $y=a+bx$, as shown on Figure 1.28. This model is based on the Box–Lucas asymptote, which is defined by Eq. 1.17 (Figure 1.29):

$$b = b_{REF} + c \cdot (1 - e^{-\xi \cdot t}) \quad \text{Eq. 1.17}$$

With b_{REF} the value of parameters b for dry specimens, t is the time in months and c and ξ are constants obtained by curve fitting.

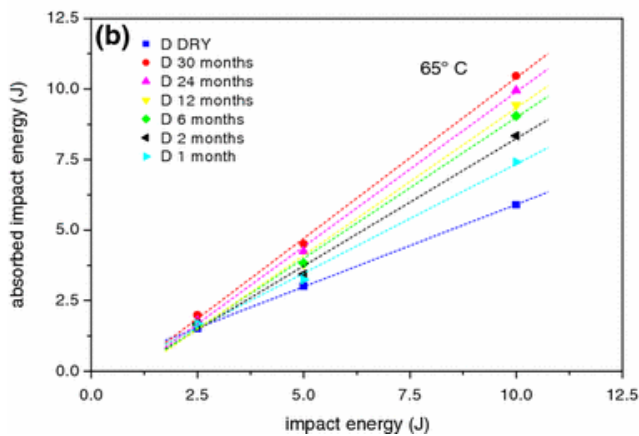


Figure 1.28 – Absorbed impact energy against nominal impact energy for plate with a lay-up $(\pm 45^\circ, 0^\circ), (\pm 45^\circ)_2, (0^\circ, \pm 45^\circ)$ (Fig. 11–b in [209])

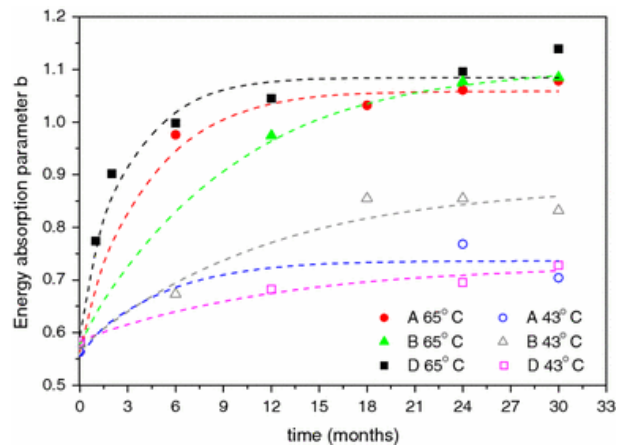


Figure 1.29 – The energy absorption parameter b against time for all types of specimens A, B and D representing different lay-ups at temperatures of 43°C and 65°C [209]

On the CAI strength, a study of woven C/Vinyl ester under dry and water saturated conditions showed that moisture absorption did not affect the dynamic impact force, but it affected the CAI strength due to degradation of the fiber/matrix interface [210].

1.4. Conclusion

To conclude this bibliography chapter, several aspects of the thesis have been reviewed. In the first part, propellers in marine environment have been discussed, and their advantages compared to metallic propellers have been shown. In the second part, low velocity impact (LVI) was reviewed, and parameters affecting the strength and durability of composites laminates subjected to impacts have been discussed. Finally, effects of the environment on composites were described: from manufacturing to the end of service life the behavior of polymeric composites can change, with a reorganization of their chemical network, leading to changes in terms of mechanical performance.

This chapter has shown a lack of information available in the literature about the effects of aging on the long term durability of a marine composite subjected to both low and medium strain rates. The following will try to explain our investigations on the effects of both physical and seawater aging on the quasi-static and dynamic properties of a CFRP suited for naval applications.

Chapter 2

—

Materials and methods

Chapter 2 – Materials and methods

2.1. MATERIALS	66
2.2. MANUFACTURING C/EPOXY PANELS	66
2.3. AGING OF PURE EPOXY AND C/EPOXY COUPONS	67
2.3.1. PHYSICAL AGING	68
2.3.2. SEAWATER AGING	68
2.3.3. AGEING PROCESS	69
2.4. PHYSICOCHEMICAL CHARACTERIZATION	70
2.4.1. DIFFERENTIAL SCANNING CALORIMETRY	70
2.4.2. THERMOGRAVIMETRIC ANALYSIS (TGA)	70
2.4.3. PYCNOMETER	70
2.5. IMAGING TECHNIQUES	70
2.5.1. SCANNING ELECTRON MICROSCOPE (SEM)	71
2.5.2. OPTICAL MICROSCOPY	71
2.5.3. X-RAY TOMOGRAPHY	71
2.5.4. ULTRASONIC C-SCAN	71
2.6. SCIENTIFIC APPROACH	72
2.6.1. BUILDING BLOCK APPROACH (BBA)	72
2.6.2. PYRAMID OF TESTS	73
2.7. CHARACTERIZATION AT COUPON SCALE	74
2.7.1. IN-PLANE PROPERTIES OF C/EPOXY	74
2.7.2. OUT-OF-PLANE PROPERTIES OF C/EPOXY	75
2.7.3. INTERFACE PROPERTIES	76
2.7.4. FLEXURAL TESTS	81
2.7.5. MECHANICAL TESTS AT HIGHER LOADING RATE	82
2.8. CHARACTERIZATION AT ELEMENT SCALE	83
2.8.1. LOW VELOCITY IMPACT (LVI).....	83
2.8.2. COMPRESSION AFTER IMPACT (CAI)	86
2.9. CHARACTERIZATION AT COMPONENT SCALE	87
2.10. NUMERICAL SIMULATION OF COMPOSITES	87
2.10.1. INTRALAMINAR DAMAGE MODEL	88
2.10.2. INTERLAMINAR DAMAGE MODEL.....	92

2.1. Materials

This project focuses on high performance composites for naval use. High-end applications need to show good stiffness while reducing composite part weight. For this reason, the choice was made to work with carbon fibers. However, as composite propellers are curved, and to control the fiber alignment during the manufacturing process, two fabrics were chosen. The first one is a unidirectional T700 Version I 12k carbon fiber reinforcement, with an area density of 600 g/m². The second one is a biaxial fabric with two unidirectional T700SC 12k carbon fibers stitched together at angles of 45° and -45°. The total areal density of the biaxial fabric is 600 g/m². For the unidirectional fabric, the stitching is made of glass while for the biaxial, the stitching is made of PET fibers (Figure 2.1).

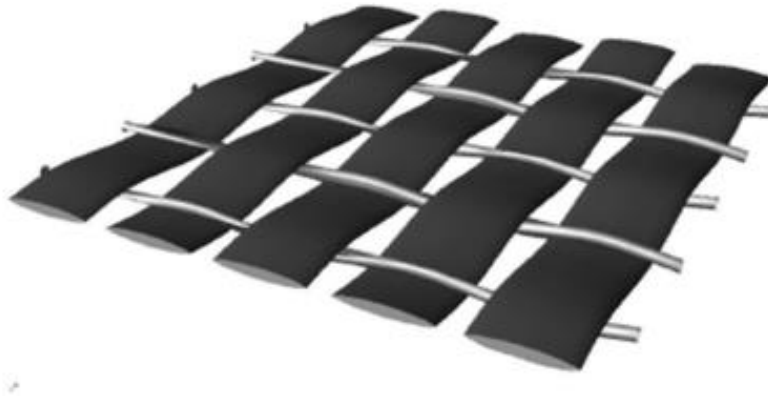


Figure 2.1 – Diagram of the UD T700 version I carbon fiber fabric studied

The matrix is an epoxy resin from the French manufacturer Sicomin. The epoxy system (SR8100 + SD 4772) was chosen. This system was developed for injection and infusion manufacturing processes, which are used for marine structures. The advantage of the SD 4772 hardener is the slow polymerization. This must be considered since marine composites parts are often thick. In that case, more time is needed to impregnate the fibers before curing, and it is important to limit exothermic reactions during the manufacturing process. The optimum infusion time was determined by Sicomin to be 53 minutes [211].

In addition, this study follows on from a previous study which focused on the influence of aging on fatigue behavior [170]. The same material has been chosen for this study, which investigates how aging affects impact behavior.

2.2. Manufacturing C/Epoxy panels

The C/Epoxy and pure Epoxy panels were manufactured at Ifremer (Table 2.1). For pure Epoxy panels, a semi-closed mould was developed in a previous study with the help of Sicomin. It relies on two aluminum plates covered by Teflon tape so that the cast resin can be removed easily from the mold. The two plates are separated by a U-shaped frame of 3mm in thickness. A silicon tube is placed along the U-frame to make the

seal between the two aluminum plates, leaving only a small surface in contact with air during resin curing. Pure epoxy panels were used for both hygroscopic and mechanical tests. Coupons were then cut from the panels using Charlyrobot™ CNC equipment.

For the C/Epoxy, several panels were manufactured by infusion (Table 2.1). The standard dimensions of the final panels were 500 x 500 mm². Except for QI coupons, which were cut by a high–pressure waterjet, all coupons were cut using a wet diamond saw to the specimen dimensions, and all cut surfaces were wet polished to avoid rough surfaces that can lead to an early failure. Coupons destined for fracture toughness tests were manufactured with a PTFE insert at mid–thickness.

Manufacturing was performed at 20°C. Complete curing is necessary, to avoid post curing during aging. The influence of incomplete curing on water uptake has been characterized recently [170]. To obtain a fully cured epoxy, the curing was divided in three successive steps. First, a 24h cure at ambient temperature was applied. Then, a post–cure at 60°C for 16 hours, followed by a second post cure at 120°C for 2 hours. This curing process was established in a previous study on the same material [170], and results in a stable cure state, with no glass transition temperature change between two successive DSC temperature sweeps.

Table 2.1 – Panels manufactured and properties measured

Name	Layup	Thickness [mm]	Mechanical test performed	Fiber volume ratio [%]	Void content [%]	T_g [°C]
Pure Epoxy	–	2.3	Tension (ISO 527-2) Shear (ASTM D5379)	–	< 1	74
Thin UD	$[0]_4$	2.2	In-plane Tension (ISO 527-5) In-plane compression (ASTM D6641)	65	2.2	78
Thick UD	$[0]_{42}$	23.1	Out-of-plane tension (ISO 527-5) Out-of-plane shear (ASTM D5379)	67	9.0	82
Fracture toughness	$[0]_6$	3.3	Mode I (ASTM D5528) Mode II (ISO 15114) Mixed-mode Bending (ASTM D6671)	66	2.2	75
Biaxial	$[-45,45]_{2S}$	2.4	In-plane tension (ASTM D3518)	61	6	76
Quasi isotropic (QI)	$[0, (-45,45)_S, 90]_S$	4.4	Aging (ASTM D5229) Out-of-plane impact (ASTM D7136) Compression after impact (ASTM D7137) In-plane impact	64	3.2	75

2.3. Aging of pure Epoxy and C/Epoxy coupons

This project considers two aging mechanisms. The first is linked to the manufacturing process, and was characterized previously on the same material [171]. The second is linked to the service environment, i.e. the

marine environment where the material is subjected to humidity or immersion in seawater. These aging processes can be studied separately thanks to the reversibility of the chemical processes occurring. After the post cure, the material T_g was measured to be 78°C.

2.3.1. Physical aging

As noted previously physical aging is a process that occurs in some epoxy systems when the material is cooled below the T_g . Since physical aging is a reversible process, exposing the material to above- T_g temperatures removes the physical aging in the material. This process is called rejuvenation, and the material state devoid of physical aging is called 'rejuvenated'. To be sure to have an initial state without physical aging effects, a rejuvenation is performed after the post cure. This process is performed in vacuum bags to prevent unwanted reactions such as oxidation. The bags are immersed in water at 90°C for 10 minutes, and then immersed in water at 4°C to quench the material. The choice of water immersion rather than air exposure in ovens was made due to the thermal inertia of the environment. The rejuvenated state corresponds to the first aging state of interest in this thesis work.

A second state noted 'physically aged' was also studied. It is obtained after rejuvenation by placing vacuum bags in ovens for 30 days at 60°C. This duration and the temperature have been chosen from the modified KWW model (Kohlrausch–Williams–Watts) applied in a previous study [171] on the same material. For this aging time and at this aging temperature, the maximum stress stays constant when the aging time increases. The material has reached a plateau, and the physical state can be considered as stable. After this aging, the T_g was measured to be 84°C. The physically aged state corresponds to the second aging state of interest in this thesis work.

2.3.2. Seawater aging

Hygroscopic characterization to determine the change of the diffusion coefficient with the temperature was performed. This type of study is useful because under service conditions, the seawater temperature may be variable; close to 4°C (in deep water) while it can reach 35°C at the surface near the equator region. Polymeric parts are therefore exposed to a large seawater temperature spectrum. A model predicting the diffusion coefficient as a function of the aging temperature considered is therefore necessary to predict the water profile in thick composite parts. To identify such a model, seawater aging is performed, to diffuse water into the composite and to understand how the material will absorb this water. For this study, two types of samples were aged. First, pure epoxy coupons with dimensions of 50x50x2mm³. Second, quasi-isotropic composite coupons with dimensions of 40x40x4.4mm³. These coupons had all been previously physically aged to stabilize the material.

Since the aging is accelerated by the temperature, coupons have been immersed in different tanks filled with seawater continuously renewed from the Brest estuary. Depending on the tank, the seawater is cooled or heated. In the case of this study, the initial T_g of the material after physical aging (physical stabilization) and

before immersion was 84°C. The maximal seawater aging temperature was therefore determined to be 60°C. Samples were placed in seawater aging tanks at 4, 15, 25, 40 and 60°C (Figure 2.2).



Figure 2.2 – Seawater aging tanks at IFREMER

During the immersion, coupons were removed from water after different aging times, then weighed. The water uptake is expressed as the mass change in percent calculated as in Eq. 2.1. $M(t)$ being the mass uptake value in percent, at a time t , m_0 the initial mass and m_t the mass at time t .

$$M(t) = \frac{m_t - m_0}{m_0} \quad \text{Eq. 2.1}$$

2.3.3. Ageing process

A schematic diagram representing the overall ageing process is shown in Figure 2.3.

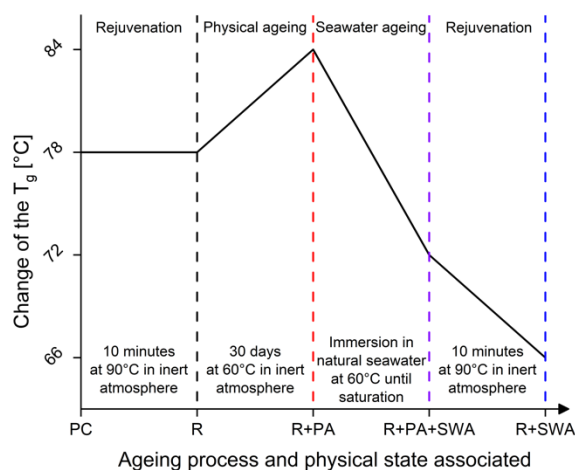


Figure 2.3 – Ageing processes used in this study to obtain rejuvenated, physically aged and seawater aged materials

Three cases are considered in this study. First, a rejuvenated and dried material. Second, a physically aged and dried material. Finally, a seawater saturated and rejuvenated material. For each state, an equilibrium is assumed to be reached.

After the saturation, the T_g was measured to be 72°C. To remove the physical aging, a rejuvenation process was performed in a vacuum bag at 90°C for 10 minutes. With this last step, the material is saturated and devoid of physical aging. The T_g was measured to be 66°C. The seawater aged state corresponds to the third aging state of interest in this thesis work.

2.4. Physicochemical characterization

2.4.1. Differential Scanning Calorimetry

Glass transition temperature (T_g) and physical ageing effects were measured by Differential Scanning Calorimetry (DSC), with TA Instruments Q200™ equipment. The heating rate was 10 °C/min. Two ramps were performed on each sample, both from –5 to 120 °C, in order to measure T_g . The tests were performed under N₂ gas at a flowrate of 50 mL/min.

2.4.2. Thermogravimetric Analysis (TGA)

ThermoGravimetric Analysis (TGA) was used to measured fiber mass ratio. These analyses were performed on a TA Instrument SDT Q600™. Resin burn-off was carried out under nitrogen, in order not to oxidize carbon fibers. The burn-off conditions were 800 °C for 20 minutes.

2.4.3. Pycnometer

Both composite and matrix densities were measured using a Micromeritics AccuPyc II™ 1340 helium pycnometer. Based on TGA and pycnometer values, the fibre, resin and void volume ratios can be calculated with respect to ISO 14127 standard. Equations are given Eq. 2.2, Eq. 2.3 and Eq. 2.4.

The fiber mass ratio m_f was measured by TGA, while ρ_c and ρ_f correspond respectively to composite and resin densities that are measured by the pycnometer.

$$V_f = \frac{m_f \times \rho_c}{\rho_f} \quad \text{Eq. 2.2}$$

$$V_r = \frac{(1 - m_f) \times \rho_c}{\rho_r} \quad \text{Eq. 2.3}$$

$$V_v = 1 - (V_f + V_r) \quad \text{Eq. 2.4}$$

2.5. Imaging techniques

Imaging techniques are powerful methods that serve many purposes across the physical sciences. The results that are obtained mainly depend on the incoming “wave” that is used (e.g. light, electrons, X-rays etc).

2.5.1. Scanning Electron Microscope (SEM)

Scanning Electron Microscopy (SEM) images of fracture surfaces were recorded at IFREMER. The system used is a FEI Quanta 200™ by Thermo Fisher. Images were made at 0.15 μbar. The samples were covered by pure gold with Balzers SCD 400® equipment under argon gas. The gold layer was 15 to 20nm and allowed good reflection of electrons from the specimen surface without charging. The electron beam is generated by a tungsten filament.

2.5.2. Optical microscopy

The quality in term of voids of the different panels that were manufactured was checked using optical microscopy with a Leica DM ILM microscope. The void contents were determined using *ImageJ* on polished sections. This microscope has also been used to localize delaminated interfaces after impacts.

2.5.3. X-Ray tomography

In addition to C-scan, impacted coupons were cut for X-ray tomography scanning. The measurements were performed at the Technical Resource Center in Morlaix (CRT Morlaix). The high-resolution tomograph is a GE/Phoenix V|Tome|xsv. Its power is 240kV with a 2048 by 2048 sensor and minimum 5 μm resolution. The measurements performed in this thesis were made at a 10μm resolution. The reconstructed volumes were then analyzed by *VG Studio*™ in order to identify defects and damage present in the material.

2.5.4. Ultrasonic C-scan

Ultrasonic C-scan inspection was performed on impacted composite coupons. This provided information on whether delaminations were present (Figure 2.4). Coupons were immersed in a tank filled with tap water. A fixture has been designed for inspecting up to 9 coupons at the same time (Figure 2.5). A 5 MHz US probe is fixed to a scanning arm, which moves along X and Y axis. An electronic system controls the displacement to scan all the surface. The signal is acquired by a Sonatest *Prisma*™ system, and the X-Y displacement is synchronized with the A-Scan. Due to the inhomogeneity of the material, it has not been possible to use a multi-element sensor to determine delaminated surfaces between two successive plies. Thus, the results of the NDE shown in this document are projected delamination shapes through the thickness.

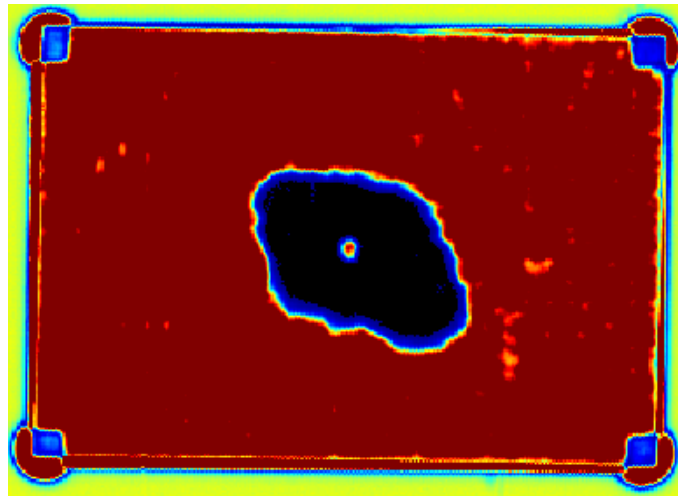


Figure 2.4 – Example of an impacted coupon (150x100 mm²) with through the thickness delamination visible at the coupon center



Figure 2.5 – Fixture designed for scanning several coupons at the same time

2.6. Scientific approach

The aim of the study presented in this document is to characterize, understand and simulate the effects of aging on the impact behavior of a high-performance C/Epoxy material. To do that, the Building Block Approach (BBA) was followed. With this approach, a test pyramid is set up to validate experimental results using numerical simulations.

2.6.1. Building Block Approach (BBA)

Performing a test which is representative of real conditions in a laboratory must consider the propeller materials, geometry, and the conditions of impact. As composite materials are studied, material effects must include reinforcement type, orientation and resin type. Geometry is complex because a propeller blade shape is designed to be efficient under hydrodynamic flow, resulting often in a double curvature. Finally, the conditions of impact must be accurately known. These conditions are defined by relative velocity between

the impactor and the structure impacted, and the mass of each component. The nature of impacts on propellers will vary considerably and there are no standard test conditions, so a range of conditions must be examined.

With respect to modeling aspects, the complexity depends on the number of simplifying assumptions. Modeling techniques must be reviewed to make representative choices.

The scientific approach used in this document is based on the Building Block Approach (BBA) used in aerospace and aeronautical industries [212][213]. In this method, the knowledge of the composite material and structure is built up step by step from the coupon level up to the final full scale structure [214]. This method was created to reduce the very high costs of large-scale crash testing of composite aircraft fuselage structures for the wide range of composite materials and crash concepts being considered (Figure 2.6).

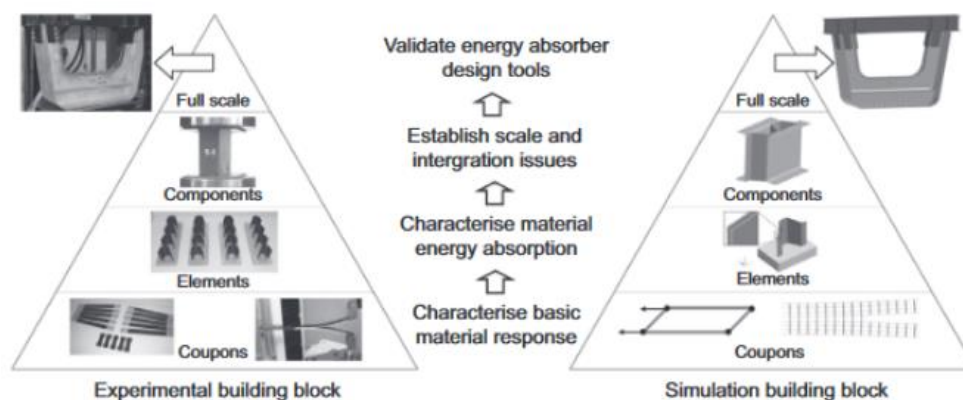


Figure 2.6 – Building block approach with test and simulation pyramids as basis for the design of a crashworthy helicopter frame structure [212].

For this study, a building block approach around marine propellers has been established. Since impacts can happen at different locations on a propeller blade, mechanical tests and simulations need to consider a wide range of geometries.

2.6.2. Pyramid of tests

The first step concerns the choice of a material. For this study, a C/Epoxy material was chosen. Then, at coupon scale, there is a need to characterize the mechanical properties. These properties will then be used to simulate a complex quasi static test, to validate the properties experimentally obtained. Then, these properties will be used to simulate impact tests performed at the element scale. At element scale, it has been decided to perform both out-of-plane and in-plane impacts since an impact event can happen anywhere on a propeller blade. Finally, the last step of this work is the characterization of an in-plane impact on a representative propeller part from the *Fabheli* project. This project, has been described in Chapter 1, and led to the design, manufacture and full-scale test under real operative conditions of a CFRP propeller to replace a metallic one.

2.7. Characterization at coupon scale

An extensive experimental campaign was carried out to obtain a complete set of data to predict the mechanical behavior of composite structures after aging. To do so, several mechanical tests were performed. The section hereafter describes these different tests, first in-plane, then out-of-plane behavior.

2.7.1. In-plane properties of C/Epoxy

The first step is the determination of both design and ultimate properties of the C/Epoxy.

2.7.1.1. Tensile tests

First, tension tests were performed on pure Epoxy. Prior to aging, coupons were cut using a CNC machine. The standard ISO 527–2 with the coupon shape 1B was followed. Surfacing was carried out to avoid thickness variations along the coupon. Second, tension tests were carried out on three composite orientations. The standard ISO 527–5 was followed for tensile tests on 0° and 90°, while the standard ASTM D3518 was followed for tensile tests on ±45° laminates. Panels were cut using a wet diamond saw. The dimensions of the specimens were 250x25x2.2 mm³. Prior the test, glass/epoxy tabs were bonded to the ends of the composite coupons to avoid premature failure in the machine jaws. Tensile tests in the 0° direction were carried out using an Instron™ universal testing machine with a load cell of 200kN, while other tensile tests were carried out using an Instron™ UTS 5966 with a 10kN load cell. All tensile tests were performed at 1, 10, 100 and 1000 mm/min, to examine the strain-rate dependency of results. Strain measurements were obtained by digital image correlation, by applying a random graphite pattern on the specimen surfaces. For quasi–static tests, images were captured by a Basler™ camera at 2 frames per second and correlated offline with the commercial software Aramis GOM™. For high–speed tests, a high–speed camera Photron™ AX200 Mini was used to capture images during the test for DIC post processing. A DaQ HBM Genesis™ HighSpeed system with a universal DaQ card GN 1640B was used to acquire the force and displacement data from the testing machine at these displacement velocities. The synchronization between the camera and the DaQ system was performed by a trigger generated by the DaQ system when the measured force exceeded 10N. A specific intermediate loading fixture with an oblong hole was designed to load the coupons with a constant velocity, (see section 2.7.5).

2.7.1.2. Compression tests

Compression tests following the ASTM D6641 standard were performed on 0° and 90° oriented coupons. This test, known as the combined loading compression (CLC) test method, was chosen to prevent a failure from structural buckling. The loading rate was fixed at 1 mm/min. Carbon/Epoxy tapered tabs with a lay-up of 0/90/0° were bonded on both sides of the coupon to avoid the crushing of the coupon near the compression platens. Strain gages were bonded to both sides of the central gage section of the sample (Figure 2.7) to determine the buckling ratio which must be below 10% for the test to be valid. Five specimens per aging

condition were tested for UD and 90° oriented fibers, with a thickness of 2.15 mm. Coupons were cut with a water jet to obtain a precise parallelism between faces in contact with compression platens. A DaQ system HBM *Quantum*™ MX840B was used to record the synchronized force, displacement and strains.

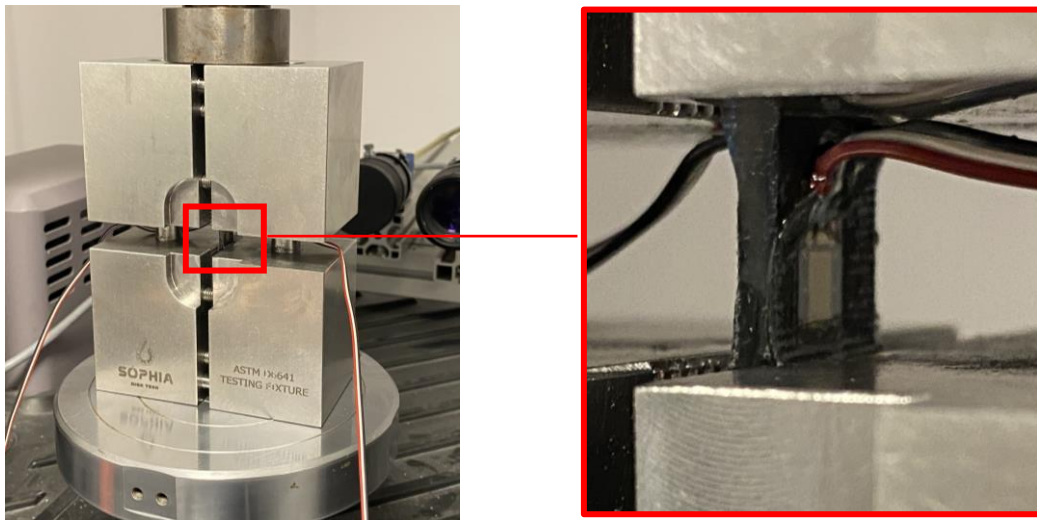


Figure 2.7 – ASTM D6641 fixture and a zoom on one of the two strain gages bonded to determine the compression modulus

2.7.1.3. Shear tests

Shear tests were performed on pure epoxy coupons in accordance with ASTM D5379. A CNC machine was used to machine the V-notched beam test coupon. Prior to the test, a random graphite pattern was applied in order to measure the strains by DIC. The shear tests were carried out at 1 mm/min using an Instron UTS 5966 up to the failure of the coupon. The shear strain data are determined from an average of ϵ_{xx} and ϵ_{yy} over the area of interest highlighted in red in Figure 2.8. The area of interest was defined to be at the coupon center to avoid edge effects close to the V-notches.

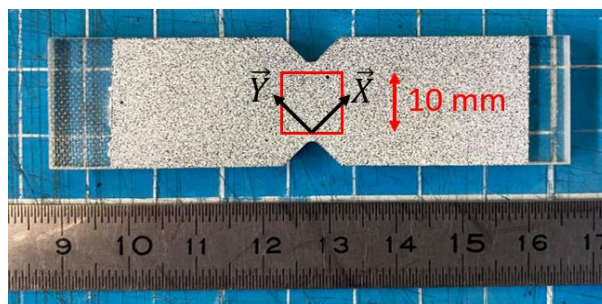


Figure 2.8 – V-notched pure Epoxy coupon speckled before the test and the area used to compute the shear strain

2.7.2. Out-of-plane properties of C/Epoxy

A thick unidirectional panel was manufactured to characterize the out of plane properties of the composite. The panel was sliced along the thickness direction using a wet diamond saw to obtain composite slices with the transverse direction representative of the thickness direction.

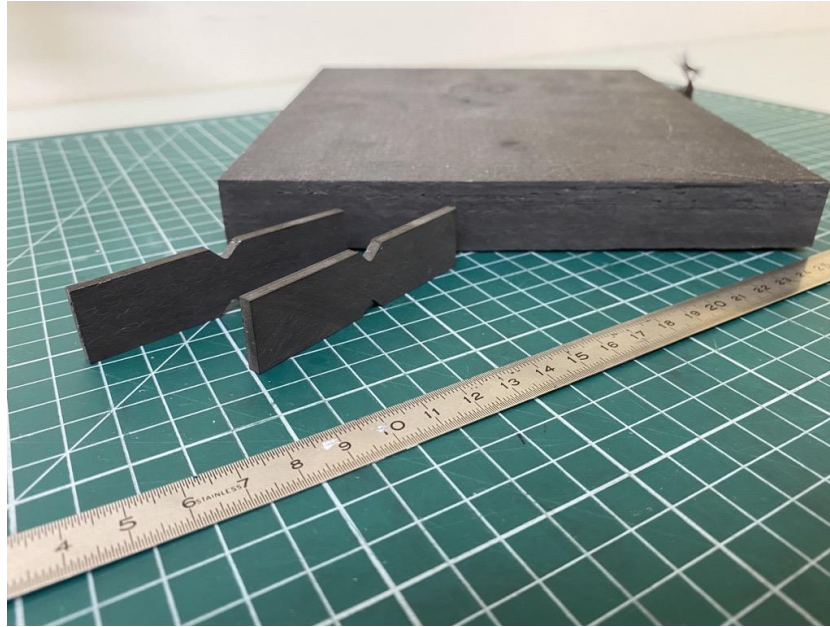


Figure 2.9 – V-Notched C/Epoxy coupons to determine the out-of-plane shear properties

For tensile tests, slices were machined using a CNC machine. Due to manufacturing issues, it was not possible to cut coupons in accordance with ISO 527–5. Finally, the dimensions of coupons in the 1–3 plane were $100 \times 20 \times 3 \text{ mm}^3$ while they were $200 \times 20 \times 3 \text{ mm}^3$ for the coupons in plane 2–3. A biaxial strain gage was bonded to measure both longitudinal and transverse strains during the tensile test. These measures are needed to determine the out-of-plane Poisson ratios. The tensile tests were performed on an Instron™ UTS 5966 with a 10kN load cell at 1 mm/min.

For shear tests, the ASTM D5379 standard was followed. Slices were machined using a CNC machine to obtain the V-notched beam test coupon (Figure 2.9). Prior to the test, a random graphite pattern was applied to measure the strains by DIC. The shear tests were carried out at 1 mm/min using an Instron™ UTS 5966 up to the failure of the coupon.

2.7.3. Interface properties

Despite exceptional in-plane properties, the weakness of laminated composites is their low tolerance to delamination due to out-of-plane loading. To have a good description of the interface behavior and to predict the tolerance to delamination of a composite structure, cracking tests following different modes are needed [215]. For each mode, test possibilities are numerous: Mode I [216], Mode II [217] and also Mixed-Mode fracture [218]. A recent study [207] focused on cracking properties of the same material as studied herein. In comparison with that previous study, the present work considers well-defined aging states. During the tests, images of the coupon were recorded, and these were then post-processed to determine the crack tip position. Prior to the tests, all coupons were pre-cracked in Mode-I with a loading-rate of 5 mm/min (ASTM D5528).

2.7.3.1. Pure Mode I tests

The fracture toughness from crack initiation is defined from the Force–Displacement curve. This value is taken either from the nonlinear part (99% of the slope) or from the maximal force value or at 95% of the initial slope (Figure 2.10). Before the post processing step, it was necessary to shift the curves horizontally, to get a linear part from the beginning of the test at the origin.

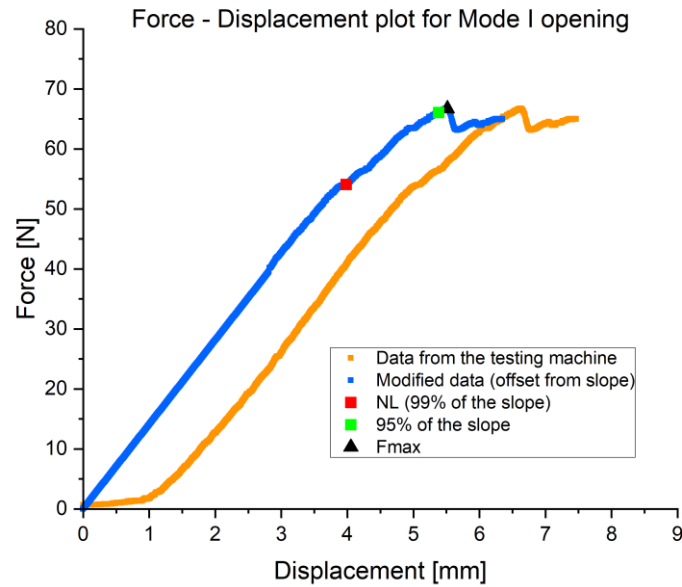


Figure 2.10 – Force–Displacement plot for crack initiation in pure Mode–I opening

The Double Cantilever Beam (DCB) test method (ASTM D5528) was chosen to determine the Mode–I fracture toughness. Specimens were cut to dimensions of 20 by 195 mm². All coupons edges were painted in white to assist the crack tip detection, then marks were drawn every 10 mm to precisely localize the crack tip. The Compliance Calibration (CC) method allowed the data reduction for calculating the value of pure Mode–I fracture toughness G_I . In this method, the least squares plot of $\log(\frac{\delta_i}{P_i})$ vs. $\log(a_i)$, with δ_i and P_i respectively the traverse displacement and load, and a_i the visually observed delamination onset, is generated. The slope is defined as variable n , which is introduced in Eq. 2.5 to calculate G_{IC} . The interlaminar fracture toughness corresponds to the average value of experimental points in the plateau of the R curve.

$$G_{IC} = \frac{nP\delta}{2ba} \quad \text{Eq. 2.5}$$

Data acquisition was performed at 10 Hz for the testing machine and 2 Hz for the camera. The beginning of the acquisition is synchronized. A *Python* program was used to automatically generate a table with the force, the displacement and the picture taken at the same time on the propagation part. This facilitated the data treatment. Figure 2.11 shows the interlaminar crack propagation during the test, the white face helps to localize the crack tip.

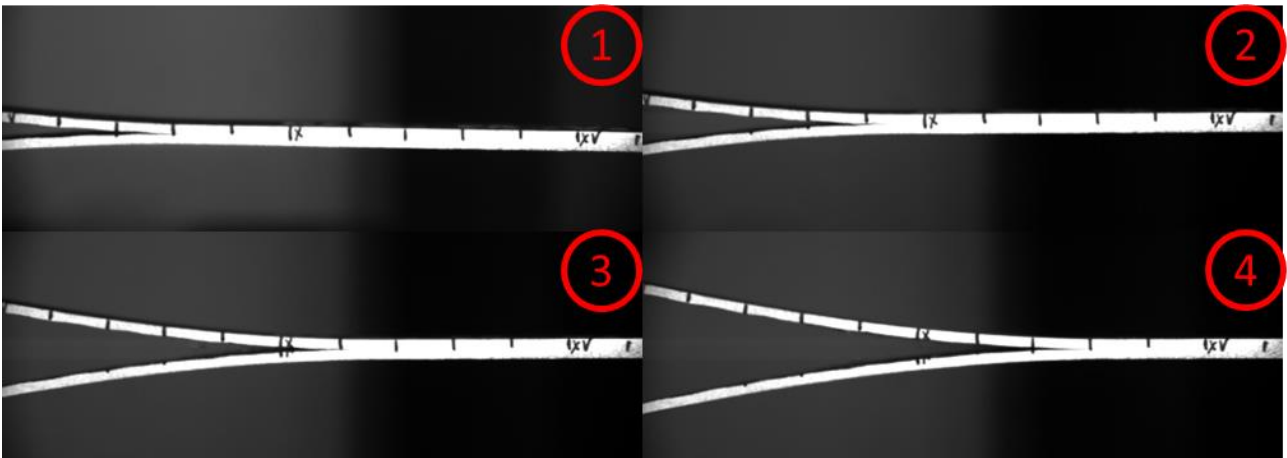


Figure 2.11 – Propagation of the crack in the interlaminar area during the DCB test

2.7.3.2. Pure Mode II tests

The Calibrated End-Loaded Split (C-ELS) test method (ISO 15114) was chosen to determine the Mode-II fracture toughness. Specimens were cut to dimensions of 20 by 195 mm². A first step to calibrate the flexural modulus (Figure 2.12) of each coupon was performed with free lengths of 60mm, 70mm, 80mm and 90mm and loads up to 100N. This limit of 100N was determined to remain in the linear part of the load-displacement plot, avoiding coupon damage prior to the test.

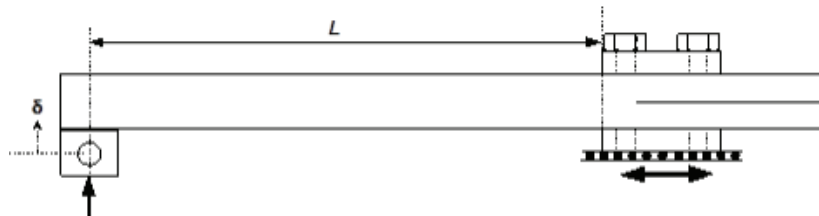


Figure 2.12 – Calibration step of to determine the flexural modulus

The fixture is shown in Figure 2.13. For each test, the clamp was tightened with a torque wrench to 5 N.m. All coupon through-the-thickness faces were covered with a white paint, and markers were drawn every 10mm to localize the crack tip during propagation. Data acquisition was performed at 10 Hz for the testing machine and 2 Hz for the camera. The *Python* program used for DCB tests post-processing was also used for this test.

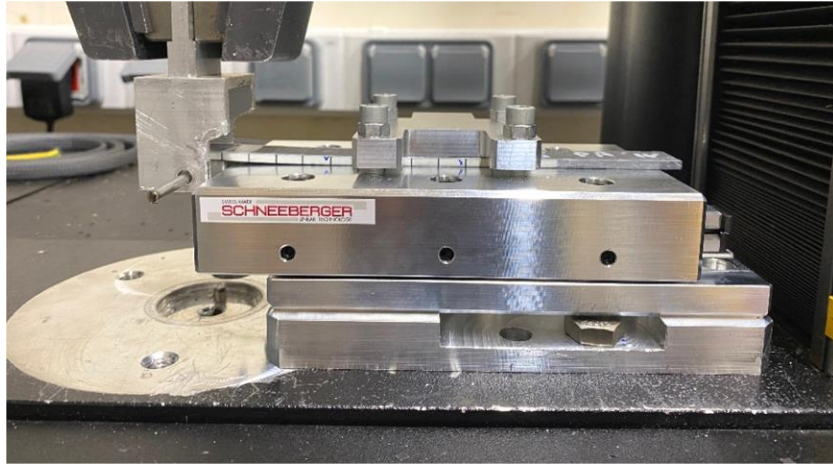


Figure 2.13 – C-ELS fixture during a pure Mode-II propagation test

Figure 2.14 shows an example of the Force–Displacement curves for the calibration step of a coupon and the slope determined by plotting the cubic root of the compliance as a function of the free length.

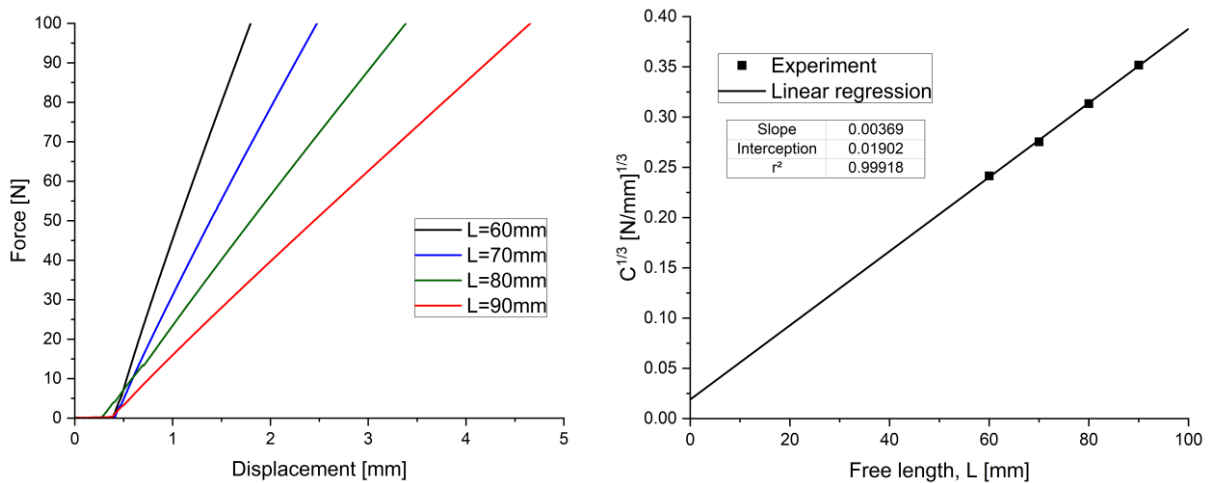


Figure 2.14 – Calibration of the flexural modulus with four free lengths and determination of the slope to determine the flexural modulus

Once the slope is known, it is possible to determine the flexural modulus using Eq. 2.6, with b and h representing respectively the width (mm) and the thickness (mm).

$$E_1 = \frac{1}{2b(h \times slope)^3} \quad \text{Eq. 2.6}$$

Finally, the corrected beam theory using effective crack length is applied (Eq. 2.7) and allows the determination of the Mode-II fracture toughness G_{IIC} . The interlaminar fracture toughness corresponds to the average value of experimental points in the plateau of the R curve. A diagram of the test is shown in Figure 2.15 and images showing the crack tip in Figure 2.16.

$$G_{IIC} = \frac{9P^2 a_e^2}{4b^2 h^3 E_1} \quad \text{Eq. 2.7}$$

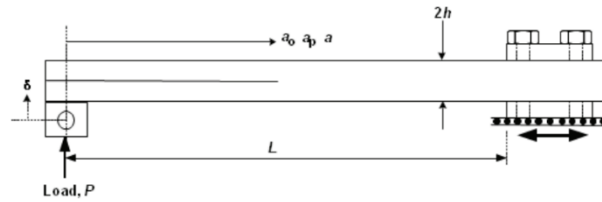


Figure 2.15 – Diagram of the pure Mode-II fracture toughness test (ISO 15114)

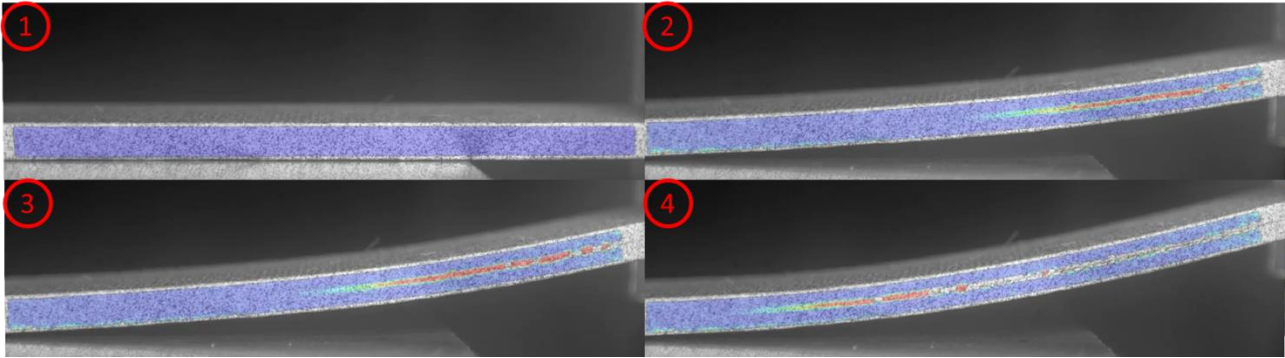


Figure 2.16 – 2D Digital Image Correlation view of the crack during pure Mode-II fracture toughness test

2.7.3.3. Mixed-Mode Bending tests

The Mixed Mode Bending (MMB) method, (ASTM D6671), was chosen to determine the mixed Mode I–Mode II fracture toughness. For this test, contributions of both modes affect the crack propagation. A diagram representing the test is shown in Figure 2.17. The mode ratio is determined using Eq. 2.8 from [219]. For this study, tests were performed at four levels of mode II contribution: 23%, 43%, 60% and 80%.

$$\frac{G_I}{G_{II}} = \frac{3(e + L)^2}{3(e + L)^2 + 4(3e - L)^2} \quad \text{Eq. 2.8}$$

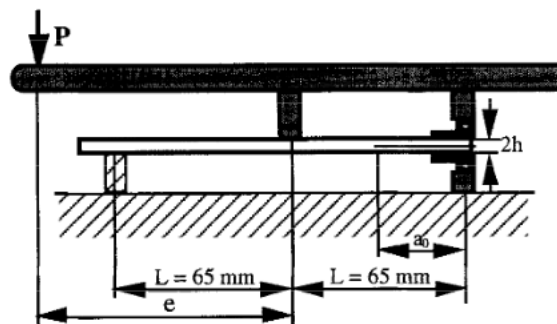


Figure 2.17 – MMB specimen

Calculations of fracture toughness need to consider both in-plane and out-of-plane properties by determining the crack length correction factor χ (Eq. 2.9, Eq. 2.10). Values from experimental tests were chosen.

$$\Gamma = 1,18 \cdot \frac{\sqrt{E_{11} \cdot E_{22}}}{G_{13}} \quad \text{Eq. 2.9}$$

$$\chi = \sqrt{\frac{E_{11}}{11 \cdot G_{13}} \cdot \left(3 - 2 \cdot \left(\frac{\Gamma}{1 + \Gamma} \right)^2 \right)} \quad \text{Eq. 2.10}$$

Finally, mode I and mode II contributions to strain energy release rates were calculated from Eq. 2.11 and Eq. 2.12. In these equations, P represents the load (N), C the lever length of the fixture (mm), L the half span length (L=68.7mm), B and h respectively the width and the half thickness of the coupon and a the crack tip location (mm). The reduction of these data allows the calculation of the mode mixture fracture toughness G_C using Eq. 2.13 and Eq. 2.14.

$$G_I = \frac{12 \cdot P^2 \cdot (3c - L)^2}{16 \cdot b^2 \cdot h^3 \cdot L^2 \cdot E_{1f}} \cdot (a + \chi \cdot h)^2 \quad \text{Eq. 2.11}$$

$$G_{II} = \frac{9 \cdot P^2 \cdot (c + L)^2}{16 \cdot b^2 \cdot h^3 \cdot L^2 \cdot E_{1f}} \cdot (a + 0,42 \cdot \chi \cdot h)^2 \quad \text{Eq. 2.12}$$

$$G = G_I + G_{II} \quad \text{Eq. 2.13}$$

$$\frac{G_{II}}{G} = \frac{G_{II}}{G_I + G_{II}} \quad \text{Eq. 2.14}$$

Finally, G_C is determined once again from the average of fracture toughness values on the plateau of the R curve.

2.7.4. Flexural tests

Three–point bending tests were performed on $[0]_4$ specimens to determine the composite flexural modulus. The standard ASTM D7264 was followed. The support span was set to 100mm. A strain gage was bonded on the coupon back face to determine the flexural modulus E_1 of UD material. The stress is calculated from Eq. 2.15.

$$\sigma = \frac{3PL}{2bh^2} \quad \text{Eq. 2.15}$$

Four point bending tests were also performed on $[0]_4$ specimens to compare the influence of the three-point bending test on the flexural results. The standard ASTM D6272 was followed. A load span of one half of the support span was chosen. The support span was set to 80mm. The stress is calculated from Eq. 2.156.

$$\sigma = \frac{3PL}{4bd^4} \quad \text{Eq. 2.16}$$

Four point bending tests were also performed on $[0,(-45,45)_2,90^\circ]_5$ coupons in order to provide experimental data to compare with model predictions. The ASTM D6272 standard was followed (Figure 2.18). The depth to span ratio was set at 12 to increase the shear effects leading to the coupon failure. 3D digital image

correlation was performed with the commercial system Aramis GOM™ to characterize through the thickness strains.

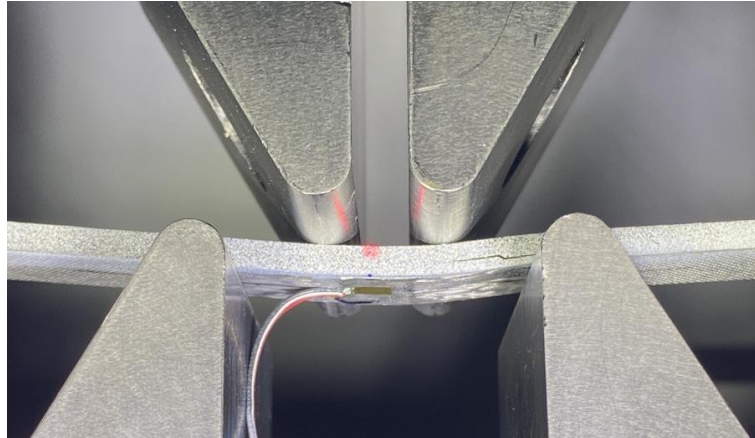


Figure 2.18 – Four–point bending test on QI C/Epoxy coupon

2.7.5. Mechanical tests at higher loading rate

Because an impact event loads a structure at a higher loading–rate than those obtained following the different standards, some tests have been performed at rates up to 1000 mm/min. A universal testing system Instron 5966 has been used. Up to 100 mm/min, the acceleration of the traverse to the targeted velocity was faster than the mechanical response of the coupon. At 1000 mm/min, coupons failure happened during the traverse acceleration phase. To load the coupon at a constant loading–rate, a fixture with an oblong hole has been developed (Figure 2.19). This allows the crosshead to accelerate and reach the target value before to load the coupon.



Figure 2.19 – Fixture used to load a coupon at the same loading–rate

2.8. Characterization at element scale

Quasi-static mechanical tests have been performed in order to have the input data necessary to simulate the impact behavior of C/Epoxy panels after aging. At the element scale, experiments considered both impact and post-impact behavior. These tests have been performed on a quasi-isotropic layup $[0,(-45,45)_2,90]_s$. The choice of the layup was a requirement of the funder of this study.

A new drop weight impact tower was designed and built for this study. The energy range is up to 330J, with a minimal mass of 4.4 kg which can be increased to 10.6 kg. The drop height is superior to 3m (Figure 2.20). This impact tower has been designed to improve the stiffness of the fixture, compared to an existing fixture, and to accelerate the post processing.

The drop weight impact tower is instrumented by four piezoelectric load cells (Kistler™ 9331C) with a measurement range of $\pm 24\text{kN}$ per sensor. The raw signals are conditioned by a charge amplifier, then exported in the form of 0–10V signals. A medium speed laser (Keyence™ LK-G) is used to determine the impactor velocity a few milliseconds before the contact, and a high-speed laser (Keyence™ LK-H157) is used to measure the deflection of the composite coupon during the impact. Both laser signals are conditioned by two conditioners from Keyence™ and exported to our DaQ system in the form of a 0–10V signal. The data acquisition is performed by a DaQ HBM Genesis™ HighSpeed with a universal DaQ card GN 1640B able to acquire data at a frequency of 500kHz and with a resolution of 24 bits.



Figure 2.20 – IFREMER drop weight impact tower

2.8.1. Low Velocity Impact (LVI)

Because impacts in marine environment can occur over the entire surface of the propeller blade, impacts must be performed over a large range of configurations. For this study, both out-of-plane and in-plane impacts were performed.

2.8.1.1. Out-of-plane impact on flat panels

Several standards exist to characterize the impact behavior of composite panels. For this study, the test was carried out based on the guidance of ASTM D7136.

For this test, a C/Epoxy coupon of 150x100mm² and a layup of $[0,(-45,45)_2,90]_s$ is placed on an 80mm thick steel fixture. The coupon is supported on all four borders over a width of 12.5 mm. A rectangular hole of 125x75 mm² in the center of the fixture allows the deflection of the coupon, favoring multiple delamination. No clamps were used, to simplify the test and the simulation. A steel hemispherical impactor with a diameter of 50 mm was released electrically from a known height. The impact energy is determined from the mass and the initial velocity of the impactor measured by a laser before the contact. To avoid a second rebound, the impactor is caught by an automatic pneumatic anti-rebound system. The choice of a larger impactor than recommended by the standard (16mm) was made because it appears that impacts in the marine environment are more common with larger objects.

2.8.1.2. Out-of-plane impacts on curved panels

Another test performed is an impact test on curved C/Epoxy coupons. Tests have been performed on curved panels (Figure 2.21) manufactured around halfpipes with diameters of 30mm, 50mm, and 70mm. A coupon with a diameter of 90mm has also been manufactured but was used for preliminary tests and no measurements were performed for this diameter. Four fixtures have been manufactured to maintain the different coupons. The coupons are simply supported by the fixture. A window allows the coupon to deflect during the impact (Figure 2.22).

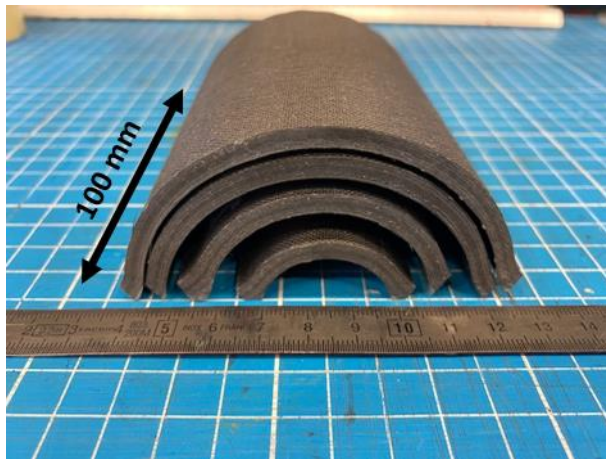


Figure 2.21 – Curved coupons with different diameters (30, 50, 70 and 90 mm) to be impacted

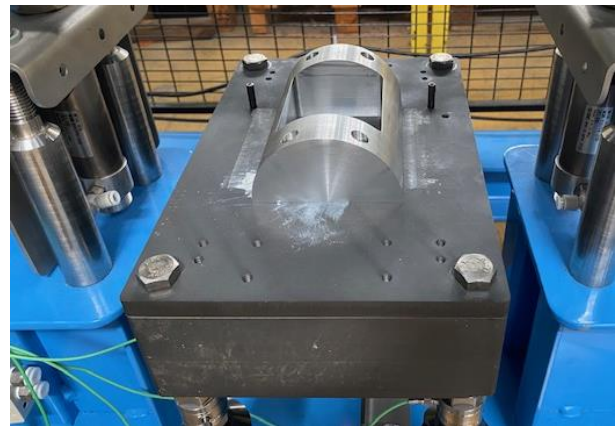


Figure 2.22 – Fixture manufactured to impact Ø70mm curved panels

The window dimension corresponds to an angle of 90° (Figure 2.23). The coupon is 100mm wide and the window is 75mm wide. This allows the coupon to be in contact with the fixture on 12.5 mm on each side. Impacts are monitored: the impact force and the out-of-plane deflection are measured. After the test, a C-Scan is performed to determine if the delamination threshold has been reached and if the coupon is delaminated. The fixture dimensions are proportional, in order to only compare the effects of the curvature.

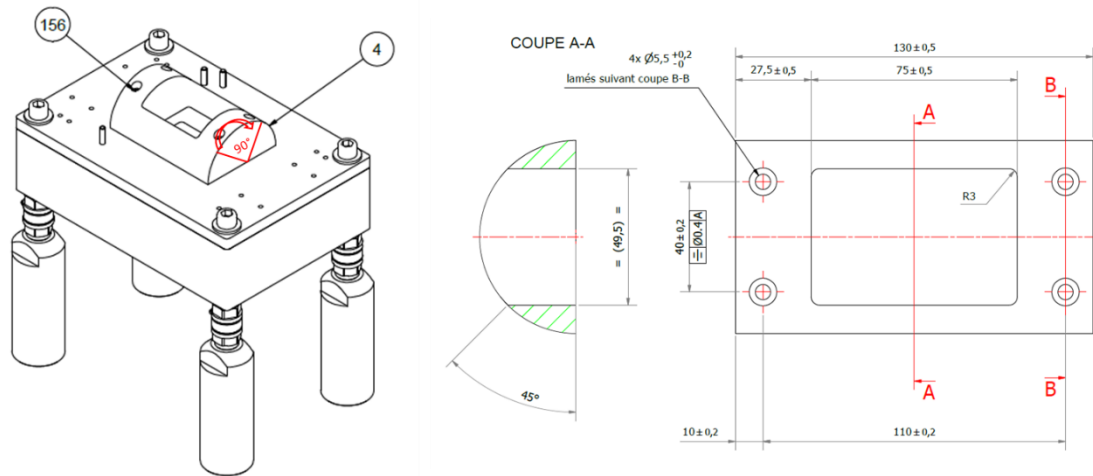


Figure 2.23 – Dimensions of the fixture used for impacts on $\Phi 70$ mm curved coupons

2.8.1.3. On-edge impact

In comparison with out-of-plane impacts, on-edge impact has not been studied extensively in the literature but a small number of previous studies have been found [167][169]. These impact tests were performed here with a $\phi 50$ mm steel hemi-cylindrical impactor (Figure 2.24). The weight of the impactor is 10.6 kg. These tests have been performed on a quasi-isotropic layup $[0,(-45,45)_2,90^\circ]_s$. The coupon is placed vertically on a thick steel fixture with a thickness of 80mm. Coupons dimensions are $150 \times 100 \text{ mm}^2$. Post-contact impactor displacement and force are measured. Impacts have been performed on both rejuvenated and seawater aged states.

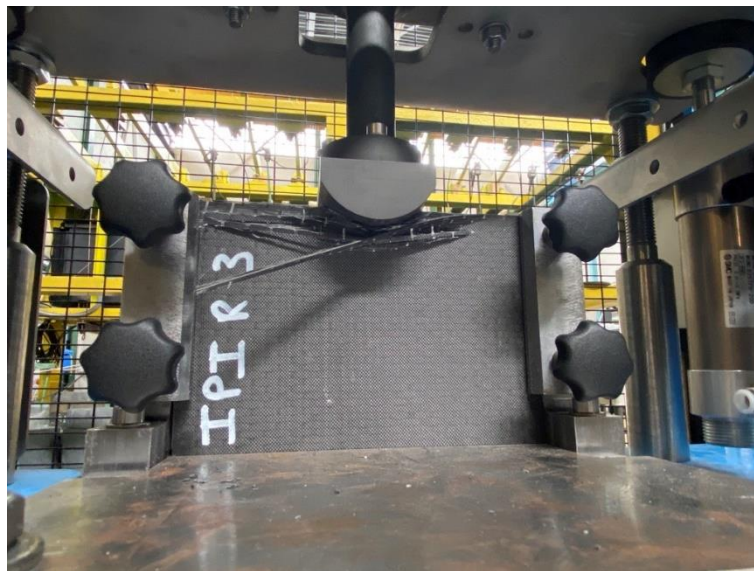


Figure 2.24 – In-plane impact fixture developed from the work of [169]

Figure 2.25 shows images of the test. A trigger is generated by the DAQ system when the contact is established. The image acquisition by the high-speed camera is then started.

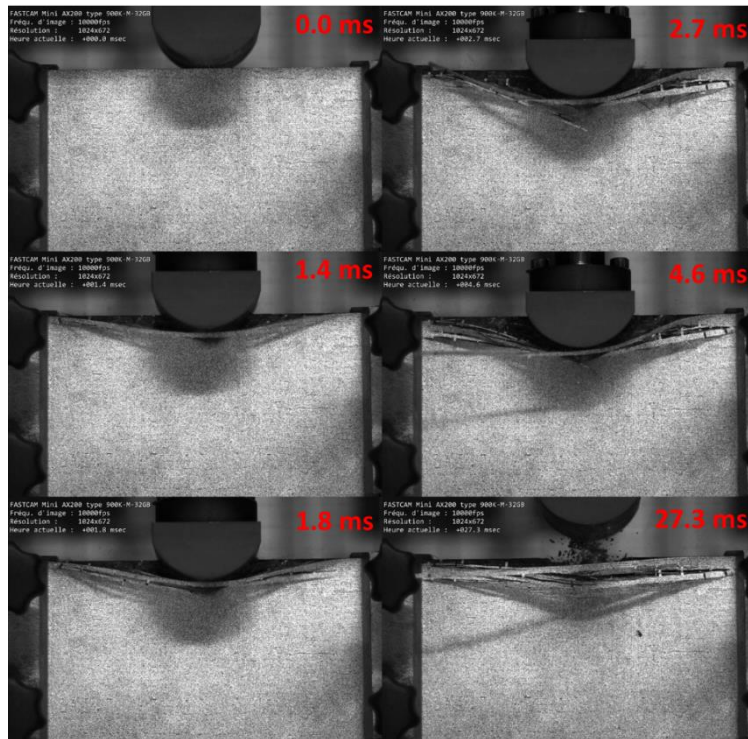


Figure 2.25 – In-plane impact progress, from contact to crush, high speed camera images

2.8.2. Compression After Impact (CAI)

The compression after impact standard (ASTM D7136) has been followed to characterize the post out-of-plane impact behavior of impacted C/Epoxy coupons. The coupon was placed vertically in the fixture (Figure 2.26). Displacement of coupon borders is restrained by the fixture, avoiding early buckling. Screws are tightened with a torque of 7 N.m. Before the test, a random graphite pattern was applied to the specimen surface. The DIC system Aramis™ Adjustable was calibrated then used for the test at a frame rate of 2Hz. This system was used to observe the buckling of the coupon and the location of the failure. The post-processing was performed using the commercial DIC system Aramis™ V6.3. Tests were performed on an Instron™ 5585 testing machine with a load cell of 200kN.

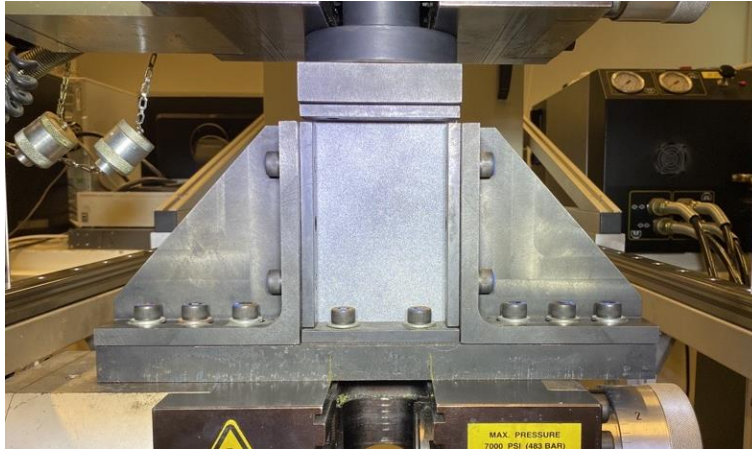


Figure 2.26 – CAI fixture with a speckled coupon

2.9. Characterization at component scale

The final test performed was an impact on a blade component. To do this, blade sections based on the propeller *Fabheili* [34] have been manufactured by the French company LoireTech. The coupon was placed on a thick metallic fixture, then the bottom part was fully constrained (Figure 2.27). A hemi-cylindrical 50mm diameter steel tup was used with a 10.6 kg impactor. The lower impact energy was 35J and the higher was 160J. A high-speed camera was used to observe the behavior of the part. The coupon's geometry is asymmetric, and bending was expected during the test. Two strain-gages were bonded on each side of the coupon to detect this.

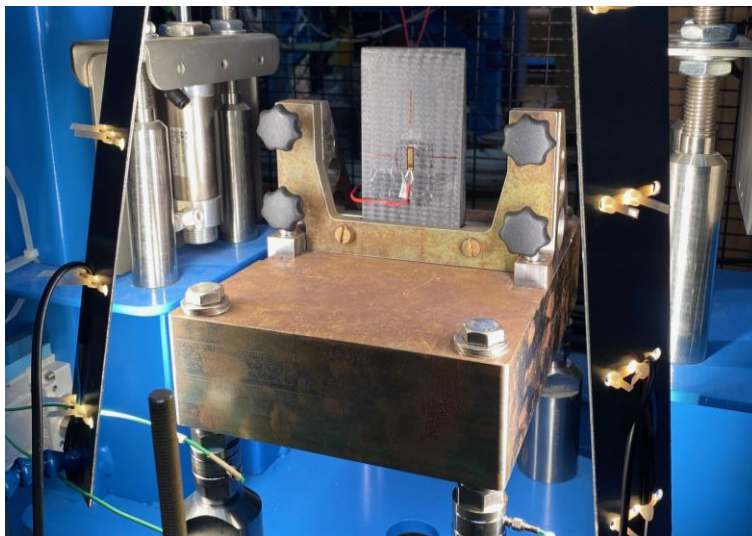


Figure 2.27 – Image of the composite blade section (dimensions not provided due to confidentiality)

2.10. Numerical simulation of composites

To simulate the impact behavior of unaged C/Epoxy coupons, a numerical model has been developed using Abaqus Explicit™ software. The choice of a commercial solver was a requirement of the funder of this study.

It should also be noted that one of the aims of the study was to develop as simple a methodology as possible, which would provide information on impact and seawater aging that could be used in design.

2.10.1. Intralaminar damage model

In Abaqus™, a damage model enables the onset of damage to be predicted and damage evolution to be modelled for elastic–brittle materials with anisotropic behavior. This type of behavior is exhibited by fiber–reinforced materials. This model requires that the undamaged response of the material be linearly elastic, and is based on a damage initiation criterion and a damage evolution response. It works with elements having a plane stress formulation such as shells. This section is based on the Abaqus Analysis User’s manual [220], specifically the part 23.3 which focuses on the “Damage and failure for fiber–reinforced composites”.

2.10.1.1. Computation of the stiffness matrix

Under plane stress conditions ($\sigma_{33} = 0$), only the values of E_1 , E_2 , ν_{12} , G_{12} , G_{13} and G_{23} are required to define an orthotropic material. The shear moduli G_{13} and G_{23} are included because they may be required to model transverse shear deformation in the shell. The Poisson’s ratio ν_{21} is calculated with Eq. 2.17.

$$\nu_{21} = \frac{E_2}{E_1} \nu_{12} \quad \text{Eq. 2.17}$$

For plane stress elements, the in–plane stress–strain relationship is given by Eq. 2.18.

$$\begin{Bmatrix} \varepsilon_1 \\ \varepsilon_2 \\ \gamma_{12} \end{Bmatrix} = \begin{bmatrix} 1/E_1 & -\nu_{12}/E_1 & 0 \\ -\nu_{12}/E_1 & 1/E_2 & 0 \\ 0 & 0 & 1/G_{12} \end{bmatrix} \begin{Bmatrix} \sigma_{11} \\ \sigma_{22} \\ \tau_{12} \end{Bmatrix} \quad \text{Eq. 2.18}$$

2.10.1.2. Computation of the damaged stiffness matrix

The damage is characterized by the degradation of the stiffness matrix. In this model, four different modes of failure are considered: fiber rupture in tension, fiber buckling and kinking in compression, matrix cracking under transverse tension and shear, and matrix crushing under transverse compression and shear. The response of the material is computed from Eq. 2.19.

$$\sigma = C_d \varepsilon \quad \text{Eq. 2.19}$$

Where σ is the stress, ε is the strain, and C_d is the elasticity matrix, which considers any damage and is developed in Eq. 2.20. To simplify the reading, the variable D is shown in Eq. 2.21.

$$C_d = \frac{1}{D} \begin{bmatrix} (1-d_f)E_1 & (1-d_f)(1-d_m)v_{21}E_1 & 0 \\ (1-d_f)(1-d_m)v_{12}E_2 & (1-d_m)E_2 & 0 \\ 0 & 0 & (1-d_s)GD \end{bmatrix} \quad \text{Eq. 2.20}$$

$$D = 1 - (1-d_f)(1-d_m)v_{12}v_{21} \quad \text{Eq. 2.21}$$

In Eq. 2.20 and Eq. 2.21, d_f reflects the current state of fiber damage, d_m reflects the current state of matrix damage, d_s reflects the current state of shear damage, E_1 is the Young's modulus in the fiber direction, E_2 is the Young's modulus in the transverse direction, G is the shear modulus and v_{12} and v_{21} are Poisson's ratios.

2.10.1.3. Damage initiation criterion

The damage initiation criteria for fiber-reinforced composites are based on Hashin's theory [44], which describes the onset of degradation at a material point. These criteria consider four different damage initiation mechanisms, with the general form explained below: fiber tension (Eq. 2.22), fiber compression (Eq. 2.23), matrix tension (Eq. 2.24) and matrix compression (Eq. 2.25). In these equations, the ultimate mechanical properties of plies are used. X^T denotes the longitudinal tensile strength, X^C the longitudinal compressive strength, Y^T the transverse tensile strength, Y^C the transverse compressive strength, and S^L and S^T denote respectively the longitudinal and the transverse shear strength. An additional coefficient α describes the contribution of the shear stress to the fiber tensile initiation criterion.

$$F_f^t = \left(\frac{\hat{\sigma}_{11}}{X^T} \right)^2 + \alpha \left(\frac{\hat{\tau}_{12}}{S^L} \right)^2 \quad \text{Eq. 2.22}$$

$$F_f^c = \left(\frac{\hat{\sigma}_{11}}{X^C} \right)^2 \quad \text{Eq. 2.23}$$

$$F_m^t = \left(\frac{\hat{\sigma}_{22}}{Y^T} \right)^2 + \left(\frac{\hat{\tau}_{12}}{S^L} \right)^2 \quad \text{Eq. 2.24}$$

$$F_m^c = \left(\frac{\hat{\sigma}_{22}}{2S^T} \right)^2 + \left[\left(\frac{Y^C}{2S^T} \right)^2 - 1 \right] \left(\frac{\hat{\sigma}_{22}}{Y^C} \right) + \left(\frac{\hat{\tau}_{12}}{S^L} \right)^2 \quad \text{Eq. 2.25}$$

Finally, $\hat{\sigma}_{11}$, $\hat{\sigma}_{22}$ and $\hat{\tau}_{12}$ are the components of the effective stress tensor $\hat{\sigma}$ which is computed from Eq. 2.26, and is used to evaluate the initiation criteria. In this equation, σ is the true stress and M is the damage operator computed from Eq. 2.27.

$$\hat{\sigma} = M\sigma \quad \text{Eq. 2.26}$$

$$M = \begin{bmatrix} \frac{1}{(1-d_f)} & 0 & 0 \\ 0 & \frac{1}{(1-d_m)} & 0 \\ 0 & 0 & \frac{1}{(1-d_s)} \end{bmatrix} \quad \text{Eq. 2.27}$$

In this equation, d_f , d_m and d_s are the internal damage variables that characterize respectively the fiber, matrix and shear damage. The numerical value assigned to these variables depends on the load seen by the element. The conditions are exposed Eq. 2.28.

$$d_f = \begin{cases} d_f^t & \text{if } \hat{\sigma}_{11} \geq 0 \\ d_f^c & \text{if } \hat{\sigma}_{11} < 0 \end{cases} \quad \text{Eq. 2.28}$$

$$d_m = \begin{cases} d_m^t & \text{if } \hat{\sigma}_{22} \geq 0 \\ d_m^c & \text{if } \hat{\sigma}_{22} < 0 \end{cases}$$

$$d_s = 1 - (1 - d_f^t)(1 - d_f^c)(1 - d_m^t)(1 - d_m^c)$$

Prior to damage initiation, the damage operator M is equal to the identity matrix. Once a first damage has occurred for at least one mode, the damage operator becomes significant. Abaqus™ offers the opportunity to export at each material point some variables that indicates whether an initiation criterion has been satisfied (≥ 1) or not (< 1). Among these variables, we can use HSNFTCRT and HSNFCCRT which respectively report the maximum value of the initiation value experienced during the analysis for the fiber in tension and compression. For the matrix in tension and compression, HSNMTCRT and HSNMCCRT are the variables to use to follow the matrix damage.

2.10.1.4. Damage propagation

Once the damage initiation has occurred a damage propagation law can be used to simulate the post damage behavior. To avoid the mesh dependency during the material softening, the formulation considers a characteristic length. The constitutive law is then expressed as stress versus displacement. The damage will evolve as shown in Figure 2.28. The first part corresponds to an undamaged material with a positive slope, while the second part, with a negative slope, corresponds to the damage evolution.

The value of δ_{eq}^t is determined for all damage modes by the equations summarized in Table 2.2. For shells, the characteristic length L^c is computed as the square root of the element reference surface. The symbol $\langle \rangle$ in the equations represents the Macaulay bracket operator defined Eq. 2.29.

$$\forall \alpha \in \mathfrak{R}, \langle \alpha \rangle = (\alpha + |\alpha|)/2 \quad \text{Eq. 2.29}$$

After the damage initiation, the damage variable for a particular mode is computed with Eq. 2.30.

$$d = \frac{\delta_{eq}^f (\delta_{eq} - \delta_{eq}^0)}{\delta_{eq} (\delta_{eq}^f - \delta_{eq}^0)} \quad \text{Eq. 2.30}$$

In this equation, δ_{eq}^0 represents the initial equivalent displacement at which the initiation criterion for a mode is met and δ_{eq}^f represents the displacement at which the material is completely damaged in this failure mode.

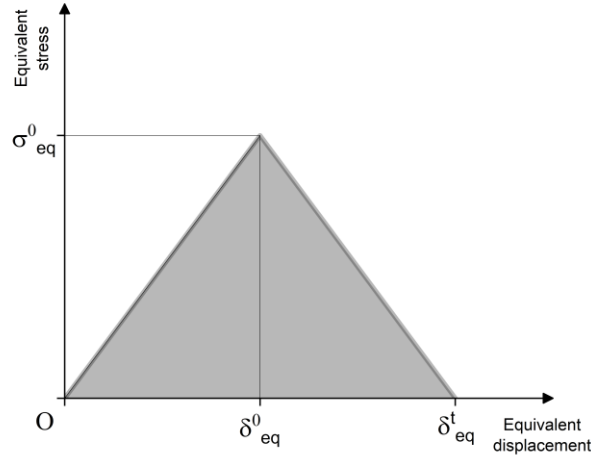


Figure 2.28 – Equivalent displacement and stress for each of the four damage modes

Table 2.2 – Equations used to determine the equivalent stress and displacement

Damage mode	Condition on the stress	Computation of the equivalent stress and displacement
Fiber tension	$\hat{\sigma}_{11} \geq 0$	$\delta_{eq}^{ft} = L^c \sqrt{\langle \varepsilon_{11} \rangle^2 + \alpha \varepsilon_{12}^2}$ $\sigma_{eq}^{ft} = \frac{\langle \sigma_{11} \rangle \langle \varepsilon_{11} \rangle + \alpha \tau_{12} \varepsilon_{12}}{\delta_{eq}^{ft} / L^c}$
Fiber compression	$\hat{\sigma}_{11} < 0$	$\delta_{eq}^{fc} = L^c \langle -\varepsilon_{11} \rangle$ $\sigma_{eq}^{fc} = \frac{\langle -\sigma_{11} \rangle \langle -\varepsilon_{11} \rangle}{\delta_{eq}^{fc} / L^c}$
Matrix tension	$\hat{\sigma}_{22} \geq 0$	$\delta_{eq}^{mt} = L^c \sqrt{\langle \varepsilon_{22} \rangle^2 + \varepsilon_{12}^2}$ $\sigma_{eq}^{mt} = \frac{\langle \sigma_{22} \rangle \langle \varepsilon_{22} \rangle + \tau_{12} \varepsilon_{12}}{\delta_{eq}^{mt} / L^c}$
Matrix compression	$\hat{\sigma}_{22} < 0$	$\delta_{eq}^{mc} = L^c \sqrt{\langle -\varepsilon_{22} \rangle^2 + \varepsilon_{12}^2}$ $\sigma_{eq}^{mc} = \frac{\langle -\sigma_{22} \rangle \langle -\varepsilon_{22} \rangle + \tau_{12} \varepsilon_{12}}{\delta_{eq}^{mc} / L^c}$

For each failure mode, the energy dissipated due to failure G^C is required by Abaqus™ to consider a post damage behavior. This value corresponds to the area of the triangle shown in Figure 2.28. The value of δ_{eq}^f is determined from the value of G^C .

2.10.2. Interlaminar damage model

Cohesive surfaces with a bi-linear traction separation law are defined between every layer to predict the onset and propagation of delamination under LVI. This is a convenient method to model cohesive connections between plies without having to define cohesive elements and tie constraints. A schematic representation of damage initiation and evolution under pure normal, pure shear, and mixed loads is presented in Figure 2.29.

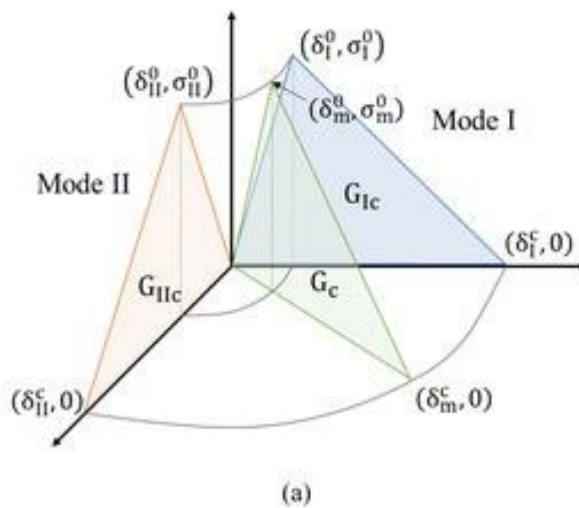


Figure 2.29 – Constitutive cohesive traction–separation law

The initial response is linear and stiffness softening occurs once the damage criterion is met. Delamination initiation under mixed mode loading was determined using a quadratic stress criterion, presented in Eq. 2.31.

$$\left\{ \frac{\langle \tau_n \rangle}{\tau_n^0} \right\}^2 + \left\{ \frac{\tau_s}{\tau_s^0} \right\}^2 + \left\{ \frac{\tau_t}{\tau_t^0} \right\}^2 = 1 \quad \text{Eq. 2.31}$$

In this equation, τ_i ($i = n, s, t$) are respectively the normal and in-plane shear stresses, and τ_i^0 denotes the maximum traction stresses associated with each direction. The Macauley brackets are used to signify that a purely compressive displacement or a purely compressive stress does not initiate damage. The progressive failure of the cohesive interaction is driven with an energy based criterion and the ultimate failure is governed by the Benzeggagh–Kenane criterion [221], presented in Eq. 2.32.

$$G_{TC} = G_{IC} + (G_{IIC} - G_{IC}) \left(\frac{G_{II}}{G_T} \right)^\eta \quad \text{Eq. 2.32}$$

In this equation, G_{IC} and G_{IIC} are respectively the critical fracture energies under mode I and II loading, G_{TC} is the total critical fracture energy, and G_T is the sum of G_I and G_{II} , the fracture energies in mode I and II. The parameter η describes the shape of the interaction model.

Chapter 3

—

Influence of aging on quasi–static mechanical properties

Chapter 3 – Influence of aging on quasi-static mechanical properties

3.1. SEAWATER AGING.....	96
3.1.1. EXPERIMENTAL OBSERVATIONS.....	96
3.1.2. MODELING THE WATER UPTAKE IN EPOXY AND C/EPOXY COUPONS.....	97
3.1.3. SEAWATER AGING RESULTS.....	97
3.1.4. PREDICTION OF THE WATER DIFFUSION IN THICK COMPOSITES.....	99
3.1.5. CONCLUSION ON SEAWATER AGING.....	103
3.2. PLY PROPERTIES.....	104
3.2.1. IN-PLANE PROPERTIES.....	104
3.2.2. OUT-OF-PLANE PROPERTIES.....	109
3.3. INTERFACE PROPERTIES.....	113
3.3.1. DAMAGE INITIATION.....	113
3.3.2. FRACTURE PROPAGATION.....	117
3.3.3. DISCUSSION.....	121
3.4. NORMALIZATION OF THE PROPERTIES CHANGE.....	121
3.5. APPLICATION OF AGED PROPERTIES TO A STRUCTURAL TEST.....	123
3.5.1. EXPERIMENTAL TESTS.....	123
3.5.2. NUMERICAL SIMULATION.....	124
3.5.3. INTRALAMINAR AND TRANSLAMINAR FRACTURE PROPERTIES.....	126
3.5.4. COMPARISON EXPERIMENT/SIMULATION.....	127
3.6. CONCLUSION.....	128

This chapter will be devoted to the characterization of the influence of aging on the change of mechanical properties of the C/Epoxy studied. Several previous studies have examined physical aging [185][222][223], seawater aging [89][190][196][207][224][225], or both [171], but none presents results with a complete dataset of properties obtained experimentally to provide an overall view of the effects of aging.

The aim of this chapter is to summarize all the tests performed and their results, to obtain a complete dataset of unaged and aged properties that will then be used to simulate a four–point bending test on a structure. First, the seawater diffusion into the material will be presented. The diffusion coefficients determined experimentally at the coupon scale will be used to simulate the water uptake of a propeller component. Then, the quasi–static results will be presented and discussed. Two aspects will be discussed: the ply and the interface properties. Finally, as mentioned above, the complete dataset will be used to simulate a four–point bending test intermediate between a short and a long beam test. This results in a complex stress state that will be simulated using Abaqus™, and allows the simulation to be compared with the experimental dataset, before to using it to simulate an impact event.

3.1. Seawater aging

3.1.1. Experimental observations

Plots representing the weight gain as a function of immersion time for pure epoxy coupons (Figure 3.1) and C/Epoxy coupons (Figure 3.2) are presented below. The material is considered saturated when a plateau is reached. Error bars are shown, and the scatter is small in comparison with the data measured. It may be noted that the epoxy coupons show a plateau at 60°C, but not the C/Epoxy. This may be due to the porosity ratio, that was measured to be higher for the composite, or a degradation of the interface between the fibers and the matrix.

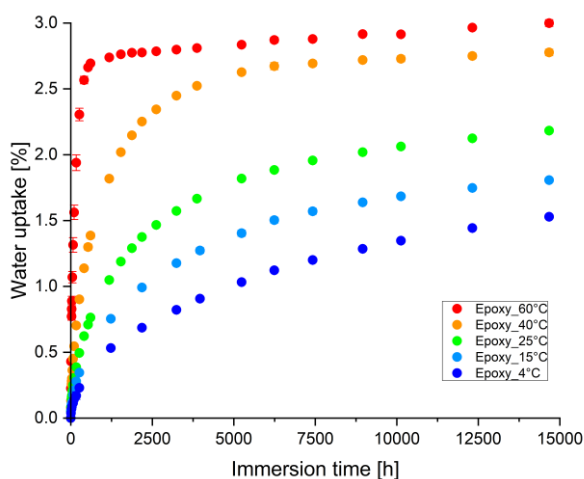


Figure 3.1 – Water uptake of pure Epoxy coupons immersed in seawater at different temperatures

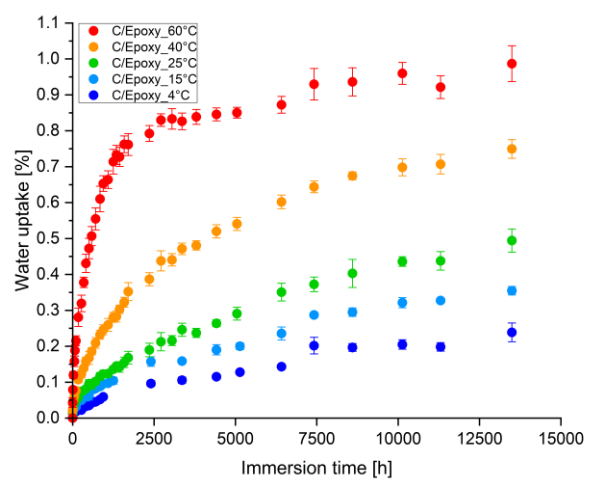


Figure 3.2 – Water uptake of C/Epoxy coupons immersed in seawater at different temperatures

3.1.2. Modeling the water uptake in Epoxy and C/Epoxy coupons

The increase of the water uptake with the increasing temperature is due to the change in the solubility. A normalization is needed to account for the variable thickness due to the manufacturing process. To do that, the water uptake is defined as a function of the square root of time divided by the coupon thickness. With these values, a comparison is performed with the Fick 1D diffusion model. Results are respectively presented for pure Epoxy coupons (Figure 3.3) and C/Epoxy (Figure 3.4).

At 60°C, the weight of the C/Epoxy continues to increase, possibly due to a chemical degradation. This may be due to the small gap between the decreasing T_g and the seawater temperature. For this reason, the model was fitted with experimental data up to $25 \sqrt{h}/mm$ for the pure Epoxy coupons and $17 \sqrt{h}/mm$ for the C/Epoxy. For the resin, the fit was obtained with an optimization of two parameters: the diffusion coefficient D and the mass at saturation m_∞ . For the composite, only the diffusion coefficient was optimized, and a value of $m_\infty=0.85\%$ was chosen: this value corresponds to the mass at saturation at 60°C. There is an over-prediction of m_∞ at 4°C, 15°C and 25°C for the resin when the two parameters are optimized, because experimental data have not reached the inflexion point.

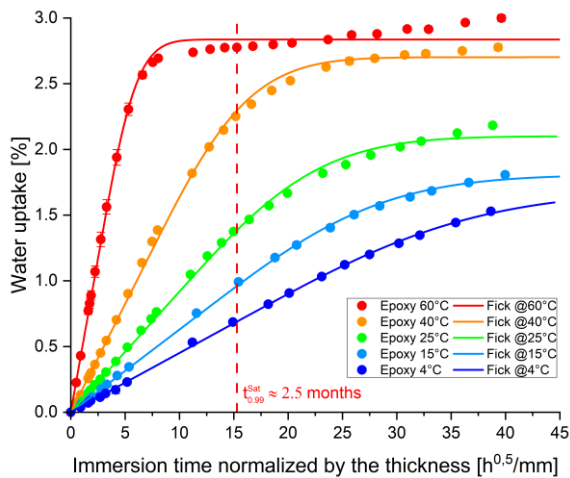


Figure 3.3 – Water uptake of pure Epoxy coupons immersed in seawater at different temperatures

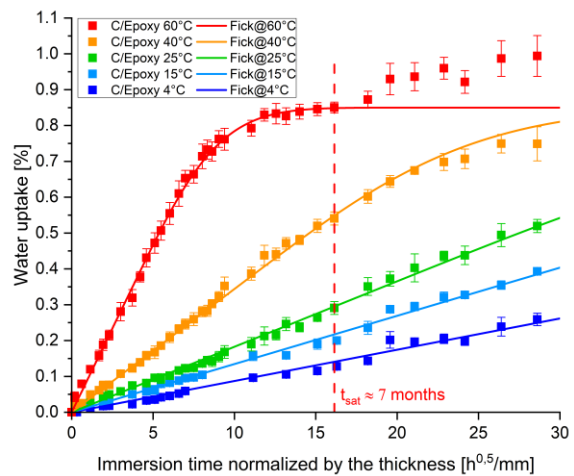


Figure 3.4 – Water uptake of pure Epoxy coupons immersed in seawater at different temperatures

It must be noted that even if the identification method is not the same for the pure Epoxy and the C/Epoxy coupons, the results are conservative. Aging of these specimens is continuing, but for the thicknesses we have, this PhD project was not long enough to saturate the material at a lower temperature.

3.1.3. Seawater aging results

Results from seawater ageing are summarized in Table 3.1. For the five different temperatures, the diffusion coefficients have been determined. However, under real conditions, the seawater temperature will not be at these levels. An Arrhenius law can be applied to interpolate the diffusion coefficients as a function of the temperature (Eq. 3.1).

$$D(T) = D_0 \cdot \exp\left(\frac{-E_a}{R \cdot T}\right) \quad \text{Eq. 3.1}$$

With $D(T)$, the diffusion coefficient which depends on the temperature [m^2/s], D_0 the diffusion coefficient when the temperature goes to infinity [m^2/s], E_a the activation energy for diffusion [J/mol], R the universal gas constant [$\text{J}\cdot\text{mol}^{-1}\cdot\text{K}^{-1}$], and T the temperature of immersion [K].

The two materials parameters D_0 and E_a must be found, and plotting $\ln D = f\left(\frac{1}{R \cdot T}\right)$ gives a linear function with $-E_a$ the coefficient and $\ln D_0$ the intercept. It is then possible to determine E_a , and finally D_0 .

Table 3.1 – Results of Fickian modeling of pure Epoxy and C/Epoxy ageing data (*extrapolated value)

Seawater ageing temperature [°C]	Epoxy		C/Epoxy	
	D_R [mm^2/s]	m_∞ [%]	D_C [mm^2/s]	m_∞ [%]
4	3.92E-08*	1.68*	5.74E-09*	0.85*
15	6.63E-08*	1.81*	1.37E-08*	0.85*
25	1.04E-07*	2.10*	2.52E-08*	0.85*
40	2.03E-07	2.70	8.93E-08*	0.85*
60	1.48E-06	2.84	6.08E-07	0.85

The Arrhenius law was fitted from all temperature data except $T=60^\circ\text{C}$ (Figure 3.5), as at this temperature, the Arrhenius law diverges from the experimental data. This is due to chemical damage or a non-Fickian diffusion reported in the literature [226]. For the other temperatures, the Arrhenius law is respected. For diffusion, the activation energy was found to be 32.9 kJ/mol for pure Epoxy coupons and 54.3 kJ/mol for C/Epoxy coupons. These data are in accordance with values in the literature [227], but can vary depending on the Epoxy system chemistry [228].

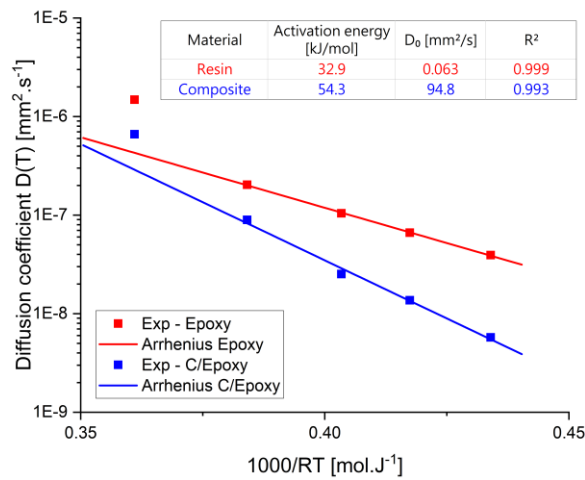


Figure 3.5 – Diffusion coefficient $D(T)$ as a function of the immersion temperature

For coupons dedicated to mechanically testing after seawater immersion, it was decided at the beginning of the project to immerse them at 60°C. This choice was made based on results from a previous study [170], but can be criticized based on Figure 3.3 and Figure 3.4; there is not a stable saturation plateau at this temperature. A solution could have been to decrease the immersion temperature, but the time needed to reach the saturation would have been higher. At 40°C, the time to saturate (99.9%) the pure Epoxy coupons would have been multiplied by 7 (from 50 days to 360 days) and for the C/Epoxy coupons multiplied by 8 (135 to 1120 days).

3.1.4. Prediction of the water diffusion in thick composites

The benefit of identifying this diffusion model is that for thick CFRP structures to be immersed in seawater for 50 years or more, it is now possible to predict the water profile from the experimental diffusion coefficient obtained previously. An example of the application to a thick geometry will now be described.

3.1.4.1. Geometry

The prediction is performed on a technological coupon developed from the *Fabheli* project [34]. It represents a trailing edge, the thinnest part of the propeller. It has been chosen because under operational conditions, the water diffusion is a slow process and the thinner the part, the faster the saturation. The part studied is presented in Figure 3.6.

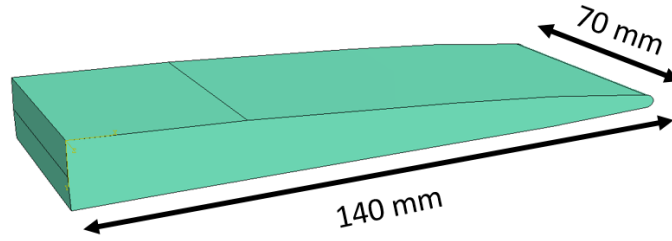


Figure 3.6 – Representative coupon of a marine propeller leading edge

3.1.4.2. Finite elements model

The part is an extrusion of a 2D sketch. To reduce the computation time, it has been decided to work with a 2D model. The water uptake is simulated using the Abaqus™ Heat transfer module. This approach is valid thanks to an analogy between heat transfer (Eq. 3.2) and water diffusion (Eq. 3.3), proposed by Shen and Springer [229]. The same approach has been used recently to predict the water profile in a thick tidal composite blade [230].

$$\rho C \frac{\partial T}{\partial t} = \frac{\partial}{\partial x} K_x \frac{\partial T}{\partial x} \quad \text{Eq. 3.2}$$

$$\frac{\partial c}{\partial t} = \frac{\partial}{\partial x} D_x \frac{\partial c}{\partial x} \quad \text{Eq. 3.3}$$

We suppose here that the diffusion is isotropic in the blade, a more detailed model would require identification of the coefficients in the three directions. The diffusion coefficient D_c obtained experimentally allows the thermal conductivity K_c to be calculated from the material density ρ , the specific heat C obtained experimentally by DSC, and D_x the water diffusion coefficient. Eq. 3.4 is the expression used to determine K_c .

$$K_c = \rho \cdot C \cdot D_c \quad \text{Eq. 3.4}$$

In the case of the C/Epoxy studied here, $\rho=1.55E^{-3} \text{ g/mm}^3$, $C=2.0E-4 \text{ kJ/g/K}^{-1}$, and D_c is the value obtained experimentally for a diffusion supposed isotropic. Table 3.2 summarizes the values of K_c used for the model. The blade is in contact with a heat source on its external surface. The amplitude is equal to 1. Boundary conditions are assumed to be the same as for a real part. Except for the part on the left which is the continuation of the propeller, all the surfaces are exposed to the temperature.

Eight diffusion times have been examined, from 1 day to 50 years for the different conditions. Four sections have been chosen, in order to study in more detail the water profiles for different composite thicknesses.

Table 3.2 – Thermal conductivity data used to predict the water profile in the composite blade

Temperature [°C]	Diffusion coefficient D_x [mm ² /ms]	Thermal conductivity K_c [kJ.ms ⁻¹ .mm ⁻¹ .K ⁻¹]
4	5.74E-12	1.78E-18
15	1.37E-11	4.25E-18
25	2.52E-11	7.81E-18
40	8.93E-11	2.77E-17

3.1.4.3. Results

3.1.4.3.1. Global behavior

The simulation time with this geometry is less than one minute. A mesh sensitivity study has been performed and showed no influence of the mesh when its dimensions were less than 0.25mm.

Figure 3.7 shows the water profile in the composite coupon for an aging performed at 40°C and for four immersion times.

After a simulated immersion time of 50 years at 40°C, the coupon seems to be fully saturated. The thickest part of the coupon is 15 mm thick. After 10 years, the thinnest part seems to be saturated.

3.1.4.3.2. Local behavior

Water concentrations along four paths have been exported for five aging times: 1 year, 5 years, 10 years, 25 years and 50 years. Two temperatures are presented in Table 3.3: 15°C and 40°C. The first corresponds to a common temperature in a marine environment, while the second is considered as an extreme condition. When the water concentration is equal to 0, no water uptake is predicted. When the water concentration is equal to 1, the structure is locally saturated with water.

At 40°C, the thinnest part of the coupon (Path 4) is almost saturated after 5 years. This 3 mm thick section is representative of the thickness of the coupons mechanically tested in the remainder of this chapter. However, this saturation time is not suitable for the duration of a PhD project, and so a higher temperature, not representative of an operative condition, is necessary to accelerate the water diffusion.

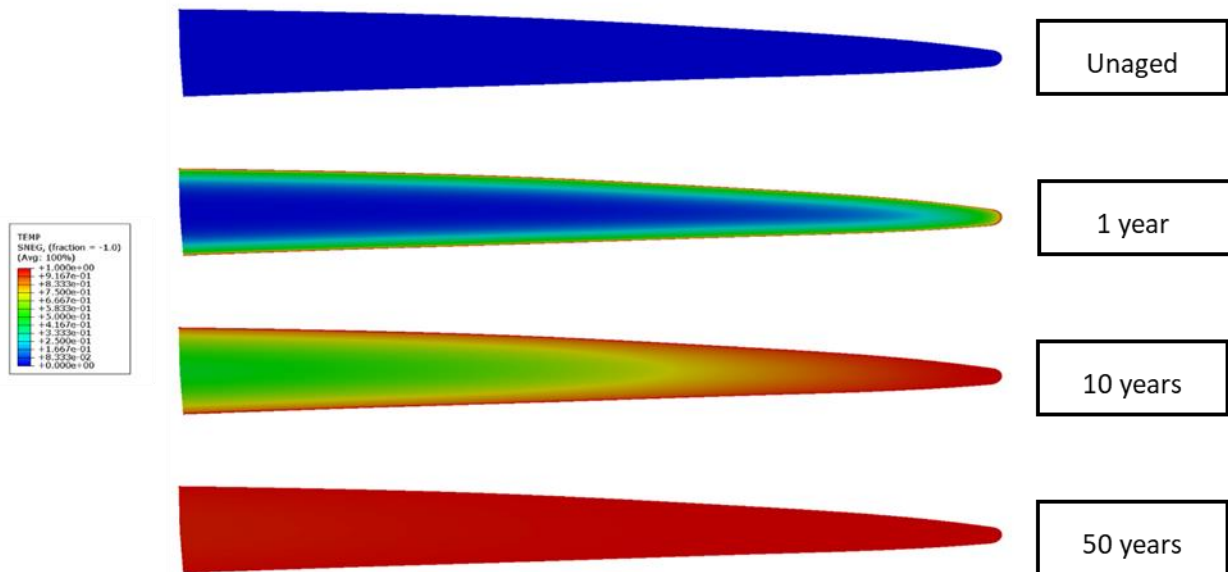


Figure 3.7 – Simulation of water diffusion in the composite coupon at 40°C

At 15°C, the saturation in the thinnest part (Path 4) is reached after more than 25 years in immersion. This time is extremely long compared to the part life duration. However, the mechanical properties are affected by the aging at lower concentrations [6]. Even if the thinnest part is not fully saturated after 5 years, its entire thickness is still affected by water ingress. It is therefore necessary to investigate whether sea water aging has an effect on the mechanical properties of the composite. For thicker sections (Path 1), the saturation is not reached after 50 years. Figure 3.8 shows the change of the water concentration in the plies. The diffusion process is very slow and only the first three plies will absorb more than half of their saturation level.

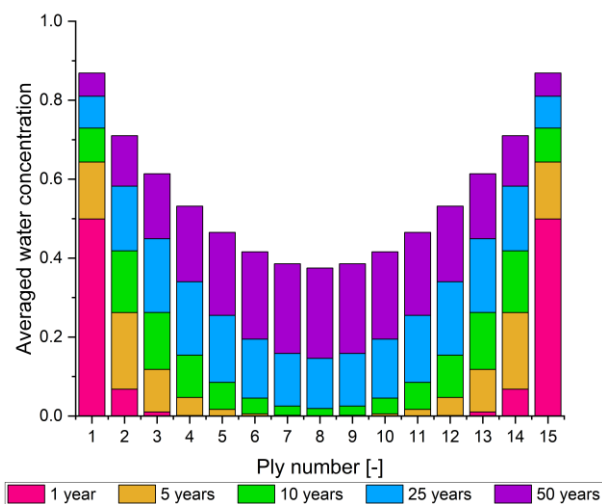
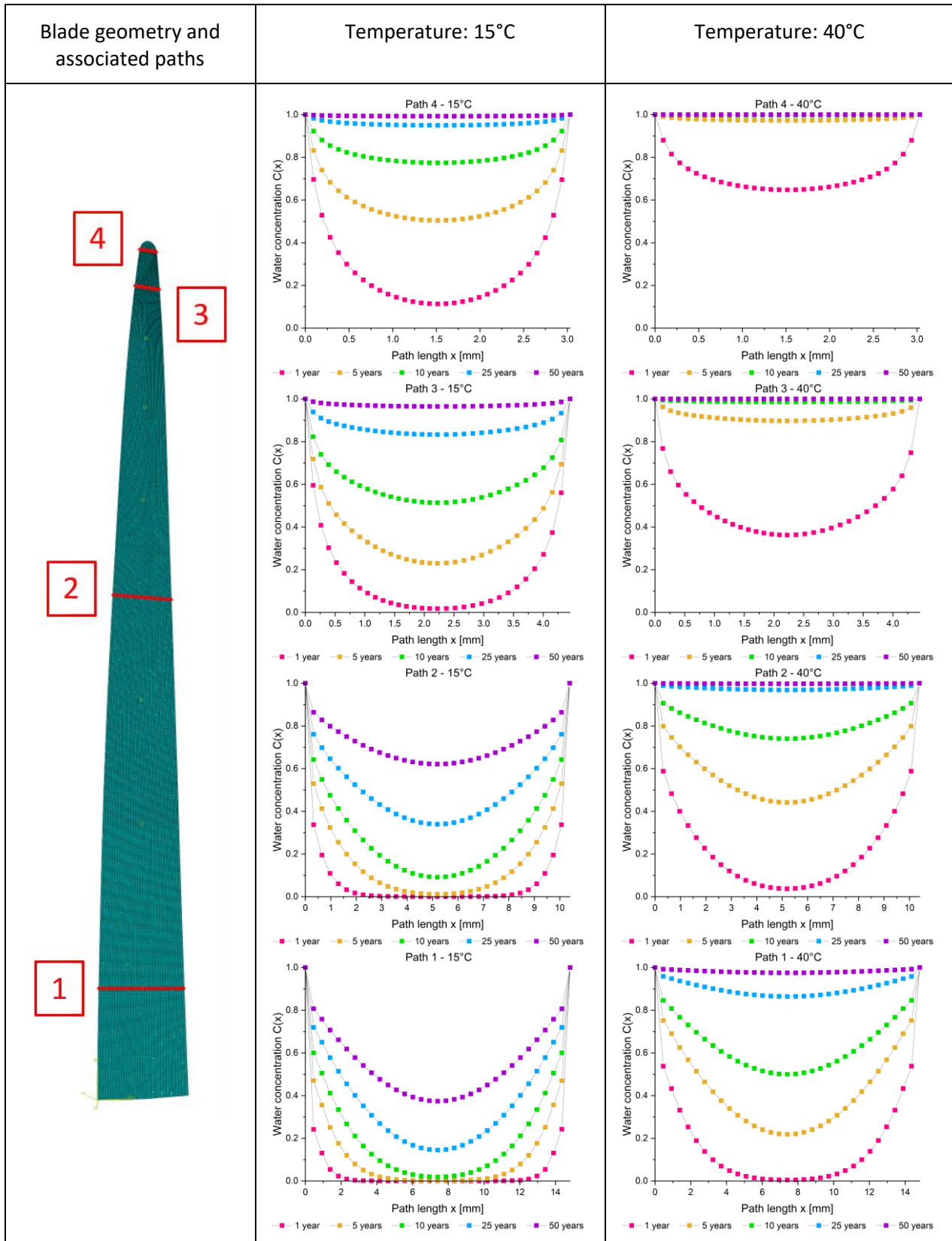


Figure 3.8 – Plies averaged concentration of water (15mm thick at 15°C)

Table 3.3 – Comparison of water profiles for different paths in the blade



3.1.5. Conclusion on seawater aging

Pure Epoxy and C/Epoxy coupons have been immersed in seawater at different temperatures. After 2 years of immersion, Fickian behavior has been found to be applicable for simple coupons. Fickian diffusion

coefficients have been used to predict the long-term water diffusion through a real composite leading edge. Results show an acceleration of the water uptake when increasing the temperature. In addition, at lower immersion temperatures, and when the composite thickness is increased, the water may not reach the middle section of the blade. The saturation condition appears almost impossible to reach during service. Only the external plies in contact with the water will then be affected by the aging effects. Also, under real conditions, structures would be coated, further reducing the rate of water uptake. However, impacts do happen on the external plies and if these were previously affected by water during service, the effect of aging on the mechanical properties of the composite may be significant and should be investigated. This is the aim of the following sections.

3.2. Ply properties

In order to perform a numerical simulation of the deformation of a composite structure, a stiffness matrix is required (Eq. 3.5). Both in-plane and out-of-plane elastic properties are needed. These properties depend on the fiber and the resin system. To investigate the influence of aging on the mechanical properties, it was decided to perform as far as possible the characterization of the material chosen, suitable for a naval application.

$$\begin{bmatrix} \varepsilon_{11} \\ \varepsilon_{22} \\ \varepsilon_{33} \\ \varepsilon_{23} \\ \varepsilon_{31} \\ \varepsilon_{12} \end{bmatrix} = \begin{bmatrix} \frac{1}{E_1} & \frac{-\nu_{21}}{E_2} & \frac{-\nu_{31}}{E_3} & 0 & 0 & 0 \\ \frac{-\nu_{12}}{E_1} & \frac{1}{E_2} & \frac{-\nu_{32}}{E_3} & 0 & 0 & 0 \\ \frac{-\nu_{13}}{E_1} & \frac{-\nu_{23}}{E_2} & \frac{1}{E_3} & 0 & 0 & 0 \\ 0 & 0 & 0 & \frac{1}{2G_{23}} & 0 & 0 \\ 0 & 0 & 0 & 0 & \frac{1}{2G_{31}} & 0 \\ 0 & 0 & 0 & 0 & 0 & \frac{1}{2G_{12}} \end{bmatrix} \begin{bmatrix} \sigma_{11} \\ \sigma_{22} \\ \sigma_{33} \\ \sigma_{23} \\ \sigma_{31} \\ \sigma_{12} \end{bmatrix} \quad \text{Eq. 3.5}$$

In addition, if the failure of the structure is to be determined a set of failure properties corresponding to these different loading cases is necessary. A further aspect to consider is delamination propagation. An extensive experimental campaign was carried out in this study to obtain a complete set of data to predict the mechanical behavior of composite structures after aging. The section hereafter describes the results of these tests, first to characterize in-plane, then out-of-plane behavior.

3.2.1. In-plane properties

3.2.1.1. Tensile tests

Tensile tests have been performed on UD, 90° and ±45° specimens. All in-plane properties used for structural design were affected by the seawater aging (Table 3.4). Unlike the coupons of composite oriented at ±45°

(Figure 3.11), matrix dominated mechanical tests show improvements of the modulus with the physical aging and a decrease with the seawater aging. The influence of physical aging on the shear behavior has been investigated in the past [7]. In [8], the embrittlement of the epoxy during the physical aging was shown to result in the growth of microcracks at lower load, and as the toughness is also reduced, the growth of microcracks leads to global failure more quickly. With respect to the increase of the modulus, one explanation is that as the modulus is defined between 0.2% and 0.4%, the load is still low, and so the microcracks have not appeared yet. Thus, the modulus is calculated on an undamaged material, and this may be the reason why the modulus is slightly higher after physical aging.

Table 3.4 – Change of the in-plane mechanical properties with the aging conditions

	Rejuvenated	Physically aged	Seawater aged
E_{11} [GPa]	127.54 ± 3.18	128.03 ± 4.45	128.41 ± 6.92
E_{22} [GPa]	7.94 ± 0.6	9.23 ± 0.78	4.39 ± 0.45
ν_{12} [-]	0.274 ± 0.010	0.320 ± 0.025	0.341 ± 0.026
G_{12} [GPa]	3.72 ± 0.12	4.07 ± 0.05	2.70 ± 0.08

Figure 3.9 and Figure 3.10 shows the stress vs. strain response for tensile tests performed respectively on the fiber direction and perpendicular to the fiber direction. For both orientation, the curves are brittle until the coupon failure. For the test on the fiber direction, it must be noted that the behavior is purely linear and does not reveal a non-linearity, as observed on aerospace materials [231]. This is mainly due to the stitching that keeps the fibers aligned during the infusion.

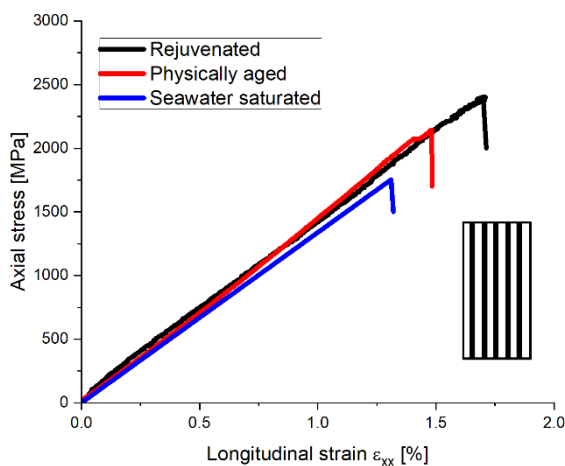


Figure 3.9 – Comparison of Stress vs. Strain curves with the aging for tensile tests on $[0]_4$

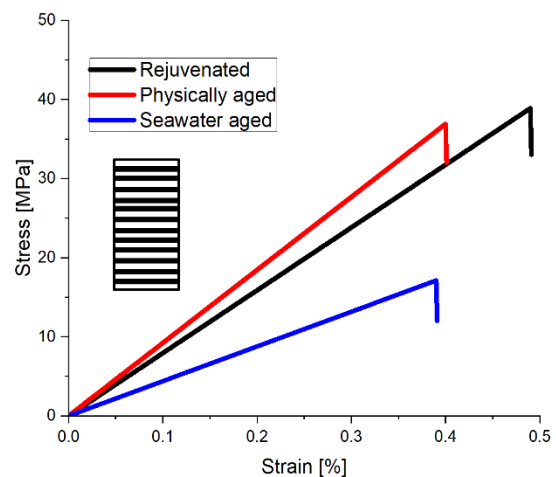


Figure 3.10 – Comparison of Stress vs. Strain curves with the aging for tensile tests on $[90]_4$

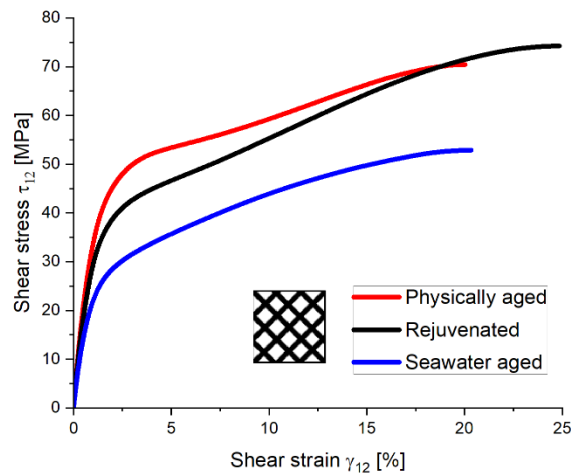


Figure 3.11 – Shear stress vs. shear strains plots of $[-45,45]_{25}$ C/Epoxy before and after aging

The transverse strain field has been checked for the tensile test on $[0]_4$. As shown Figure 3.12, it is heterogeneous. A periodic pattern which corresponds to the wavy yarns can be seen. It must be noted that the Poisson ratio ν_{12} has been determined for the widest surface as far as possible.

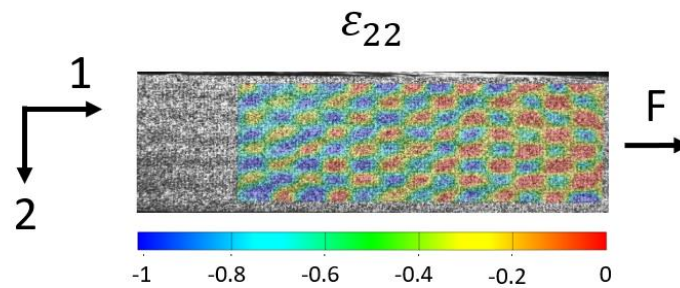


Figure 3.12 – Visualization of the transverse strain measured by DIC during a tensile test on $[0]_4$

The last aspect considered is the change in ultimate ply properties after aging. Tension tests have also been performed on $\pm 45^\circ$ coupons to determine the shear stress at failure. Results are shown in Table 3.5. In tension, the physical aging improves the stress at failure for both orientations while the seawater aging decreases it. For the seawater saturated coupons, a loss is observed in the UD strength. This is unexpected because the aging is only supposed to change the matrix properties. A fractography study has been performed and showed a cohesive failure between two carbon plies below the tabs. The pressure generated by the jaws induces a stress at the interface which leads to a premature failure of the coupon. Coupled with the drop in transverse strength, it is possible to suspect the degradation of the fiber/matrix interface during the seawater aging.

Table 3.5 – C/Epoxy in-plane strength before and after aging

	Rejuvenated	Physically aged	Seawater aged
X^T [MPa]	2271.7 ± 136.5	2140.3 ± 24.7	1760 ± 96
Y^T [MPa]	38.3 ± 1.7	36.4 ± 5.5	16.6 ± 1.3
S^T [MPa]	73.3 ± 3.0	68.7 ± 1.6	54.0 ± 1.0

3.2.1.2. Compression tests

Compression tests have been performed on UD and 90° C/Epoxy coupons. Strain gages have been bonded on both faces of the coupons to measure the buckling, then to validate or not the results. An example of a buckling result is shown in Figure 3.13. At the end of the test, the strain increases on one face and becomes negative in the other. This is due to buckling and the test result is invalid and cannot be used.

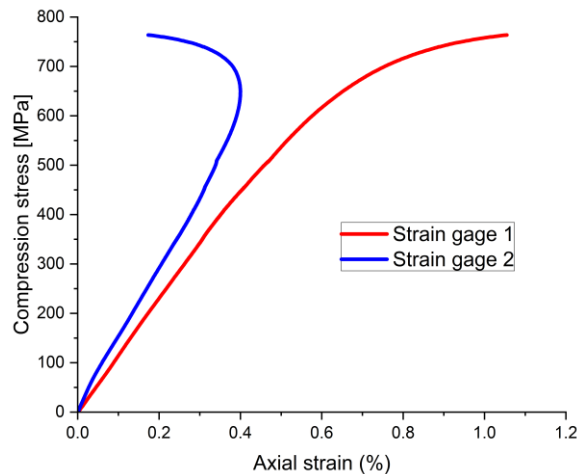


Figure 3.13 – Example of a buckling failure observed with two strain gages

A comparison of the compressive stress vs. compressive strain curves is shown Figure 3.14 and Figure 3.15 respectively for tests on the longitudinal and transverse direction. While the behavior is purely linear until failure for the unidirectional layup, the transverse layup exhibits a nonlinear part which is reduced after seawater aging. One hypothesis is the interface degradation that allows crack to propagate for a lower load. It must also be noted that the gage section is relatively small for this test. The measure is performed by a strain gage bonded on a surface with an area of 13x12 mm². This represents four carbon fiber yarns on the width with a stitching that promotes microbuckling. To avoid this measurement issue, the use of a DIC system could help to determine if the strain is homogeneous or affected by the wavy yarns.

Figure 3.16 shows the post-mortem observation for the [0]₄. It must be noted that for all the tests, the failure was obtained on the gage section.

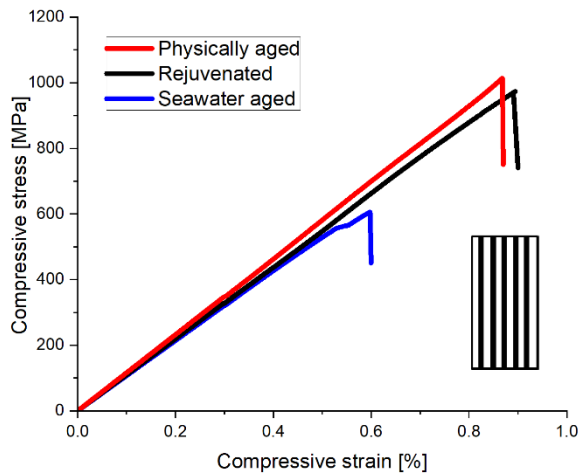


Figure 3.14 – Comparison of Stress vs. strain curves pour compression tests performed on $[0]_4$

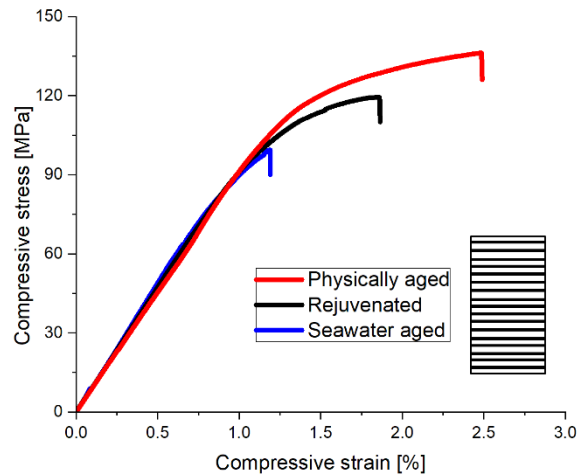


Figure 3.15 – Comparison of Stress vs. strain curves pour compression tests performed on $[90]_4$

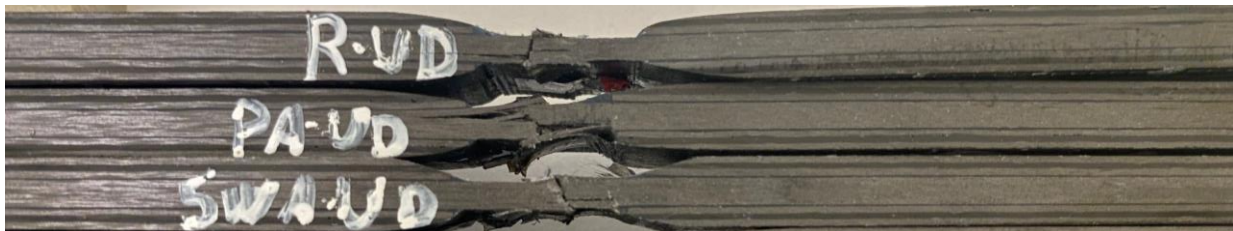


Figure 3.16 – Comparison of the post-mortem observation for the $[0]_4$ coupons tested in compression

The influence of aging on compressive properties has previously been studied on open-hole compression properties [232]. In that study, the T800 carbon fiber–epoxy quasi-isotropic composite coupons were aged in humidity chambers at 70°C and 85% RH during 40 days until the equilibrium was reached. The authors noted a loss of 4% of the stress at failure. In this present study, results for the compressive strength and modulus are summarized in Table 3.6.

Table 3.6 – In-plane compression stress at failure with the aging

	Rejuvenated	Physically aged	Seawater aged
E_{11}^C [GPa]	117 ± 4	112 ± 1	115 ± 11
E_{22}^C [GPa]	9.98 ± 0.05	10.0 ± 0.03	9.17 ± 0.03
X^C [MPa]	934 ± 50	950 ± 76	607 ± 33
Y^C [MPa]	124 ± 4	134 ± 3	94 ± 3

After seawater aging, the compression strength loss is estimated to be 35% for 0° and 24% for 90°. For the 90° orientation, the failure begins in rich resin regions due to the inhomogeneity of the material at the mesoscale. For the 0° coupons, as the compression is in the fiber direction, the loss was not expected to be

so high. The main reason for the drop appears to be the presence of weft stitching (Figure 3.17). Carbon fibers in the warp direction are deviated by the presence of these PET weft threads, and the main consequence is a reduced compression resistance [233] due to fiber misalignment, in comparison with the straight fibers in a prepreg-based composite. After seawater aging, the properties of the matrix drop due to water ingress in the material. Swelling of the stitching during immersion may also contribute to the loss in strength. In all cases, failure occurred in the gage section.

No explicit change has been observed for the longitudinal and transverse modulus.

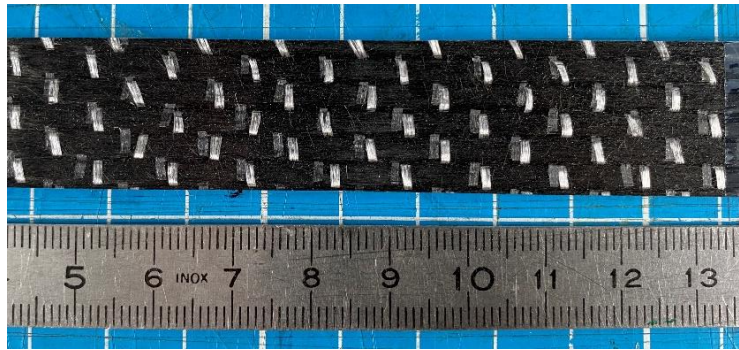


Figure 3.17 – PET weft threads added to maintain the carbon fiber yarn during the composite manufacturing process

3.2.1.3. Intralaminar and translaminar fracture toughness

In-plane damage propagation tests have been performed in order to evaluate the change of fracture toughness with the aging, both in tension and compression. These tests were based on previous studies [234]–[236]. Compact Tension (CT) and Compact Compression (CC) coupons have been manufactured then cut with a waterjet. Two layups were tested: $[0]_8$ and $[0, 90]_{2S}$. However, for all coupon, a premature failure was observed, away from the area of interest. Other tests are possible, and designing a coupon knowing the mechanical properties could help to get a failure where it is expected. Another coupon has been developed [237] and showed a reduced scatter for a woven composite. For unidirectional composites, results shows a high scatter [234] and often depend on the testing procedure.

3.2.2. Out-of-plane properties

3.2.2.1. Three-point bending tests

Flexural tests have been performed on $[0]_4$ coupons. Flexural modulus values E_{1f} are necessary in order to calculate the mixed mode bending fracture toughness. Tests have been performed up to the coupon failure. A comparison of the bending stress as a function of the backface strain is shown Figure 3.18. The physical aging does not change the flexural modulus but increases the threshold that leads to a nonlinearity, then to the coupon failure. The consequences of the seawater aging are reductions in both the flexural modulus and the strength. A hypothesis is a local damage bellow the pin due to a stress concentration. It could have been interesting to perform the test with rubber sheet between the pin and the composite to distribute the load to a larger area, and then to avoid a failure caused by an indentation.

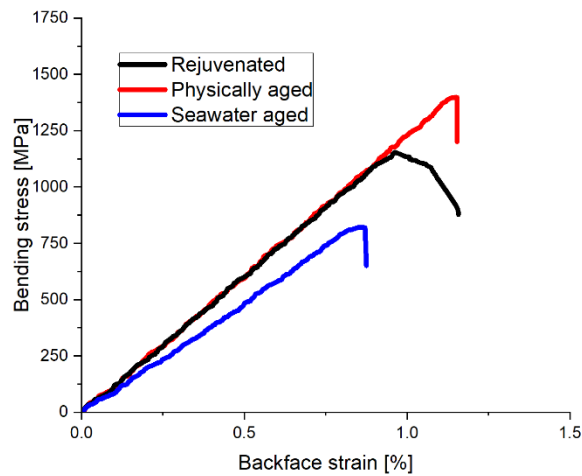


Figure 3.18 – Effects of aging on the bending stress vs. backface strain of coupons tested

Results are shown in Table 3.7. The flexural modulus after seawater aging is reduced by 16%, while the strength is reduced by 36%.

Table 3.7 – Three-point bending modulus and strength as a function of aging

	Rejuvenated	Physically aged	Seawater aged
E_{1f} [GPa]	121.2 ± 3.1	120.3 ± 3.2	101.4 ± 4.8
Strength [MPa]	1212 ± 67	1379 ± 36	776 ± 28

3.2.2.2. Four-point bending tests

To highlight the effects of seawater aging on the three-point bending results, a comparison has been performed from four-point bending tests. This test is known to distribute the load over a larger region, avoiding local damage on the elastic part and a premature failure. $[0]_4$ coupons have been tested.

Strain gages have been bonded on both sides of the coupon. Bending stress as a function of strain measured on the external surfaces is shown Figure 3.19.

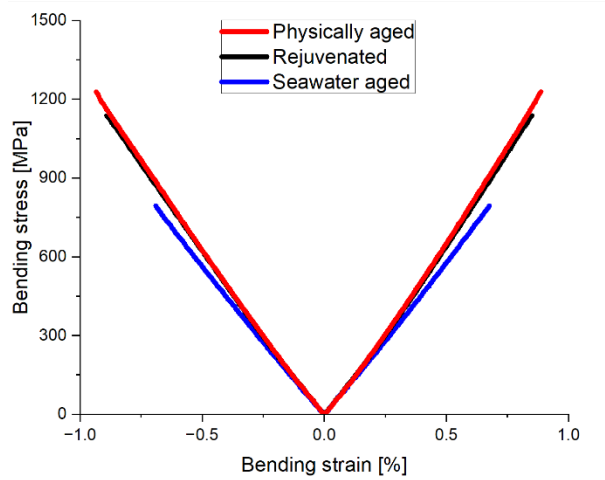


Figure 3.19 – Effects of aging on the Stress vs. strain curves of coupons experiencing a four-point bending test

Results are reported Table 3.8. The physical aging seems to improve the strength but the bending modulus is not affected by this aging, while the physical aging decreases by 15% the flexural modulus and by 30% the bending stress at failure.

Table 3.8 - Four-point bending modulus and strength as a function of aging

	Rejuvenated	Physically aged	Seawater aged
E_{1f} [GPa]	142.1 ± 4.4	142.2 ± 1.8	121.2 ± 2.3
Strength [MPa]	1136 ± 37	1267 ± 33	796 ± 7

Even if the failure seems to be more affected by the stress concentration in the case of the three-point bending test, the flexural modulus drop observed after seawater aging is at the same level for both tests.

3.2.2.3. Out-of-plane shear tests

Figure 3.20 shows shear stress versus shear strain plots for a rejuvenated coupon cut in the 13 and 23 planes. For the shear test in the 13 direction, irregularities are noted on Figure 3.20 and correspond to matrix cracking in the V-notched part of the coupon. The failure modes are quite different since the shear plane is normal to the fiber direction in one case and parallel to the fiber direction in the other case where it leads to a brittle failure. This is clearly illustrated by digital image correlation (Figure 3.21).

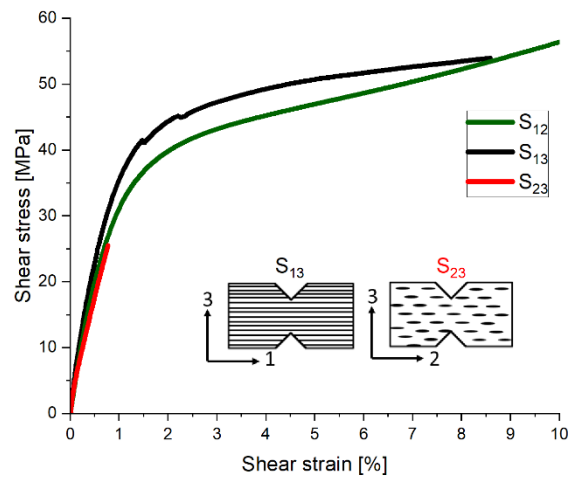


Figure 3.20 – Differences in Shear stress [MPa] vs. Shear strain [%] plots for rejuvenated coupons cut in the 12 and 13 planes

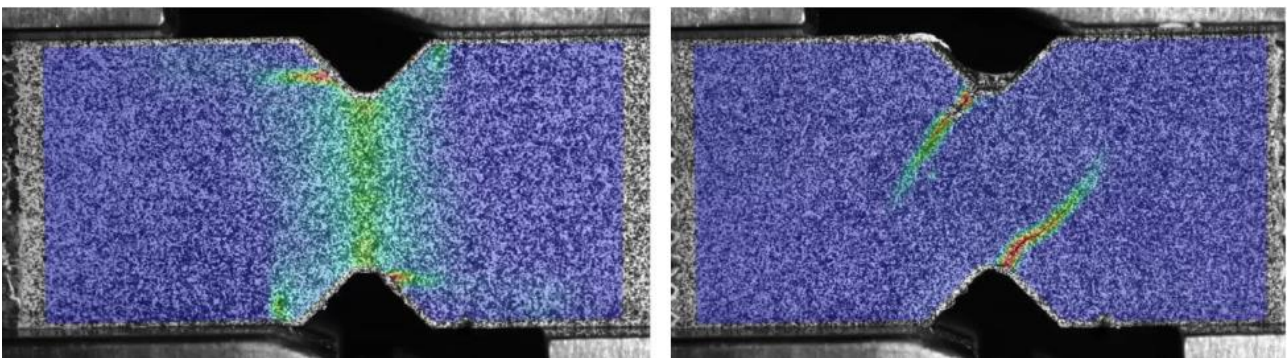


Figure 3.21 – Difference of failure mode observed by DIC in red for a shear test on the 1–3 plane (left) and on the 2–3 plane (right)

Changes to out-of-plane shear modulus and shear stress at failure after aging are shown in Table 3.9. With respect to the reference state, the seawater aging reduces both modulus values, while only G_{13} is affected by the physical aging. Because of the nature of the Iosipescu coupons, values of τ_{13} were determined at the first load drop. For seawater aged coupons all values are significantly lower than those for unaged specimens.

Table 3.9 – Out-of-plane shear properties of the C/Epoxy studied before and after aging

	Rejuvenated	Physically aged	Seawater aged
G_{13} [GPa]	4.60 ± 0.17	5.17 ± 0.27	3.21 ± 0.17
G_{23} [GPa]	3.07 ± 0.12	3.02 ± 0.23	2.48 ± 0.28
τ_{13} [MPa]	43.4 ± 2.9	41.7 ± 3.0	25.8 ± 1.6
τ_{23} [MPa]	24.6 ± 2.2	21.2 ± 2.7	18.6 ± 1.3

3.2.2.4. Out-of-plane tensile tests

Results for Poisson's ratios are shown in Table 3.10. Compared to the rejuvenated state, the physical aging increases all Poisson's ratios. A value of $\nu_{23} > 0.5$ was measured after seawater aging. While this value is not

possible for isotropic materials, higher values have been measured experimentally in the past [238][239] on orthotropic materials.

Table 3.10 – Out-of-plane Poisson ratio of the C/Epoxy studied before and after aging

	Rejuvenated	Physically aged	Seawater aged
ν_{13}	$0.29 \pm 0,01$	0.32 ± 0.01	0.39 ± 0.01
ν_{23}	0.48 ± 0.01	0.48 ± 0.01	0.52 ± 0.01

3.3. Interface properties

Delamination in composite laminates is a two-step process. The initiation of a crack is due to high interfacial stress, while the propagation happens when the fracture toughness of the material is exceeded.

3.3.1. Damage initiation

3.3.1.1. Pure Epoxy coupon

Tensile and shear tests have been performed on pure Epoxy coupons in order to characterize the influence of aging on ultimate properties. A comparison of the stress as a function of the strain is shown Figure 3.22 for pure epoxy coupons during a tensile test. Results are shown on Table 3.11. These clearly indicate that the resin is sensitive to physical aging, which results in increases in the tensile and shear stresses at failure of 41 and 23% respectively compared to the rejuvenated values. Seawater saturation results in a drop of 24 and 26%.

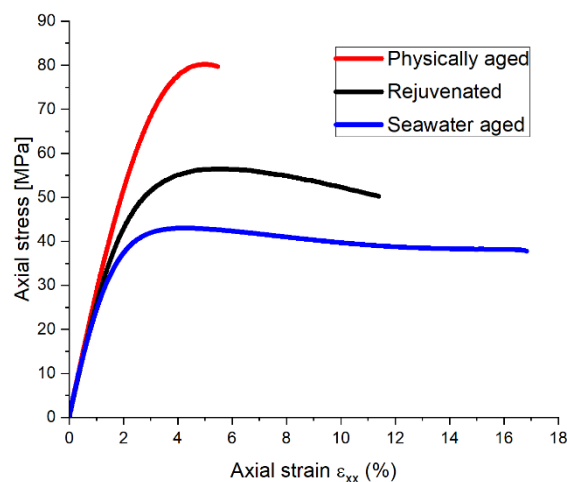


Figure 3.22 – Stress vs. strain plots of pure Epoxy coupons in tension

Table 3.11 – Epoxy ultimate properties versus aging

	Rejuvenated	Physically aged	Seawater aged
Tensile stress at failure [MPa]	56,4 ± 0,6	79,5 ± 1,9	42,9 ± 0,3
Shear stress at failure [MPa]	45,5 ± 0,4	56 ± 2,7	33,7 ± 0,3

3.3.1.2. Fracture toughness from film insert

Another aspect to be considered in the design of marine composite structures is the initiation and propagation of a crack within a composite laminate. In order to characterize the resistance to these events, $[0]_6$ laminates have been manufactured with a Teflon insert between the two middle layers. These coupons are opened in Mode I, which enables a value of the Mode I fracture toughness from the insert to be determined. This test is performed until a crack propagation is visually observed. The force versus displacement curves is shown Figure 3.23 for the three aging. An inflexion point is observed for the seawater saturated coupon but not for the two other aging conditions.

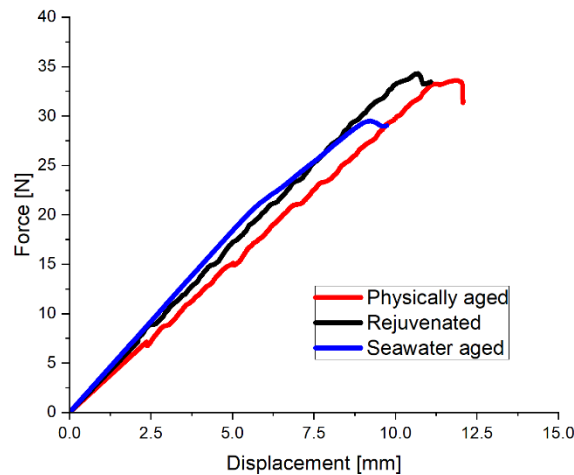


Figure 3.23 – Force vs. displacement of DCB coupons opened in Mode I

Two initiation criteria are proposed in the ASTM D5528 standard. A first fracture toughness (non-linear) is determined from the deviation from linearity of the Force vs. Displacement slope. A second is determined either from a loss of 5% of the F-u slope or from the maximal force F_{max} . The comparison between these values is presented in Figure 3.24. The fracture toughness from the non-linear deviation is lower than for the other criterion. This is due to the nonlinear behavior of the resin around the insert film at a low load, which induces a loss of the stiffness of the coupon.

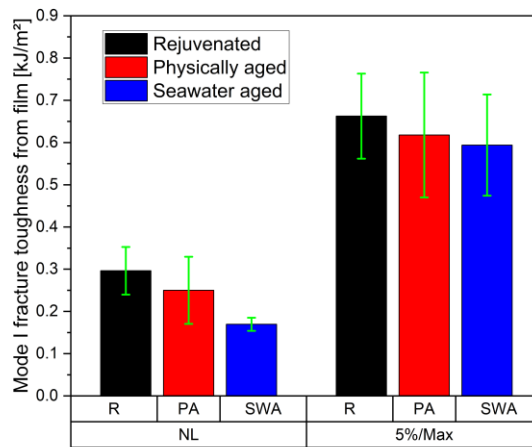


Figure 3.24 – Comparison of the Mode-I initiation fracture toughness from insert film for the two criteria

3.3.1.3. Fracture toughness from precrack

The fracture toughness from a natural precrack is more interesting, because the nonlinear behavior of the resin around the film is no longer considered. This time, precracked coupons are tested in pure Mode I, pure Mode II or Mixed-Mode, which considers both Mode I and Mode II.

3.3.1.3.1. Mode I fracture toughness from precrack

Figure 3.25 shows the change of the fracture toughness with the aging for the two criteria. In comparison with the tests from film, the nonlinear fracture toughness is higher, because the process zone does not interact with the film. Given the error bars, the rejuvenated and the physically aged states show equivalent results. The fracture toughness of seawater aged composite is a little lower.

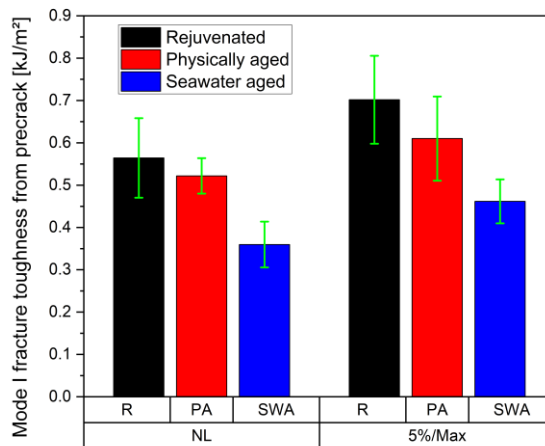


Figure 3.25 – Mode I fracture toughness from precrack for the two criteria

3.3.1.3.2. Mixed-Mode fracture toughness from precrack

Mixed-mode bending tests have been performed for different contributions of Mode II: 23%, 43%, 60% and 80%. The same initiation criteria as for mode I above are compared (Figure 3.26). For some tests, the error bars are large compared to the average fracture toughness. This may be related to scatter in the coupon thickness caused by the manufacturing process. For both rejuvenated and physically aged states, whichever

the criterion, the fracture toughness increases when the mode II contribution II increases. For the seawater aged state, the fracture toughness does not increase as much as the other states. One hypothesis is the seawater aging degrades the interface, leading to a premature crack propagation in the coupon.

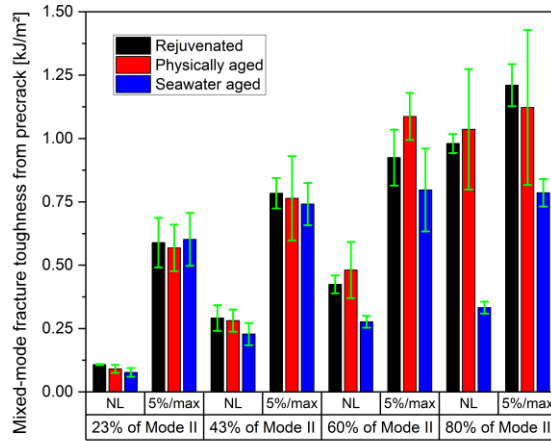


Figure 3.26 – Mixed-Mode fracture toughness from precrack for the two criteria

3.3.1.3.3. Mode II fracture toughness from precrack

Figure 3.27 shows the change of fracture toughness with aging for the two criteria in pure Mode II. Fracture toughness values obtained with this test are higher than those obtained in pure Mode I. It is difficult to conclude on the influence of aging because the scatter is high compared to the averaged values.

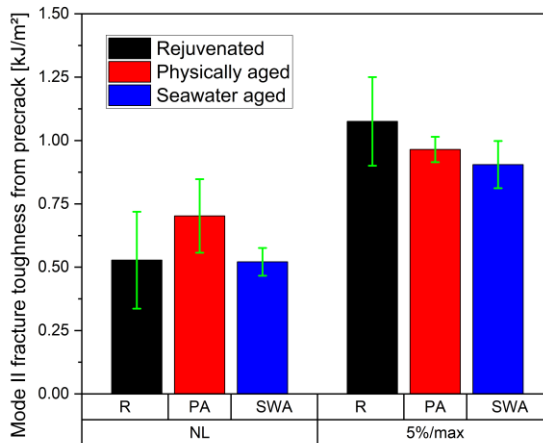


Figure 3.27 – Mode II fracture toughness from precrack for the two criteria

3.3.1.3.4. Conclusion on results obtained from precrack

Fracture toughness values calculated based on two initiation criteria have been compared for the three aging conditions considered here. From the nonlinearity, the fracture toughness is always lower than for the 5%/Max. This is because the material exhibits a nonlinear behavior at a much lower load than the load where the 5%/Max criterion is calculated. The effects of seawater aging seem to be higher when the contribution of Mode II is increased. When comparing with the results on pure resin, both tensile and shear strength are affected by the aging. The physical aging increases the strength of the pure Epoxy coupon, while the seawater

aging reduces it. The seawater aging induces a decrease of both the strength measured on pure Epoxy coupons and fracture toughness from precracks on C/Epoxy coupons. The physical aging induces an increase of the strength of pure Epoxy coupon but no explicit effect on the composite fracture toughness. This may be due to the interface between the fiber and the matrix. When the interface between the fiber and the matrix is strong, the crack propagates only in the matrix. When the interface is weak, the crack propagates both in the matrix and at the interface. Effects of aging on the interface need to be studied to clarify their role on the crack propagation.

3.3.2. Fracture propagation

The mechanical tests performed were chosen to promote stable propagation. Once the crack has begun to propagate, it is possible to calculate an averaged value of the fracture toughness using several points on the Force–Displacement plot together with the corresponding crack tip localization.

3.3.2.1. Mode I fracture toughness

Figure 3.28 shows examples of the Force vs. Displacement curves for DCB tests for the three aging conditions. The seawater saturated coupon has a lower force peak than the two other aging conditions.

In all cases, the crack propagation seems stable. The averaged Mode I fracture toughness G_{1c} is determined from 30 data points of the R–curve, as shown Figure 3.29. Drops are observed because of the complexity of the surface that delaminates, with wavy yarns and a stitching that could locally reduce the critical fracture toughness.

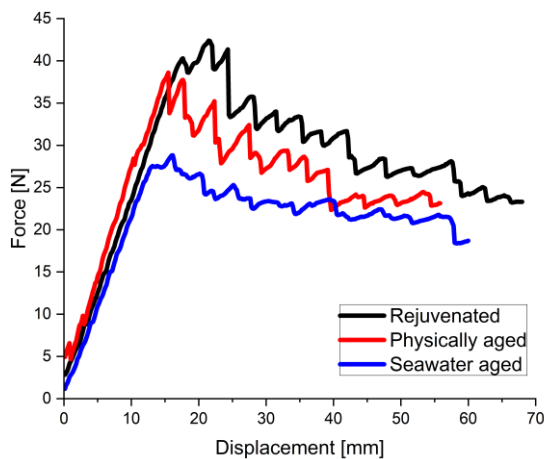


Figure 3.28 – Force vs. Displacement for DCB test from precrack

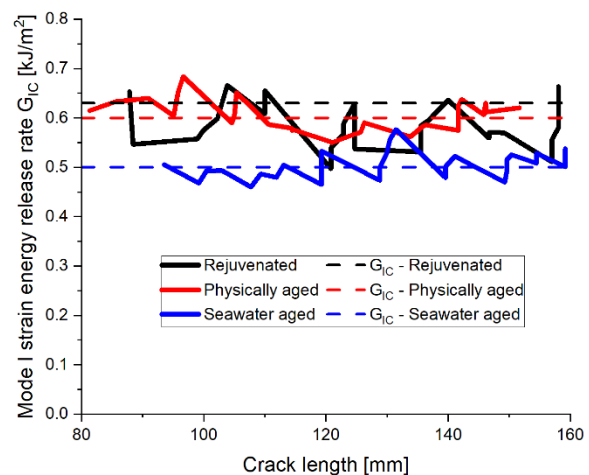


Figure 3.29 – R-curves of DCB tests for the three aging

Averaged fracture toughness values during propagation are shown in Table 3.12. No difference is seen between the unaged and the physically aged state. Even though the scatter is significant, the Mode I fracture toughness is lower after seawater aging. SEM observations have been performed to examine the fiber/matrix interface region for the rejuvenated and seawater aged states (Figure 3.30). After seawater aging, no resin is found on the fibers while after rejuvenation, resin is observed to remain on the fibers. The main conclusion

is that the seawater aging degrades both the matrix strength and the interface, and the DCB test peels off the matrix from the fibers. The propagation path is then more within this interface region than in the resin.

Table 3.12 – Averaged Mode I fracture toughness for propagation

	Rejuvenated	Physically aged	Seawater aged
Mode I fracture toughness G_{IC} during propagation [kJ/m ²]	0.63 ± 0.06	0.60 ± 0.06	0.50 ± 0.06

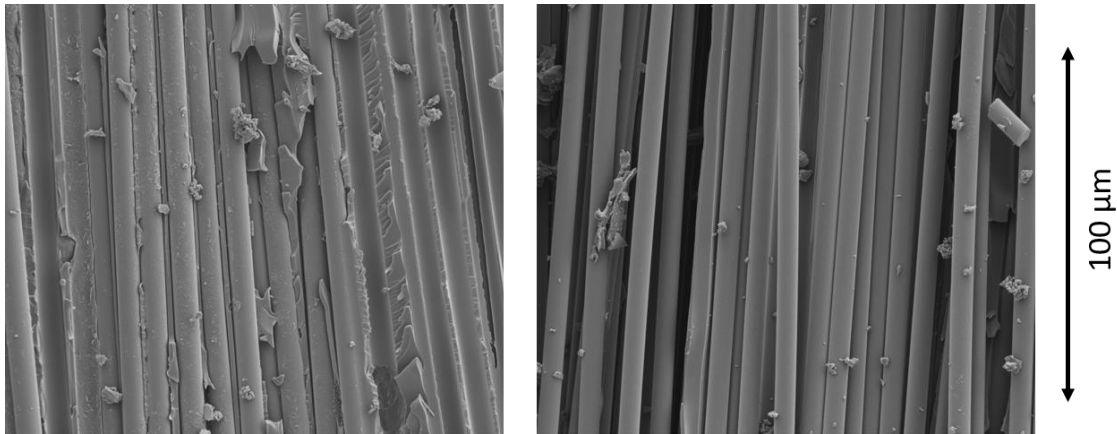


Figure 3.30 – Comparison of fiber interface after Mode I test : (L) Rejuvenated (R) Seawater aged

3.3.2.2. Mixed-Mode fracture toughness

Propagation tests have been performed for mode ratios of 23%, 43%, 60% and 80% of Mode II. A comparison of Force vs. Displacement curves is presented in Figure 3.31. When increasing the contribution of Mode II, the coupon is stiffer and the propagation range is smaller.

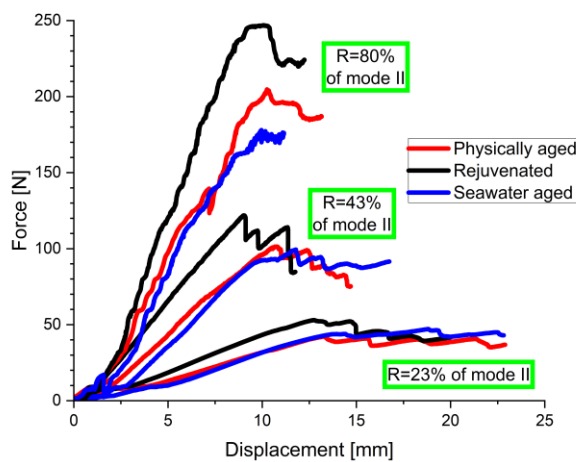


Figure 3.31 – Force vs. Displacement for MMB tests from precrack with three mode II ratios

Results from these tests are presented in Table 3.13. When the contribution of Mode II is lower than 60%, the fracture toughness does not change with aging. However, for an 80% Mode II contribution, the seawater aging reduces the fracture toughness significantly.

Table 3.13 – Mixed mode propagation fracture toughness G_c as a function of aging and Mode II contribution

Contribution of Mode II	Rejuvenated	Physically aged	Seawater aged
23%	0.63 ± 0.04	0.60 ± 0.11	0.72 ± 0.02
43%	0.82 ± 0.14	0.87 ± 0.19	0.83 ± 0.08
60%	1.04 ± 0.17	0.94 ± 0.04	0.93 ± 0.11
80%	1.29 ± 0.08	1.22 ± 0.06	0.94 ± 0.03

3.3.2.3. Mode II fracture toughness

Figure 3.32 shows the Force vs. Displacement curves of the ELS tests. While the rejuvenated and physically aged curves have a very similar shape, the response after seawater aging is lower. The main cause is a decrease of the Mode II fracture toughness G_{IIc} .

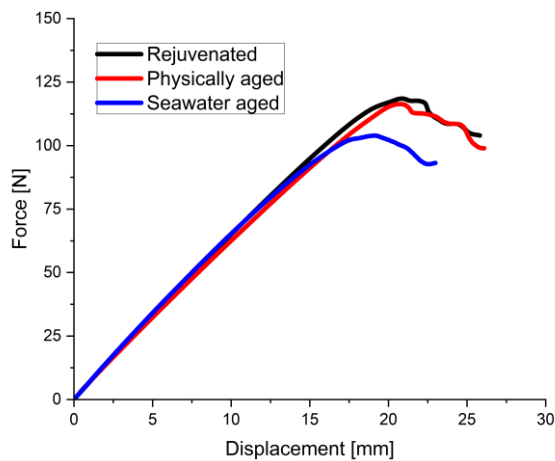


Figure 3.32 – Force vs. Displacement for ELS tests from precrack

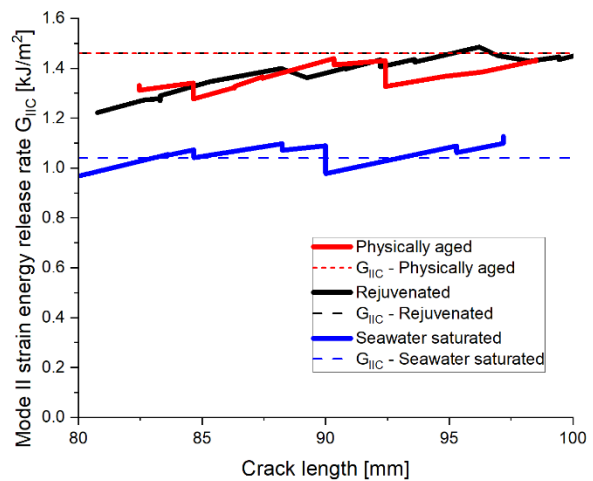


Figure 3.33 – R-curves of ELS tests for all aging

Averaged values from pure Mode II fracture toughness tests are presented in Table 3.14. Five tests were performed for each condition. Even if it is difficult to track the mode II crack tip accurately, the scatter is mainly due to differences between coupons. The panels manufactured by infusion do not have the same thickness and the resin volume ratio can also change. SEM fractography images are shown in Figure 3.34. At the same magnification, we can observe large hackles for the seawater aged coupons and smaller hackles for the physically aged coupons. These observations are corroborated by the tensile tests on pure epoxy

coupons, for which a brittle fracture was noted after physical aging and a ductile fracture after seawater aging.

Table 3.14 – Averaged Mode II fracture toughness for propagation

	Rejuvenated	Physically aged	Seawater aged
Mode II fracture toughness G_{IIc} from propagation [kJ/m ²]	1.46 ± 0.10	1.46 ± 0.24	1.04 ± 0.14

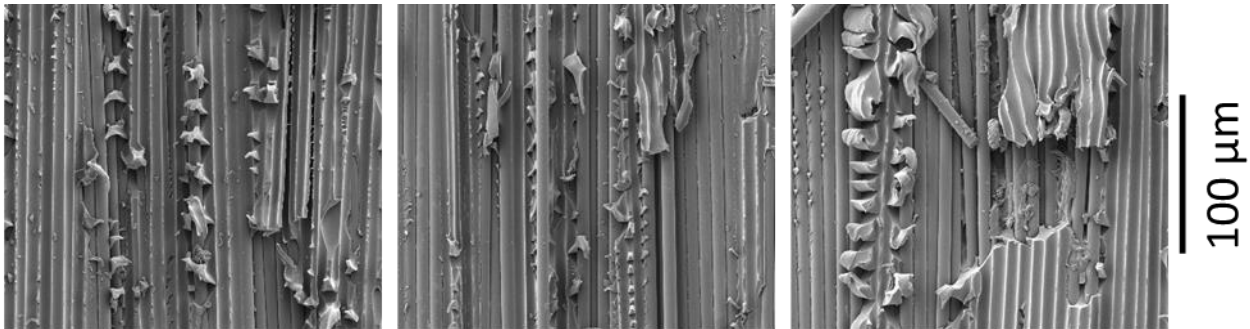


Figure 3.34 – SEM fractographies of Rejuvenated, Physically Aged and Seawater aged coupon tested in pure Mode II

3.3.2.4. Modeling the mixed-mode fracture behavior

The aim of this part of the study was to characterize the interlaminar fracture behavior of the C/Epoxy for three aging conditions. In order to represent the influence of mode ratio on the fracture toughness, the B-K criterion proposed by Benzeggagh and Kenane was applied [221]. Their equation is shown below, Eq. 3.6. An optimization of the η parameter has been performed with the least squares method to improve the fit of the model. The values of G_{Ic} , G_{IIc} , and the fitting parameter η are presented in Table 3.15.

$$G_T = G_{Ic} + (G_{IIc} - G_{Ic}) \left(\frac{G_{II}}{G} \right)^\eta \quad \text{Eq. 3.6}$$

Table 3.15 – Mixed-mode fracture toughness values and fit parameter for the BK criterion

	Rejuvenated	Physically aged	Seawater aged
G_{Ic} [kJ/m ²]	0.63 ± 0.06	0.60 ± 0.06	0.50 ± 0.06
G_{IIc} [kJ/m ²]	1.46 ± 0.09	1.46 ± 0.24	1.04 ± 0.14
η	1.59	1.67	0.58

The comparison between the experimental data and the B–K criterion is shown in Figure 3.35. As reported previously, when the contribution of Mode II increases, the loss of fracture toughness due to seawater aging becomes significant. The data appear consistent, despite the different methods used and differences between coupons.

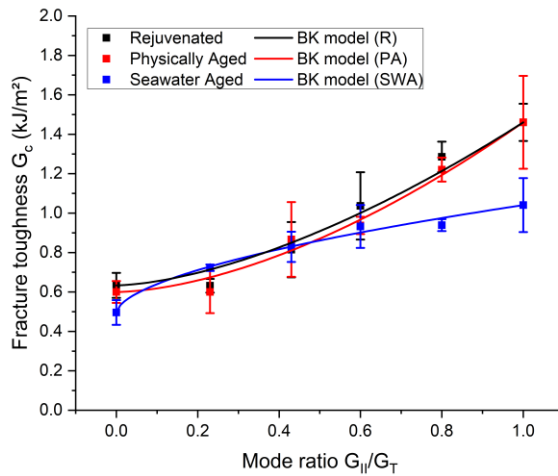


Figure 3.35 – Change of the propagation fracture toughness with the mode ratio: comparison experiments/B–K criterion

3.3.3. Discussion

The B–K fracture criterion is often applied; it is available as an option in Abaqus™, and provides a good fit to a number of sets of mixed mode data. Nevertheless, it should be remembered that it is just one of many mixed mode fracture criteria which have been proposed for composite delamination in the past [240].

While this criterion appears to fit the MMB data quite well here, it should be noted that the final points, corresponding to the pure mode Mode II fracture toughness, are obtained from a different specimen geometry (ELS) and calculated with a flexural modulus E_{1f} determined from a different method (compliance calibration). The range of values obtained with this method varies from 85 GPa to 120 GPa with significant scatter. If the same 3–point flexural modulus is used for both MMB and ELS test data then the ELS values do not fall so nicely on the same plot. There has been considerable discussion on the validity of pure mode II tests, in particular due to the important role of friction between the cracked surfaces [241], so the choice was made here to use the B–K fracture criterion identified on the mode I and mixed mode MMB data.

3.4. Normalization of the properties change

For each property determined experimentally, a normalization with respect to the rejuvenated state (reference) is applied, as summarized in Table 3.16. This provides a global view of the property changes due to aging. Properties that are not used for this percentage calculation are marked with an asterisk (*). This separation was performed because it is not expected that the fiber behavior will be affected by the aging until damage is observed.

The average change in all the mechanical properties after physical aging is a 5% increase, whereas an average loss of 30% was found after seawater aging.

Table 3.16 – Experimental values normalized with the rejuvenated and dried state (reference)

	Property considered	Rejuvenated [R]	Physically aged [PA]	Change normalized (PA/R)	Seawater aged [SWA]	Change normalized (SWA/R)
Design properties	E ₁₁ [GPa] *	127.50	128.00	1.00	128.40	1.01
	E ₂₂ [GPa]	7.94	9.23	1.16	4.39	0.55
	E ₃₃ [GPa]					
	ν ₁₂ [-] *	0.274	0.320	1.17	0.341	1.24
	ν ₁₃ [-] *	0.289	0.323	1.12	0.385	1.33
	ν ₂₃ [-] *	0.477	0.481	1.01	0.515	1.08
	G ₁₂ [GPa]	3.72	4.07	1.09	2.70	0.73
	G ₁₃ [GPa]	4.60	5.17	1.12	3.21	0.70
	G ₂₃ [GPa]	3.07	3.02	0.98	2.48	0.81
Ply properties	X _t [MPa]	2272	2140	0.94	1760	0.77
	X _c [MPa]	934	950	1.02	607	0.65
	Y _t [MPa]	38.3	36.4	0.95	16.6	0.43
	Y _c [MPa]	123.5	134.2	1.09	94.1	0.76
	S ₁₂ [MPa]	73.3	68.7	0.94	54.0	0.74
	S ₁₃ [Mpa]	43.4	41.7	0.96	25.8	0.59
	S ₂₃ [MPa]	24.6	21.2	0.86	18.6	0.76
Interface properties	Matrix tension [MPa]	56.4	79.5	1.41	42.9	0.76
	Matrix shear [MPa]	45.5	56.0	1.23	33.7	0.74
	G _{lc} [kJ/m ²]	0.63	0.60	0.95	0.50	0.79
	G _{llc} [kJ/m ²]	1.46	1.46	1.00	1.04	0.71
	n [-] *	1.590	1.670	1.05	0.580	0.36
Average				+ 5%		- 30%

3.5. Application of aged properties to a structural test

To examine the use of this set of data in a practical application, three sets of quasi-static 4-point flexural tests were performed, on reference and aged quasi-isotropic specimens.

3.5.1. Experimental tests

The ASTM D6272 standard was followed. The test geometry used is an intermediate loading condition, between a short beam test dominated by interlaminar shear ($L/t=5$) and a long beam test ($L/t=24$) closer to pure flexure. A span to thickness ratio of $L/t=12$ was chosen. The configuration of one third was chosen between the load span and the support span. The loading-rate was 1 mm/min and 3D digital image correlation was performed to measure the beam displacement throughout the test. In each case samples were tested in the rejuvenated, physically aged and seawater saturated conditions. The tests were carried out until coupon failure. Experimental plots are shown Figure 3.36.

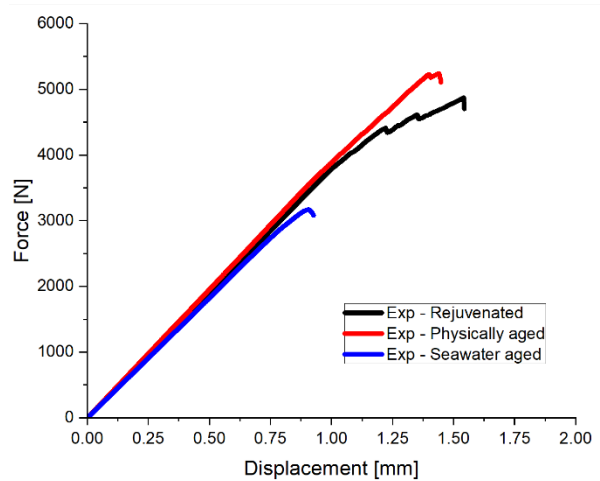


Figure 3.36 – Comparison of the force vs. displacement plots for quasi-isotropic coupons during a four-point bending test

The failure occurs at the same stress for both rejuvenated and physically aged states, but it is reduced by 36% after seawater aging (Table 3.17). The physical aging reduces the non-linearity before the failure in comparison with the rejuvenated state, the failure is more brittle after physical aging.

The 3D digital image correlation shows the difference in damage a few seconds before the coupon failure (Figure 3.37). In all cases, the failure was located between the mobile and the static support points. In the case of rejuvenated and physically aged coupons, the damage seems to be local and then propagates abruptly leading to a global failure. For seawater aged coupons, damage is more distributed. In addition, on the upper face of the coupons where compressive strains occur, fibre bundles were observed to break.

Table 3.17 – Influence of the aging on the flexural stress at failure

	Rejuvenated	Physically aged	Seawater aged
Flexural stress at failure [MPa]	620 ± 22	631 ± 27	400 ± 8

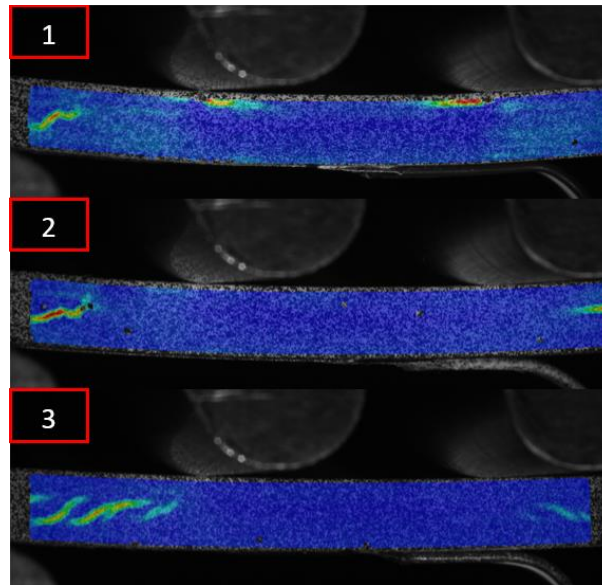


Figure 3.37 – Major strain computed by 3D DIC of four–point bending coupon a few seconds before the failure. From top to bottom: (1) Rejuvenated, (2) Physically aged and (3) Seawater aged

3.5.2. Numerical simulation

A numerical simulation of this experimental test was performed with the commercial finite element solver Abaqus™ Explicit. Plies were modeled individually using continuum shell elements (SC8R) and were stacked using cohesive surfaces. The cohesive surface elasticity coefficients K_{nn} , K_{ss} and K_{tt} are based on the Epoxy modulus and on the Von Mises theory. The opening modulus K_{nn} is supposed to be ten times the value of the resin modulus. The Von Mises theory tells us that for homogeneous materials, the ratio between the shear yield stress and the tensile yield stress is equal to $1/\sqrt{3}$. This ratio was used to determine the values of K_{ss} and K_{tt} from the value of K_{nn} . A linear elastic traction–separation behavior has then been defined with $K_{nn}=24600 \text{ N/mm}^3$, $K_{ss}=K_{tt}=14200 \text{ N/mm}^3$. Properties used are summarized Table 3.18.

Table 3.18 – Summary of properties used to predict the mechanical behavior of the coupons

Property	Symbol	Rejuvenated [R]	Physically aged [PA]	Seawater aged [SWA]
Density	ρ [kg/m ³]	1.55		
Friction CFRP/CFRP	$\xi_{C/C}$ [-]	0.05		
Friction metal/CFRP	$\xi_{M/C}$ [-]	0.3		
Young's moduli	$E_1=E_{1f}, E_2$ [GPa]	121.2, 7.94	120.3, 9.23	101.4, 4.39
Poisson's ratio	ν_{12} [-]	0.274	0.320	0.341
Shear moduli	G_{12}, G_{13}, G_{23} [GPa]	3.72, 4.60, 3.07	4.07, 5.17, 3.02	2.70, 3.21, 2.48
Ply strength	X^T, X^C, Y^T	2272, 934, 38.3,	2140, 950, 36.4,	1760, 607, 16.6,
	$Y^C, S^L=S^T$ [MPa]	123.5, 73.3	134.2, 68.7	94.1, 54.0
–	α	0		
Cohesive surface elasticity	K_{nn}, K_{ss}, K_{tt} [N/mm ³]	24600, 14200, 14200		
Interface strength	τ_n, τ_s, τ_t [MPa]	56.4, 45.5, 45.5	79.5, 56.0, 56.0	42.9, 33.7, 33.7
Fracture toughness [kJ/m ²]	G_{IC}, G_{IIC} [kJ/m ²]	0.63, 1.46	0.60, 1.46	0.50, 1.04
BK model parameter [-]	η	1.590	1.670	0.580
Energy dissipated for ply failure	G_{mt}, G_{mc} [kJ/m ²]	0.63, 1.46	0.60, 1.46	0.50, 1.04

The load is applied by discrete rigid rollers with a radius of 5mm, meshed with R3D4 elements. Enhanced hourglass control has been used. The friction coefficient between the material and the pins was defined at 0.3. The material constitutive model [220] is based on Hashin's failure criteria for unidirectional fiber composites [44]. This model is included in the Abaqus™ library. The experimental failure in the upper ply was observed to be at the fiber yarn scale. A mesh sensitivity study was performed with length sizes of 0.5, 1.0, 1.5 and 3.0 mm, and the stiffness did not change when the mesh was smaller than 1.5mm (Figure 3.38).

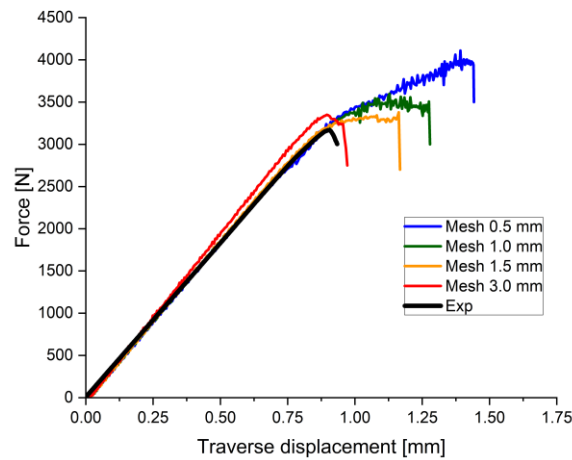


Figure 3.38 – Sensitivity of the mesh on the Force vs. Time plots of a seawater saturated coupon ($G_{Ic} = 40 \text{ kJ/m}^2$)

The mesh dimensions were therefore chosen to have a width equal to 1.5 mm, which represents two elements in the yarn width. A relatively high loading rate (0.2 m/s) was needed for the calculation because of the explicit method. A smooth step was used to apply the load gradually. The balance of energy has been checked [220] to verify inertia effects, and this loading rate did not induce significant dynamic effects on the simulation results. An image of the model is shown below (Figure 3.39).

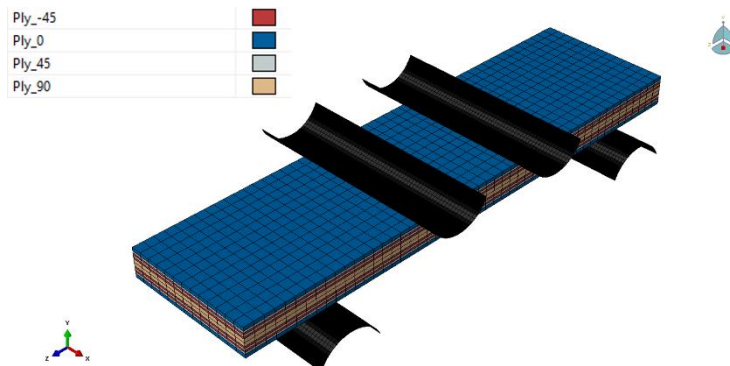


Figure 3.39 – Numerical model of the four-point bending test

3.5.3. Intralaminar and translaminar fracture properties

In the Abaqus™ model, propagation values are needed to consider the energy released when translaminar and intralaminar cracks propagate. It was not possible to get experimental data due to premature failure in compression of CC and CT coupons. The mode I and II translaminar fracture toughness prior to aging have therefore been taken from a previous study [237]. A reference value of 60 kJ/m^2 has been used for the rejuvenated material, and the comparison with the experimental results indicated that this assumption was satisfactory for this state. To correctly capture the force at failure for the seawater aged saturated material, a reduction to 40 kJ/m^2 was necessary, and an increase of 80 kJ/m^2 has been found to be suitable for the physically aged state. A comparison between a seawater saturated coupon and simulations with different values of translaminar fracture toughness is presented in Figure 3.40.

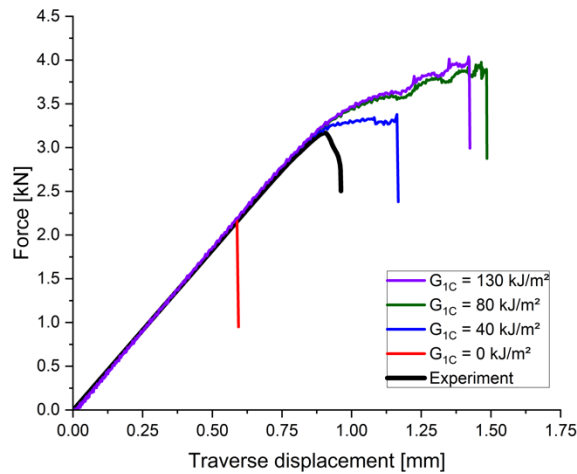


Figure 3.40 – Comparison of Force–Displacement curves for seawater saturated coupon with different values of G_{1C} (mesh = 1.5mm)

Very few studies have considered the intralaminar fracture toughness [242] mainly due to the lack of standard test methods. These properties are generally assumed to have the same values as interlaminar fracture toughness [243], determined using DCB, ELS and MMB test methods. This assumption is commonly made since interlaminar and intralaminar fracture involve matrix plasticity and degradation, and fiber–matrix interfacial debonding. For prepreg materials, this assumption makes sense, because of the material homogeneity at mesoscale. However, in the present study, weft stitching is likely to improve the transverse tensile fracture toughness. For the transverse compressive fracture toughness, no studies have been found. In the absence of alternative values, the mode I and II intralaminar fracture toughness are here supposed to be equal to the interlaminar fracture toughness, Table 3.19.

Table 3.19 – Properties used for translaminar damage propagation

	Rejuvenated	Physically aged	Seawater aged
G_{IC}^{Ten} [kJ/m ²]	60	80	40
G_{IC}^{Comp} [kJ/m ²]	60	80	40
G_{IIC}^{Ten} [kJ/m ²]	0.63	0.60	0.50
G_{IIC}^{Comp} [kJ/m ²]	1.46	1.46	1.04

3.5.4. Comparison experiment/simulation

Figure 3.41 shows the predicted and the experimental response for the four–point bending test. As expected, there is a significant influence of seawater saturation on the flexural response. The flexural model captures the coupon failure level and the stiffness quite well. For the rejuvenated material, a nonlinear behavior is experimentally observed but not well predicted. This may be due to the type of element chosen, which does not consider out-of-plane damage. Stiffness and stress at failure are compared respectively in Table 3.20 and

Table 3.21. The stiffness and the failure level are overpredicted by the model, but the difference is acceptable, and may be due to variations in the ply thickness. This shows that it is essential to include seawater aging data in design of immersed structures.

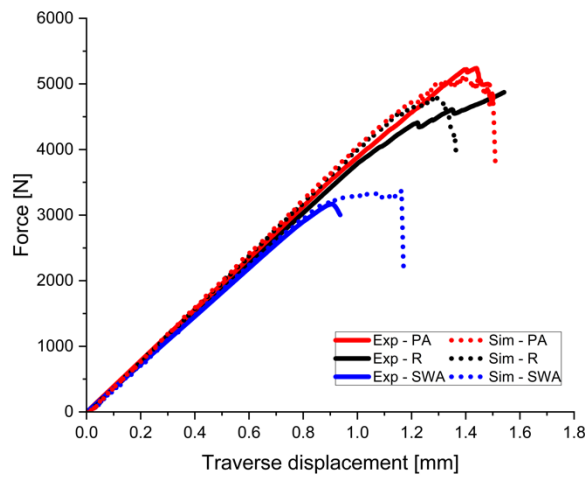


Figure 3.41 – Comparison between experiment and simulation of the 4 points bending test

Table 3.20 – Comparison between experimental and numerical bending stiffness

	Rejuvenated	Physically aged	Seawater aged
Experimental [N/mm]	3808 ± 69	3886 ± 159	3645 ± 16
Numerical [N/mm]	4074	4101	3806
Difference [%]	7	5	4

Table 3.21 – Comparison between experimental and numerical bending stress at failure

	Rejuvenated	Physically aged	Seawater aged
Experimental [Mpa]	619.8 ± 21.5	631.1 ± 26.6	400.1 ± 8.2
Numerical [Mpa]	652.8	696.2	456.0
Difference [%]	5	9	12

3.6. Conclusion

In this study, in-plane and out-of-plane properties of a C/Epoxy composite manufactured by infusion have been characterized for three aging states: dried and rejuvenated (without physical aging), physically aged, and seawater aged to saturation. It was demonstrated that physical aging had, in most cases, a beneficial effect on the mechanical properties used in design, while seawater aging results in a drop in stiffness and

strength. The latter is significant, and must be considered in design of marine structures. In terms of interlaminar crack propagation, seawater aging effects are noted for high in-plane shear (mode II) loadings. The reference, physically aged and seawater aged properties were introduced in simple numerical simulations of a flexural test, and these provided a good prediction of the unaged and aged behavior. The study also highlighted a lack of reliable input data for translaminar and intralaminar fracture, and development of test methods for these properties would improve confidence in numerical modelling of composite structures. However, the material model used can be criticized because it does not take into account the out-of-plane damage which is observed experimentally. The prediction of the coupon behavior could be improved with the use of volumic elements and with a material law that considers both in-plane and out-of-plane damage.

Chapter 4

—

Influence of aging on C/Epoxy impact behavior

Chapter 4 – Influence of aging on C/Epoxy impact behavior

4.1. INTRODUCTION.....	132
4.2. INFLUENCE OF THE LOADING-RATE ON THE MECHANICAL PROPERTIES OF THE C/EPOXY	132
4.2.1. MECHANICAL TESTS FROM 1 MM/MIN TO 1000 MM/MIN	133
4.2.2. STRAIN-RATE COMPARISON	136
4.3. DEVELOPMENT OF A NEW DROP WEIGHT IMPACT TOWE	137
4.3.1. USE AND QUALIFICATION OF AN OLD DROP WEIGHT IMPACT TOWER.....	137
4.3.2. DEVELOPMENT OF A NEW DROP WEIGHT IMPACT TOWER.....	138
4.3.3. CONCLUSIONS.....	140
4.4. EXPERIMENTAL IMPACT BEHAVIOR AT UNAGED STATE	140
4.4.1. IMPACT CURVES	140
4.4.2. C-SCANS.....	141
4.4.3. BALANCE OF ENERGY	142
4.4.4. MICROSCOPE OBSERVATIONS.....	144
4.4.5. TOMOGRAPHY ON UNAGED COUPONS.....	145
4.4.6. CONCLUSIONS ON THE LVI BEHAVIOR OF REJUVENATED COUPONS.....	146
4.5. NUMERICAL SIMULATION FOR UNAGED STATE.....	146
4.5.1. MODEL DESCRIPTION.....	147
4.5.2. MESH STRATEGY.....	147
4.5.3. INPUT DATA.....	150
4.5.4. COMPARISON BETWEEN EXPERIMENT AND SIMULATION FOR THE UNAGED STATE	151
4.5.5. CONCLUSION ON UNAGED IMPACT	155
4.6. EFFECT OF AGING ON THE IMPACT BEHAVIOR	156
4.6.1. EFFECTS OF AGING ON IMPACT CURVES	156
4.6.2. INFLUENCE OF AGING ON THE DELAMINATION.....	157
4.6.3. EFFECTS OF AGING ON THE BALANCE OF ENERGY	159
4.6.4. MICROSCOPIC OBSERVATIONS.....	160
4.6.5. TOMOGRAPHY ON AGED COUPONS.....	161
4.6.6. SIMULATION OF THE AGING EFFECTS ON THE IMPACT BEHAVIOR	162
4.6.7. CONCLUSION ON AGED IMPACTS.....	167
4.7. CONCLUSION	168

4.1. Introduction

This chapter is devoted to the study of the out-of-plane impact behavior before and after aging. The aim is to describe and explain the effects of aging on the out-of-plane impact behavior. To do this, both experimental and numerical aspects were considered.

The first section of this chapter is focused on the impact behavior when the C/Epoxy is in the unaged state. Results from experimental out-of-plane impact tests performed at different energy levels will be presented. Then, post-mortem analysis including C-scans, microscopy observations and tomography, was carried out in order to characterize the damage created by impact. Once the experimental aspects were sufficiently understood, numerical simulations were performed using the Abaqus™ finite element code. Results from experimental tests and numerical simulations were then compared.

Then, in the second section of this chapter, focus is placed on the behavior after aging with the same procedure as the one followed for the unaged composite.

A comparison between experimental and predicted impact behavior will be shown.

4.2. Influence of the loading-rate on the mechanical properties of the C/Epoxy

There is a very significant literature on this topic, but no clear universal conclusions as results are test dependent and no single test method allows the whole range of loading rates to be studied (quasi-static/servo-hydraulic/Hopkinson bar). The response will also depend on the particular fibre/matrix/manufacturing combination studied.

For the stiffness, a review [244] has summarized the strain-rate effects on CFRP stiffness and strength. In compression, it appears that the compressive elastic modulus is matrix dominated and probably increases with increasing strain-rate. However, tests are often performed using a Split Hopkinson Pressure Bar (SHPB) and effects from inertia tend to mask the initial behavior of the material under dynamic loading. For this reason, the authors concluded that the lack of general agreement in the literature regarding the sensitivity of the dynamic modulus to strain rate could be caused by the testing machine. In tension, they concluded that there is some indication of a positive sensitivity to strain-rate but high scatter and the lack of studies make this difficult to say with any certainty.

For the strength, both tensile and compression strength are seen to increase with the strain-rate. However, a large scatter is observed. Conclusions depend mainly on the material system and the manufacturing process.

Rate effects on the fracture toughness have also been studied. However, these tests are difficult to perform, particularly at high loading rates, and results difficult to post-process. A previous study [245] reviews some

results on this topic. In the introductory part of that paper, the author notes discrepancies from the available reports in the rate effect on initiation fracture toughness and dynamic delamination fracture toughness of polymer composites. It is reported that in some studies, the initiation fracture toughness increased with loading-rate [246]–[248]. In another study [249], the opposite was found. A stepwise-drop was also found [250]. On the other hand, a few researchers reported that dynamic initiation fracture toughness was insensitive to loading-rate [251] and that dynamic fracture toughness was insensitive to crack propagation speed [252]. The author concludes by noting that most of these conclusions were based upon test data that exhibited significant scatter and compared different material systems.

4.2.1. Mechanical tests from 1 mm/min to 1000 mm/min

The aim of this study is to compare the effects of the loading-rate between the quasi-static and the dynamic (impact) behavior. For this study, tensile and shear tests on pure epoxy and tensile tests on C/Epoxy on coupons oriented at 0° , $\pm 45^\circ$ and 90° have been performed at rates up to 1000 mm/s. The aim was to characterize the change in mechanical properties in a range between the quasi-static and the impact behavior.

4.2.1.1. Effects of loading-rate on the tensile and shear strength of pure Epoxy coupons

An example of a comparison between tensile stress vs. strain curves is presented in Figure 4.1 for unaged pure Epoxy coupons. These tests have been performed at crosshead displacement rates from 1mm/min to 1000mm/min. For all cases, increasing the loading-rate increases the strength while reducing the strain at failure. The same comparison is shown in Figure 4.2 for the different aging conditions.

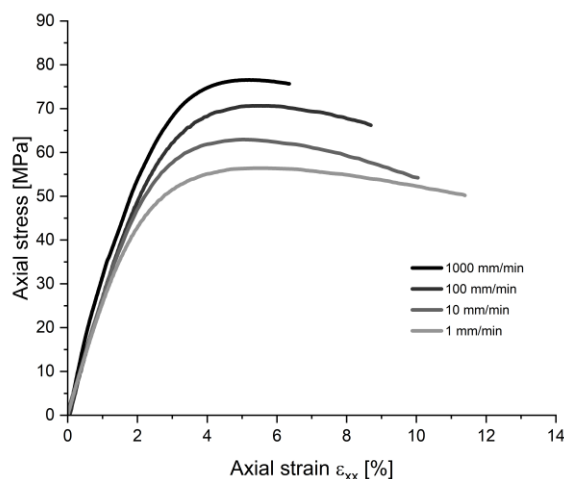


Figure 4.1 – Effects of loading-rate on the stress vs. strain curves for an unaged Epoxy coupon in tension

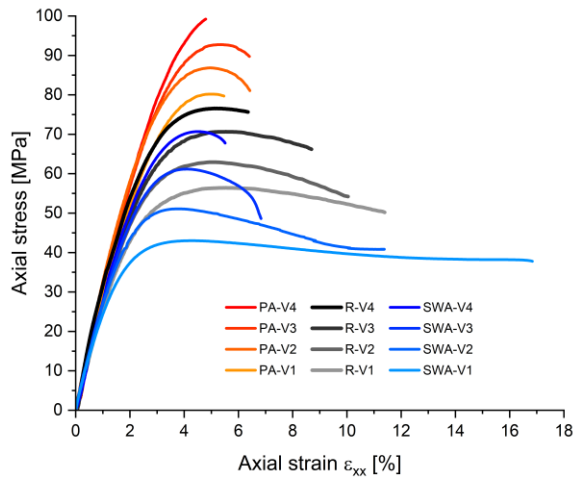


Figure 4.2 – Stress vs. strain curves comparison for unaged and aged Epoxy coupon tested at V1=1mm/min, V2=10mm/min, V3=100mm/min and V4=1000mm/min

The change of the tensile and shear strength with the increase of loading-rate is shown respectively in Figure 4.3 and Figure 4.4. Increasing the loading-rate by three decades increases the tensile strength by 21 MPa and the shear strength by 16 MPa. These values are averaged for all aging. Similar results have been found in the literature [253]. In [254], the authors proposed that the decrease of strain at failure with the increase of the strain-rate is related to chain mobility. At high strain-rate, deformations of the sample during the short duration of the test involve only short-range intermolecular interaction between polymer chains without any change in the intramolecular configuration shape of the large polymer chains. At low strain-rate, intramolecular interactions are possible, resulting in an increase of the strain during the test. Also, if the test duration is long, stress relaxation affects the sample by decreasing the effective stress.

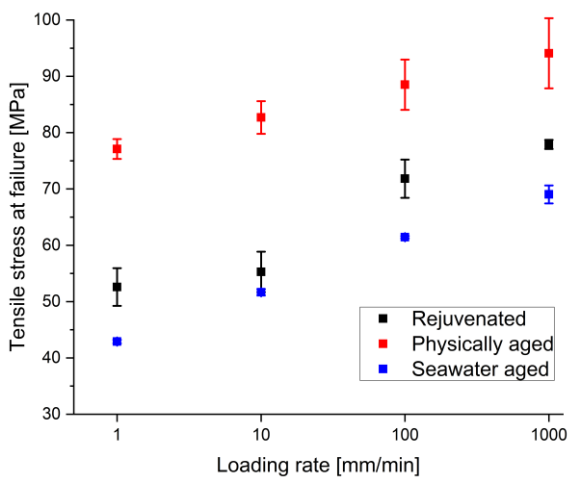


Figure 4.3 – Effect of loading-rate on the tensile strength behavior of unaged and aged coupons

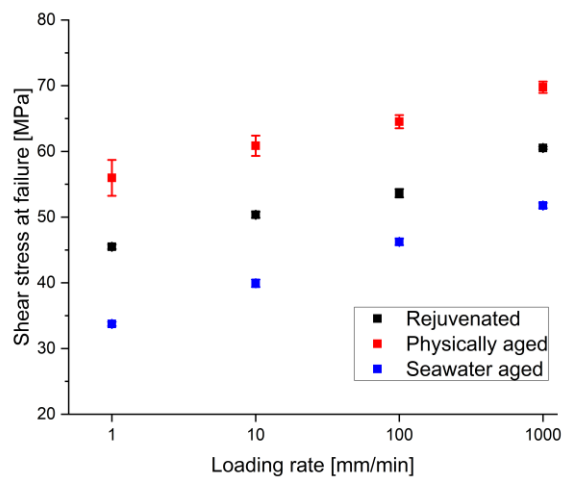


Figure 4.4 – Effect of loading-rate on the shear strength behavior of unaged and aged coupons

4.2.1.2. Effects of loading–rate on the tensile strength of C/Epoxy coupons

Tensile tests have been performed on unaged and aged composite coupons oriented at UD, $\pm 45^\circ$ and 90° . For UD coupons, no effect of the strain–rate has been observed in the range studied. For the 90° specimens, Figure 4.5 shows the change of transverse strength for unaged and aged coupons with an increase of the loading–rate. For the seawater saturated coupon, no increase of the strength is observed. The main conclusion is that a degradation of the interface occurs during ageing, and this has already been characterized in Chapter 3 for this aging condition. It must also be noted that the physically aged coupon strengths are not improved compared to an unaged state. Similar results have been found previously [170], and the author concluded that the physical aging embrittles the resin which will break at a lower strain. This hypothesis seems interesting if the transverse modulus is not affected by the physical aging, which is not our case (7.94 ± 0.6 GPa for the unaged state, 9.23 ± 0.8 GPa for the physically aged state). From these results and the conclusions in Chapter 3, a hypothesis can be a degradation of the interface which leads to a premature failure between the fibers and the matrix. This could explain why the strength is increased with the loading rate but stays below the unaged strength.

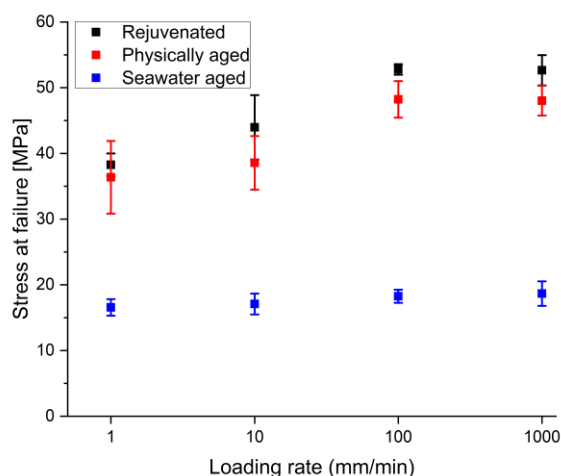


Figure 4.5 – Effect of loading–rate on the tensile strength of unaged and aged transverse C/Epoxy coupons

For the shear behavior of the composite, the change of the shear strength is equivalent to the change of the transverse strength. The change of the in–plane shear modulus is shown Figure 4.6. The loss of the shear strength with the physical aging has been investigated in the past [174][175]. In [175], the embrittlement of the epoxy during the physical aging results in the growth of microcracks at lower load, and as the toughness is also decreased, the growth of microcracks leads to global failure more quickly. For the shear modulus, one of the hypotheses is that as the modulus is defined between 0.2% and 0.4%, the load is still low, and the initiation of microcracks has not occurred. Thus, the modulus is calculated on an undamaged material, and this is why it appears to be higher than for unaged state, while the strength is higher for the unaged state.

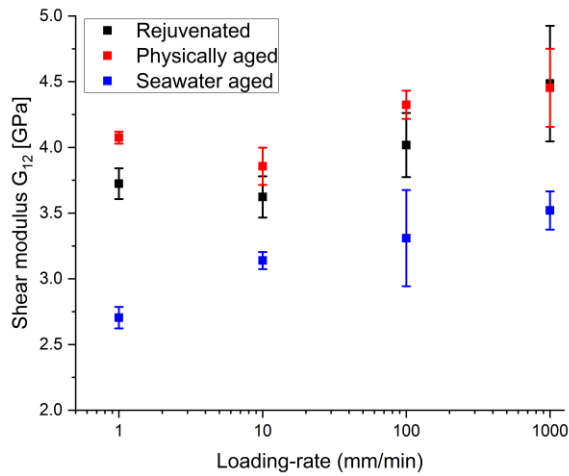


Figure 4.6 – Effect of loading-rate on the in-plane shear modulus

4.2.1.3. Rate effects on fracture toughness

Except for Mode I tests on composites that have been performed from 1 to 1000 mm/min and showed no explicit change on the fracture toughness (Figure 4.7), no further testing has been performed to evaluate the rate effects on fracture toughness. An issue is the accurate identification of the crack tip position during high rate testing. At high loading rate, the use of a high-speed camera is necessary due to the very short test duration. However, the images taken during the test need to have a good resolution. For pure mode I tests, the crack propagation is easy to determine but this is not the case during mode II and mixed mode tests.

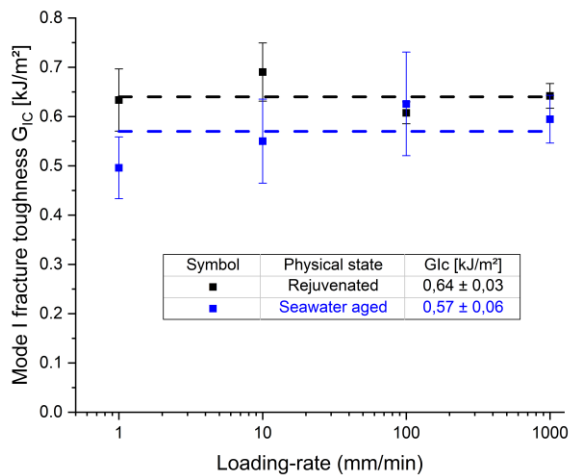


Figure 4.7 – Mode I fracture toughness change from 1 to 1000 mm/min

4.2.2. Strain-rate comparison

In order to have an idea of the strain rate during a drop weight impact event, rosettes with three strain-gages have been bonded on the back face of impact coupons. The rosettes were bonded on the coupon center where the strains are supposed to be maximal. Results from these tests are reported in Table 4.1. For the coupons impacted at 5 m/s, the 0° corresponds to the length direction, the 90° corresponds to the transverse direction and the ±45° corresponds to the direction between these. The maximum strain-rate values during impact are significantly higher than those applied during the material characterization tests,

though the differences in strain rate are less than those noted between 1 and 1000 mm/minute. One might nevertheless expect the matrix-dependent properties such as strength to be underestimated if quasi-static test values are used in modelling.

A second question is whether the strain rates during these impact tests are representative of the impacts a composite propeller will undergo during service. This is more difficult to address as a wide range of impacts is possible and the loading rates will depend on the resultant of boat speed, propeller rotational speed and current speed. An estimation of the tip speed determined for a chemical tanker propeller blade with a $\phi 2120\text{mm}$ at a max RPM of 355 was proposed to be 39.4m/s [114].

In the absence of further information on real impact conditions the drop weight impact configuration was adopted in this study.

Table 4.1 – Comparison of strain-rates measured during this project

Loading rate	Strain rate [s^{-1}]		
	C/Epoxy 0°	C/Epoxy 45°	C/Epoxy 90°
1 mm/min	2,4E-05	9,0E-05	8,0E-05
1000 mm/min	2,4E-02	9,0E-02	3,0E-02
5 m/s (Impact)	2	2	2

4.3. Development of a new drop weight impact tower

4.3.1. Use and qualification of an existing drop weight impact tower

At the beginning of the project, an existing drop weight impact tower was used to perform impact tests. Historically, it was used to perform impact test on GFRP laminates, much less stiff than the CFRP laminates of this study. A tracker was bonded on the impactor surface, and a high-speed camera was used to film the tracker few milliseconds before the impact. It required a post processing step with image analysis to determine the impact velocity. This facility was instrumented by four piezoelectric force sensors. A thin steel plate was used as a reference plane. The force sensors connected the reference plane and the ASTM D7136 fixture. The old setup is shown in Figure 4.8.

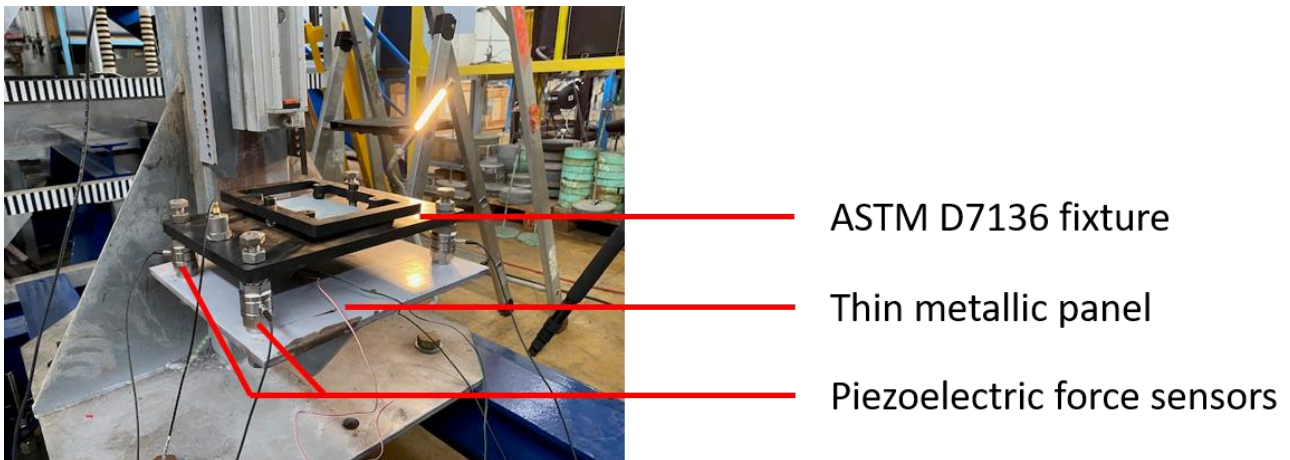


Figure 4.8 – Old drop weight impact tower used for preliminary tests

An example of the force-Time curves is shown in Figure 4.9. The contact time was less than 3ms. The curves seem good because no periodic signal due to vibrational issues are observed.

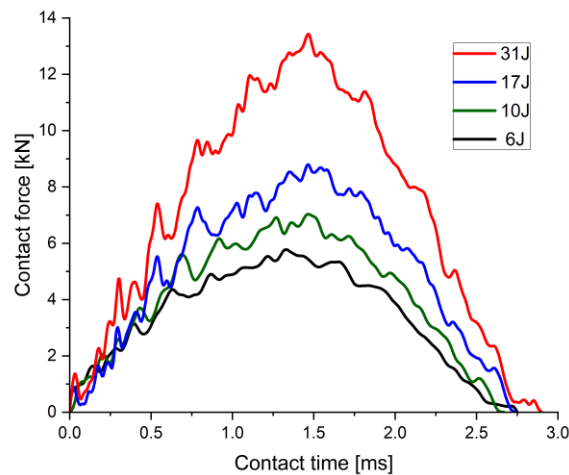


Figure 4.9 – Force vs. Time curves for impacts on the old drop weight impact tower

After several tests, a plasticization of the thin metallic support panel was observed. This was due to high force levels experienced by the panel because of high impact energies. In addition, this panel was connected to the tower with a vertical stiffener on the middle which allows the panel to bend. The use of a high-speed camera also showed bending of the ASTM D7136 support during the tests. This is unsatisfactory because the numerical simulation of experimental tests requires well-defined boundary conditions which were not experimentally verified.

4.3.2. Development of a new drop weight impact tower

Based on the observations made during preliminary tests on the existing tower, it was decided to develop a new drop weight impact facility. The new setup was designed to be stiffer: The reference metallic panel is thicker, while the ASTM D7136 fixture has been manufactured to be 75mm thick. This avoids bending during the impact. In addition, new sensors to automatically measure the impactor velocity and the out-of-plane displacement of the coupon during the impact have been added. An automatic anti-rebound system has also

been implemented for the experimenter security, together with an interlocked safety cage. This system is based on two pneumatic actuators which are triggered when the contact between the impactor and the coupon is broken. It supposes that the impactor will have a T-shape, which is suitable to measure the impactor velocity with a laser at the extremity of the horizontal bar. A photo of the new setup is shown in Figure 4.10.

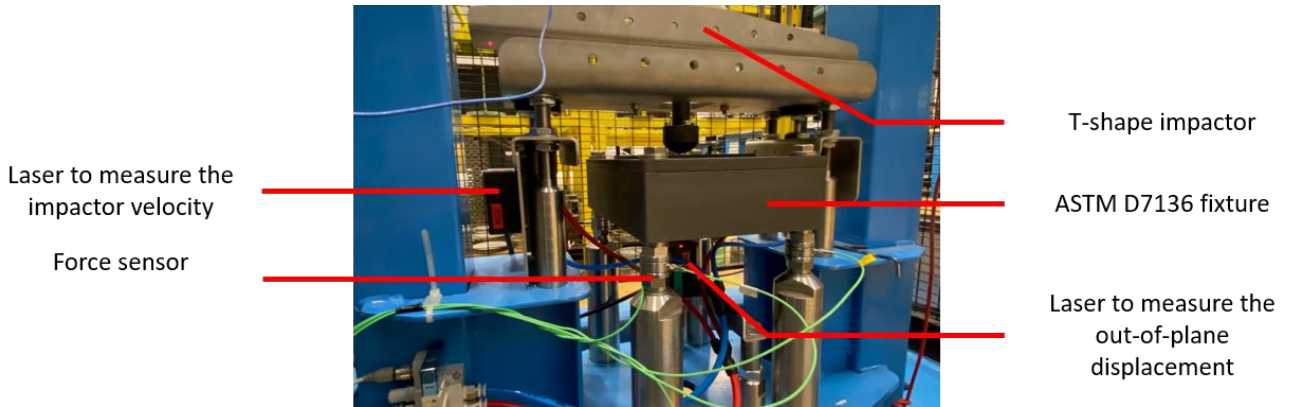


Figure 4.10 – New drop weight impact tower with improved stiffness and new sensors

The main issue with this system is the vibrations induced by the large impactor. These are visible in Figure 4.11. At 5J, the force signal presents a periodicity, which is due to the impactor response. This signal shows a frequency around 2kHz. It would be possible to filter the signal to remove these vibrations. However, filtering could remove data related to material damage, so for this study, no filter has been used. The contact time was found to be around 4ms, which is higher than those obtained with the old setup, but with well-defined boundary conditions.

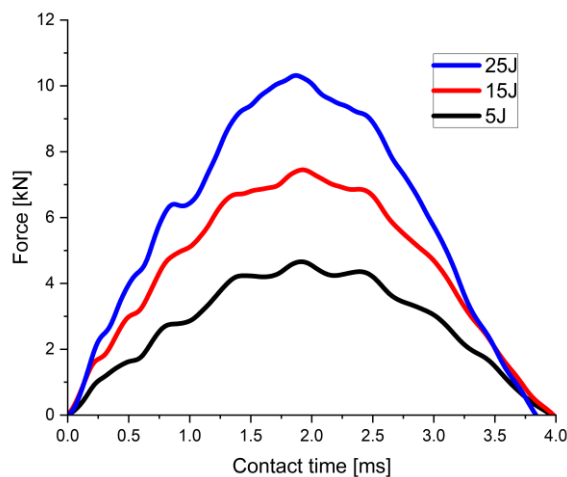


Figure 4.11 – Force vs. Time curves for impacts with the new drop weight impact tower

Another issue with the laser sensor has been observed. When the impactor is in contact with the coupon, both force and out-of-plane displacement are supposed to increase. In our case, the force was observed to increase before the out-of-plane displacement. This may be due to the laser sensor conditioner that requires more time to process the signal. This shift is shown Figure 4.12.

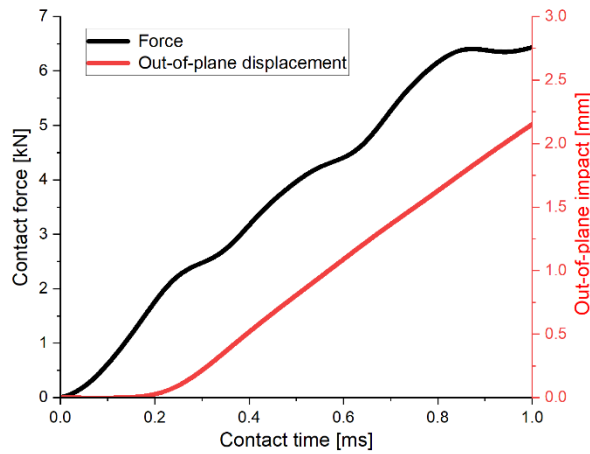


Figure 4.12 – Change of the experimental force and out-of-plane displacement in the first moments of the impact

4.3.3. Conclusions

The development of a new drop weight impact tower was necessary, in order to improve the boundary conditions during the impact tests. The implementation of a new sensor to measure the out-of-plane displacement of the coupon during the impact is also beneficial and adds an experimental value to compare with the simulation.

At low impact energy, the pneumatic actuator worked well. For higher impact energies, the impactor rebound was high, and for these conditions, the pneumatic solution was not sufficient to prevent a second impact. A solution based on a high-speed hydraulic actuator is recommended.

4.4. Experimental impact behavior in the unaged state

The first experimental campaign focused on the impact behavior of unaged coupons. Prior to the test, coupons were rejuvenated, to be sure that the physical aging did not influence the results. Impact tests have been performed at seven energy levels: 5J, 15J, 25J, 35J, 45J, 60J and 80J.

4.4.1. Impact curves

Figure 4.13 shows a comparison of the Force vs. Out-of-plane displacement curves for seven levels of energy in the range 5J to 80J. The initial stiffness seems to be the same for all coupons. An offset is observed at the end of the unloading. This is not necessary the coupons that exhibits an irreversible deformation, but it could be the stitching which is teared out during the impact and then affects the contactless measure performed by a laser. For an impact of 80J (in purple), a significant failure mechanism occurred during the test, leading to an abrupt load drop. It should be noted that this test was designed to introduce damage localized at the coupon center. With a $\phi 50$ mm hemispherical impactor, the contact area is large and at high energy levels the damage can reach the coupon borders. Except for the coupon impacted at 80J, all curves show the same shape.

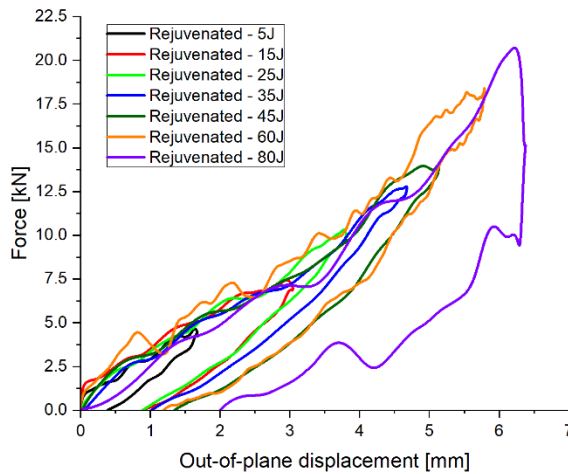


Figure 4.13 – Force-Time plot comparison for the rejuvenated state at different energy levels

The higher out-of-plane displacement, coupled with the large drop, suggests that significant damage was created at 80J. It may also be noted that when the impact energy increases, the maximal out-of-plane deflection increases considerably (from 1.5mm at 5J to nearly 6.5 mm at 80J).

Figure 4.14 compares the force and the out-of-place displacement peaks averaged for three coupons for each impact energy. The standard deviation is small compared to the averaged value. Below 45J, force and out-of-plane displacement curves show a similar shape. For higher energy levels, the out-of-plane displacement increases at a lower rate. This may be due to the impactor diameter which is large and results in a load distribution on a larger surface, and this prevents the penetration.

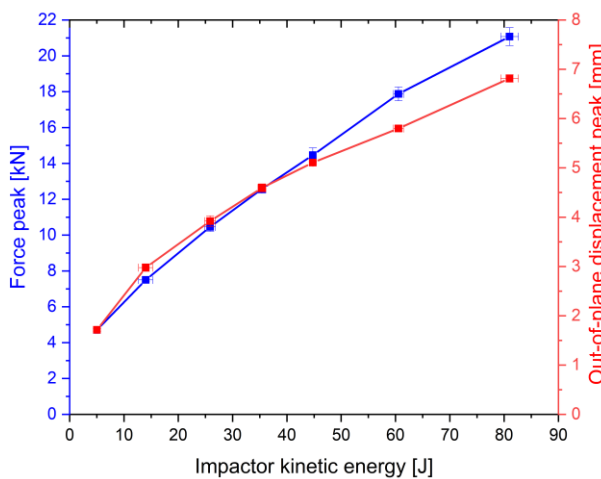


Figure 4.14 – Force peak and out-of-plane displacement peak averages for rejuvenated coupons at 7 energy levels

4.4.2. C–Scans

After the impact, the coupons were evaluated with a C–Scan measurement technique to characterize the delamination. Figure 4.15 shows the delamination detected in rejuvenated coupons, from 5J to 35J.

At 5J, no damage is observed, the delamination threshold has not been reached. For higher energy levels, a delamination is observed. The area increases when increasing the impact energy. At the center of the coupon, a dot is detected. This area is not delaminated due to the impactor contact. The delamination begins

when the initiation scalar, a mixture between the tensile and the shear strength, is exceeded at the interface. Just below the impactor, the interface is purely in compression along the impactor axis. Neither the tensile nor shear criterion is reached, that is the reason why this area does not show any delamination.

For impact energies of 45J and 60J (Figure 4.16), the delamination is stopped by the boundary conditions. It then propagates in other directions. Finally, at 80J, the delamination extends to the coupon side. As the impactor is large, the stress is distributed over a large area, which prevents the fiber failure by extending the delamination to the coupon borders.

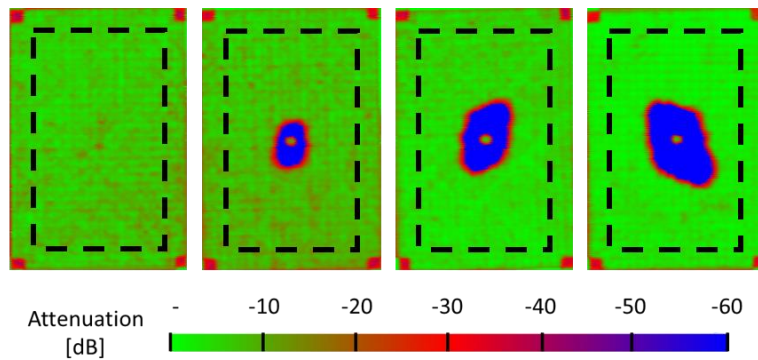


Figure 4.15 – Comparison of the delamination for rejuvenated coupons impacted at 5J, 15J, 25J and 35J

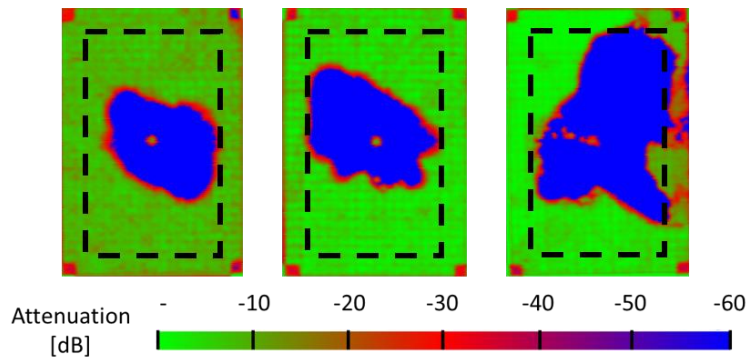


Figure 4.16 – Comparison of the delamination for rejuvenated coupons impacted at 45J, 60J and 80J

4.4.3. Balance of energy

One criterion used to compare impact tests is the balance of energy. The contact force is plotted as a function of the out-of-plane displacement. The area between the loading and the unloading part corresponds to the impact energy (Figure 4.17).

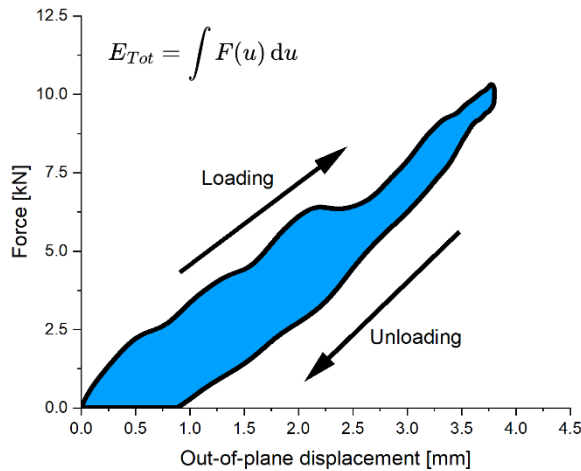


Figure 4.17 – Force vs. Out-of-plane displacement plotted to determine the impact energy

The change of energy during the impact is then plotted as a function of the contact time. The peak corresponds to the energy given by the impactor E_{tot} . Then, the impactor rebounds: this corresponds to the elastic energy E_{el} . The difference between the impact energy and the elastic energy has been used to damage the material. This is the absorbed energy E_{abs} . The balance of energy is presented Figure 4.18 for a 20J impact on an unaged coupon.

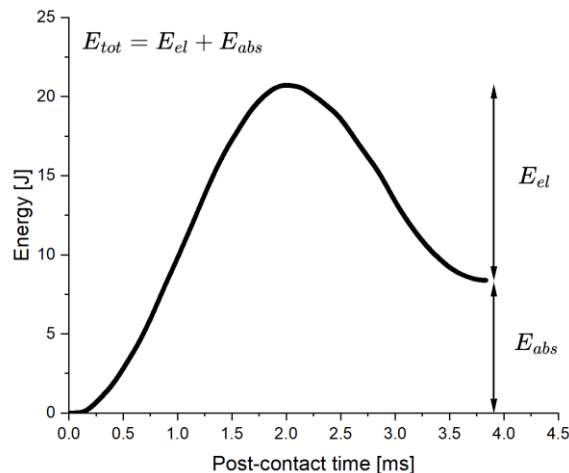


Figure 4.18 – Balance of energy during the impact test

The increase of impact energy is supposed to increase the absorbed energy. When the damage threshold has been reached, each increase of impact energy will create more damage in the coupon. Figure 4.19 shows a comparison of the balance of energy of impact tests performed from 5J to 80J. The 4ms acquisition has been found to be sufficient to stabilize the balance, and then to determine the absorbed energy. At 80J, 85% of the total energy is absorbed, i.e. used to damage the material, while at 25J, 60% is absorbed. That means at 80J, the coupon suffers more damage than at lower energy. At 5J, the absorb energy is around 45%.

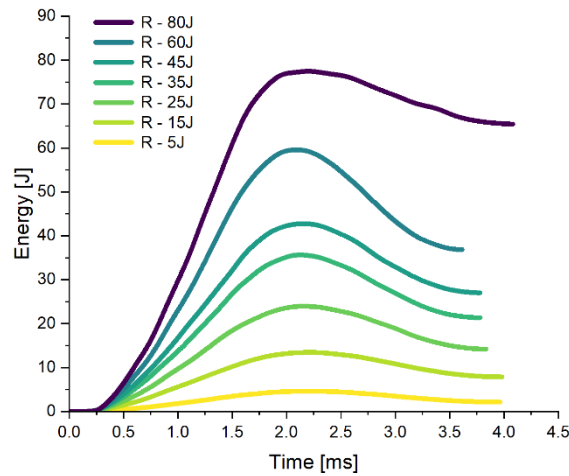


Figure 4.19 – Comparison of the balance of energy for rejuvenated coupons impacted from 5J to 80J

Figure 4.20 shows the change of absorbed energy when the impact energy is increased. Two slopes are observed. The first for $E_{tot} < 55J$. The main failure mode is the delamination (Figure 4.21). The second for $E_{tot} > 55J$. Two failure modes are observed: multiple delamination and ply damage. The latter consumes more energy to initiate then propagate. This is the reason why the absorbed energy increases more in this range.

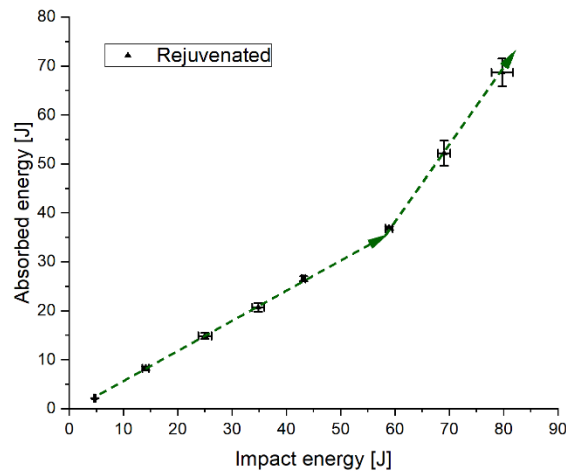


Figure 4.20 – Effect of impact energy on the increase of absorbed energy

4.4.4. Microscope observations

One coupon per impact energy has been cut then polished to determine the delamination planes. Due to the architecture of the material, it was difficult to quantitatively characterize the change in damage with the increase in impact energy. Figure 4.21 shows the through thickness damage at 15J. Observations mainly revealed delaminations between 0/45 and 0/0 interfaces. While the former seems normal, the second is rarer because the delamination is mainly due to a difference of bending stiffness of the two successive plies. For plies with the same material and the same orientation, the bending stiffness is the same. In this case the 0/0 interface delamination may be due to the weft fibers which reduce the toughness of this interface. In the case of the -45/45 interface, the stitching (Figure 4.22) prevents the delamination between the plies. It has also been observed that porosities develop around the stitching during the infusion process.

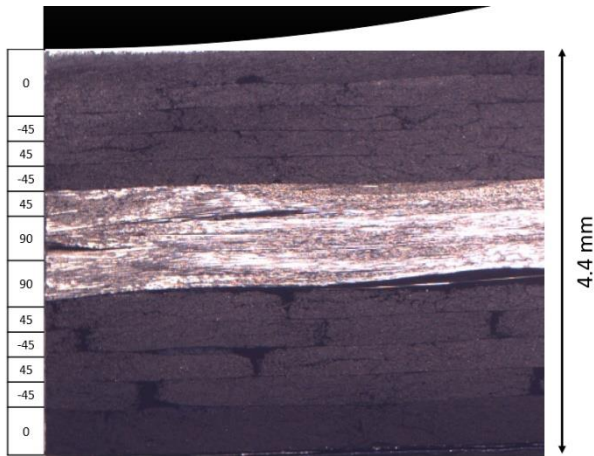


Figure 4.21 – Delamination observed with an optical microscope for rejuvenated coupon impacted at 15J

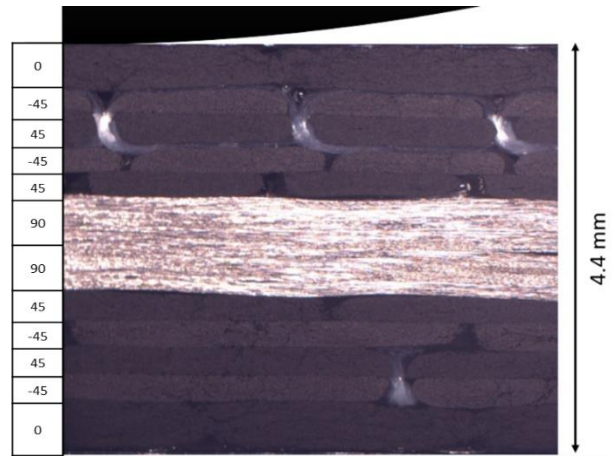


Figure 4.22 – Stitching in the -45/45 fabric

For specimens impacted at more than 55J, Figure 4.23 shows a change in the damage observed. In addition to delaminations, ply failures in yarns are seen. These correspond to intralaminar fracture. It occurs when the delamination is stopped by the boundary conditions at energy levels higher than 55J.

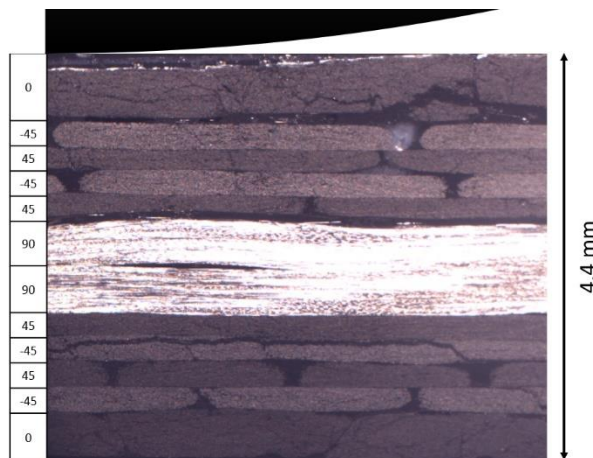


Figure 4.23 – Interlaminar and intralaminar fracture observed at 80J

4.4.5. Tomography on unaged coupons

An X-ray tomography inspection of unaged coupons impacted at 5J and 30J was performed. At 5J, the C-Scan shows no delamination on the unaged coupon. This coupon was therefore used to characterize the porosity localization through the thickness, and voids were found to be mainly located between the $\pm 45^\circ$ carbon fiber yarns (Figure 4.24).

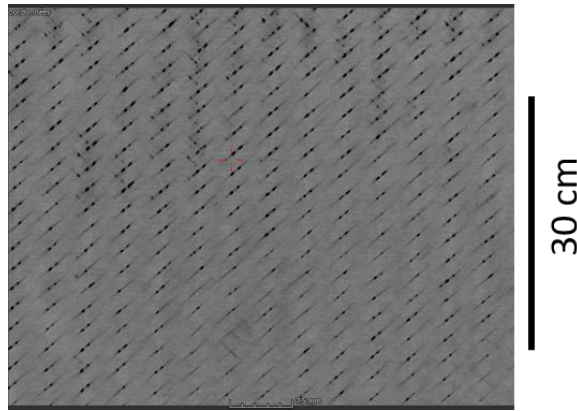


Figure 4.24 – Porosities observed between carbon fiber yarns in a +45° ply

The delamination was characterized at 30J (Figure 4.25) and is observed even if the porosities and the stitching degrade the contrast. The impact was on the upper surface of each tomography plane. In the length direction, delamination is observed at the $-45/45$ interface. In the width direction, delamination is observed between the $-45/45$, $45/0$ and also $0/0$ interfaces. The damage propagates in the thickness direction around the carbon fiber yarns, and no fiber damage is observed. It may be noted that the classic “damage tree” is observed on the bottom of the Figure 4.25.

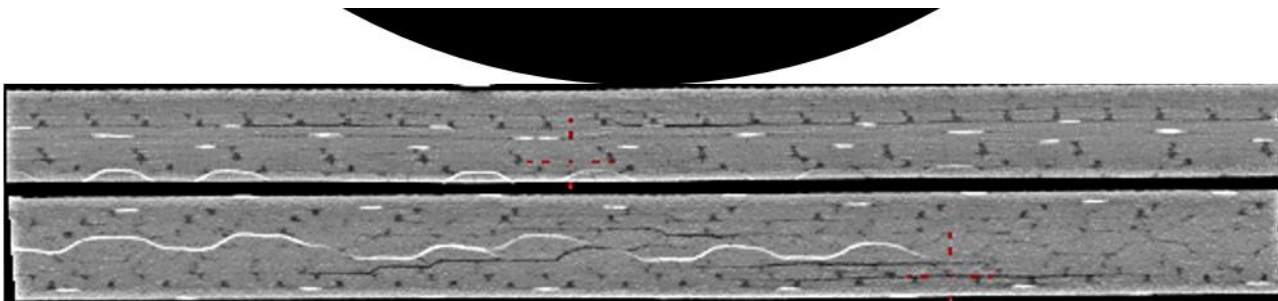


Figure 4.25 – Delamination observed in the length (top) and width direction (bottom) for an unaged coupon impacted at 30J

4.4.6. Conclusions on the LVI behavior of rejuvenated coupons

Impact tests have been performed from 5J to 80J. Coupons were then evaluated by C-Scan. At 5J, the delamination threshold was not reached. For higher impact energies, a delamination was observed. Both out-of-plane displacement and force peak have been found to increase with the impact energy. However, between 35J and 45J, the data begin to diverge. This is due to the incapacity of the coupon to deflect more because of the large impactor diameter.

4.5. Numerical simulation for unaged state

To simulate the impact behavior of unaged C/Epoxy coupons, a numerical model has been developed using Abaqus Explicit™ software. The choice of a commercial solver was a requirement of the funder of this study. It should also be noted that one of the aims of the study was to develop as simple a methodology as possible, which would provide information on impact and seawater aging that could be used in design.

4.5.1. Model description

The model reflects the geometrical, boundary and loading conditions. Both the hemispherical impactor and support were assumed to be rigid relative to the CFRP specimen. To reduce the computation time, they were defined as analytical rigid to avoid meshing them. A mass of 4.5 kg was assigned to the impactor through a point mass definition. The laminate layers were modeled individually with a nominal ply thickness of 0.55 mm for 0° and 90° plies and 0.275 mm for -45° and 45° plies. Zero thickness cohesive interactions were defined between each laminate ply. Two mesh strategies have been tested. The first involves a standard mesh, while the second is based on an oriented mesh. Mesh length was defined to be 1.5 mm long. This was found to be a suitable compromise (see Chapter 3). The composite plies were discretized with continuum shell elements (SC8R). SC8R elements have a continuum solid element topology, but their kinematic and constitutive behavior is similar to conventional shell elements that allows for finite membrane deformation and large rotations [255]. Enhanced hourglass control was used to prevent excessive distortion, which can cause the simulation to abort prematurely. The general contact algorithm was used to simulate the contact behavior between the composite layers while a surface to surface contact behavior was used to simulate the contact between the rigid and the deformable parts. A coefficient of friction of 0.05 was used for the general contact, and 0.1 for the surface-to-surface contact. A gravity load of $9.806 \text{ m} \cdot \text{s}^{-2}$ was applied in the model.

4.5.2. Mesh strategy

Standard simulations of the LVI test use elements with a square shape. Simple parts such as CFRP plies with a supposed constant thickness are easy to mesh and Abaqus™ offers the capacity to mesh the plies simply. Based on results from recent work [168][256], it was decided to study the influence of an oriented mesh on the delamination, displacement and force prediction. Even though the model studied here does not consider interlaminar or intralaminar damage by the use of intralaminar elements [256] to reduce the computation time, cohesive surfaces with oriented elements are expected to improve the results. Abaqus does not offer the capacity to orient the mesh. To do that, a python script has been written to automatically generate the Abaqus™ INP file, whether an oriented mesh or a standard mesh. To avoid damage due to the free edges, it has been decided to separate the material model in two sections (Figure 4.26): near the edges, the material is purely elastic, while near the contact area, the material is elastic with a damage model.

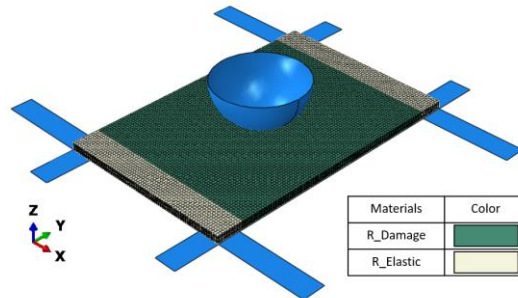


Figure 4.26 – Segregation of the mesh to avoid ply damage close to the free edges

In Abaqus™, the definition of all nodes is done with the keyword *Node, followed by the list of all nodes that are in the ply. Each line represents one node. The first value corresponds to the node ID, the second is the X coordinate, the third is the Y coordinate, and finally the fourth is the Z coordinate. Values are separated by a comma. The definition of an element is done with the keyword *Element, followed by the list of all elements that are in the ply. Each line represents an element which is defined by its nodal connectivity. It is important that the continuum shells elements are oriented properly, since the behavior in the thickness direction is different from that in the in-plane direction. By default, the element top and bottom faces and, hence, the element normal, stacking direction and thickness direction are defined by the nodal connectivity [220]. This connectivity is not the same for a standard mesh and an oriented mesh.

4.5.2.1. Generation of ORTHO mesh

The first case is the simplest. Figure 4.27 represents the mesh called ORTHO, which is the standard mesh given by Abaqus™. The Python program used to write the input file deals with the distance between nodes. Coarser or thinner mesh are possible but the mesh size will be the same in all the composite coupon.

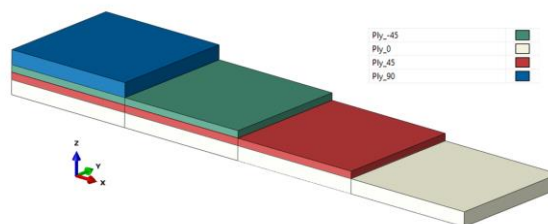


Figure 4.27 –Example of an ORTHO mesh

Figure 4.28 shows the nodal coordinates for the standard element. For the element definition, it is necessary to pair the element ID to its 8 nodes. Table 4.2 reports the order of the nodes chosen from the node coordinates.

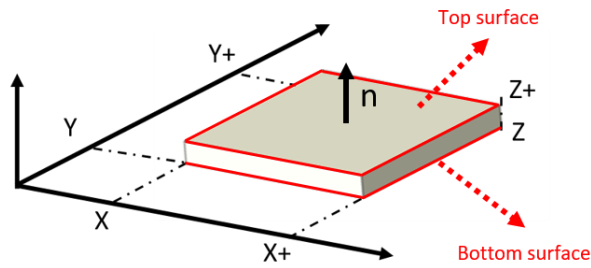


Figure 4.28 – ORTHO element definition with the coordinates of all eight nodes

Table 4.2 – Node ID and respective coordinates to assign to an ORTHO element

Node ID	Nodes coordinates
1	X, Y_+, Z_+
2	X, Y, Z_+
3	X, Y, Z
4	X, Y_+, Z
5	X_+, Y_+, Z_+
6	X_+, Y, Z_+
7	X_+, Y, Z
8	X_+, Y_+, Z_+

4.5.2.2. Generation of ORIENT mesh

The second oriented mesh is more complex to create because two types of elements coexist. Elements with material orientations at 0° and 90° are defined in the standard way. For plies oriented at -45° and 45° , the mesh is oriented in the fiber direction. An example of a composite layup is given in Figure 4.29. Nodes have the same coordinates on the top and bottom surface. Only the element connectivity changes.

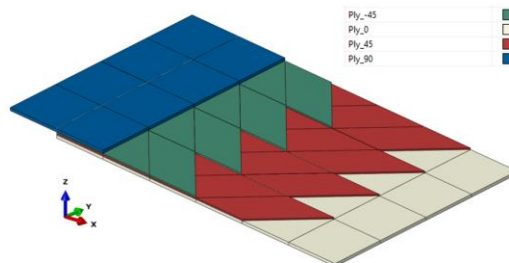


Figure 4.29 – Example of a mesh with oriented elements

As the element is oriented, three coordinates are needed in the X axis as shown Figure 4.30. Table 4.3 reports the node coordinates to use to define correctly the node connectivity.

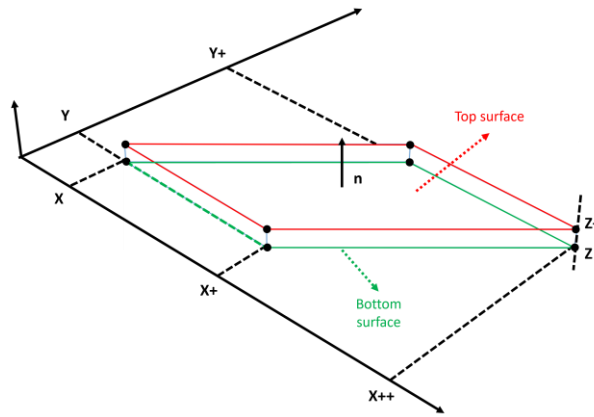


Figure 4.30 – ORIENT element definition with the coordinates of all eight nodes

Table 4.3 – Node ID and respective coordinates to assign to an ORIENT element

Node ID	Nodes coordinates
1	X_+, Y_+, Z_+
2	X, Y, Z_+
3	X, Y, Z
4	X_+, Y_+, Z
5	X_{++}, Y_+, Z_+
6	X_+, Y, Z_+
7	X_+, Y, Z
8	X_{++}, Y_+, Z

For this mesh, a cohesive behavior has been implemented between elements that are in contact with each other and that can simulate the behavior between yarns. However, no difference was found compared with a version without intralaminar cohesive contact.

4.5.3. Input data

As described in Chapter 3, a quasi-complete dataset has been obtained experimentally. This section summarizes the input data used in the model. To keep consistent units in Abaqus™, the units presented in Table 4.4 were used.

Table 4.4 – Property and unit used to keep consistent units in Abaqus™

Property	Mass	Length	Time	Force	Stress	Energy	Density
Unit	g	mm	ms	N	MPa	N.mm	g/mm ³

The mechanical properties used with this model are summarized in Table 4.5. It must be highlighted that the ply fracture toughnesses in tension and compression are not the same as used in Chapter 3 to predict the mechanical behavior of the quasi-isotropic coupon under flexural loading. The post-processing step of these tests had not been performed when the simulations were run, so the value has been supposed to be equal to 80 kJ/m², both in tension and compression.

Table 4.5 – Mechanical properties used for the rejuvenated state in the model

Property	Symbol	Numerical value
Density	ρ	1.55E-3
Friction metal/composite	$\xi_{M/C}$	0.1
Young's moduli	E_1, E_2	127540, 7940
Poisson's ratio	ν_{12}	0.274
Shear moduli	G_{12}, G_{13}, G_{23}	3720, 4600, 3070
Ply strength	$X^T, X^C, Y^T, Y^C, S^T, S^C$	2272, 934, 38, 124, 73, 73
–	α	0
Cohesive surface elasticity	K_{nn}, K_{ss}, K_{tt}	24600, 14200, 14200
Interface strength	τ_n, τ_s, τ_t	80, 56, 56
BK model parameters	G_{IC}, G_{IIC}, η	0.63, 1.46, 1.59
Friction composite/composite	ξ	0.05
Energy dissipated for ply failure	$G_{ft}, G_{fc}, G_{mt}, G_{mc}$	80, 80, 0.63, 1.46

Friction coefficients between metallic parts and the composite coupon are supposed to be the same as graphite/steel, given to be 0.1 [257].

4.5.4. Comparison between Experiment and Simulation for the unaged state

This section focuses on the comparison between the experimental results and the numerical simulations. Simulations have only been performed up to 35J because for higher energy levels, the experimental delamination was stopped by the boundary conditions.

4.5.4.1. Prediction of the force vs. out-of-plane displacement curves

Comparisons between the experimental and the predicted force vs. out-of-plane displacement curves of rejuvenated coupons impacted at 5J, 15J, 25J and 35J are respectively presented in Figure 4.31, Figure 4.32, Figure 4.33 and Figure 4.34. At these levels, the prediction is good even if the initial stiffness is not well predicted. A force drop is experimentally observed in the first moments of the impact which is not predicted

by the model. The reason could come from the laser conditioner that needs time for the signal conditioning, so the force and the out-of-plane displacement measures are not perfectly synchronized (Figure 4.12).

At 5J, both mesh techniques predict the irreversible deflection well, while at higher levels, models underpredict it. The maximum force is also predicted well. While the loading shows similar results between the two mesh techniques, the force and out-of-plane peaks are higher with the standard mesh.

On the coupon back face, the stitching has been observed to be released from the laminate. Before the impact, carbon fiber yarns are wavy because of the stitching. During the impact, the coupon back face experiences tension that stretches the yarns and could push the stitching out of the laminate. After the impact, the carbon fiber yarns are straighter, which leads to a stiffer coupon during the unloading step. This hypothesis could be experimentally validated with tomography on the coupon back face, but this was not done here. In all cases, an irreversible damage has occurred, that increases the absorbed energy.

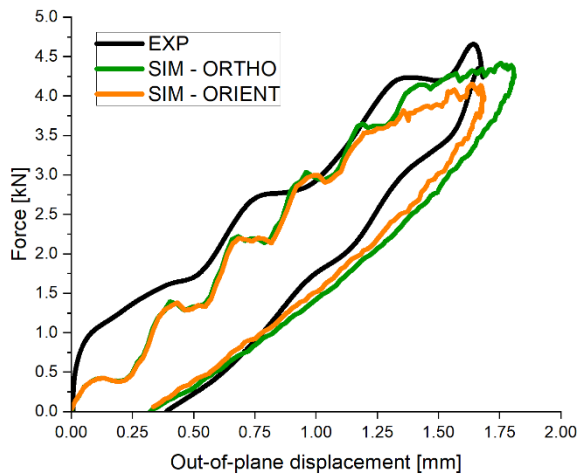


Figure 4.31 – Comparison Exp/Sim of Force vs. Out-of-plane displacement curves for a rejuvenated coupon impacted at 5J

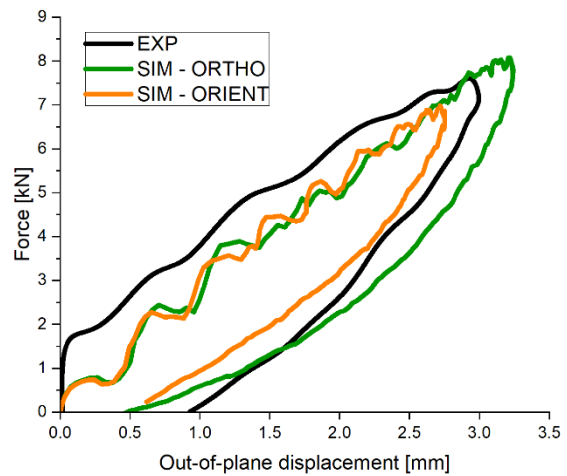


Figure 4.32 – Comparison Exp/Sim of Force vs. Out-of-plane displacement curves for a rejuvenated coupon impacted at 15J

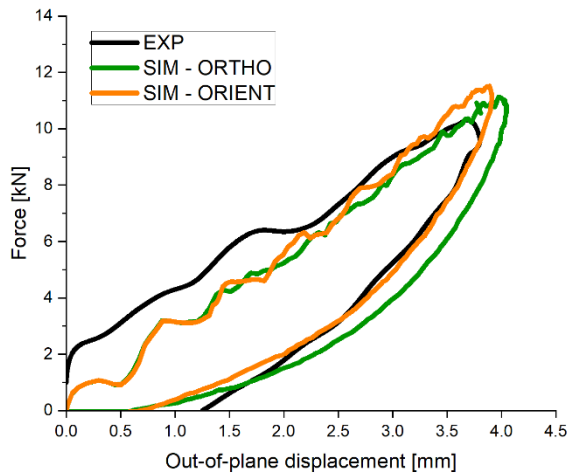


Figure 4.33 – Comparison Exp/Sim of Force vs. Out-of-plane displacement curves for a rejuvenated coupon impacted at 25J

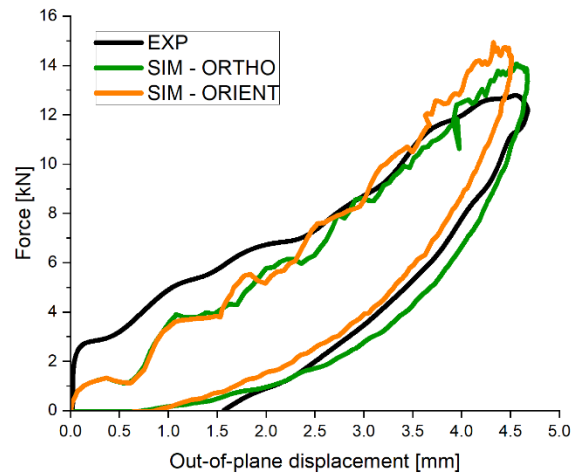


Figure 4.34 – Comparison Exp/Sim of Force vs. Out-of-plane displacement curves for a rejuvenated coupon impacted at 35J

4.5.4.2. Prediction of the energy balance

To validate the numerical simulations and the models, it is necessary to compare the balance of energy during the impact. The balance of energy is compared for impacts at 5J, 15J, 25J and 35J respectively in Figure 4.35, Figure 4.36, Figure 4.37 and Figure 4.38. The impact energy noted in the figure legend is determined from the initial velocity and the mass of the impactor.

The standard mesh shows a good correlation compared to the experiment. In some cases, the experimental total energy that corresponds to the peak is lower than the experiment. It must be noted that springs have been used in the simulation to account for the small displacement of the fixture during the impact. The values were chosen to fit the out-of-plane displacement measures, and have been set to 2500 N/mm per sensor, i.e. 10 kN/mm for the all fixture. This could explain the difference between the experiments and both models. The comparison between the two models shows that a premature failure is predicted for all simulations around 2.5kN for the oriented mesh. This comes from the delamination threshold that has been reached. Matrix damage was also seen to be more extensive than in the standard mesh.

Another issue faced with the oriented mesh is the Abaqus version used. Reading the input file then launching the job led sometimes to aborted runs. Complex contacts between oriented elements may be problematic. In this case, Abaqus 2022 was used, but results may vary between different versions.

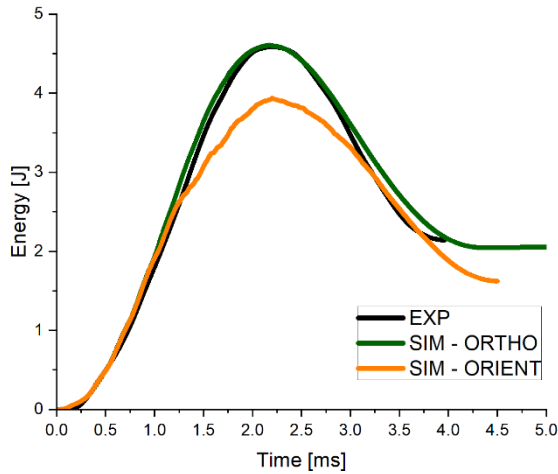


Figure 4.35 – Change of the energy balance for a rejuvenated coupon impacted at 5J

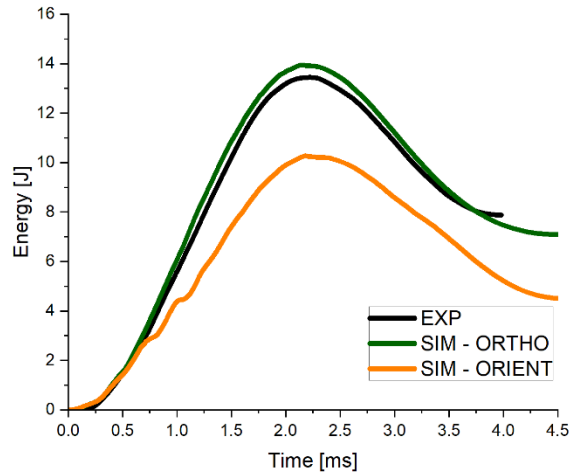


Figure 4.36 – Change of the energy balance for a rejuvenated coupon impacted at 15J

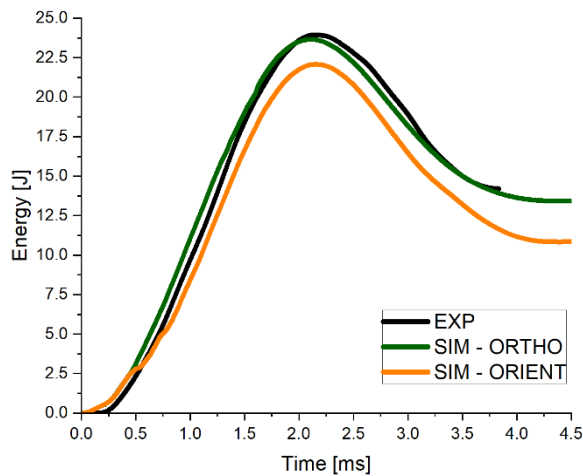


Figure 4.37 – Change of the energy balance for a rejuvenated coupon impacted at 25J

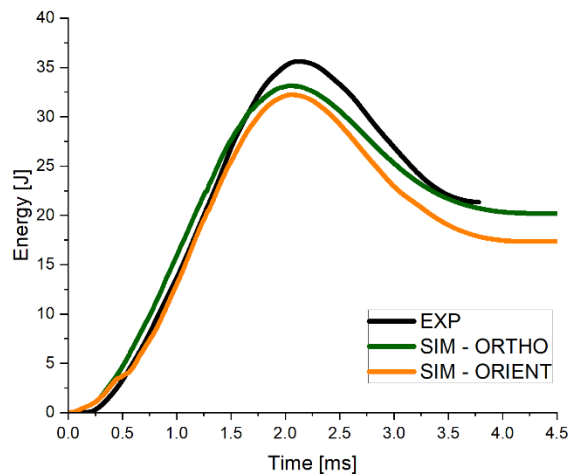


Figure 4.38 – Change of the energy balance for a rejuvenated coupon impacted at 35J

4.5.4.3. Prediction of the delamination

The delamination prediction is a possibility offered by Abaqus™. To do this, the overall value of the scalar damage variable D , named $CSDMG$, needs to be requested when using cohesive surfaces. It corresponds to the overall value of the damage variable d . The surface is considered delaminated when this variable is equal to 1. To compare with our experimental results, only the projected delamination has been exported, even if the model can predict multiple delamination. Comparisons between experimental data and numerical simulation for the two mesh types at impact energies from 5J to 35J are presented in Figure 4.39.

At 5J, both models predict damage, while experimentally no damage was observed. One hypothesis is that the interface damage initiation data, based on pure resin tests, are too low compared to the reality. Tests on composite materials should be performed instead of tests on pure resin coupons to provide this input value. This may improve the prediction. Another hypothesis is that loading-rate effects exist. The dataset used in

the simulations was obtained experimentally with a quasi-static loading-rate of 1 mm/min. As noted previously in the case of LVI, the loading-rate will be higher.

At 15J and 25J, the delamination shape is good for both models. However, the non-delaminated spot under the impactor contact is not predicted with the simulation. This means that this area is in shear. One hypothesis is a small sliding of the coupon on the fixture in the simulation which leads to this stress state. Friction coefficients can be increased to avoid this sliding but these have been shown to have an effect on the stiffness.

Finally, at 35J, an overprediction for the standard mesh is observed and for the oriented mesh, the delamination is predicted to move in the width direction, which was not experimentally the case.

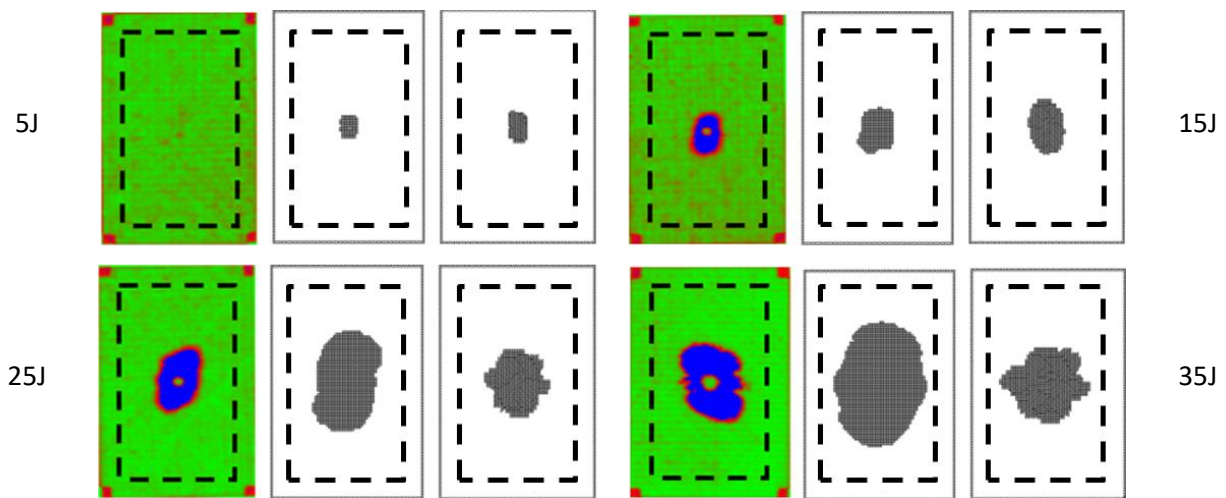


Figure 4.39 – Experimental delamination compared with prediction for impacts from 5J to 35J (Exp/standard mesh/Oriented mesh)

It must be noted that the model can predict multiple delamination but the final shape will not be accurate because continuum shell elements do not calculate σ_{23} which is mainly responsible for matrix cracking. Unless ply damage is included, the damage tree commonly observed will not be predicted because the damage will propagate in the least resistant direction, i.e. the interlaminar plane.

4.5.5. Conclusion on unaged impact

To conclude the impact study for unaged coupons, experimental test results have been compared with a numerical model for impacts at 5J, 15J, 25J and 35J. The predictions of delamination have been found to differ according to the type of mesh, standard or oriented. The standard mesh is better compared to the oriented mesh. The Force-Deflection curves have been compared. The initial slope is not well taken into account probably due to a time offset between two sensors. Then, the balance of energy has been compared, and results from the standard mesh show a good agreement with the experiments. Finally, the delamination has been compared. It is overpredicted at high energy levels, but both models show a good agreement at lower levels.

Improvements would be possible with the use of cohesive elements at the interface between plies. In addition, the tomographic analysis has shown that damage propagation initiated between plies in the thickness direction. The model with continuum shell elements is then not fully suited to simulating the impact behavior of this material because it cannot predict through thickness damage. No fiber failures have been detected or predicted. The standard meshed model provides a reasonable prediction of the experimental results with our impact setup for unaged coupons.

4.6. Effect of aging on the impact behavior

Impacts on aged coupons have also been performed. The aim was to characterize the influence of aging on the impact behavior in order to provide information for propeller design.

4.6.1. Effects of aging on impact curves

A comparison of the Force vs. Out-of-plane displacement is presented for impacts at 5J, 15J, 25J and 35J respectively in Figure 4.40, Figure 4.41, Figure 4.42 and Figure 4.43. The data are quite similar for the rejuvenated and the physically aged states. For the seawater aged coupon, the loading slope seems to be lower. In addition, the force peak is also lower, while the deflection peak is a bit higher. In this case, the effects of seawater aging are obvious.

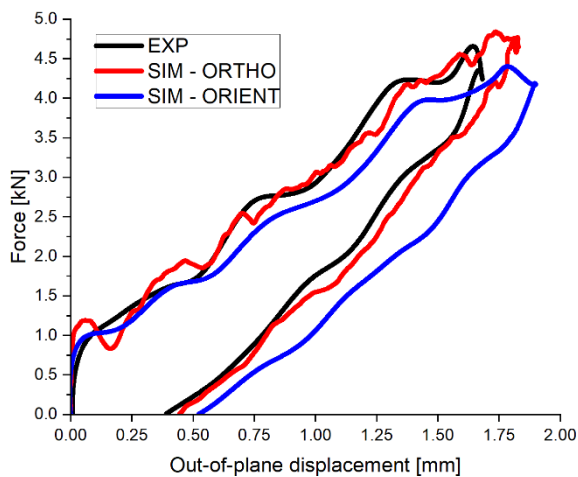


Figure 4.40 – Effects of aging on the Force vs. Out-of-plane displacement curves for coupons impacted at 5J

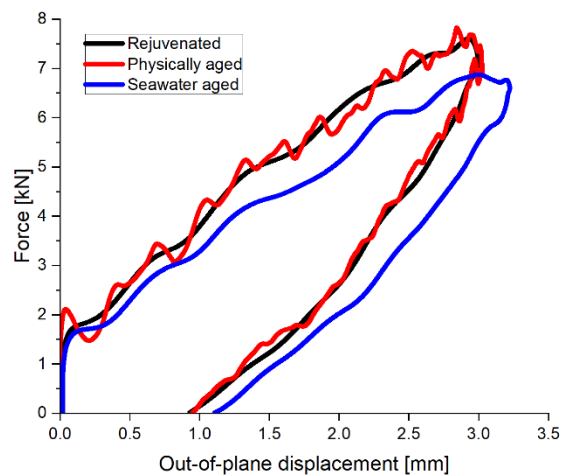


Figure 4.41 – Effects of aging on the Force vs. Out-of-plane displacement curves for coupons impacted at 15J

Figure 4.44 shows the change of the force peak with the increase of impact energy for all aging conditions. While the physical aging shows similar results with the rejuvenated state, the seawater aged coupons present lower peak forces from 45J. The maximal deflection value seems also to increase more with the seawater aging (Figure 4.45) compared to rejuvenated and physically aged coupon responses. At 45J, the impact test is slightly higher than recommended by the standard. Delamination almost reaches the coupon sides but is limited by its deflection and the support.

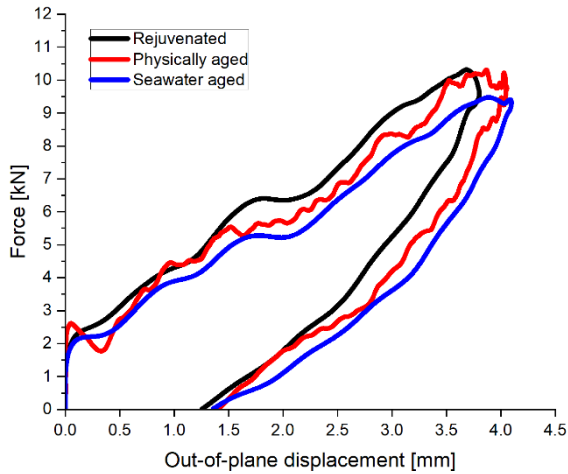


Figure 4.42 – Effects of aging on the Force vs. Out-of-plane displacement curves for coupons impacted at 25J

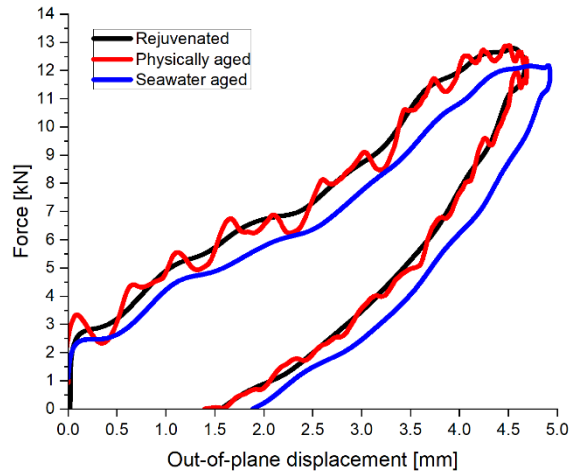


Figure 4.43 – Effects of aging on the Force vs. Out-of-plane displacement curves for coupons impacted at 35J

It should be noted that the effects of the seawater aging could be more significant. Quasi-static mechanical properties are affected by this aging condition when the matrix affects the coupon strength. The quasi-isotropic layup tested here offers the same in-plane stiffness due to unidirectional plies. As the fiber is not affected by the aging, the influence of aging on a quasi-isotropic layup could be less than for an oriented layup with less 0° plies. The use of the dataset obtained experimentally in Chapter 3 for the simulation of a layup with less plies oriented at 0° could validate this point.

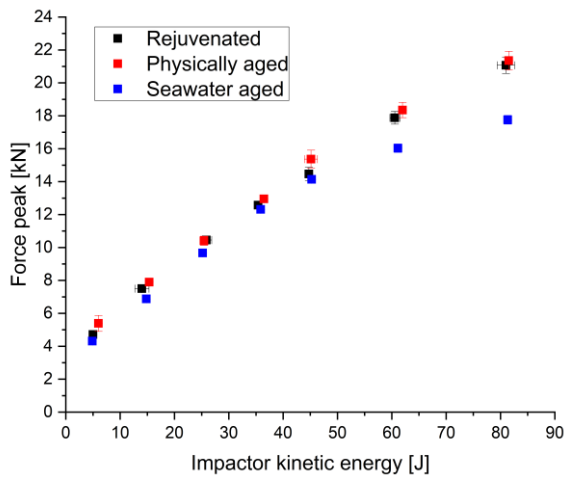


Figure 4.44 – Effect of the aging on the force peak change with the impact energy

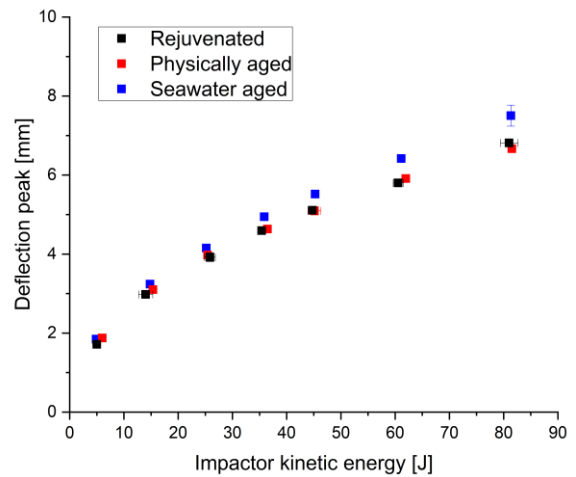


Figure 4.45 – Effect of the aging on the deflection change with the impact energy

4.6.2. Influence of aging on the delamination

Quasi-static mechanical tests on unaged and aged coupons have shown an effect of aging on properties that could affect both the damage initiation and propagation.

Figure 4.46 shows the C-scan results of physically aged coupons impacted at four energy levels. At 5J, no delamination is observed, while for higher energies, the delamination is observed. The shape is very similar

to those observed on the rejuvenated coupons, with an orientation in the 45° directions. C-scans for impact energies higher than 35J are presented Appendix 1.

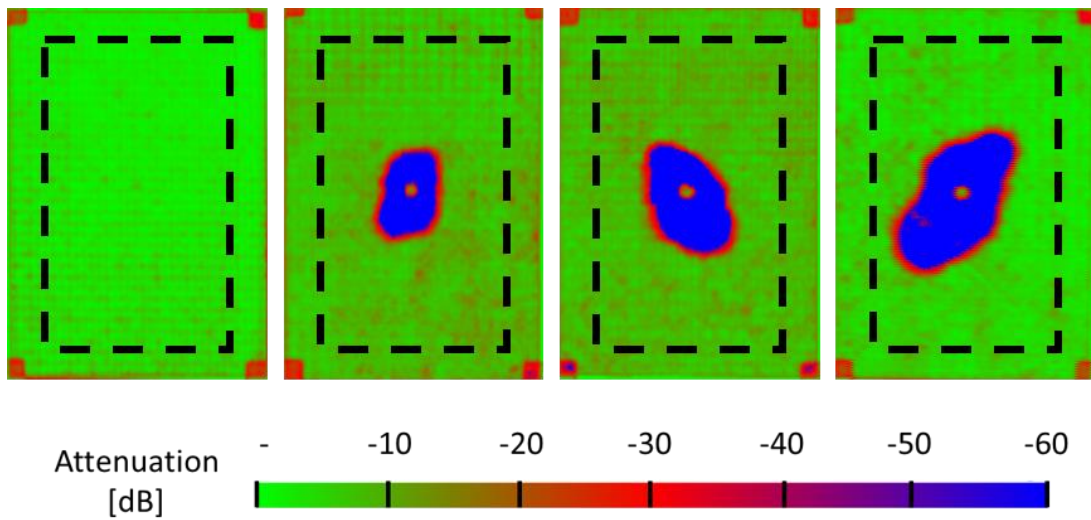


Figure 4.46 – C-scans results on impacted physically aged coupons (from left to right: 5J, 15J, 25J and 35J)

Figure 4.47 shows the C-scan results for seawater saturated coupons impacted at four energy levels. At 5J, a delamination is observed. The shape is different from those observed for rejuvenated and physically aged coupons. The undamaged point below the contact point is also larger. At 35J, a damage growth from the contact area in the width direction is noted. This may be due to the compression of UD external plies that leads to a buckling, and a delamination.

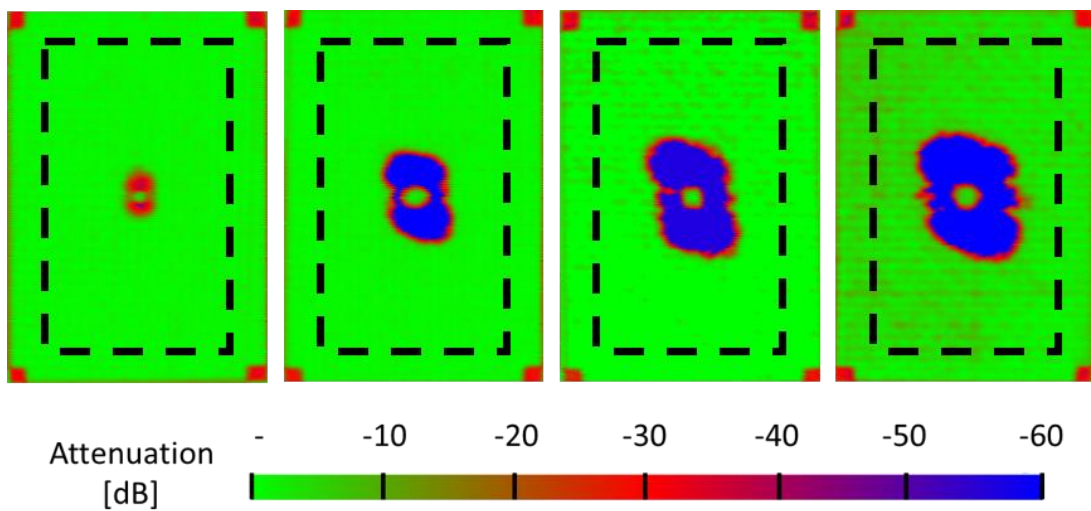


Figure 4.47 – C-scans results on impacted seawater saturated coupons (from left to right: 5J, 15J, 25J and 35J)

From the quasi-static results, it is expected that the seawater aging will reduce the interface strength and then shift the delamination initiation to a lower impact energy value. Visually, this shift is observed. At higher impact energy, the aging does not seem to affect the delamination even though the 45° orientation is less clear than for the unaged and physically aged states. In addition, after seawater aging, the small undamaged area below the contact point seems to be larger. One possible explanation is the matrix ductility, which could

lead to a smaller indentation. The area below the impactor is in pure compression, which prevents the interlaminar damage from propagating.

4.6.3. Effects of aging on the balance of energy

The effects of aging on the energy balance for impacts between 5J and 35J are shown from Figure 4.48 to Figure 4.51. At 5J, the impact energy, i.e. the peak, calculated from the force and deflection is not exactly the same for all conditions. For low impact energies, the drop height is supposed to be the same but a small difference compared to the low value measured will result in an increase of the gap between the curves. It must be noted that this gap is the same for higher impact energies.

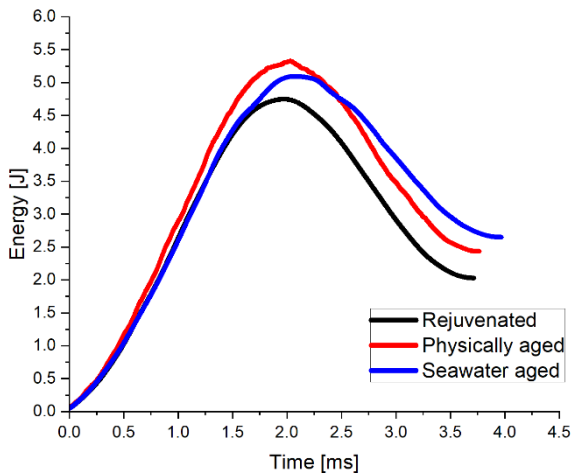


Figure 4.48 – Effects of aging on the energy balance for a 5J impact

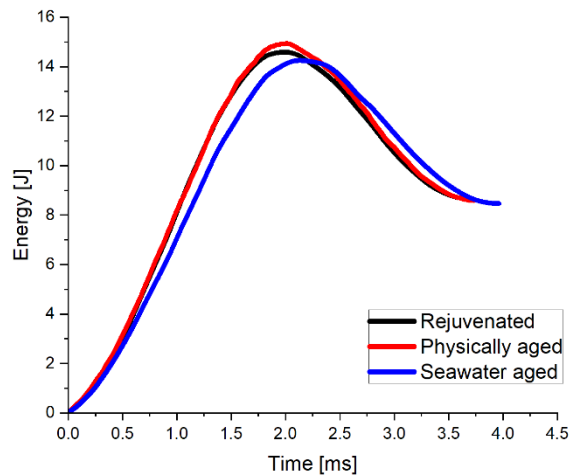


Figure 4.49 – Effects of aging on the energy balance for a 15J impact

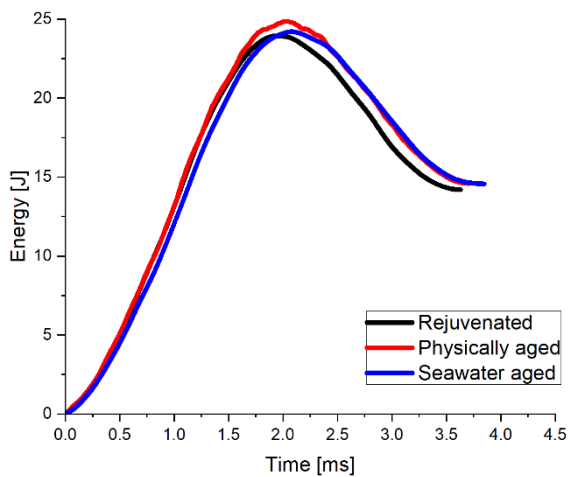


Figure 4.50 – Effects of aging on the energy balance for a 25J impact

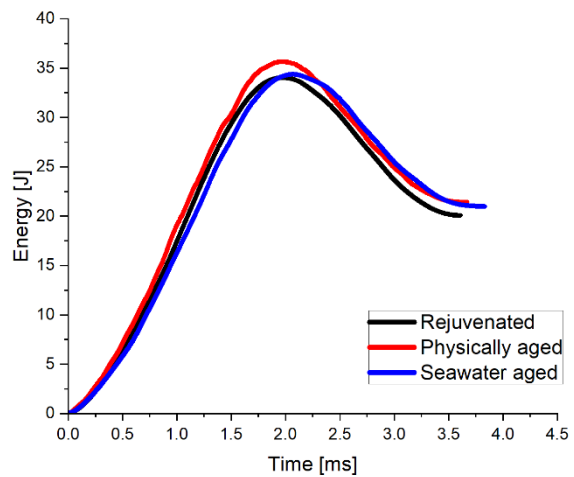


Figure 4.51 – Effects of aging on the energy balance for a 35J impact

At 15J, 25J and 35J, the slope is a bit lower for seawater aged coupons than for the other aging conditions. The coupon absorbs energy at a lower rate, which means the coupon submitted to an impact event is a bit less stiff after seawater aging. No change is observed between the unaged and the physically aged conditions. These observations make sense. In chapter 3, except in the fiber direction, every modulus was observed to decrease with the seawater aging, while a small increase was observed after physical aging.

In Chapter 3, the quasi-static characterization of the material for different aging conditions has shown that both elastic and ultimate properties are affected by the aging. However, the absorbed energy is not observed to increase more after seawater aging when the impact energy increases (Figure 4.52).

Even if the delamination threshold is obtained at a lower energy after seawater aging, the energy used to initiate then propagate the damage is low at 5J. At higher energy, the shape of the through thickness delamination is a bit larger after seawater aging, but as the difference is small, it is not explicit on the absorbed energy.

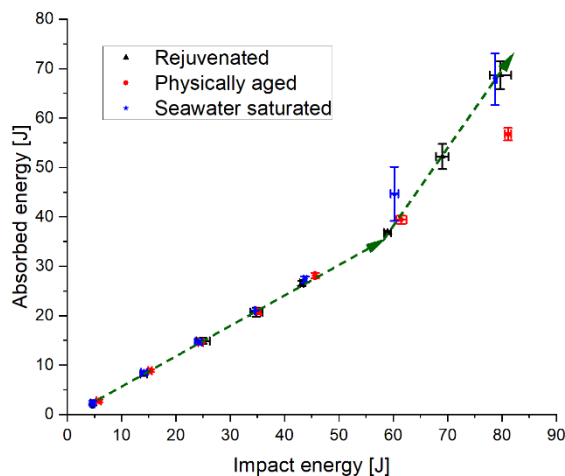


Figure 4.52 - Effect of aging on the absorbed energy for impact energy in the range 0-80J

4.6.4. Microscopic observations

Microscopic observations have been performed on sections of physically aged and seawater saturated coupons.

At 15J, both show a 0/0 delamination (Figure 4.53 and Figure 4.54). However, this delamination is less extensive in the physically aged than in the seawater saturated coupon where the damage seems also to be intralaminar. This delamination has also been observed in the unaged coupon, and is related to the weft UD fabric used.

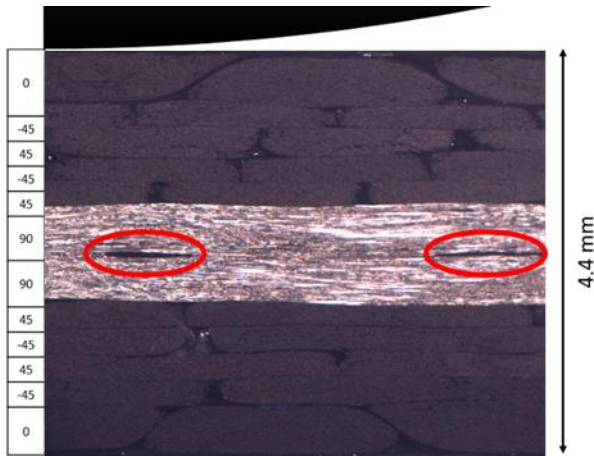


Figure 4.53 – 0/0 delamination for a physically aged coupon impacted at 15J

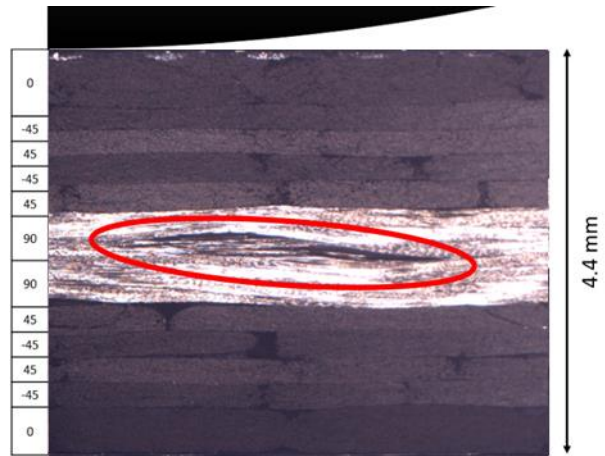


Figure 4.54 – 0/0 delamination for a seawater saturated coupon impacted at 15J

At these levels of energy, cracks have been found in the upper plies in the area of contact with the impactor. These cracks propagate in the carbon fiber strands of the ply in contact with the impactor.

4.6.5. Tomography on aged coupons

Tomography analyses have been performed on seawater saturated coupons impacted at 5J and 30J. Figure 4.55 shows images in the length and width directions, just below the contact area. On the upper photo, we can imagine a delamination at the 45/0 plane (between the red arrows). However, this delamination becomes very difficult to observe on the width direction.

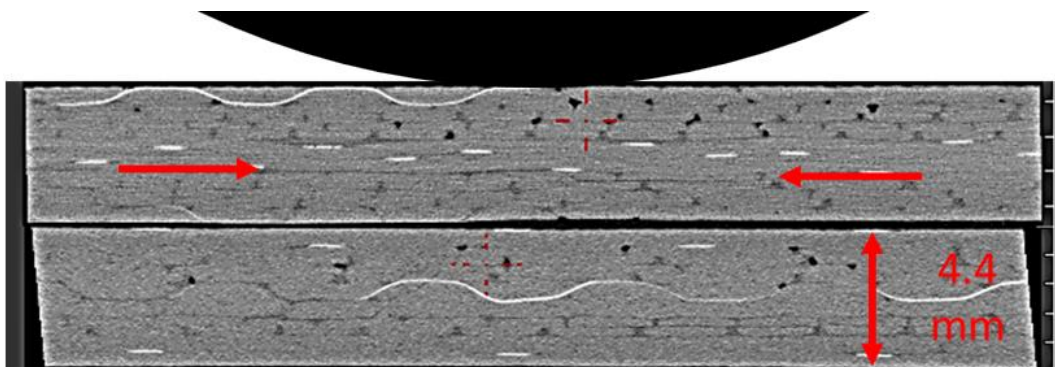


Figure 4.55 – Tomography on the length (top) and width (bottom) direction of a seawater saturated coupon impacted at 5J

At 30J, the delamination is easier to observe (Figure 4.56). The damage tree is visible on the width direction and length direction where the damage has propagated from a –45/45 interface to a 45/0 and then to a 0/0 interface. The contact with the impactor is symbolized by the white tablet on the upper face of each view. Below the contact point, no delamination is observed (bottom photo) which is in accordance with Figure 4.47. However, matrix cracking could be present but is impossible to observe at this scale due to the low resolution of the tomography scan.

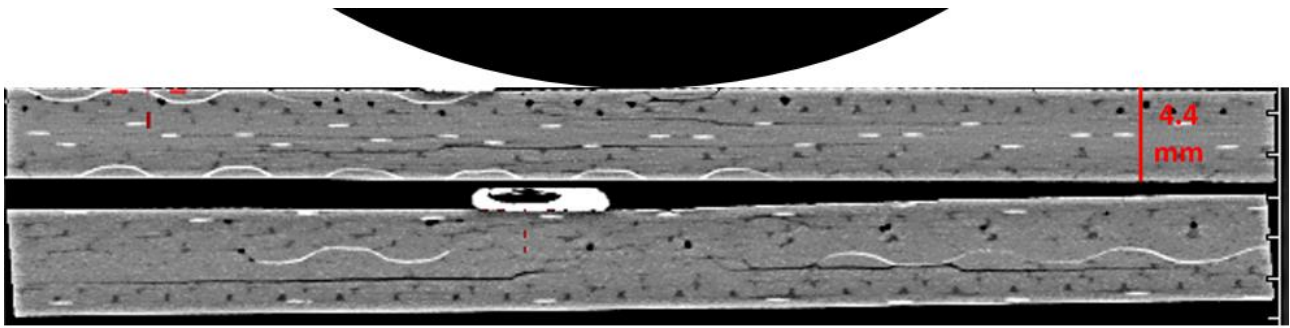


Figure 4.56 – Tomography on the length (top) and width (bottom) direction of a seawater saturated coupon impacted at 30J

The comparison with the tomography results on the unaged specimen shows that no bending stress cracks nor fiber breakage are apparent. Delaminations between $-45/45$ and $45/0$ interfaces have been characterized, as well as at $0/0$ interfaces in some cases. Improvements in the visualization could be obtained with higher resolution of tomography scans.

4.6.6. Simulation of the aging effects on the impact behavior

The experimental tests have been performed at 5J, 15J, 25J and 35J on unaged and aged coupons. This section reports the results of the comparison between these tests and the numerical simulation.

4.6.6.1. Dataset for aged materials

The complete dataset used to simulate the out-of-plane impact behavior of physically and seawater saturated aged coupons is summarized in Table 4.6. All the mechanical properties have been obtained experimentally, except the cohesive surface elasticity, the friction parameters and ply fracture toughness.

Table 4.6 – Mechanical properties used for the physically aged and seawater saturated state in the model

Property	Symbol	Physical aging	Seawater aging
Density	ρ	1.55E-3	
Friction metal/composite	$\xi_{M/C}$	0.1	
Young's moduli	E_1, E_2	127540, 9230	127540, 4390
Poisson's ratio	ν_{12}	0.320	0.341
Shear moduli	G_{12}, G_{13}, G_{23}	4070, 5170, 3020	2700, 3210, 2480
Ply strength	$X^T, X^C, Y^T, Y^C, S^T, S^C$	2140, 950, 36, 134, 69, 69	1760, 607, 17, 94, 54, 54
–	α	0	
Cohesive surface elasticity	K_{nn}, K_{ss}, K_{tt}	24600, 14200, 14200	
Interface strength	τ_n, τ_s, τ_t	80, 56, 56	43, 34, 34
BK model parameters	G_{IC}, G_{IIC}, η	0.60, 1.46, 1.67	0.50, 1.04, 0.58
Friction composite/composite	$\xi_{C/C}$	0.05	
Energy dissipated for ply failure	$G_{ft}, G_{fc}, G_{mt}, G_{mc}$	80, 80, 0.60, 1.46	80, 80, 0.50, 1.04

4.6.6.2. Prediction of the force vs. out-of-plane displacement curves

The prediction of the force-deflection curves is compared respectively for the physically aged and seawater saturated coupons Figure 4.57 and Figure 4.58, for impacts at 5J, 15J, 25J and 35J. As found for the simulations on the unaged state, the initial stiffness is not well predicted. The cause could come from the deflection measure which is performed after a delay compared to the force measure. It remains the model gives consistent results compared to the experiments, even if this simplified model is not as accurate as published approaches that use volume elements [168][258].

The meshing techniques give close results until a delamination is initiated. For the physically aged coupons, the loading part gives same results except the force peak that is higher for the standard mesh. In all cases, the model overpredicts the force. As the model is not able to predict the out-of-plane damage, the ply stiffness remains almost constant, then the force peak is overpredicted. The irreversible out-of-plane displacement once the impactor has left the coupon surface is underpredicted. As the out-of-plane displacement measure is performed on the area where the stitching is released, a change of the surface topology can lead to a measurement error.

At 35J for the seawater saturated coupon, both meshes predict an early failure. The matrix damage is extensive and reaches the boundary conditions. A drop of the force predicted is observed.

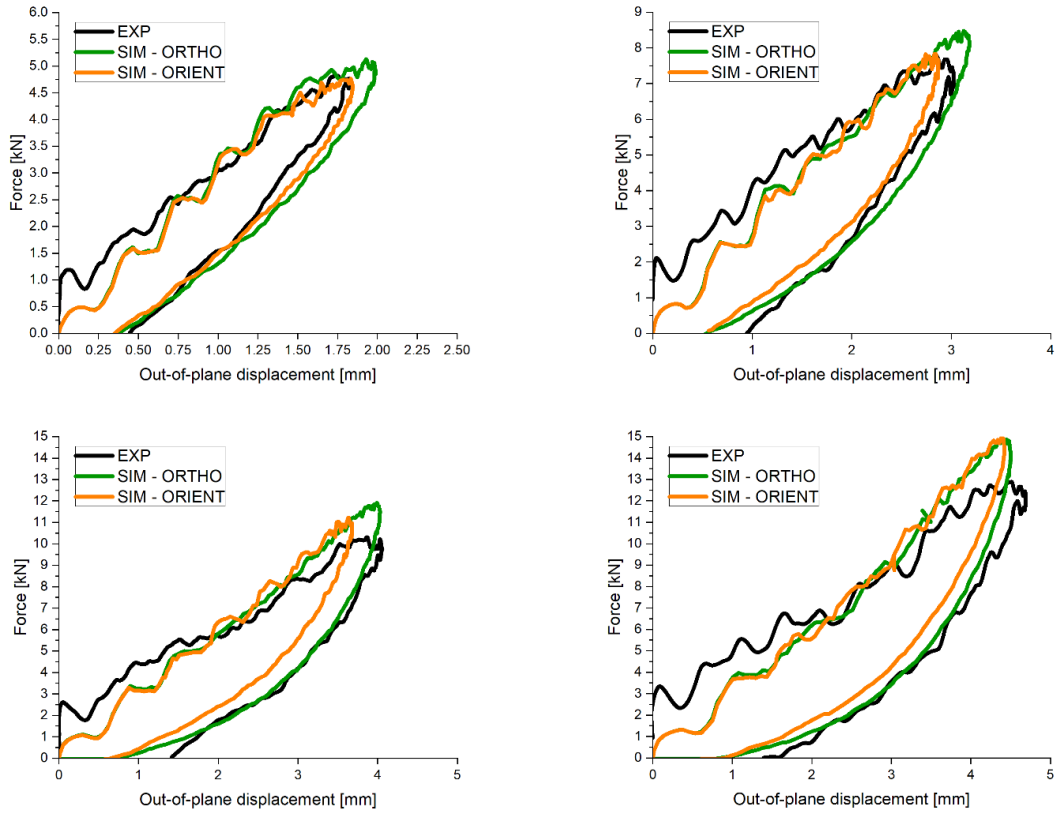


Figure 4.57 – Comparison of the force vs. deflection curves between the experiment and the simulation for physically aged coupons impacted at 5J (top left), 15J (top right), 25J (bottom left) and 35J (bottom right)

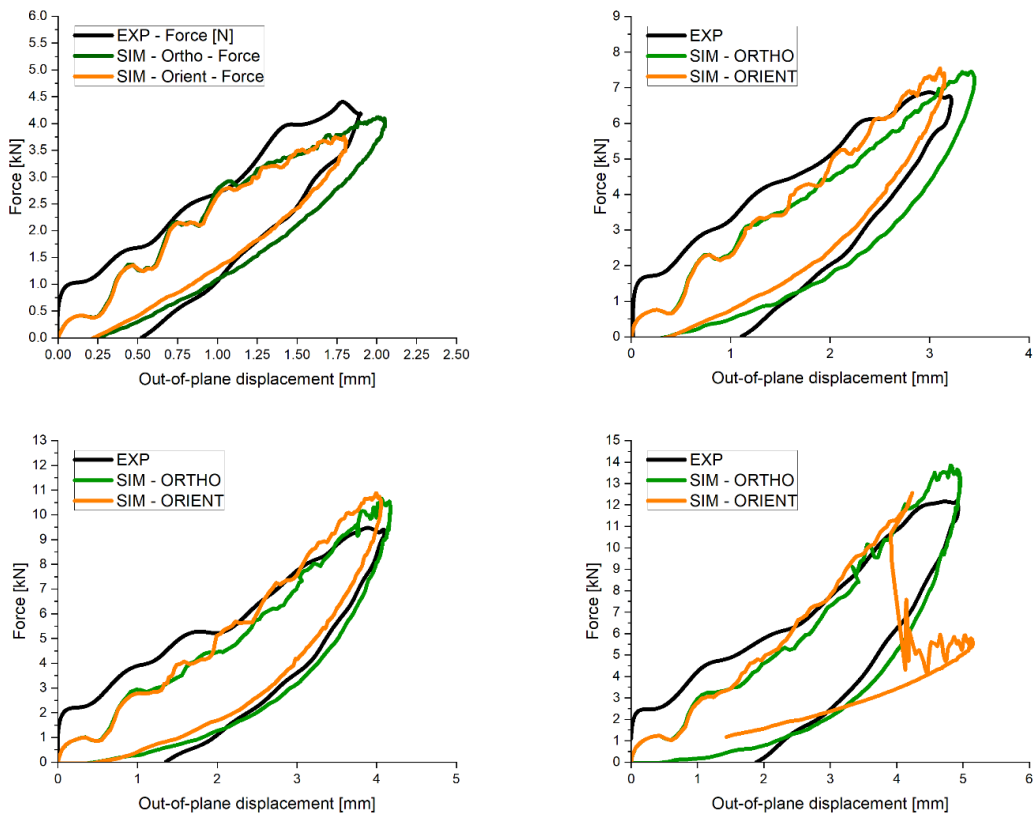


Figure 4.58 – Comparison of the force vs. deflection curves between the experiment and the simulation for seawater aged coupons impacted at 5J (top left), 15J (top right), 25J (bottom left) and 35J (bottom right)

When comparing the experimental data and the simulation results, the simple model used to predict the force and out-of-plane displacement study is also validated for the physically aged and seawater saturated materials up to 35J. While the oriented mesh was promising, the comparison between the experiment and the model shows often a load drop due to the delamination extent, and at high energy levels, a global failure which is not seen experimentally. This is mainly due to the type of elements, that does not consider out of plane damage. The energy consumed by the out of plane damage is then transferred to other damage mechanisms such as the delamination which becomes larger.

4.6.6.3. Prediction of the energy balance

The energy balance predicted by the simulation for both mesh types has been compared with the experiments for coupons aged then impacted. Results are presented for physically aged and seawater aged coupons respectively in Figure 4.59 and Figure 4.60.

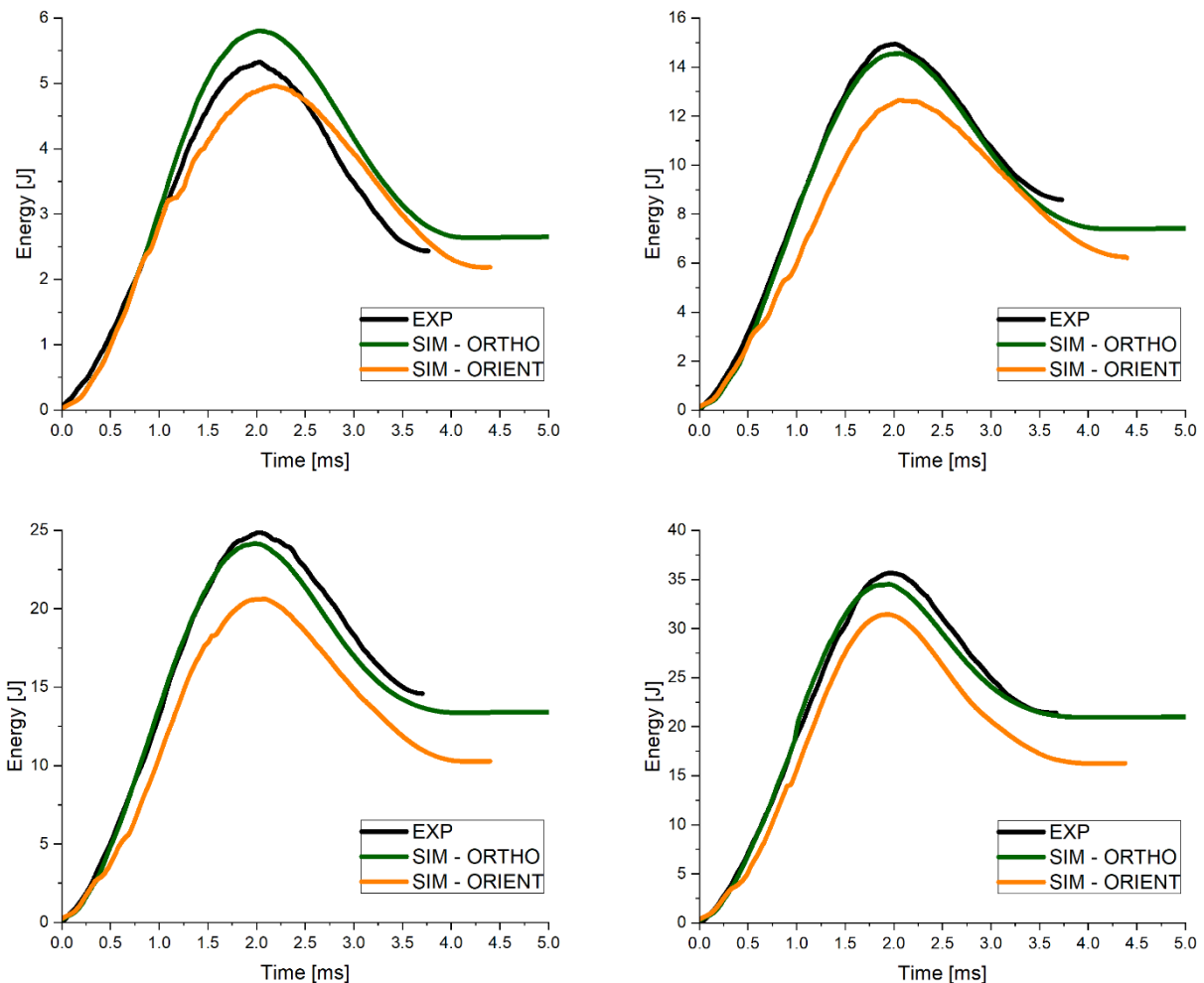


Figure 4.59 – Comparison of the energy balance between the experiment and the simulation for physically aged coupons impacted at 5J (top left), 15J (top right), 25J (bottom left) and 35J (bottom right)

For physically aged coupons, the prediction is better for the standard mesh. The absorbed energy is predicted well in the range of these energy levels. The oriented mesh predicts an early failure around 3kN. This is the point where the matrix damage is initiated then propagates abruptly to the width direction of the coupon.

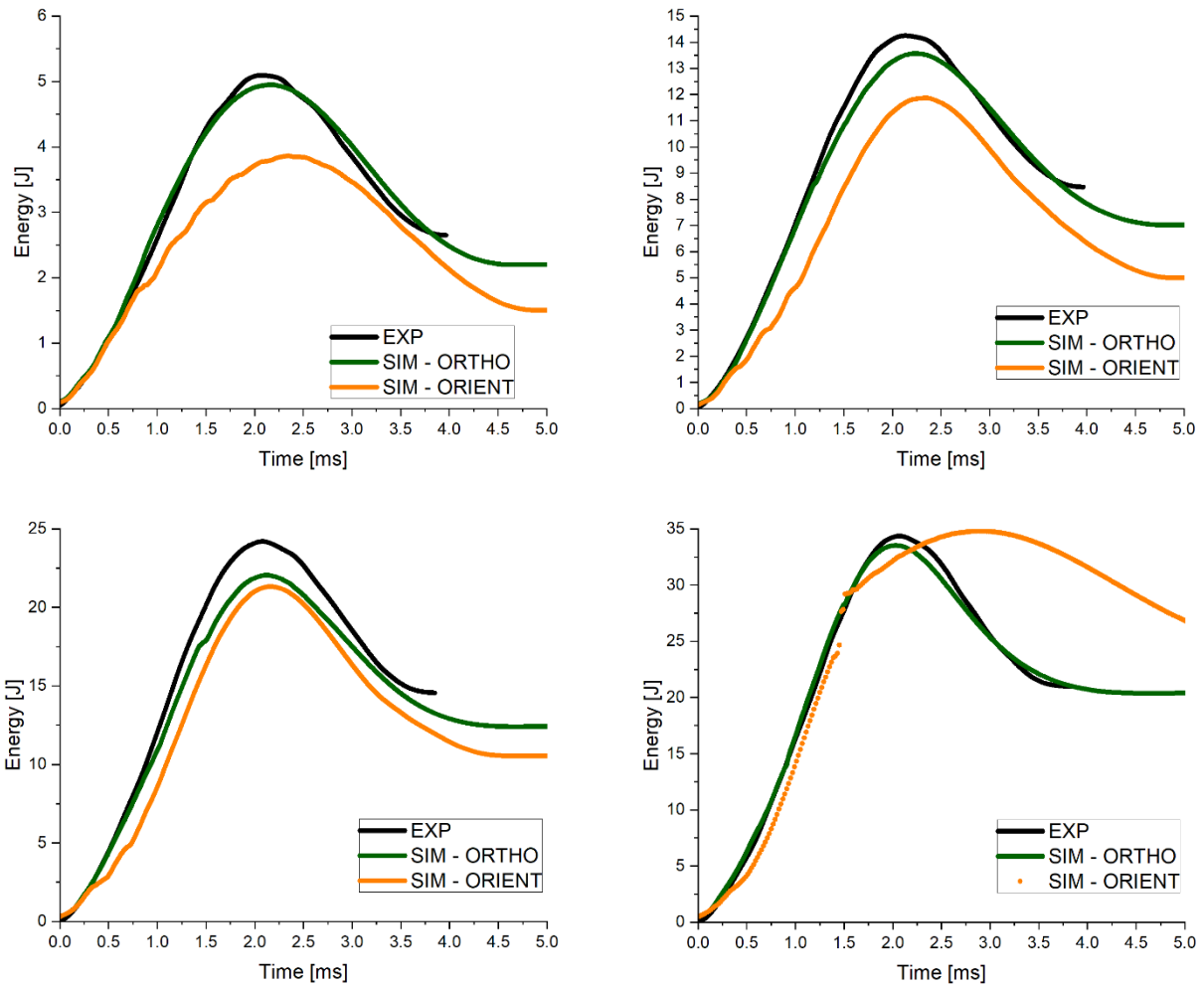


Figure 4.60 – Comparison of the energy balance between the experiment and the simulation for seawater aged coupons impacted at 5J (top left), 15J (top right), 25J (bottom left) and 35J (bottom right)

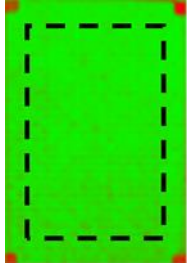
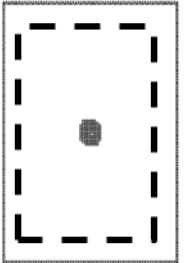
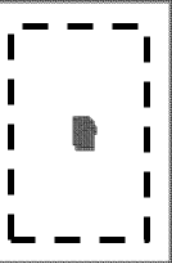
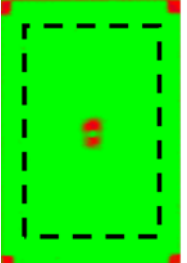
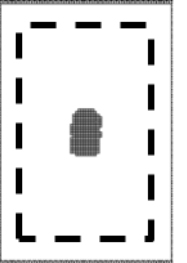
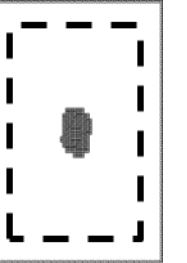
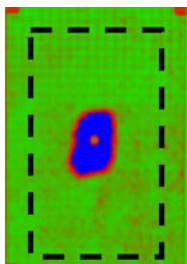
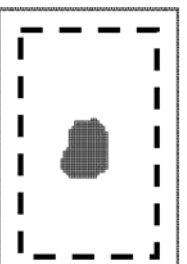
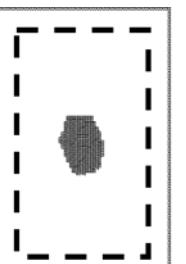
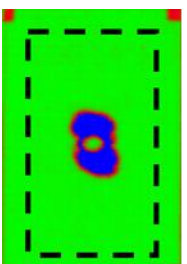
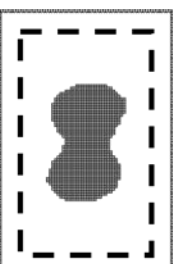
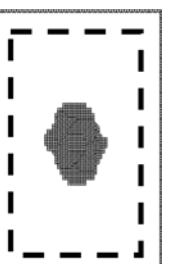
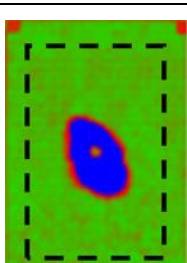
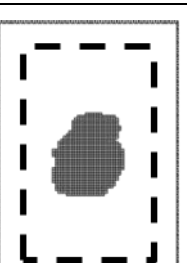
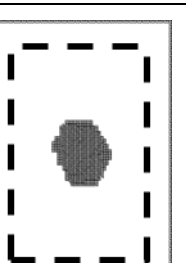
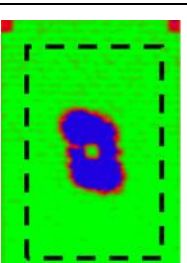
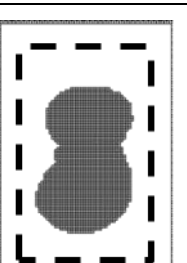
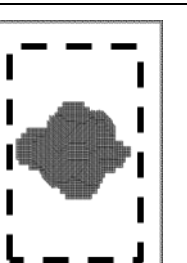
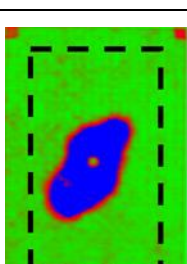
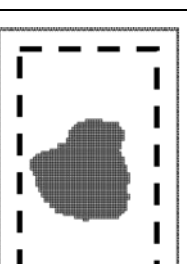
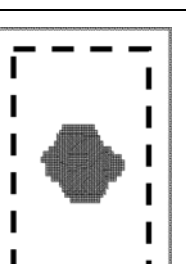
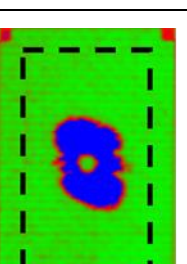
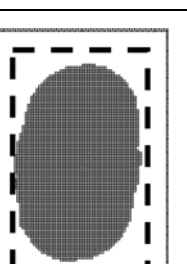
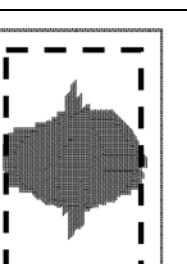
The absorbed energy is also much higher for the oriented mesh. At 35J on the seawater aged coupon, the oriented mesh predicts a drop of the out-of-plane displacement that leads to a discontinuity of the energy balance.

4.6.6.4. Prediction of the delamination

A comparison of the experimental and predicted delamination is presented Table 4.7. Both mesh predicts a delamination at 5J, while only the seawater saturated coupons is experimentally delaminated. At 15J, the shape and the delaminated surface are in accordance with the experiment,

Both mesh techniques predict a good delamination shape for the physically aged coupon, while for the seawater saturated coupon, the standard mesh over-predicts the delaminated area. Neither of these meshes predict the undamaged region below the contact point.

Table 4.7 - Comparison between the experimental and predicted delamination (standard and oriented meshes) for aged coupons impacted from 5J to 35J

	Physically aged			Seawater saturated		
5J						
15J						
25J						
35J						

For an impact energy of 35J, the shape prediction seems reasonable even though the model does not capture the overall orientation at -45° of the delamination. For the seawater saturated coupon, at this level of energy, the standard mesh over-predicts the delaminated area, and the oriented mesh predicts in-plane matrix damage.

4.6.7. Conclusion on aged impacts

Impacts on physically aged and seawater saturated coupons have been performed up to 80J. Only the experimental results for impacts up to 35J have been presented because for higher impact energies, the delamination is limited by the boundary conditions, and is thus difficult to simulate. C-scans and tomography

have shown delamination at the same interfaces as for the unaged coupons. The model developed with Abaqus™ is consistent with the experimental data, even if when the impact energy is increased, the predicted force peak is higher than the experiment. The forces and deflections predicted by the model based on continuum shell elements show a reasonably good correlation.

4.7. Conclusion

To conclude, investigations have been performed into the effects of aging on the out-of-plane impact behavior of unaged and aged C/Epoxy coupons studied for a naval application. Compared to materials used in the aerospace industry, this material has been found to show higher porosity, and the role of the stitching in the damage propagation requires further study. In the unaged and physically aged states, a delamination threshold between 5J and 15J was found, while for the seawater saturated state, the damage threshold is below 5J. This is in accordance with interface strength results in Chapter 3. The contact time for seawater saturated coupons was higher than for unaged and physically aged coupons, indicating either a stiffness decrease due to aging or an out-of-plane damage. A numerical model has been developed with the Abaqus™ commercial code. Two meshing techniques have been tested: standard orthotropic and oriented. While results are reasonable for both, premature failure has been predicted with the oriented mesh for an impact at 35J. Given the additional time needed to set up the oriented model, it is recommended to follow a standard approach for meshing these quasi-isotropic flat composite coupons. A parametric study has been performed and showed that the cohesive surface stiffnesses have a strong influence on the prediction of the delamination. Different values have been tested, and the higher the stiffness, the lower the delamination and the longer the computation time. With respect to the stiffness prediction, the friction coefficient between the metallic parts and the composite affects the stiffness and the value chosen was optimized to improve the results. Improvements of the model are possible. First, the use of volume elements with an implementation of the out-of-plane damage could improve both the prediction of contact time and the force peak. For a given impact energy, experimental out-of-plane damage occurs. The predicted delamination area could then be less with other elements than with the continuum shells, and volume elements will probably be better suited for thick plies such as those studied here. Another improvement is the use of cohesive elements to replace the cohesive surfaces. It has been shown that cohesive elements are more accurate than cohesive surfaces but the computation time is also increased, and limiting this was a priority for this study. At a certain scale, this model is consistent with the experiment. Meshing a real propeller blade with continuum shells could represent a compromise between a high-fidelity model with volume elements and a lower fidelity element but with a reduced computation time. Impacts on marine propellers are not limited to flat composite parts. Chapter 5 will introduce an experimental approach with different geometries to try to understand the impact behavior of more representative propeller parts.

Chapter 5

–

*Towards more
representative tests for
composite propellers*

Chapter 5 – Towards more representative tests for composite propellers

5.1. INTRODUCTION.....	172
5.2. INFLUENCE OF AGING ON THE CAI STRENGTH.....	172
5.2.1. CAI PROCEDURE.....	173
5.2.2. CAI RESULTS.....	173
5.2.3. COMPARISON WITH UNDAMAGED MATERIAL STRENGTH	177
5.2.4. DISCUSSION ON CAI RESULTS.....	179
5.3. INFLUENCE OF CURVATURE ON THE OUT-OF-PLANE IMPACT BEHAVIOR	179
5.3.1. PRESENTATION OF THE TEST	180
5.3.2. EXPERIMENTAL RESULTS.....	181
5.3.3. MICROSCOPY OBSERVATIONS	184
5.3.4. CONCLUSION ON THESE PRELIMINARY TESTS.....	186
5.4. IN-PLANE IMPACT: FROM ELEMENT LEVEL TO COMPONENT LEVEL	186
5.4.1. EDGE IMPACT AT ELEMENT LEVEL	186
5.4.2. IN-PLANE IMPACT AT COMPONENT LEVEL.....	190
5.5. CONCLUSION	194

5.1. Introduction

In the previous chapters the influence of seawater aging on impact behavior has been examined for a particular idealized impact configuration. However, impacts on a real marine composite propeller could be more severe than indicated by the out-of-plane flat plate impact tests performed and summarized in Chapter 4. During this thesis work, several additional tests have been developed and performed to investigate these effects, and this chapter will describe these complementary tests. Given the time available it was not possible to explore all these avenues in as much detail as those in the previous chapter, and in particular numerical modelling was not developed in parallel. Nevertheless, a description of the work done is important as it provides a basis for future studies.

A propeller blade section is presented in Figure 5.1. Different regions are visible and each can be subjected to impact events. Region (1) represents a planar section. The impact study of this section has already been studied in Chapter 4, but the residual strength will be investigated in this chapter. The section (2), the trailing edge, is curved and will be studied in the third part of this chapter. Three curvatures were studied at three energy levels. Finally, region (3) represents the most probable area for an impact, the leading edge. For this test, the impact is in-plane, which is probably the most severe for a marine propeller blade. A coupon similar to a real leading-edge section has been designed and manufactured and a preliminary study was carried out.

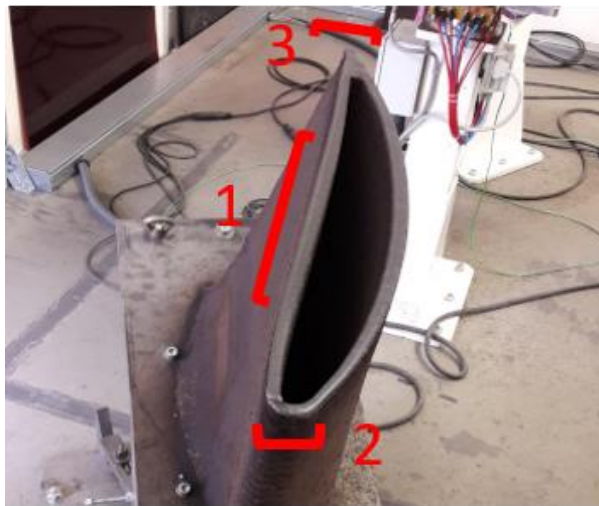


Figure 5.1 – Propeller blade section, from the RAMSSES project (@Naval Group)

5.2. Influence of aging on the CAI strength

The compression after impact test (ASTM D7137) has been developed to characterize the residual strength of a composite coupon impacted and damaged (ASTM D7136). For this study, coupons have been impacted at 5J, 15J, 25J, 35J, 45J, 60J and 80J. The results in Chapter 4 have shown that the interlaminar damage was limited by the boundary conditions for impact energies higher than 35J. The CAI method provides a structural

strength which can be compared with a reference undamaged material compression strength experimentally characterized with the standard ASTM D6641. It is widely used in the aircraft industry, much less for marine applications.

5.2.1. CAI procedure

The ASTM D7137 standard recommends bonding four strain gages on the upper part of the composite coupon to check if buckling occurs. In the present work we have preferred a stereo digital image correlation system, which is able to measure the out-of-plane displacement of the coupon during the test. This technique can also verify the uniformity of the loading. Three coupons per impact energy have been tested.

5.2.2. CAI results

Figure 5.2 shows an example of the Force vs. Displacement plots for seawater saturated coupons impacted at 7 levels of energy. When the impact energy is high, extensive damage is present, which leads to a decrease of the post impact strength. For the stiffness, except after the highest energy impact where the delamination reached the coupon borders, no significant change is observed.

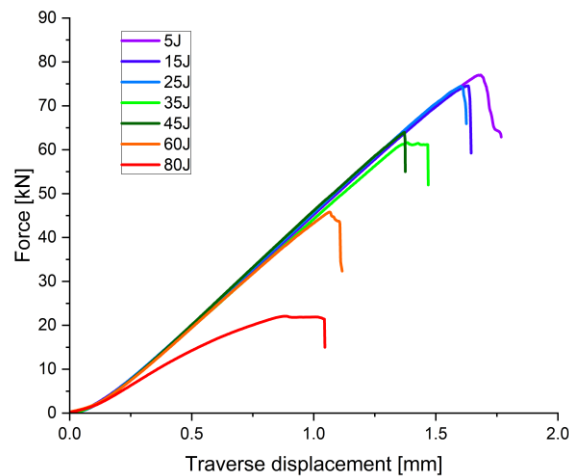


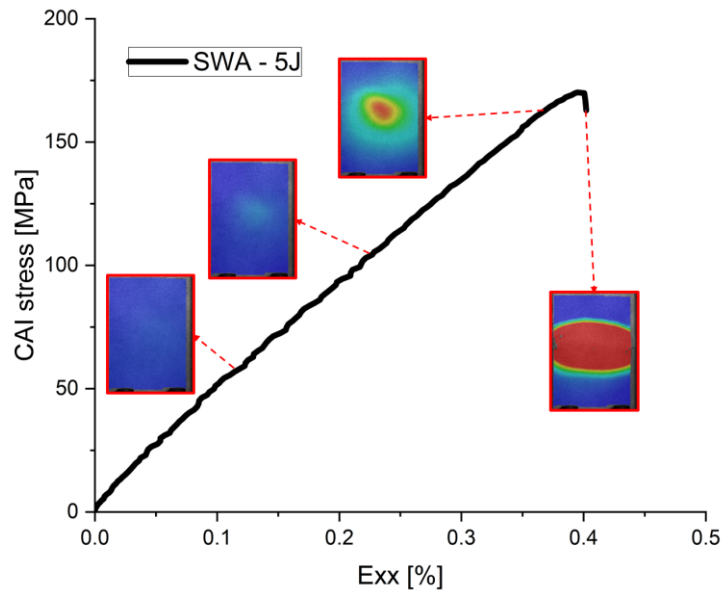
Figure 5.2 – CAI Force vs. Displacement for seawater saturated coupons

The DIC system allowed an elastic modulus to be determined from low stress and strain data. Initial stiffness values have been determined for all tests, and the aging had no influence on them, with an average value around 44 GPa for all aged coupons (Table 5.1). This was expected because in a quasi-isotropic lay-up, the stiffness is given by the contribution of all plies, and the elastic modulus of the 0° plies, the stiffest in the layup, is not influenced by the aging.

Table 5.1 – Elastic compression modulus after impact, influence of seawater aging versus reference

Impact energy [J]	Rejuvenated [GPa]	Seawater saturated [GPa]
5	45.0 ± 1.1	43.5 ± 0.8
15	45.3 ± 1.0	42.5 ± 1.2
25	46.1 ± 2.0	45.7 ± 0.7
35	45.7 ± 1.4	41.9 ± 1.0

Figure 5.3 shows the CAI Stress vs. Axial strain for a seawater saturated coupon impacted at 5J. The DIC images show the out-of-plane displacement of the coupon. At the beginning of the test, no deflection is observed, but when the stress increases, the deflection becomes high in the area where the impactor damaged the coupon. Finally, the damage propagates to the coupon borders, which is also seen in Figure 5.4 below.

**Figure 5.3 – CAI stress vs. axial strains for a CAI test of a seawater saturated coupon impacted at 5J**

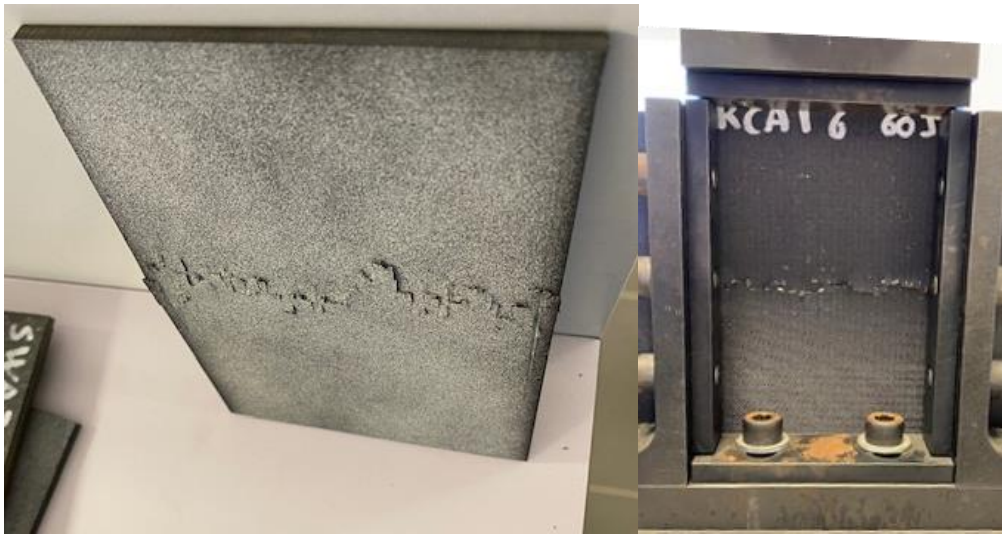


Figure 5.4 – Images of a failure due to a fiber yarn micro buckling for an unaged (left) and seawater saturated (right) coupons impacted at 60J

The CAI residual strength vs. impact energy is shown in Figure 5.5. The seawater saturated coupons have a significantly reduced strength compared to the unaged and physically aged coupons. Two slopes are visible. A first up to 35J, where the delamination is local and has not reached the impact fixture limits. Then a second, steeper drop, where the delamination has reached the impact fixture limits, and probably where the impact has created other damage due to edge effects.

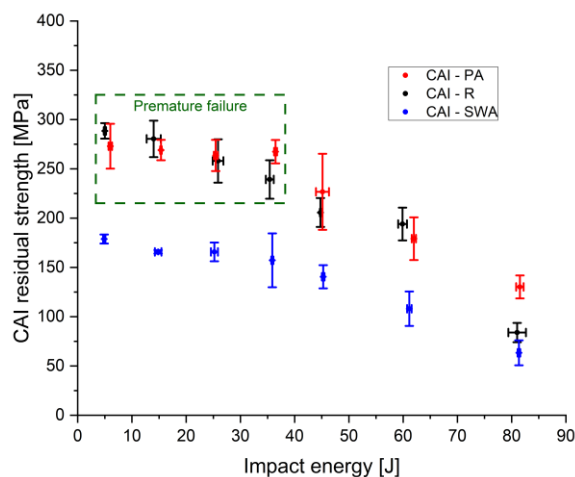


Figure 5.5 – CAI residual strength for impacts from 5J to 80J for 3 aging conditions

A coupon edge of a seawater saturated coupon impacted at 75J is shown in Figure 5.6. This section is far from the impact point, but extensive damage is visible. Multiple delaminations are observed, together with intralaminar fractures. The boundary condition is complex at this location because the delamination from the center of the coupon is stopped by the fixture edge while the impactor continues to indent the coupon. The energy release is then brutal. This type of damage has only been observed on coupons where the delamination has interacted with the edge of the fixture.

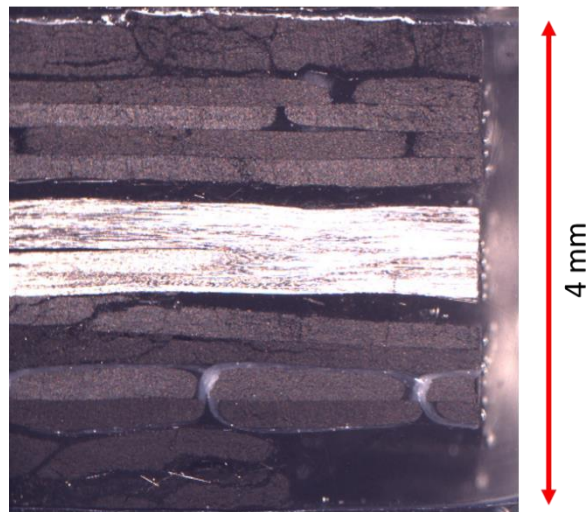


Figure 5.6 – Seawater saturated coupon impacted at 75J (side of the coupon far from the impact point)

In terms of failure, two modes have been observed. First, as shown in Figure 5.4, a failure in the middle of the coupon. This is due to the local micro buckling of fiber yarns and is initiated by the stitching. This is important, whitening of the stitching that maintains the carbon fibers during the manufacturing process is noted and local flexure of these PET stitching fibers leads to an early failure. This is highlighted in Figure 5.7.

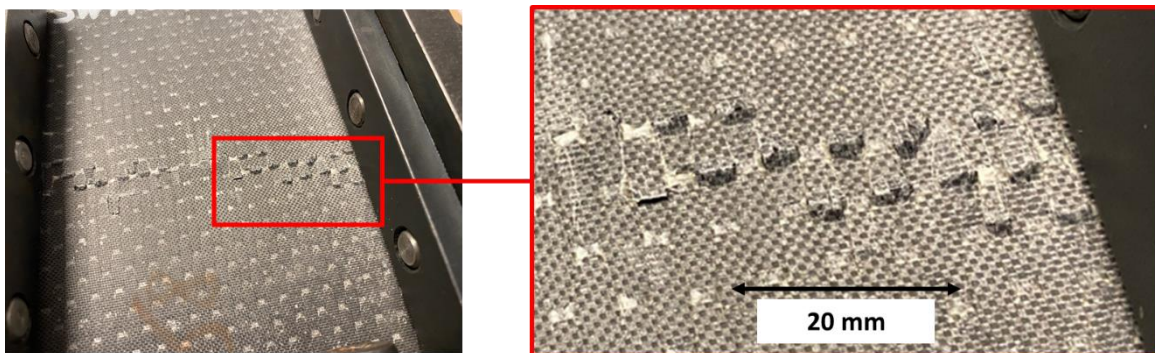


Figure 5.7 – Micro buckling due to transverse stitching

The influence of stitching has been noted in several previous studies [259][260]. An influence was also observed in Chapter 3 for uniaxial compression tests on $[0]_4$ coupons, where the seawater aging reduced the strength by 35% in comparison with the unaged and physically aged coupons. The other failure mode observed during these tests on coupons with low impact damage was a local crushing damage close to the compression platens. As the material is brittle, the friction and maybe a small defect of parallelism can cause an early failure. Such a defect could be caused by the water jet divergence at the nozzle outlet during coupon preparation. In order to avoid these defects trials were made with a conventional machining machine, but this worsened the effect because of cracks that were generated by the milling cutter. Tests where an early failure was observed are indicated in Figure 5.5.

In the literature, a study on a woven aramid–glass fibre/epoxy composite found a decrease of the CAI strength of 42% at 32J after humid aging [206]. This can be compared with another study [261] where the authors sealed together E–Glass reinforced vinyl–ester specimens to manufacture a tank that they filled with

artificial seawater to perform a monofacial aging. They found a loss of 10% of the CAI strength. Another previous study was performed on a woven carbon/vinylester [210]. The author measured a loss of the CAI strength of around 20% between an unaged and seawater aged specimen, and the effect of increasing seawater aging temperature was also reported to result in larger strength loss.

It should be noted that there is a strong influence of stacking sequence on impact damage tolerance. The layup used in the present study with external plies oriented at 0° cannot prevent microbuckling from occurring. The results would have been different if the layup proposed by the standard, with a 45° or -45° external ply, had been tested. The strain at failure would have been higher, with probably a higher strength due to the containment of the microbuckling. The lay-up in our study was based on the funder's requirements, and fabrics were chosen based on previous work in the laboratory [170] to complete the investigations into the effects of aging on mechanical property changes.

5.2.3. Comparison with undamaged material strength

The validation of CAI results is performed by checking if structural buckling occurs, and if the failure is not caused by a load concentration around the boundary conditions. Compression tests at the coupon scale have been performed following the ASTM D6641 standard. The aim of these tests was to determine if for low impact energies, the structural strength (coupon almost undamaged) reaches the 'intrinsic' material strength, as this can validate the CAI tests. For all these coupon tests, the failure was caused by the external ply failure. The microbuckling of external UD plies is shown in Figure 5.8.

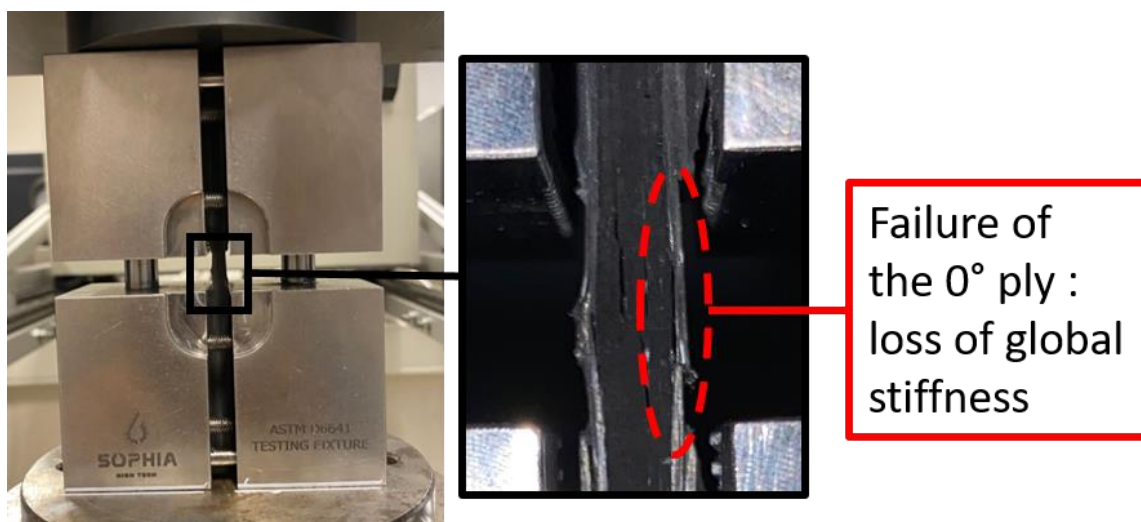


Figure 5.8 – Failure of the quasi-isotropic coupon due to the external ply failure

In terms of ultimate properties, the unaged and physically aged materials have the same strength, while the seawater aged strength is reduced by 50% (Table 5.2).

Table 5.2 – Change of the compression material strength with the aging (ASTM 6641)

	Rejuvenated	Physically aged	Seawater aged
ASTM D6641 strength	373 ± 34	374 ± 42	184 ± 14

A comparison is proposed in Figure 5.9. The unaged and physically aged materials exhibit the same behavior. However, at low impact energy, the CAI strength does not reach the same value as that found on undamaged coupons using the ASTM 6641 fixture. This is due to the premature failure mode during the CAI test, where damage initiates due to stress concentrations around the compression platens when no or little damage is present in the center of the specimen (Figure 5.10). For these aging conditions, the CAI test does not therefore provide a valid result at low impact energy. For the seawater saturated coupons, at low impact energy, the CAI strength reaches the material strength. The failure modes are the same for these tests, which indicates that for seawater aging the CAI test is valid.

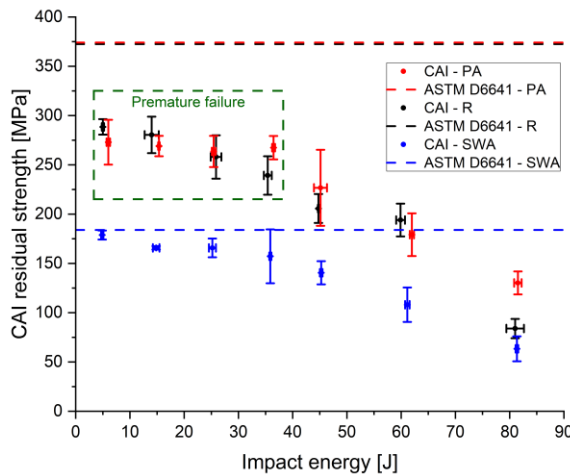


Figure 5.9 – Comparison between the material and the structural strength for all aging

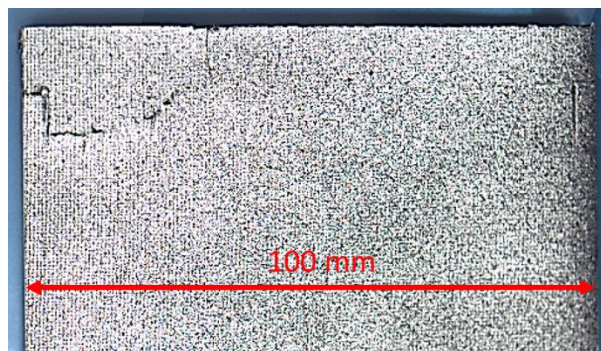


Figure 5.10 – Premature failure of a rejuvenated coupon impacted at 5J (top left corner)

5.2.4. Discussion of CAI results

Even though the CAI tests provided interesting results, the gap between the CAI strength at low impact energy and the material strength for the unaged and physically aged states is a problem for design. The impact standard ASTM D7136 proposes a smaller impactor radius, 16mm instead of the 50mm radius for this present study, which undoubtedly tends to concentrate the damage in a smaller composite volume. When the energy is too high, fibers begin to break which has severe consequences. A reduction of the post-impact strength is observed because the coupon is locally less stiff. In the present study, no fiber breakage has been experimentally observed nor numerically predicted (see Chapter 4). Delamination was the main damage mechanism. For the unaged and physically aged states, the delamination was not sufficient to initiate the structural failure, which happened locally close to the contact area between the coupon edges and the compression platens.

For the seawater saturated state, the test appears to be valid because even at low impact energy, the CAI strength reaches the material strength. Then, the CAI strength is decreased when the impact energy is increased. In addition to the delamination, impact tests on seawater saturated coupons have probably generated matrix cracking in the material. This damage coupled with the delamination characterized in Chapter 4 leads to a global failure. Numerical simulation of this test has not been performed here, but examples in the literature show good agreement with the experiments, whether with volumic or shell elements [262].

5.3. Influence of curvature on the out-of-plane impact behavior

All the work described previously was performed on flat samples, both the identification tests and the impacts. However, given the complex shape of a propeller the relevance of such tests can be questioned. For this reason, some preliminary work was initiated to investigate the influence of specimen curvature. This work was inspired by a published study [142]. In that work, the authors have performed impacts on GFRP curved panels, at energies from 5 to 30J, with curvature radii between 75mm and 125mm. These dimensions are standard in the piping industry, and there is a rich literature on impact of glass reinforced composite tubes [153][263][264]. These authors have looked at residual tube strength under internal and external pressure, and manufacture of tubes of different diameters would have been one way to examine the influence of curvature. However, that approach introduces a major difficulty which is the influence of the manufacturing process. The composite propellers are produced by infusion and tube-making processes such as filament winding will not produce a representative composite (fiber content, porosities, internal stresses...). There are alternative ways to produce both curved sections and propellers, such as automated tape laying, and these are being studied in a parallel thesis at UNSW [265][266], but at present infusion molding is the preferred manufacturing route for propellers.

In this study, tests have been performed on curved panels manufactured by infusion around half-pipes with diameters of 30mm, 50mm, and 70mm. In order to fix the specimens to the impact support frame our first approach was to integrate a flat flange (Figure 5.11). This avoided having to manufacture a specific fixture for each curvature, and this required some work as this inverse curvature is very sensitive to defects. However, high speed camera images during preliminary tests showed that the contact area between the flange and the fixture is not constant which was a problem for this study because the friction changes during the test.

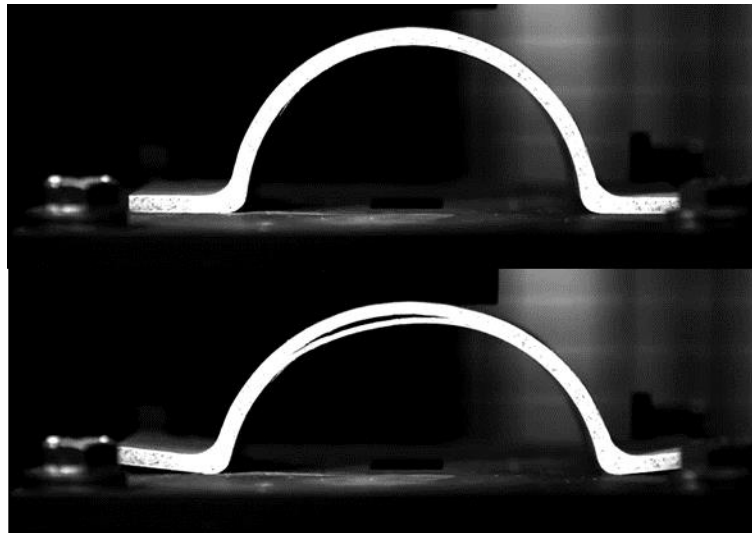


Figure 5.11 – Curved coupon with flat flange taken by a high-speed camera (top: before the impact / bottom: during the impact with delamination)

A second version of this test has been designed with only the curved part of the specimen, without the flat flange. This requires a specific fixture per curvature studied. The coupons and the fixture used for the impact on the $\phi 70$ mm curved panel have been presented previously (Figure 2.22).

5.3.1. Presentation of the test

Four fixtures have been manufactured to maintain the different coupons. The coupons are simply supported by the fixture. A window allows the coupon to deflect during the impact. Impacts are monitored: the impact force and the out-of-plane deflection are measured. Then, a C-Scan was performed after impact to determine if the delamination threshold had been reached and if the coupon was delaminated. Table 5.3 shows the tests performed. One coupon per condition was tested on unaged samples.

Table 5.3 – Experimental impact tests on curved panels performed

	7J	12J	17J	Preliminary
Φ30mm	X	X	X	
Φ50mm	X	X	X	
Φ70mm	X	X	X	
Φ90mm				X

5.3.2. Experimental results

5.3.2.1. Analysis of force and deflection data

The force signals were found to be more irregular than those recorded on flat plates (Figure 5.13). This may be due to the vibrations that occur during the impact. In addition, the delamination between plies and the residual stress released during the test can lead to a sudden loss of stiffness. In [142], the authors found the same type of curves but on GFRP curved laminates. In their case the first load drop happened at the force peak, and they concluded that once the delamination is initiated, it leads to a sudden stiffness loss. In our case, the first force drop does not occur at the force peak. The most probable reason is the smaller curvature tested here and the stiffer reinforcement. Once the delamination threshold has been reached, the force drops. But then, as the impactor continues to deflect the coupon, the structural stiffness takes over until another delamination.

The out-of-plane displacement has been measured and seems continuous. A residual deflection is measured, around 0.25mm for the test at 15J. On the back face, just below the contact area, the stitching has been torn off by the impact (Figure 5.12). A similar observation was made in Chapter 4, and the explanation was that before the impact, yarns of the external plies are wavy due to the stitching, and when the impact occurs, carbon fibers are straightened, which locally tears off the stitching (the white points in Figure 5.12).

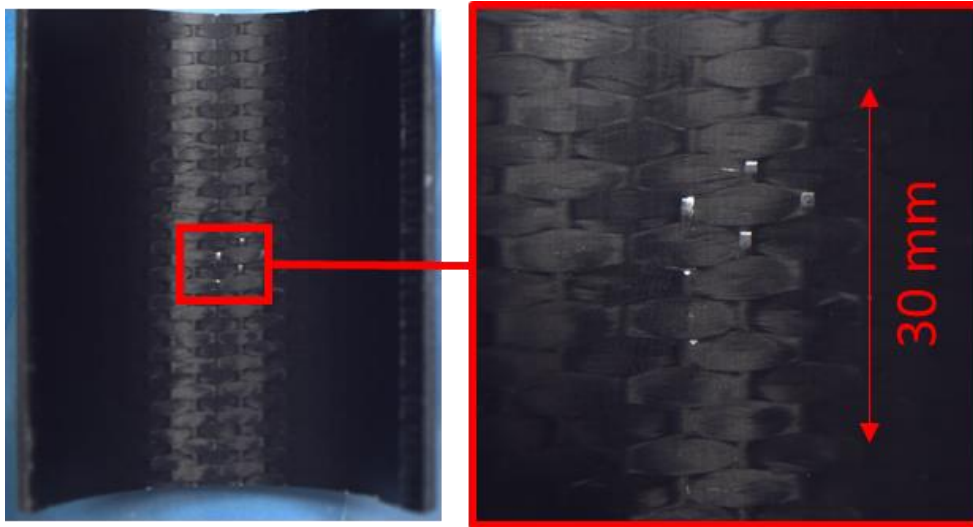


Figure 5.12 – Stitching torn off by the impact (15J on Φ 70mm)

No clear change in the out-of-plane displacement has been found (Figure 5.14). The same conclusion was made for the force data, whether the first drop or the peak force. This may be due to the lack of experimental data for these tests that were preliminary and require more investigations before making any conclusions.

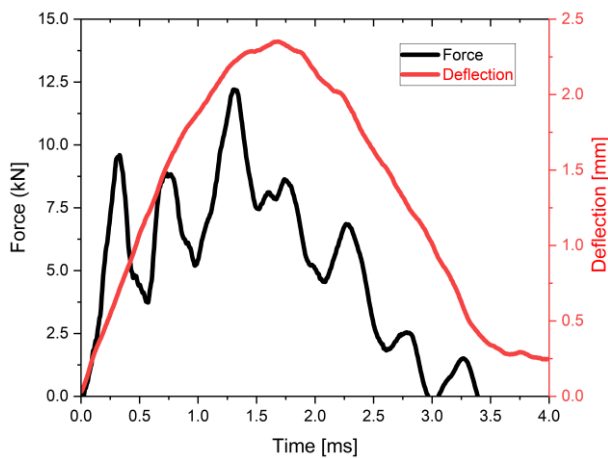


Figure 5.13 – Comparison of the force and deflection data for an impact of 15J on a curved coupon with a diameter of 70mm

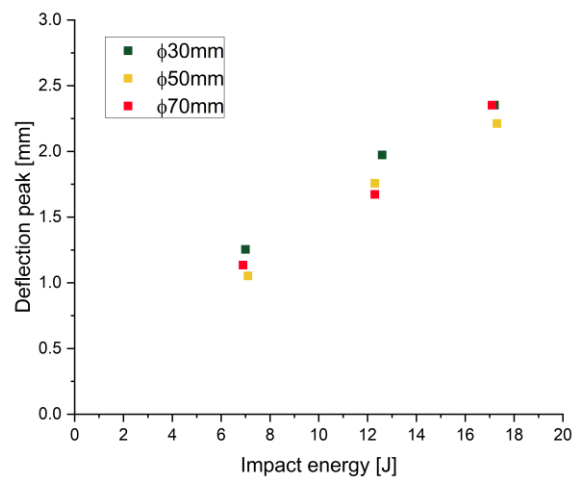


Figure 5.14 – Comparison of deflection peak for curved coupons impacted from 7J to 17J

In term of contact duration, impacts on curved coupons have been found to be shorter than impacts on flat coupons (Table 5.4). This may be due to the curvature or to the boundary conditions. The dimensions of the window that allows the coupon to deflect have a strong influence at high energy: the larger the window, the higher the deflection and the higher the contact time. However, after impacts, coupons did not show visual damage linked to the boundary conditions. The hypothesis of the increased structural stiffness due to the curvature is therefore preferred.

Table 5.4 – Comparison of the contact durations [ms] for impacts on curved coupons impacted from 7J to 17J

	Φ30mm	Φ50mm	Φ70mm	Φ∞
7J	2.67	2.53	2.59	≈ 4.0
12J	2.99	2.85	2.86	
17J	2.86	2.91	2.96	

5.3.2.2. Analysis of C-scans

The C-scan results are presented in Figure 5.15 for the smallest diameter coupons (30mm) impacted from 5J to 15J. Due to the small diameter, the impact is severe. Even at the lowest impact energy, the delamination is already clearly visible, and it seems to have reached the limit on the coupon circumference at 10J. When the energy is further increased, the delamination extends in the length direction of the coupon. This seems normal because the window which allows the coupon to deflect is rectangular.

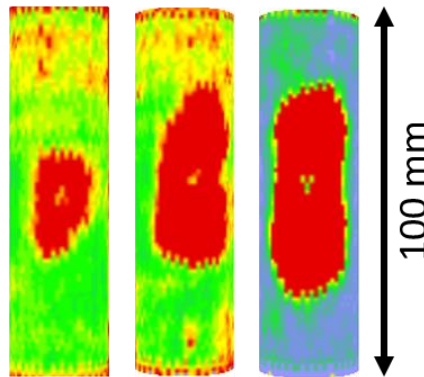


Figure 5.15 – Projected delamination of Φ30mm curved coupons impacted (from left to right: 7J, 12J and 17J)

For larger diameters, the increase of impact energy does not affect the delamination in the length direction (Figure 5.16). In the circumferential direction, when the impact energy increases, the delamination becomes wider. It must be highlighted that the C-scan technique used here is only able to measure the projected delamination. With the increase of impact energy, multiple delaminations through the thickness occur (see next section) and have been observed elsewhere [142] but these cannot be characterized with this inspection system. At these energy levels, the shape is almost the same as found in the literature for glass/epoxy [142].

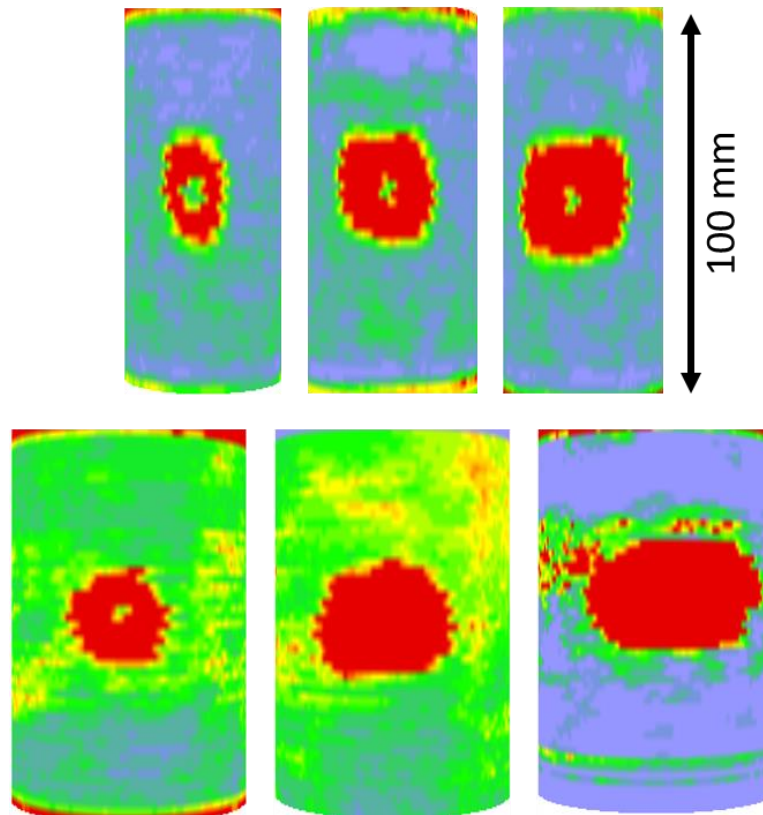


Figure 5.16 – C-scan results of Φ 50mm and Φ 70mm curved coupons impacted (from left to right: 7J, 12J and 17J)

5.3.3. Microscopy observations

Coupons impacted at 17J have been cut then polished. Due to the curvature and the dimensions of the coupons, many photos have been taken, then the freeware Hugin™ has been used to rebuild the complete section in a panorama. However, some pictures present a distortion on the corners which is due to the software. The microscopic observations (Figure 5.17) show fiber failures of the upper and lower plies with fibers oriented at 0° . In addition, a damage tree is visible. Both delamination and intralaminar damage are visible. The damage seems more severe than that observed for out-of-plane impacts performed at the same levels of energy.

A section has also been prepared for an impact of 7J on the Φ 50mm curved coupon. The aim was to define the first type of damage that the coupons experienced during the impact. The photo of the section is presented in Figure 5.18. Delamination is observed at $-45/45$ and $45/90$ interfaces, and matrix cracks are also visible. Even if the upper ply shows fiber failure, the lower ply does not seem damaged.

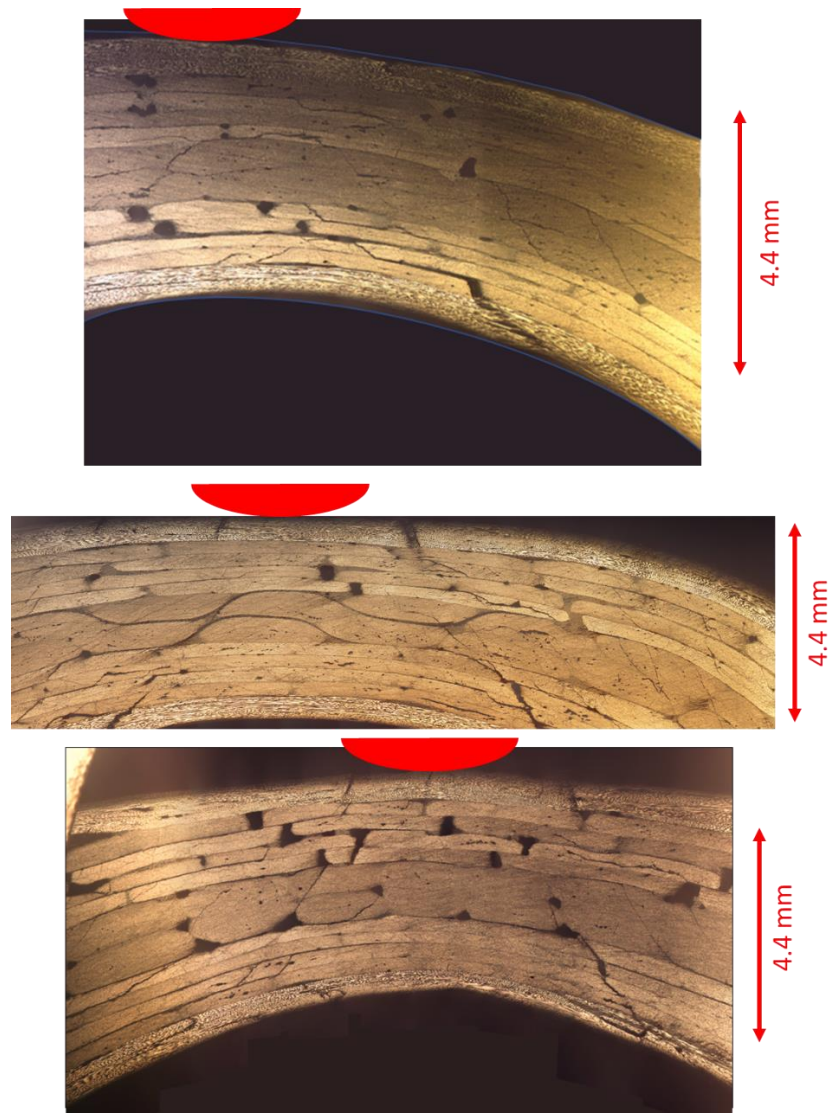


Figure 5.17 – Damage observed in curved coupons impacted at 17J. From top to bottom: $\Phi 30\text{mm}$, $\Phi 50\text{mm}$ and $\Phi 70\text{mm}$

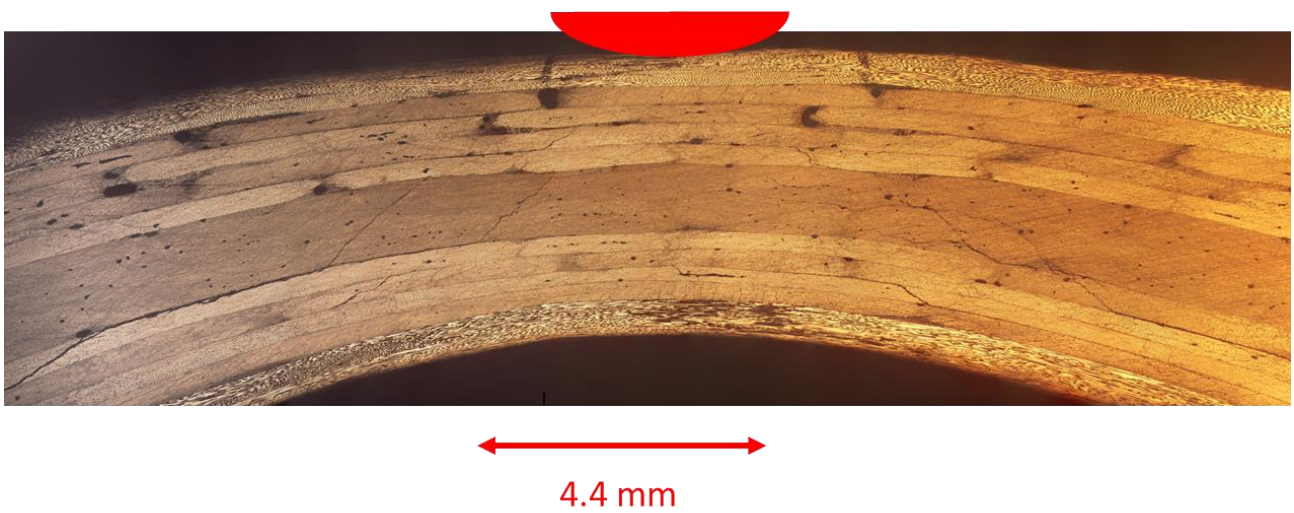


Figure 5.18 – Damage observed on a $\Phi 50\text{mm}$ curved coupon impacted at 7J

5.3.4. Conclusion on these preliminary tests

Preliminary tests to evaluate the influence of the curvature on the impact behavior of unaged CFRP coupons have been performed. The curvature radii are smaller than in another recent study [142] but similar trends in force curves have been found. When the delamination threshold is reached, a sudden force drop is measured, because of a stiffness loss. Then, a second higher force peak is noted, due to the curvature that resists the further deflection of the coupon. C-scan analyses have shown delamination at low impact energy. Microscopy observations on sections have shown multiple damage features, including delamination, intra and translaminar fractures. More investigations are needed to conclude on the effects of the curvature on the impact behavior but these impacts seem more severe for the composite, that shows more damage than in planar coupons at the same energy levels. It must be underlined that the observations made with the microscope have shown a wide range of damage types, including intralaminar matrix damage. The numerical simulation of such tests would be considerably more complex than for out-of-plane damage, but in future work it will be important to investigate the effects of the curvature on the damage extent in the composite propeller.

5.4. In-plane impact: from element level to component level

As explained in the introduction of this chapter, in-plane impacts are likely to happen on a marine propeller, as the rotating edge encounters immersed objects. Two different tests have been performed in this thesis to account for this particular loading case: A first at element level and a second at component level on a representative CFRP propeller part.

5.4.1. Edge impact at element level

The first test is based on a paper found during the literature study [169]. In that work, the authors studied a laminate with a stacking sequence based on 0° , $\pm 45^\circ$ and 90° plies. The lay-up was chosen to evaluate different failure mechanisms. They used a $\phi 12.7\text{mm}$ cylindrical steel impactor and performed impacts at 5 energy levels (that are not detailed in the paper).

For our study, a $\phi 50\text{mm}$ hemi-cylindrical impactor was used. This shape was preferred to a hemispherical shape to avoid an asymmetric impact on the thin edge in the case where the impactor is not perfectly centered. The same coupons as those used in Chapter 4 were tested, but this time the impact was performed in the width direction and required a specific fixture (Figure 2.24).

Impacts have been performed on unaged and seawater aged coupons, at 7 energy levels: 20, 40, 60, 80, 100, 200 and 330J. The highest energy level is the maximal capacity of the Ifremer drop weight impact tower. The measurement of the indentation was made by a high-speed laser targeting the horizontal bar of the T-shaped impactor carriage. This also allowed the impactor initial velocity to be measured. As this was an exploratory study, only one impact test was performed for each aging condition at each impact energy level.

5.4.1.1. Analysis of force and deflection data

A curve representing the contact force vs. contact time is presented for four energy levels on Figure 5.19. When increasing the impact energy, the maximal force value is increased, as well as the contact time. Around the peak force, a plateau is observed which suggests that crushing is occurring. High speed camera images confirm this hypothesis (Figure 5.20). Then, the last part of the curve is the impactor rebound with the release of the stored elastic energy from the coupon.

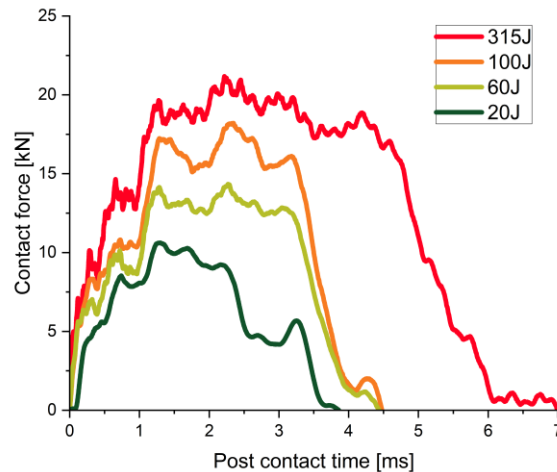


Figure 5.19 – Comparison of force vs. contact time for coupons impacted at four energy levels in the in-plane direction

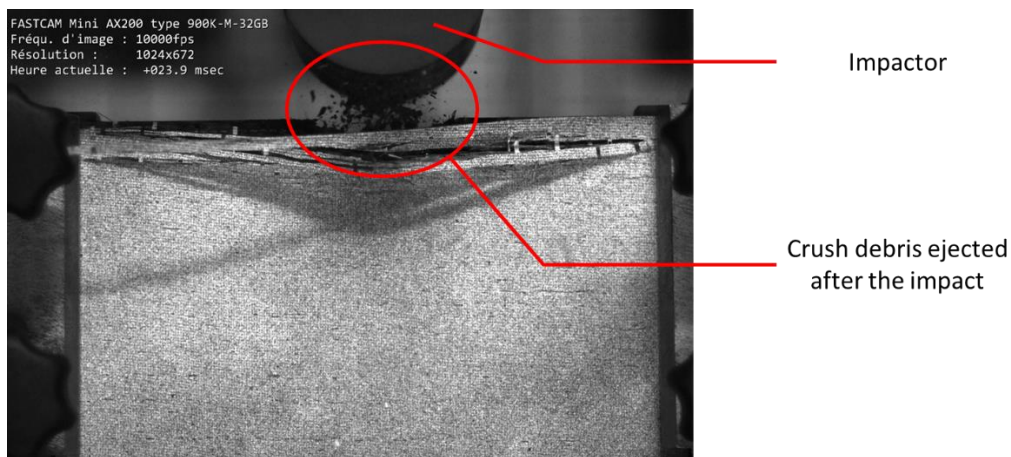


Figure 5.20 – Crush debris ejected during the impactor rebound for an unaged coupon impacted at 330J, high speed camera image

Comparisons of the force and penetration peak are shown in Figure 5.21 and Figure 5.22. On both figures, a shift is observed. For the force peak, two trends are apparent. First, for impact energies lower than 80J, the mechanical response is given by the in-plane stiffness of the coupon.

Then, for impact energies higher than 80J, the force peak seems to stabilize with the increase of impact energy. This limit is associated with the crushing of the material as noted above. Seawater aged coupons show a lower peak force compared to the rejuvenated coupons. A decrease in the peak force after humid

aging has been observed in the literature [267]. In that work, SEM observations showed a degradation of the interface between the fiber and the matrix, which reduced the on-edge impact strength.

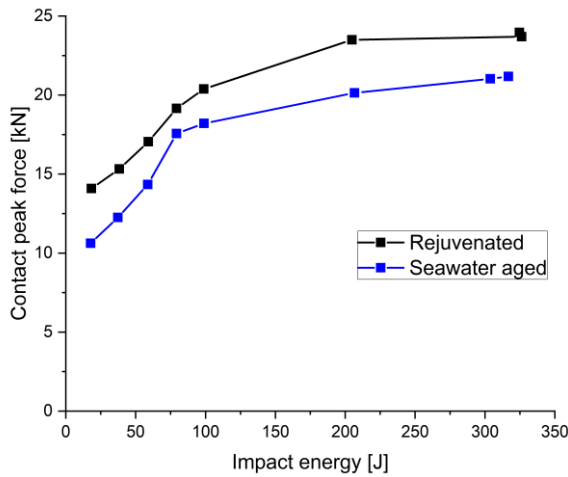


Figure 5.21 – Comparison of the peak force between unaged and seawater saturated coupons aged up to 330J

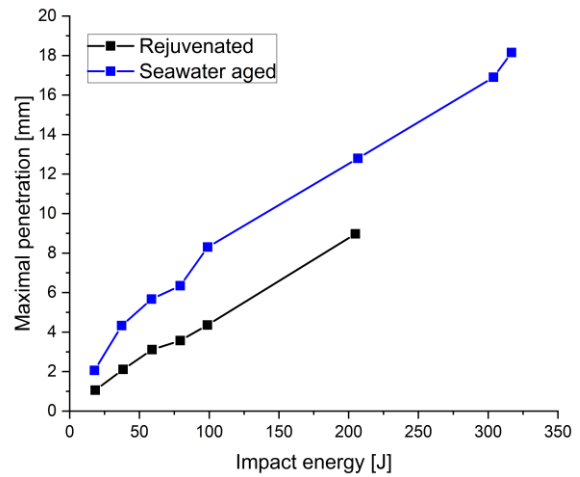


Figure 5.22 – Comparison of the maximal penetration between unaged and seawater saturated coupons aged up to 330J

5.4.1.2. Observations and C-scans

C-scan inspections have been performed to investigate the damage extent in the coupon. This is not an easy exercise as there is considerable out-of-plane expansion at higher energies. However, results for the rejuvenated coupons (Figure 5.23) have been found to be equivalent to those from seawater saturated coupons. The part seen as delaminated corresponds to the part where the fibers have moved the most (Figure 5.25) out of the coupon plane. An important conclusion is that the damage seems to be very local, and did not propagate to the coupon center. This was confirmed, by polishing cut sections of coupons impacted at 330J (Figure 5.24). In this figure, the crush is visible on the upper part. Delamination is visible in the zone affected by the impactor penetration, but this damage is local.

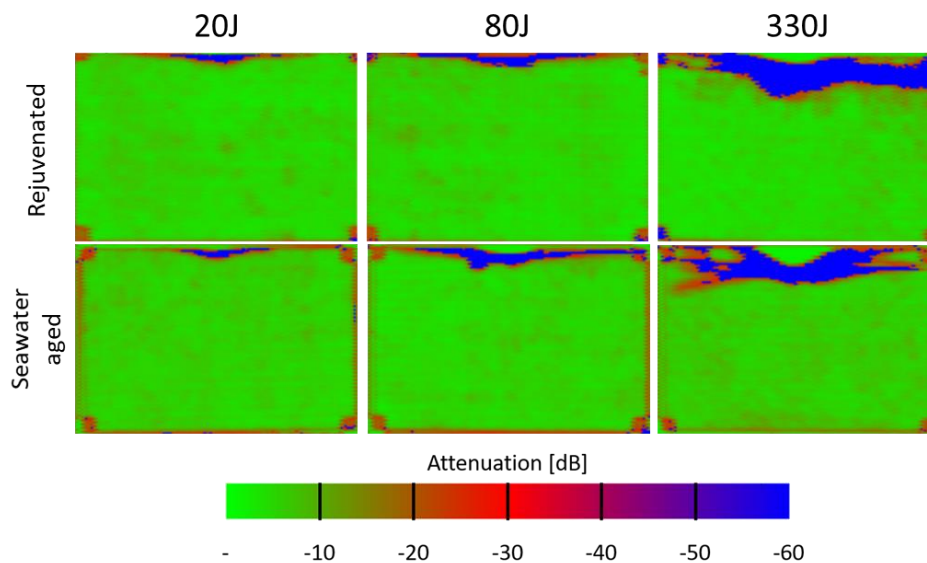


Figure 5.23 – Comparison of delamination extent in unaged and seawater saturated coupons impacted in the in-plane direction from 20J to 330J



Figure 5.24 – Polished sections of unaged (left) and seawater saturated (right) coupons impacted at 330J

Further investigations with X-ray tomography could be performed to visualize the fiber crush and the interface damage in these coupons. A post-impact compression test has been described in the literature [169] to investigate the influence of in-plane impact energy on the residual strength. The main challenge was to design such a test. Because of the damage to one side of the impacted coupon, the compression coupon is mechanically asymmetric. To deal with this issue, the compression fixture ASTM D6641 was used, but the dimensions of the coupons were modified: 150x25mm². Results showed a decrease of the

compression strength by 20% for the impact energy range studied in that work (which is actually not given in the paper due to confidentiality).

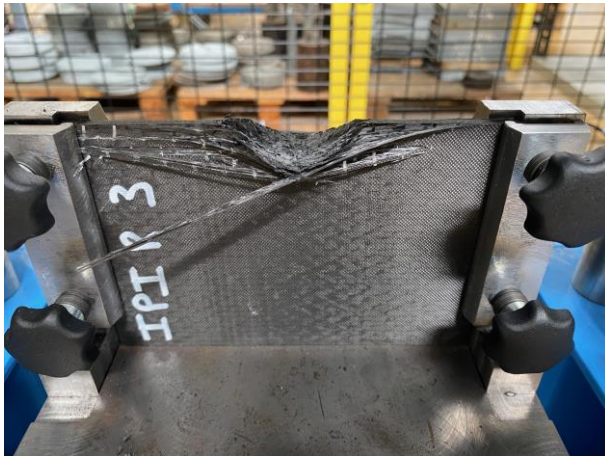


Figure 5.25 – Photo of a coupon impacted in the in-plane direction at 330J

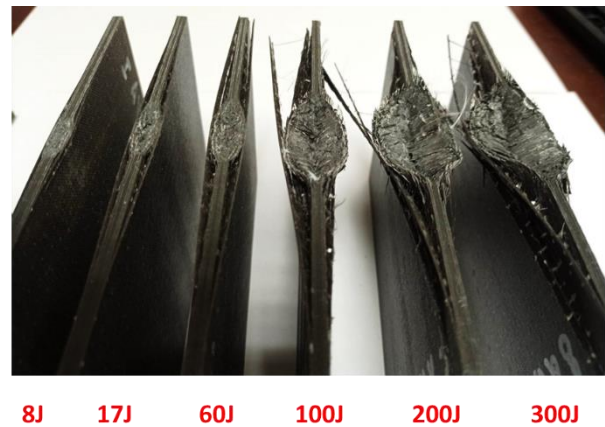


Figure 5.26 – Photo of coupons impacted from 8J to 300J

On-edge impacts have shown visible damage even at low impact energy (Figure 5.26).

5.4.2. In-plane impact at component level

Finally, moving up the test pyramid (Figure 2.6), some preliminary impact tests have also been performed on a leading edge from the Fabheli propeller blade. The aim of this study was to investigate the effects of a hard impact on the behavior of the leading edge. The same tests have been performed previously elsewhere with a wooden impactor but are not presented here. Interpretation of tests in which both impactor and coupon are damaged is complex. The idea here was to simplify the impact by using a non-deformable material for a first simulation of this test, and once the simulation has been validated, to simulate a composite/wood impact.

In order to obtain data to compare to the simulation (performed outside the scope of the thesis) coupons were impacted at 24J, 35J, 50J, 70J, 100J and 160J. A specific fixture was designed to block the coupon base on the drop weight impact tower (Figure 2.27). The Epoxy system is the same as used in this thesis, but two slightly different carbon fiber fabrics were used for this geometry: UD PANEX35 50K 600g/m² and a Serge 2-2 T700 600g/m².

Figure 5.27 shows the Force versus Time curves at the different energy levels. For impact energies lower than 100J, the contact time is slightly lower than 4.5ms. At 160J, the contact time has been measured to be much higher than this value. This may be due to severe damage developed at that energy level, which seems to have affected a larger area.

Figure 5.28 shows the change in visible damage close to the contact area for impacts from 24J to 160J. At the lowest impact energy, fiber crushing is present even though it is not extensive. At 160J, the penetration of the impactor has led to severe damage. It should be noted that these hard impacts damaged all the coupons, even when the impact energy was low.

Once again further investigations including microscopy on polished areas around the crushed section are underway within the project, in order to characterize the damage sequence during the impact. High speed camera images provide some indications of the damage progression (Figure 5.29).

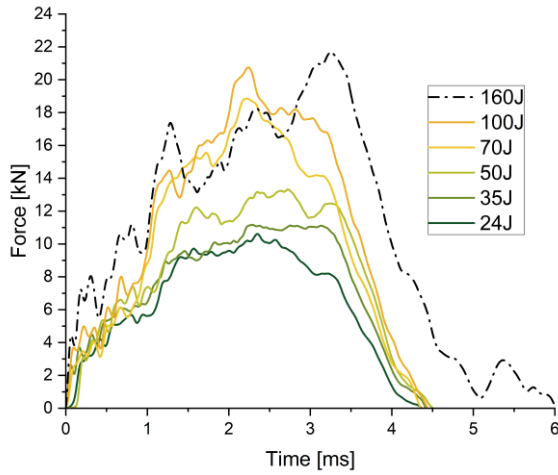


Figure 5.27 – Force vs. time curves for leading edges impacted from 24J to 160J

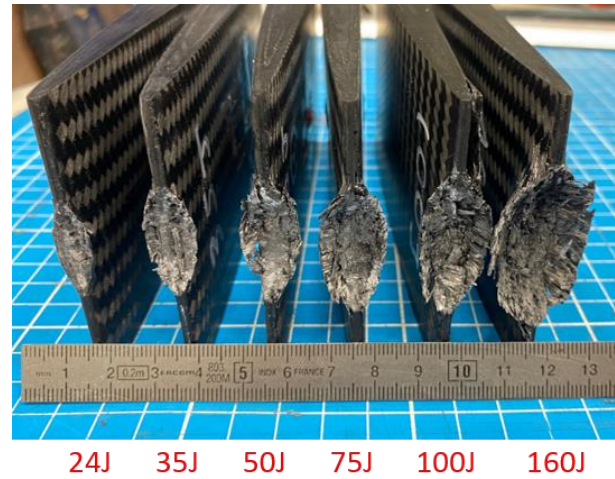


Figure 5.28 – Comparison of damage observed for impacts up to 160J on leading edge

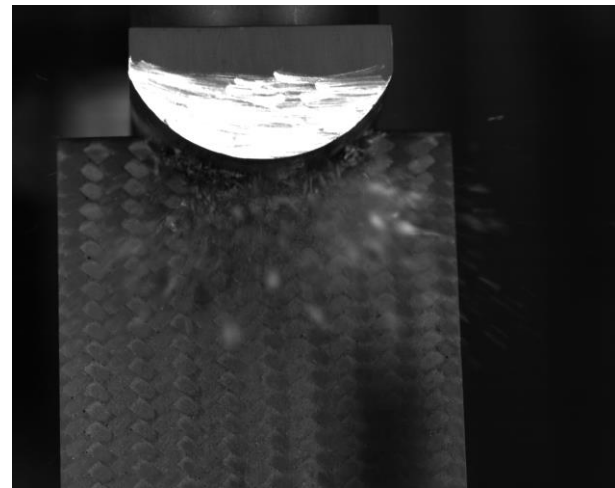
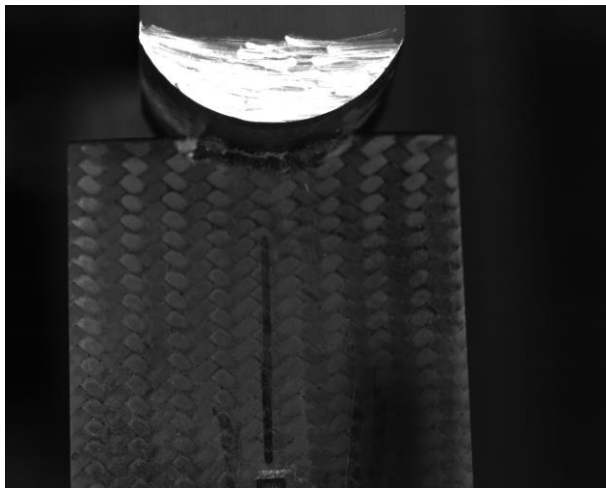


Figure 5.29 – Comparison of the maximal penetration in the leading edge for impacts at 50J (left) and 330J (right) : the presence of CFRP debris generated by the impact is visible at 330J, high speed camera images

From the force and deflection signals, the energy balance has been plotted (Figure 5.30) and compared (Table 5.5) for the different tests from 35J to 100J. (At 24J and 160J, there was a problem with the high-speed laser so the data are not available). It appears that the elastic energy is very low compared to the energy used to damage the material (~6%). In addition, a comparison of the impact energy measured prior to the impact by the high-speed laser and the impact energy measured by the integration of the force-displacement curve has shown some differences, with a maximal value around 10%. This may be due to the T-shaped impactor.

In fact, measurements on both ends of the horizontal beam have shown a difference which indicates that the T-shaped impactor, with a length of 460mm, may not be perfectly horizontal during his drop. Another hypothesis is the displacement of the support fixture, but preliminary measurements during out-of-plane impact tests have shown very low displacements compared to the deflection of the coupon. However, as the force level was lower for out-of-plane tests, we can expect larger effects for in-plane impact tests.

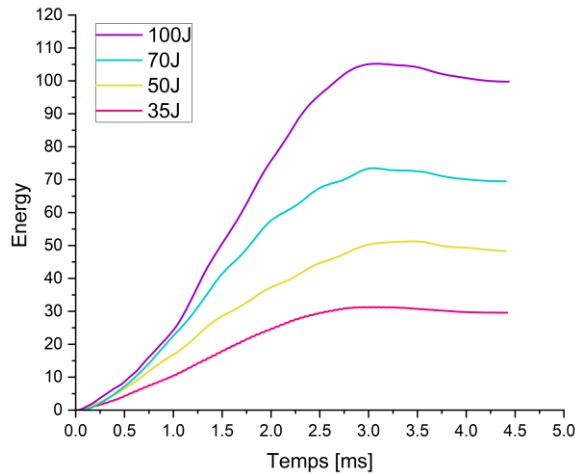


Figure 5.30 – Energy balance for leading edges impacted at 35J, 50J, 70J and 100J

Table 5.5 – Comparison of the energy balance measured for impacts on leading-edges

Impact energy from the impactor velocity [J]	Impact energy from F-U data [J]	Absorbed energy [J]	Elastic energy [J]	Part of elastic energy [%]	Averaged part of elastic energy [%]
34.3	31.3	29.6	1.7	5.5	5.5
49.6	50.1	46.4	3.7	7.3	6.6
49.2	51.3	48.3	3.0	5.8	
69.8	76.2	70.3	5.9	7.7	6.5
70.0	73.5	69.5	4.0	5.4	
100.7	105.2	99.6	5.6	5.3	5.3

Strain-gages have been bonded on the flat surfaces of coupons impacted at 25J, 50J and 70J. The aim was to estimate the strain-rate on a blade during an impact. Axial compression strains measured on the flat surface are presented at three energy levels on Figure 5.31. The initial slope gives the strain-rates that are summarized in Table 5.6.

Table 5.6 – Strain-rates measured for impacts at 35J, 50J and 70J

Impact energy [J]	Strain-rate measured [s^{-1}]
35	1.51
50	0.42
70	0.96

It can be noted that these strain rates are only one decade higher than those of the quasi-static tests performed at 1000mm/min and discussed in Chapter 4. However, this response was measured away from the impact point. To develop a numerical simulation of this test, dynamic properties of the material are needed closer to the contact point. However, these results suggest that quasi-static input data may be adequate to provide a global simulation of the response of the structure. Another interesting point is the difference in strain-rates between the tests. As the impact energy is given by the impactor velocity (the impactor mass is constant during the test), the higher the energy, the higher the impactor velocity and the higher the expected strain-rate. However, this is not observed here. A possible cause is the geometric differences between coupons. The external ply was also observed to delaminate at 100J (Figure 5.32), which was not observed at the other energy levels. The number of tests performed is small, and some scatter exists mainly due to the manufacturing process. The damping effect of the damage mechanisms may also affect the strains seen by the strain gauges further from the impact.

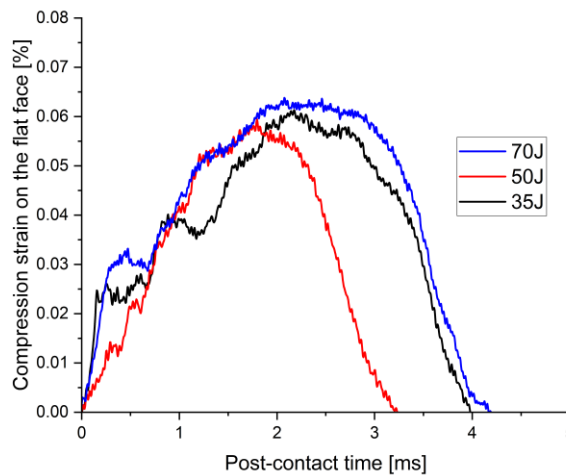
**Figure 5.31 – Compressive strain measured on leading-edges impacted at 35J, 50J and 70J**



Figure 5.32 – Delamination of the external ply due to the impact at 100J

5.5. Conclusion

In contrast to Chapters 3 and 4, which present more complete studies of the integration of aging behavior into the prediction of static and impact performance, this chapter has mainly focused on the ongoing development of tests aiming to be more representative of operating conditions of a composite propeller.

First, a complement to the out-of-plane impact tests presented in Chapter 4 has been described. The post-impact strength has been characterized and showed a significant decrease of the compression residual strength after seawater aging. However, the difference with respect to the unaged and physically aged materials cannot be quantified, because for those conditions, the coupons failed early, due to high stresses close to the loading boundary conditions. A comparison with the undamaged material strength allowed the results for the seawater saturated coupons to be validated but not those for the unaged and physically aged tests. For the valid tests, the failure always involved microbuckling failure of the transverse stitching. These results have underlined the well-known difficulties in performing compression tests on composites and a focus on the role of stitching parameters during these tests could help to improve propeller blade performance.

Then, custom tests have been developed and performed to investigate the material behavior under more realistic conditions. As propellers present different section geometries, impact tests should be performed which allow us to analyze the critical loading conditions. Curved coupons have been manufactured and impacts performed from 5J to 15J. Except for the smallest radii, the projected delamination did not interact with the boundary conditions. More investigations are needed to relate ply damage to curvatures, and evaluate which interfaces are delaminated but curvature does appear to concentrate damage.

On-edge impacts have been performed on unaged and seawater saturated coupons. Results show a decrease of the force peak after seawater aging. A shift is also observed on the deflection peak, which is higher after seawater aging. One hypothesis is that crushing consumes less energy after seawater aging than for the unaged and physically aged materials. This could be further investigated by performing CC and CT tests as discussed in Chapter 3.

Finally, impact tests on leading-edges more representative of a propeller geometry have been performed from 24J to 160J. Even at the lowest impact energy, damage is visible. This is mainly due to the stiffness of the steel impactor used, and the thickness of the leading edge, which is thin at the blade tip.

Results from these exploratory tests have provided indications of areas to investigate in more detail in the future, but they have also underlined the difficulty in dimensioning of a complex composite component working under dynamic loading conditions in a hostile environment.

*Conclusions
&
perspectives*

Conclusions

The aim of this study was to investigate the effects of aging on the long-term durability and impact behavior of a CFRP composite manufactured by infusion for naval applications. A Carbon/Epoxy material sensitive to both physical aging and seawater aging has been studied.

In the first part of this thesis, an extensive experimental campaign has been proposed. The aim was to characterize the change of elastic, strength and interface fracture toughness properties with aging. Both in-plane and out-of-plane tests have been performed. It was demonstrated that physical aging had, in most cases, a beneficial effect on the mechanical properties used in design, while seawater aging results in a reduction in stiffness and strength. The latter is significant, and must be considered in design of marine structures. In terms of interlaminar crack propagation, significant seawater aging effects were noted for in-plane shear (mode II) loadings, for which a reduction of G_{IIC} by 30% was measured. The reference, physically aged and seawater aged properties were introduced in numerical simulations of four point bending tests combining flexure and shear loads, and a good prediction of the unaged and aged behavior was obtained. The study also highlighted a lack of reliable input data for translaminar and intralaminar fracture, and development of test methods for these properties would improve confidence in numerical modelling of composite structures.

In the second part of this thesis, out-of-plane impacts have been performed and simulated with a finite element (FE) model. Compared to materials used in the aerospace industry, the material studied has been found to show higher porosity, and the role of the stitching in the damage propagation requires further study. In the unaged and physically aged states, a delamination threshold between 5J and 15J was found, while for the seawater saturated state, the damage threshold is below 5J. This is in accordance with interface strength results in Chapter 3. The contact time for seawater saturated coupons was higher than for unaged and physically aged coupons, indicating either a stiffness decrease due to aging or an out-of-plane damage. A numerical model has been developed with the Abaqus™ commercial code. Two meshing techniques have been tested: standard orthotropic and oriented. While results are reasonable for both, force and displacement drops are observed for the mesh with oriented elements. A parametric study has been performed and showed that the cohesive surface stiffnesses have a strong influence on the prediction of the delamination. Different values have been tested, and the higher the stiffness, the lower the delamination and the longer the computation time. With respect to the stiffness prediction, the friction coefficient between the metallic parts and the composite affects the stiffness and the value chosen was optimized to improve the results. In terms of damage, no fiber failure has been found and the model is in accordance with this observation, delamination is the main damage mechanism. The model over-predicts the delamination because the elements used cannot predict the out-of-plane damage, in particular σ_{23} which is mainly responsible for matrix cracking.

Finally, in the third, more prospective part of this thesis, a focus on the ongoing development of tests aiming to be more representative of operating conditions of a composite propeller is proposed.

First, a complement of the out-of-plane impact tests presented in Chapter 4 has been described. The post-impact strength has been characterized and showed a decrease of the compression residual strength after seawater aging. However, the difference with respect to the unaged and physically aged materials cannot be quantified because for those conditions, the coupons failed prematurely. A comparison with the undamaged material strength allowed the results for the seawater saturated coupons to be validated but not those for the unaged and physically aged tests. For the valid tests, the failure always initiated at the transverse stitching causing microbuckling failure. These results have underlined the well-known difficulties in performing compression tests on composites.

Then, custom tests have been developed and performed to investigate the material behavior under more realistic conditions. As propellers present different section geometries, impact tests should be performed which allow us to analyze the critical loading conditions. Curved coupons have been manufactured and impacts performed from 7J to 17J. Except for the smallest radii, the projected delamination did not interact with the boundary conditions. Even at the lowest impact energy, delamination, intra- and translaminar fracture have been observed. Curved coupons seem to be more affected by an out-of-plane damage than flat coupons. This is relevant for propellers, since propeller shapes are almost always highly curved.

On-edge impacts have been performed on unaged and seawater saturated coupons. Results show a decrease of the force peak after seawater aging. A shift is also observed on the deflection peak, which is higher after seawater aging. One hypothesis is that crushing consumes less energy after seawater aging than for the unaged and physically aged materials. This could be investigated further by performing CC and CT tests, as explained in Chapter 3.

Finally, impact tests on leading-edge specimens more representative of a propeller geometry have been performed from 24J to 300J. Even at the lower impact energy, damage is visible. This is mainly due to the stiffness of the steel impactor used, and the geometry of the leading edge, which is thin at the blade tip.

Results from these exploratory tests have provided indications of areas to investigate in more detail in the future, but they have also underlined the difficulty in dimensioning of a complex composite component working under dynamic loading conditions in a hostile environment.

Perspectives

Composite propeller developments are recent and published studies of industrial solutions do not exist. Very few studies that have proven the interest of using composites have been published, and those focus more on hydrodynamic aspects. There are a number of material aspects which require further examination:

- Investigation of the water uptake effects.

Effects of aging must be considered if adequate safety factors are to be applied, particularly in the case of thin sections. For thicker sections, as the water diffusion is very slow, composite plies located far from the propeller surface will not be exposed to water diffusion because of the transient regime. Thus, mechanical tests on composites with a water profile through the thickness will be closer to reality. At coupon scale, coupons will need to be aged for different humidity levels, in a climate chamber at an elevated temperature to accelerate the humidity diffusion into the composite. The implementation of humidity dependent mechanical properties to simulate the composite behavior will give a more accurate prediction of the blade behavior. In addition, vibration problems exist and for specific applications, the shape is chosen to reduce the reflected noise. A change of local properties may change the blade behavior and result in increased noise over time, which may not be acceptable for some application.

To reduce water ingress, the use of an appropriate coating may be a solution. This has not been investigated here. However, replacing the coating needs to be performed regularly and is not environment friendly.

In this work we have concentrated on the influence of seawater immersion on impact, but impacts will also affect water ingress. There is scope for studies of coupling between the two phenomena which may lead to accelerated degradation. In this case, cracks initiated by the impact could create paths that will accelerate the diffusion of water into the composite. Then, local hygroscopic swelling may initiate and propagate damage. This is a complex area but a logical future step to extend our understanding of diffusion and mechanical behavior. A recent study created a first framework to examine coupling effects [267]-[268].

Another aspect is the effect of ageing on the intra- and translaminar fracture toughness of the composite. A preliminary campaign was performed, but premature failures out of the area of interest prevented useful data from being obtained. Development of these tests is of interest since no values are available in the literature for seawater saturated composites and this leads to uncertainty in modelling.

- Investigations of the dynamic effects on the composite

The effects of strain-rate have been investigated briefly in this study, and mechanical tests have been performed with strain-rates up to 0.1 s^{-1} . Out-of-plane impact tests instrumented by strain-gages have shown strain-rates up to 2 s^{-1} for impacts at 4 m/s. For impact velocities of 40 m/s defined in the literature [114], strain-rates should be at least equal to 20 s^{-1} . An experimental campaign could be launched to investigate the strain-rate effects on the composite behavior. Using a high-speed hydraulic system may help to reach the target strain-rate but to design for specific applications knowledge of the type and characteristics of expected impacts is necessary.

A numerical simulation has been proposed in this thesis work with shell elements. The use of volumic elements will improve the simulation if a constitutive material law is implemented. Different approaches have been proposed in the literature, and can be tested with the complete dataset obtained experimentally in this PhD. However, the relatively simple and rapid simulation presented here gave good results for the stiffness. Depending on the design requirements, this may be sufficient.

As impacts happen underwater, the effect of the impact environment must also be investigated. The interaction between the fluid and the composite part must be studied, and simulated. This topic is being developed in the PhD study of Rowan Caldwell from UNSW, within this project.

➤ From laboratory to full scale operation

Finally, the last point to consider is the experience on a real propeller blade. Even if numerical fluid–structure interaction models (FSI) give information about the strain experienced by the propeller blades when rotating, experimental measurements are necessary to validate the models. The use of strain gages allows measurement of the strain on the external surface of the blade, and the development of optical fibers can give information about the internal strains. The use of sensors in the composite to measure the presence of humidity could also be interesting, since thick coupons manufactured in this project showed a higher porosity ratio, which can assist the water diffusion into the composite. In addition, monitoring impacts and following damage is possible using piezoelectric sensors in the propeller blade. This technique can be used to localize the damaged section by triangulation. It requires signal processing analysis, but can be done in service. Another aspect is the material system. The development of thermoplastic materials allows the manufacture of complex shapes using an Automated Fiber Placement (AFP) system, and also provides opportunities for repair. As impacts are unpredictable, a certified repair process needs to be set up. Effects of aging on the repair capabilities of composite propeller blades will also need to be investigated.

Composites offer great potential for a range of highly loaded marine structures. The very fast development of composite foil structures for racing yachts over the last 5 years is providing a rapid learning curve. Extending the lifetime of these structures, by improving understanding of ageing and fatigue response, will encourage their use in a new range of marine applications.

List of figures

FIGURE I.1 – SVR LAZARTIGUE ULTIM MADE OF CFRP COMPOSITE ©THIERRY MARTINEZ	5
FIGURE I.2 – SCHEME OF THE STUDY PERFORMED	6
CHAPTER 1 – STATE OF THE ART	12
FIGURE 1.1 – CFRP MARINE PROPELLERS COMMERCIALIZED BY NAKASHIMA (FROM NAKASHIMA WEBSITE) – IN THE ORDER : I) FIXED PITCH PROPELLER (FPP) II) CONTROLLABLE PITCH PROPELLER (CPP) III) SIDE THRUSTER	15
FIGURE 1.2 – SCHEMATIC DIAGRAM OF THE SECTION OF THE WIND TURBINE BLADE [5].....	16
FIGURE 1.3 – ENGINE POWER (%) VS. ENGINE REVOLUTIONS (%) : UNDER-PITCH AND OVER-PITCHED PROPELLER BLADE COMPARISON [14].	19
FIGURE 1.4 – COMPARISON OF CAVITATION EFFECTS ON METALLIC PROPELLER (LEFT) AND COMPOSITE PROPELLER (RIGHT) [25]	22
FIGURE 1.5 – FABHELI COMPOSITE PROPELLER AT JEC ASIA 2018.....	24
FIGURE 1.6 – MEASURED PROPELLER DEFLECTION AT INCREASING RPM FOR BOLLARD PULL CONDITION [62]	28
FIGURE 1.7 – IMPACT REGIMES ON STRUCTURES (ADAPTED FROM [74])	31
FIGURE 1.8 – EXAMPLES OF STRUCTURAL DAMAGE ON VESSELS DUE TO MARINE IMPACTS [91]	34
FIGURE 1.9 – INITIAL DAMAGE IN AN IMPACTED 0/90/0 COMPOSITE PLATE [76]	36
FIGURE 1.10 – DIAGRAM OF THE STRESS COMPONENTS CONTRIBUTING TO A BENDING MATRIX CRACK IN A TRANSVERSE LAYER.....	36
FIGURE 1.11 – IMPACTORS USED TO CHARACTERIZE THE INFLUENCE OF SHAPE AND TIP ON COMPOSITE DAMAGE [102]	38
FIGURE 1.12 – DELAMINATION AREA MEASURED AFTER LVI FOR TWO FIBER ARCHITECTURES [105].....	40
FIGURE 1.13 – DAMAGE AREA (MM ²) VS. IMPACT ENERGY (J) : COMPARISON BETWEEN TS AND TP RESIN SYSTEM [140].....	41
FIGURE 1.14 – EXAMPLE OF A MICROGRAPH ON C/EPOXY COUPON IMPACTED AT 80J	43
FIGURE 1.15 – SCHEMATIC DIAGRAM OF THE NON-DESTRUCTIVE EVALUATION OF AN IMPACTED COUPON (FROM [144])	44
FIGURE 1.16 – HELICOPTER SECTION BLADE [159] AND WIND TURBINE SECTION (SANDIA NATIONAL LABORATORIES)	47
FIGURE 1.17 – BLADE CROSS SECTION IN THE PLANE OF IMPACT [66] FOR DIFFERENT ENERGY LEVELS.	48
FIGURE 1.18 – SECTION OF THE BLADE STUDIED IN [165]	49
FIGURE 1.19 – IDEALIZED DMA SCAN SHOWING THE TYPES OF TRANSITIONS (PERKINELMER) – (1) CHAIN SLIPPAGE (2) LARGE SCALE CHAIN (3) GRADUAL MAIN CHAIN (4) SIDE GROUPS (5) BEND AND STRETCH (6) LOCAL MOTION	52
FIGURE 1.20 – SCHEMATIC DIAGRAM OF ENTHALPY EVOLUTION DURING CYCLES CORRESPONDING TO VARIOUS AGING TIMES (TOP) AND THE HEAT CAPACITY DURING THE CORRESPONDING HEATING CYCLES (BOTTOM) [175] (ADAPTED FROM [176]).	52
FIGURE 1.21 – VARIATION OF A <i>T_g</i> ON RESIN AND COMPOSITE AFTER AGEING AT 210°C [177].....	52
FIGURE 1.22 – STRESS (MPa) – STRAIN (%) CURVES OF TENSION TESTING ON [±45]4s IMS/977-2 LAMINATE : INFLUENCE OF PHYSICAL AGEING [177]	54
FIGURE 1.23 – COMPARISON OF ULTIMATE AXIAL STRAIN OF DIFFERENT LAMINATE LAY-UPS BEFORE AND AFTER PHYSICAL AGING [177]..	54
FIGURE 1.24 – MECHANISM OF THE FREE VOLUME DIFFUSION OF WATER IN A POLYMER NETWORK	56
FIGURE 1.25 – EFFECT OF THE PROCESS AND TEMPERATURE AGEING ON WATER UPTAKE [196].....	57
FIGURE 1.26 – DIFFERENT DIFFUSION KINETICS [197].....	57

FIGURE 1.27 – FORCE – TIME PLOT FOR PLATES WITH A LAY–UP $(\pm 45^\circ, 0^\circ), (\pm 45^\circ)_2, (0^\circ, \pm 45^\circ)$ IMPACTED AT 10J BOTH DRY AND AFTER WATER IMMERSION AT 65°C FOR DIFFERENT AGEING DURATIONS (FIG. 13 IN [209]).	61
FIGURE 1.28 – ABSORBED IMPACT ENERGY AGAINST NOMINAL IMPACT ENERGY FOR PLATE WITH A LAY–UP $(\pm 45^\circ, 0^\circ), (\pm 45^\circ)_2, (0^\circ, \pm 45^\circ)$ (FIG. 11–B IN [209]).	62
FIGURE 1.29 – THE ENERGY ABSORPTION PARAMETER B AGAINST TIME FOR ALL TYPES OF SPECIMENS A, B AND D REPRESENTING DIFFERENT LAY–UPS AT TEMPERATURES OF 43°C AND 65°C [209].	62
CHAPTER 2 – MATERIALS AND METHODS	64
FIGURE 2.1 – DIAGRAM OF THE UD T700 VERSION I CARBON FIBER FABRIC STUDIED	66
FIGURE 2.2 – SEAWATER AGING TANKS AT IFREMER	69
FIGURE 2.3 – AGEING PROCESSES USED IN THIS STUDY TO OBTAIN REJUVENATED, PHYSICALLY AGED AND SEAWATER AGED MATERIALS	69
FIGURE 2.4 – EXAMPLE OF AN IMPACTED COUPON (150x100 MM ²) WITH THROUGH THE THICKNESS DELAMINATION VISIBLE AT THE COUPON CENTER	72
FIGURE 2.5 – FIXTURE DESIGNED FOR SCANNING SEVERAL COUPONS AT THE SAME TIME	72
FIGURE 2.6 – BUILDING BLOCK APPROACH WITH TEST AND SIMULATION PYRAMIDS AS BASIS FOR THE DESIGN OF A CRASHWORTHY HELICOPTER FRAME STRUCTURE [212].	73
FIGURE 2.7 – ASTM D6641 FIXTURE AND A ZOOM ON ONE OF THE TWO STRAIN GAGES BONDED TO DETERMINE THE COMPRESSION MODULUS	75
FIGURE 2.8 – V–NOTCHED PURE EPOXY COUPON SPECKLED BEFORE THE TEST AND THE AREA USED TO COMPUTE THE SHEAR STRAIN	75
FIGURE 2.9 – V–NOTCHED C/EPOXY COUPONS TO DETERMINE THE OUT-OF-PLANE SHEAR PROPERTIES	76
FIGURE 2.10 – FORCE–DISPLACEMENT PLOT FOR CRACK INITIATION IN PURE MODE–I OPENING	77
FIGURE 2.11 – PROPAGATION OF THE CRACK IN THE INTERLAMINAR AREA DURING THE DCB TEST	78
FIGURE 2.12 – CALIBRATION STEP OF TO DETERMINE THE FLEXURAL MODULUS	78
FIGURE 2.13 – C–ELS FIXTURE DURING A PURE MODE–II PROPAGATION TEST	79
FIGURE 2.14 – CALIBRATION OF THE FLEXURAL MODULUS WITH FOUR FREE LENGTHS AND DETERMINATION OF THE SLOPE TO DETERMINE THE FLEXURAL MODULUS	79
FIGURE 2.15 – DIAGRAM OF THE PURE MODE–II FRACTURE TOUGHNESS TEST (ISO 15114)	80
FIGURE 2.16 – 2D DIGITAL IMAGE CORRELATION VIEW OF THE CRACK DURING PURE MODE–II FRACTURE TOUGHNESS TEST	80
FIGURE 2.17 – MMB SPECIMEN	80
FIGURE 2.18 – FOUR–POINT BENDING TEST ON QI C/EPOXY COUPON	82
FIGURE 2.19 – FIXTURE USED TO LOAD A COUPON AT THE SAME LOADING–RATE	82
FIGURE 2.20 – IFREMER DROP WEIGHT IMPACT TOWER	83
FIGURE 2.21 – CURVED COUPONS WITH DIFFERENT DIAMETERS (30, 50, 70 AND 90 MM) TO BE IMPACTED	84
FIGURE 2.22 – FIXTURE MANUFACTURED TO IMPACT $\Phi 70$ MM CURVED PANELS	84
FIGURE 2.23 – DIMENSIONS OF THE FIXTURE USED FOR IMPACTS ON $\Phi 70$ MM CURVED COUPONS	85
FIGURE 2.24 – IN–PLANE IMPACT FIXTURE DEVELOPED FROM THE WORK OF [169]	85
FIGURE 2.25 – IN–PLANE IMPACT PROGRESS, FROM CONTACT TO CRUSH, HIGH SPEED CAMERA IMAGES	86
FIGURE 2.26 – CAI FIXTURE WITH A SPECKLED COUPON	87
FIGURE 2.27 – IMAGE OF THE COMPOSITE BLADE SECTION (DIMENSIONS NOT PROVIDED DUE TO CONFIDENTIALITY)	87
FIGURE 2.28 – EQUIVALENT DISPLACEMENT AND STRESS FOR EACH OF THE FOUR DAMAGE MODES	91

FIGURE 2.29 – CONSTITUTIVE COHESIVE TRACTION–SEPARATION LAW	92
CHAPTER 3 – INFLUENCE OF AGING ON QUASI–STATIC MECHANICAL PROPERTIES.....	94
FIGURE 3.1 – WATER UPTAKE OF PURE EPOXY COUPONS IMMERSSED IN SEAWATER AT DIFFERENT TEMPERATURES.....	96
FIGURE 3.2 – WATER UPTAKE OF C/EPOXY COUPONS IMMERSSED IN SEAWATER AT DIFFERENT TEMPERATURES.....	96
FIGURE 3.3 – WATER UPTAKE OF PURE EPOXY COUPONS IMMERSSED IN SEAWATER AT DIFFERENT TEMPERATURES.....	97
FIGURE 3.4 – WATER UPTAKE OF PURE EPOXY COUPONS IMMERSSED IN SEAWATER AT DIFFERENT TEMPERATURES.....	97
FIGURE 3.5 – DIFFUSION COEFFICIENT D(T) AS A FUNCTION OF THE IMMERSION TEMPERATURE	99
FIGURE 3.6 – REPRESENTATIVE COUPON OF A MARINE PROPELLER LEADING EDGE	100
FIGURE 3.7 – SIMULATION OF WATER DIFFUSION IN THE COMPOSITE COUPON AT 40°C.....	102
FIGURE 3.8 – PLYS AVERAGED CONCENTRATION OF WATER (15MM THICK AT 15°C)	102
FIGURE 3.9 – COMPARISON OF STRESS VS. STRAIN CURVES WITH THE AGING FOR TENSILE TESTS ON [0] ₄	105
FIGURE 3.10 – COMPARISON OF STRESS VS. STRAIN CURVES WITH THE AGING FOR TENSILE TESTS ON [90] ₄	105
FIGURE 3.11 – SHEAR STRESS VS. SHEAR STRAINS PLOTS OF [-45,45] ₂₅ C/EPOXY BEFORE AND AFTER AGING	106
FIGURE 3.12 – VISUALIZATION OF THE TRANSVERSE STRAIN MEASURED BY DIC DURING A TENSILE TEST ON [0] ₄	106
FIGURE 3.13 – EXAMPLE OF A BUCKLING FAILURE OBSERVED WITH TWO STRAIN GAGES	107
FIGURE 3.14 – COMPARISON OF STRESS VS. STRAIN CURVES POUR COMPRESSION TESTS PERFORMED ON [0] ₄	108
FIGURE 3.15 – COMPARISON OF STRESS VS. STRAIN CURVES POUR COMPRESSION TESTS PERFORMED ON [90] ₄	108
FIGURE 3.16 – COMPARISON OF THE POST-MORTEM OBSERVATION FOR THE [0] ₄ COUPONS TESTED IN COMPRESSION.....	108
FIGURE 3.17 – PET WEFT THREADS ADDED TO MAINTAIN THE CARBON FIBER YARN DURING THE COMPOSITE MANUFACTURING PROCESS	109
FIGURE 3.18 – EFFECTS OF AGING ON THE BENDING STRESS VS. BACKFACE STRAIN OF COUPONS TESTED.....	110
FIGURE 3.19 – EFFECTS OF AGING ON THE STRESS VS. STRAIN CURVES OF COUPONS EXPERIENCING A FOUR-POINT BENDING TEST	111
FIGURE 3.20 – DIFFERENCES IN SHEAR STRESS [MPa] VS. SHEAR STRAIN [%] PLOTS FOR REJUVENATED COUPONS CUT IN THE 12 AND 13 PLANES.....	112
FIGURE 3.21 – DIFFERENCE OF FAILURE MODE OBSERVED BY DIC IN RED FOR A SHEAR TEST ON THE 1–3 PLANE (LEFT) AND ON THE 2-3 PLANE (RIGHT)	112
FIGURE 3.22 –STRESS VS. STRAIN PLOTS OF PURE EPOXY COUPONS IN TENSION.....	113
FIGURE 3.23 – FORCE VS. DISPLACEMENT OF DCB COUPONS OPENED IN MODE I.....	114
FIGURE 3.24 – COMPARISON OF THE MODE–I INITIATION FRACTURE TOUGHNESS FROM INSERT FILM FOR THE TWO CRITERIA	115
FIGURE 3.25 – MODE I FRACTURE TOUGHNESS FROM PRECRACK FOR THE TWO CRITERIA	115
FIGURE 3.26 – MIXED–MODE FRACTURE TOUGHNESS FROM PRECRACK FOR THE TWO CRITERIA.....	116
FIGURE 3.27 – MODE II FRACTURE TOUGHNESS FROM PRECRACK FOR THE TWO CRITERIA	116
FIGURE 3.28 – FORCE VS. DISPLACEMENT FOR DCB TEST FROM PRECRACK	117
FIGURE 3.29 – R-CURVES OF DCB TESTS FOR THE THREE AGING.....	117
FIGURE 3.30 – COMPARISON OF FIBER INTERFACE AFTER MODE I TEST : (L) REJUVENATED (R) SEAWATER AGED.....	118
FIGURE 3.31 – FORCE VS. DISPLACEMENT FOR MMB TESTS FROM PRECRACK WITH THREE MODE II RATIOS.....	118
FIGURE 3.32 – FORCE VS. DISPLACEMENT FOR ELS TESTS FROM PRECRACK.....	119
FIGURE 3.33 – R-CURVES OF ELS TESTS FOR ALL AGING.....	119
FIGURE 3.34 – SEM FRACTOGRAPHIES OF REJUVENATED, PHYSICALLY AGED AND SEAWATER AGED COUPON TESTED IN PURE MODE II .	120

FIGURE 3.35 – CHANGE OF THE PROPAGATION FRACTURE TOUGHNESS WITH THE MODE RATIO: COMPARISON EXPERIMENTS/B–K CRITERION	121
FIGURE 3.36 – COMPARISON OF THE FORCE VS. DISPLACEMENT PLOTS FOR QUASI-ISOTROPIC COUPONS DURING A FOUR-POINT BENDING TEST.....	123
FIGURE 3.37 – MAJOR STRAIN COMPUTED BY 3D DIC OF FOUR-POINT BENDING COUPON A FEW SECONDS BEFORE THE FAILURE. FROM TOP TO BOTTOM: (1) REJUVENATED, (2) PHYSICALLY AGED AND (3) SEAWATER AGED	124
FIGURE 3.38 – SENSITIVITY OF THE MESH ON THE FORCE VS. TIME PLOTS OF A SEAWATER SATURATED COUPON ($G_{Ic} = 40 \text{ kJ/m}^2$). 126	
FIGURE 3.39 – NUMERICAL MODEL OF THE FOUR-POINT BENDING TEST	126
FIGURE 3.40 – COMPARISON OF FORCE-DISPLACEMENT CURVES FOR SEAWATER SATURATED COUPON WITH DIFFERENT VALUES OF G_{Ic} (MESH = 1.5MM).....	127
FIGURE 3.41 – COMPARISON BETWEEN EXPERIMENT AND SIMULATION OF THE 4 POINTS BENDING TEST	128
CHAPTER 4 – INFLUENCE OF AGING ON C/EPOXY IMPACT BEHAVIOR	130
FIGURE 4.1 – EFFECTS OF LOADING-RATE ON THE STRESS VS. STRAIN CURVES FOR AN UNAGED EPOXY COUPON IN TENSION.....	133
FIGURE 4.2 – STRESS VS. STRAIN CURVES COMPARISON FOR UNAGED AND AGED EPOXY COUPON TESTED AT $V_1=1\text{MM}/\text{MIN}$, $V_2=10\text{MM}/\text{MIN}$, $V_3=100\text{MM}/\text{MIN}$ AND $V_4=1000\text{MM}/\text{MIN}$	134
FIGURE 4.3 – EFFECT OF LOADING-RATE ON THE TENSILE STRENGTH BEHAVIOR OF UNAGED AND AGED COUPONS.....	134
FIGURE 4.4 – EFFECT OF LOADING-RATE ON THE SHEAR STRENGTH BEHAVIOR OF UNAGED AND AGED COUPONS.....	134
FIGURE 4.5 – EFFECT OF LOADING-RATE ON THE TENSILE STRENGTH OF UNAGED AND AGED TRANSVERSE C/EPOXY COUPONS	135
FIGURE 4.6 – EFFECT OF LOADING-RATE ON THE IN-PLANE SHEAR MODULUS	136
FIGURE 4.7 – MODE I FRACTURE TOUGHNESS CHANGE FROM 1 TO 1000 MM/MIN	136
FIGURE 4.8 – OLD DROP WEIGHT IMPACT TOWER USED FOR PRELIMINARY TESTS	138
FIGURE 4.9 – FORCE VS. TIME CURVES FOR IMPACTS ON THE OLD DROP WEIGHT IMPACT TOWER.....	138
FIGURE 4.10 – NEW DROP WEIGHT IMPACT TOWER WITH IMPROVED STIFFNESS AND NEW SENSORS.....	139
FIGURE 4.11 – FORCE VS. TIME CURVES FOR IMPACTS WITH THE NEW DROP WEIGHT IMPACT TOWER.....	139
FIGURE 4.12 – CHANGE OF THE EXPERIMENTAL FORCE AND OUT-OF-PLANE DISPLACEMENT IN THE FIRST MOMENTS OF THE IMPACT	140
FIGURE 4.13 – FORCE-TIME PLOT COMPARISON FOR THE REJUVENATED STATE AT DIFFERENT ENERGY LEVELS.....	141
FIGURE 4.14 – FORCE PEAK AND OUT-OF-PLANE DISPLACEMENT PEAK AVERAGES FOR REJUVENATED COUPONS AT 7 ENERGY LEVELS	141
FIGURE 4.15 – COMPARISON OF THE DELAMINATION FOR REJUVENATED COUPONS IMPACTED AT 5J, 15J, 25J AND 35J	142
FIGURE 4.16 – COMPARISON OF THE DELAMINATION FOR REJUVENATED COUPONS IMPACTED AT 45J, 60J AND 80J	142
FIGURE 4.17 – FORCE VS. OUT-OF-PLANE DISPLACEMENT PLOTTED TO DETERMINE THE IMPACT ENERGY.....	143
FIGURE 4.18 – BALANCE OF ENERGY DURING THE IMPACT TEST	143
FIGURE 4.19 – COMPARISON OF THE BALANCE OF ENERGY FOR REJUVENATED COUPONS IMPACTED FROM 5J TO 80J	144
FIGURE 4.20 – EFFECT OF IMPACT ENERGY ON THE INCREASE OF ABSORBED ENERGY	144
FIGURE 4.21 – DELAMINATION OBSERVED WITH AN OPTICAL MICROSCOPE FOR REJUVENATED COUPON IMPACTED AT 15J	145
FIGURE 4.22 – STITCHING IN THE -45/45 FABRIC.....	145
FIGURE 4.23 – INTERLAMINAR AND INTRALAMINAR FRACTURE OBSERVED AT 80J	145
FIGURE 4.24 – POROSITIES OBSERVED BETWEEN CARBON FIBER YARNS IN A +45° PLY	146
FIGURE 4.25 – DELAMINATION OBSERVED IN THE LENGTH (TOP) AND WIDTH DIRECTION (BOTTOM) FOR AN UNAGED COUPON IMPACTED AT 30J	146

FIGURE 4.26 – SEGREGATION OF THE MESH TO AVOID PLY DAMAGE CLOSE TO THE FREE EDGES	148
FIGURE 4.27 –EXAMPLE OF AN ORTHO MESH.....	148
FIGURE 4.28 – ORTHO ELEMENT DEFINITION WITH THE COORDINATES OF ALL EIGHT NODES.....	149
FIGURE 4.29 – EXAMPLE OF A MESH WITH ORIENTED ELEMENTS	149
FIGURE 4.30 – ORIENT ELEMENT DEFINITION WITH THE COORDINATES OF ALL EIGHT NODES	150
FIGURE 4.31 – COMPARISON EXP/SIM OF FORCE VS. OUT-OF-PLANE DISPLACEMENT CURVES FOR A REJUVENATED COUPON IMPACTED AT 5J	152
FIGURE 4.32 – COMPARISON EXP/SIM OF FORCE VS. OUT-OF-PLANE DISPLACEMENT CURVES FOR A REJUVENATED COUPON IMPACTED AT 15J	152
FIGURE 4.33 – COMPARISON EXP/SIM OF FORCE VS. OUT-OF-PLANE DISPLACEMENT CURVES FOR A REJUVENATED COUPON IMPACTED AT 25J	153
FIGURE 4.34 – COMPARISON EXP/SIM OF FORCE VS. OUT-OF-PLANE DISPLACEMENT CURVES FOR A REJUVENATED COUPON IMPACTED AT 35J	153
FIGURE 4.35 – CHANGE OF THE ENERGY BALANCE FOR A REJUVENATED COUPON IMPACTED AT 5J	154
FIGURE 4.36 – CHANGE OF THE ENERGY BALANCE FOR A REJUVENATED COUPON IMPACTED AT 15J	154
FIGURE 4.37 – CHANGE OF THE ENERGY BALANCE FOR A REJUVENATED COUPON IMPACTED AT 25J	154
FIGURE 4.38 – CHANGE OF THE ENERGY BALANCE FOR A REJUVENATED COUPON IMPACTED AT 35J	154
FIGURE 4.39 – EXPERIMENTAL DELAMINATION COMPARED WITH PREDICTION FOR IMPACTS FROM 5J TO 35J (EXP/STANDARD MESH/ORIENTED MESH)	155
FIGURE 4.40 – EFFECTS OF AGING ON THE FORCE VS. OUT-OF-PLANE DISPLACEMENT CURVES FOR COUPONS IMPACTED AT 5J.....	156
FIGURE 4.41 – EFFECTS OF AGING ON THE FORCE VS. OUT-OF-PLANE DISPLACEMENT CURVES FOR COUPONS IMPACTED AT 15J.....	156
FIGURE 4.42 – EFFECTS OF AGING ON THE FORCE VS. OUT-OF-PLANE DISPLACEMENT CURVES FOR COUPONS IMPACTED AT 25J.....	157
FIGURE 4.43 – EFFECTS OF AGING ON THE FORCE VS. OUT-OF-PLANE DISPLACEMENT CURVES FOR COUPONS IMPACTED AT 35J.....	157
FIGURE 4.44 – EFFECT OF THE AGING ON THE FORCE PEAK CHANGE WITH THE IMPACT ENERGY.....	157
FIGURE 4.45 – EFFECT OF THE AGING ON THE DEFLECTION CHANGE WITH THE IMPACT ENERGY	157
FIGURE 4.46 – C-SCANS RESULTS ON IMPACTED PHYSICALLY AGED COUPONS (FROM LEFT TO RIGHT: 5J, 15J, 25J AND 35J).....	158
FIGURE 4.47 – C-SCANS RESULTS ON IMPACTED SEAWATER SATURATED COUPONS (FROM LEFT TO RIGHT: 5J, 15J, 25J AND 35J)	158
FIGURE 4.48 – EFFECTS OF AGING ON THE ENERGY BALANCE FOR A 5J IMPACT.....	159
FIGURE 4.49 – EFFECTS OF AGING ON THE ENERGY BALANCE FOR A 15J IMPACT.....	159
FIGURE 4.50 – EFFECTS OF AGING ON THE ENERGY BALANCE FOR A 25J IMPACT.....	159
FIGURE 4.51 – EFFECTS OF AGING ON THE ENERGY BALANCE FOR A 35J IMPACT.....	159
FIGURE 4.52 - EFFECT OF AGING ON THE ABSORBED ENERGY FOR IMPACT ENERGY IN THE RANGE 0-80J.....	160
FIGURE 4.53 – 0/0 DELAMINATION FOR A PHYSICALLY AGED COUPON IMPACTED AT 15J	161
FIGURE 4.54 – 0/0 DELAMINATION FOR A SEAWATER SATURATED COUPON IMPACTED AT 15J	161
FIGURE 4.55 – TOMOGRAPHY ON THE LENGTH (TOP) AND WIDTH (BOTTOM) DIRECTION OF A SEAWATER SATURATED COUPON IMPACTED AT 5J	161
FIGURE 4.56 – TOMOGRAPHY ON THE LENGTH (TOP) AND WIDTH (BOTTOM) DIRECTION OF A SEAWATER SATURATED COUPON IMPACTED AT 30J	162
FIGURE 4.57 – COMPARISON OF THE FORCE VS. DEFLECTION CURVES BETWEEN THE EXPERIMENT AND THE SIMULATION FOR PHYSICALLY AGED COUPONS IMPACTED AT 5J (TOP LEFT), 15J (TOP RIGHT), 25J (BOTTOM LEFT) AND 35J (BOTTOM RIGHT)	164

FIGURE 4.58 – COMPARISON OF THE FORCE VS. DEFLECTION CURVES BETWEEN THE EXPERIMENT AND THE SIMULATION FOR SEAWATER AGED COUPONS IMPACTED AT 5J (TOP LEFT), 15J (TOP RIGHT), 25J (BOTTOM LEFT) AND 35J (BOTTOM RIGHT)	164
FIGURE 4.59 – COMPARISON OF THE ENERGY BALANCE BETWEEN THE EXPERIMENT AND THE SIMULATION FOR PHYSICALLY AGED COUPONS IMPACTED AT 5J (TOP LEFT), 15J (TOP RIGHT), 25J (BOTTOM LEFT) AND 35J (BOTTOM RIGHT)	165
FIGURE 4.60 – COMPARISON OF THE ENERGY BALANCE BETWEEN THE EXPERIMENT AND THE SIMULATION FOR SEAWATER AGED COUPONS IMPACTED AT 5J (TOP LEFT), 15J (TOP RIGHT), 25J (BOTTOM LEFT) AND 35J (BOTTOM RIGHT)	166
CHAPTER 5 – TOWARDS MORE REPRESENTATIVE TESTS FOR COMPOSITE PROPELLERS	170
FIGURE 5.1 – PROPELLER BLADE SECTION, FROM THE RAMSSES PROJECT (©NAVAL GROUP).....	172
FIGURE 5.2 – CAI FORCE VS. DISPLACEMENT FOR SEAWATER SATURATED COUPONS	173
FIGURE 5.3 – CAI STRESS VS. AXIAL STRAINS FOR A CAI TEST OF A SEAWATER SATURATED COUPON IMPACTED AT 5J	174
FIGURE 5.4 – IMAGES OF A FAILURE DUE TO A FIBER YARN MICRO BUCKLING FOR AN UNAGED (LEFT) AND SEAWATER S<ATURATED (RIGHT) COUPONS IMPACTED AT 60J	175
FIGURE 5.5 – CAI RESIDUAL STRENGTH FOR IMPACTS FROM 5J TO 80J FOR 3 AGING CONDITIONS	175
FIGURE 5.6 – SEAWATER SATURATED COUPON IMPACTED AT 75J (SIDE OF THE COUPON FAR FROM THE IMPACT POINT)	176
FIGURE 5.7 – MICRO BUCKLING DUE TO TRANSVERSE STITCHING	176
FIGURE 5.8 – FAILURE OF THE QUASI-ISOTROPIC COUPON DUE TO THE EXTERNAL PLY FAILURE	177
FIGURE 5.9 – COMPARISON BETWEEN THE MATERIAL AND THE STRUCTURAL STRENGTH FOR ALL AGING	178
FIGURE 5.10 – PREMATURE FAILURE OF A REJUVENATED COUPON IMPACTED AT 5J (TOP LEFT CORNER)	178
FIGURE 5.11 – CURVED COUPON WITH FLAT FLANGE TAKEN BY A HIGH-SPEED CAMERA (TOP: BEFORE THE IMPACT / BOTTOM: DURING THE IMPACT WITH DELAMINATION)	180
FIGURE 5.12 – STITCHING TORN OFF BY THE IMPACT (15J ON Φ 70MM)	182
FIGURE 5.13 – COMPARISON OF THE FORCE AND DEFLECTION DATA FOR AN IMPACT OF 15J ON A CURVED COUPON WITH A DIAMETER OF 70MM	182
FIGURE 5.14 – COMPARISON OF DEFLECTION PEAK FOR CURVED COUPONS IMPACTED FROM 7J TO 17J	182
FIGURE 5.15 – PROJECTED DELAMINATION OF Φ 30MM CURVED COUPONS IMPACTED (FROM LEFT TO RIGHT: 7J, 12J AND 17J)	183
FIGURE 5.16 – C-SCAN RESULTS OF Φ 50MM AND Φ 70MM CURVED COUPONS IMPACTED (FROM LEFT TO RIGHT: 7J, 12J AND 17J)..	184
FIGURE 5.17 – DAMAGE OBSERVED IN CURVED COUPONS IMPACTED AT 17J. FROM TOP TO BOTTOM: Φ 30MM, Φ 50MM AND Φ 70MM	185
FIGURE 5.18 – DAMAGE OBSERVED ON A Φ 50MM CURVED COUPON IMPACTED AT 7J.....	185
FIGURE 5.19 – COMPARISON OF FORCE VS. CONTACT TIME FOR COUPONS IMPACTED AT FOUR ENERGY LEVELS IN THE IN-PLANE DIRECTION	187
FIGURE 5.20 – CRUSH DEBRIS EJECTED DURING THE IMPACTOR REBOUND FOR AN UNAGED COUPON IMPACTED AT 330J, HIGH SPEED CAMERA IMAGE	187
FIGURE 5.21 – COMPARISON OF THE PEAK FORCE BETWEEN UNAGED AND SEAWATER SATURATED COUPONS AGED UP TO 330J	188
FIGURE 5.22 – COMPARISON OF THE MAXIMAL PENETRATION BETWEEN UNAGED AND SEAWATER SATURATED COUPONS AGED UP TO 330J	188
FIGURE 5.23 – COMPARISON OF DELAMINATION EXTENT IN UNAGED AND SEAWATER SATURATED COUPONS IMPACTED IN THE IN-PLANE DIRECTION FROM 20J TO 330J	189
FIGURE 5.24 – POLISHED SECTIONS OF UNAGED (LEFT) AND SEAWATER SATURATED (RIGHT) COUPONS IMPACTED AT 330J	189

FIGURE 5.25 – PHOTO OF A COUPON IMPACTED IN THE IN–PLANE DIRECTION AT 330J	190
FIGURE 5.26 – PHOTO OF COUPONS IMPACTED FROM 8J TO 300J	190
FIGURE 5.27 – FORCE VS. TIME CURVES FOR LEADING EDGES IMPACTED FROM 24J TO 160J	191
FIGURE 5.28 – COMPARISON OF DAMAGE OBSERVED FOR IMPACTS UP TO 160J ON LEADING EDGE	191
FIGURE 5.29 – COMPARISON OF THE MAXIMAL PENETRATION IN THE LEADING EDGE FOR IMPACTS AT 50J (LEFT) AND 330J (RIGHT) : THE PRESENCE OF CFRP DEBRIS GENERATED BY THE IMPACT IS VISIBLE AT 330J, HIGH SPEED CAMERA IMAGES	191
FIGURE 5.30 – ENERGY BALANCE FOR LEADING EDGES IMPACTED AT 35J, 50J, 70J AND 100J	192
FIGURE 5.31 – COMPRESSIVE STRAIN MEASURED ON LEADING–EDGES IMPACTED AT 35J, 50J AND 70J	193
FIGURE 5.32 – DELAMINATION OF THE EXTERNAL PLY DUE TO THE IMPACT AT 100J.....	194
CONCLUSIONS & PERSPECTIVES	196
LIST OF FIGURES	201
LIST OF TABLES	209
APPENDIX 1 – C-SCANS OF AGED C/EPOXY COUPON IMPACTED FROM 5J TO 80J.....	211
FIGURE A.1 – C-SCANS OF PHYSICALLY AGED COUPONS IMPACTED (FROM LEFT TO RIGHT) : (TOP) 5J, 15J, 25J, 35J (BOTTOM) 45J, 60J AND 80J.....	211
FIGURE A.2 – C-SCANS OF SEAWATER SATURATED COUPONS IMPACTED (FROM LEFT TO RIGHT) : (TOP) 5J, 15J, 25J, 35J (BOTTOM) 45J, 60J AND 80J.....	211
APPENDIX 2 – COMPARISON EXP/SIM FOR UNAGED COUPONS.....	212
APPENDIX 3 – COMPARISON EXP/SIM FOR PHYSICALLY AGED COUPONS	214
APPENDIX 4 – COMPARISON EXP/SIM FOR SEAWATER SATURATED COUPONS.....	216
APPENDIX 5 – EXTENDED FRENCH ABSTRACT	218
FIGURE A.3 – PRISE EN EAU EN FONCTION DU TEMPS D’IMMERSION NORMALISE PAR L’EPAISSEUR DES ECHANTILLONS : COMPARAISON EXPERIMENTAL/MODELE DE FICK.....	219
FIGURE A.4 – CONCENTRATION MOYENNE EN EAU DE PLIS DE COMPOSITES D’UNE SECTION DE 15MM VIEILLIE A 15°C	219
FIGURE A.5 – ÉVOLUTION DES MODULES DE CISAILLEMENT EN FONCTION DU VIEILLISSEMENT	220
FIGURE A.6 – COMPARAISON Exp/SIM POUR L’ESSAI DE FLEXION 4 POINTS.....	221
FIGURE A.7 – COMPARAISON FORCE–TEMPS POUR DES ESSAIS D’IMPACT HORS–PLAN DE 5J A 25J	222
FIGURE A.8 – CONTROLES US REALISES SUR DES EPROUVETTES NON VIEILLIES IMPACTEES A 5J, 15J, 25J ET 35J (DE GAUCHE A DROITE)	222
FIGURE A.9 – CONTROLES US REALISES SUR DES EPROUVETTES VIEILLIES ET SATUREES EN EAU DE MER IMPACTEES A 5J, 15J, 25J ET 35J (DE GAUCHE A DROITE)	223
FIGURE A.10 – VUE DE COTE D’UNE EPROUVETTE VIEILLIE EN EAU DE MER IMPACTEE A 30J.....	223
FIGURE A.11 – 0/0 DELAMINATION IN THE MID–THICKNESS OF A COUPON SATURATED AND IMPACTED AT 15J	224
FIGURE A.12 – COMPARAISON Exp/SIM DES COURBES FORCE–TEMPS D’UN MATERIAU NON VIEILLI IMPACTE A 15J.....	225
FIGURE A.13 – COMPARAISON Exp/SIM DES COURBES DEFLECTION–TEMPS D’UN MATERIAU NON VIEILLI IMPACTE A 15J	225
FIGURE A.14 – COMPARAISON DU DELAMINAGE EXPERIMENTAL (GAUCHE) AUX DELAMINAGES PREDITS PAR LE MAILLAGE ORIENTE (CENTRE) ET STANDARD (DROITE) POUR UN IMPACT DE 15J SUR UNE EPROUVETTE NON VIEILLIE.....	225

FIGURE A.15 – COMPARAISON EXP/SIM DES COURBES FORCE–TEMPS D’UN MATERIAU NON VIEILLI IMPACTE A 35J	226
FIGURE A.16 – COMPARAISON EXP/SIM DES COURBES DEFLECTION–TEMPS D’UN MATERIAU NON VIEILLI IMPACTE A 35J	226
FIGURE A.17 – COMPARAISON DU DELAMINAGE EXPERIMENTAL (GAUCHE) AUX DELAMINAGES PREDITS PAR LE MAILLAGE ORIENTE (CENTRE) ET STANDARD (DROITE) POUR UN IMPACT DE 35J SUR UNE EPROUVETTE NON VIEILLIE	226
FIGURE A.18 – COMPARAISON ENTRE LA CONTRAINTE RESIDUELLE POST–IMPACT ET LA CONTRAINTE MAXIMALE DONNEE PAR UN ESSAI DE COMPRESSION UNIAXIALE	227
FIGURE A.19 – CONTROLES US REALISES SUR LES EPROUVETTES COURBEES DE Φ 50MM (HAUT) ET Φ 70MM (BAS) IMPACTEES (DE GAUCHE A DROITE) A 5J, 10J ET 15J	228
FIGURE A.20 – EPROUVETTE IMPACTEE DANS LE PLAN A 330J	228
FIGURE A.21 – EVOLUTION DE LA FORCE MAXIMALE MESUREES EN FONCTION DE L’ENERGIE D’IMPACT	228
FIGURE A.22 – COMPARAISON DES COURBES FORCE–TEMPS POUR DES IMPACTS SUR BORDS D’ATTAQUE POUR DES ENERGIES DE 24J A 160J	229
FIGURE A.23 – COMPARAISON DU BORD D’ATTAQUE IMPACTE DE 24J A 160J	229
APPENDIX 6 – SCIENTIFIC CONTRIBUTIONS	232
REFERENCES	233

List of tables

CHAPTER 1 – STATE OF THE ART	12
TABLE 1.1 – DEVELOPMENT SITES AND PROCUREMENT OF THE EU FUNDED TIDAL STREAM INDUSTRY ENERGISER PROJECT (TIGER)	18
TABLE 1.2 – BUILD UP OF FIRST-ORDER FATIGUE CYCLES ON A BLADE OF PROPELLER [19]	21
TABLE 1.3 – TYPE OF IMPACTS DEPENDING ON VELOCITY RANGE [73]	30
TABLE 1.4 – ADVANTAGES AND DRAWBACKS OF TS AND TP COMPOSITES [89]	34
TABLE 1.5 – ADVANTAGES AND DRAWBACKS GIVEN FOR THREE NUMERICAL ANALYSIS TECHNIQUES [164].....	49
TABLE 1.6 – TEMPERATURE RANGE OF SOLVENT AGEING AND IMPACT ON POLYMER PROPERTIES	59
CHAPTER 2 – MATERIALS AND METHODS	64
TABLE 2.1 – PANELS MANUFACTURED AND PROPERTIES MEASURED	67
TABLE 2.2 – EQUATIONS USED TO DETERMINE THE EQUIVALENT STRESS AND DISPLACEMENT.....	91
CHAPTER 3 – INFLUENCE OF AGING ON QUASI-STATIC MECHANICAL PROPERTIES.....	94
TABLE 3.1 – RESULTS OF FICKIAN MODELING OF PURE EPOXY AND C/EPOXY AGEING DATA (*EXTRAPOLATED VALUE)	98
TABLE 3.2 – THERMAL CONDUCTIVITY DATA USED TO PREDICT THE WATER PROFILE IN THE COMPOSITE BLADE	101
TABLE 3.3 – COMPARISON OF WATER PROFILES FOR DIFFERENT PATHS IN THE BLADE	103
TABLE 3.4 – CHANGE OF THE IN-PLANE MECHANICAL PROPERTIES WITH THE AGING CONDITIONS.....	105
TABLE 3.5 – C/EPOXY IN-PLANE STRENGTH BEFORE AND AFTER AGING	107
TABLE 3.6 – IN-PLANE COMPRESSION STRESS AT FAILURE WITH THE AGING	108
TABLE 3.7 – THREE-POINT BENDING MODULUS AND STRENGTH AS A FUNCTION OF AGING	110
TABLE 3.8 - FOUR-POINT BENDING MODULUS AND STRENGTH AS A FUNCTION OF AGING	111
TABLE 3.9 – OUT-OF-PLANE SHEAR PROPERTIES OF THE C/EPOXY STUDIED BEFORE AND AFTER AGING.....	112
TABLE 3.10 – OUT-OF-PLANE POISSON RATIO OF THE C/EPOXY STUDIED BEFORE AND AFTER AGING	113
TABLE 3.11 – EPOXY ULTIMATE PROPERTIES VERSUS AGING.....	114
TABLE 3.12 – AVERAGED MODE I FRACTURE TOUGHNESS FOR PROPAGATION.....	118
TABLE 3.13 – MIXED MODE PROPAGATION FRACTURE TOUGHNESS G_c AS A FUNCTION OF AGING AND MODE II CONTRIBUTION.....	119
TABLE 3.14 – AVERAGED MODE II FRACTURE TOUGHNESS FOR PROPAGATION	120
TABLE 3.15 – MIXED-MODE FRACTURE TOUGHNESS VALUES AND FIT PARAMETER FOR THE BK CRITERION	120
TABLE 3.16 – EXPERIMENTAL VALUES NORMALIZED WITH THE REJUVENATED AND DRIED STATE (REFERENCE)	122
TABLE 3.17 – INFLUENCE OF THE AGING ON THE FLEXURAL STRESS AT FAILURE	124
TABLE 3.18 – SUMMARY OF PROPERTIES USED TO PREDICT THE MECHANICAL BEHAVIOR OF THE COUPONS	125
TABLE 3.19 – PROPERTIES USED FOR TRANSLAMINAR DAMAGE PROPAGATION	127
TABLE 3.20 – COMPARISON BETWEEN EXPERIMENTAL AND NUMERICAL BENDING STIFFNESS.....	128
TABLE 3.21 – COMPARISON BETWEEN EXPERIMENTAL AND NUMERICAL BENDING STRESS AT FAILURE	128
CHAPTER 4 – INFLUENCE OF AGING ON C/EPOXY IMPACT BEHAVIOR	130
TABLE 4.1 – COMPARISON OF STRAIN-RATES MEASURED DURING THIS PROJECT.....	137

TABLE 4.2 – NODE ID AND RESPECTIVE COORDINATES TO ASSIGN TO AN ORTHO ELEMENT	149
TABLE 4.3 – NODE ID AND RESPECTIVE COORDINATES TO ASSIGN TO AN ORIENT ELEMENT	150
TABLE 4.4 – PROPERTY AND UNIT USED TO KEEP CONSISTENT UNITS IN ABAQUS™	150
TABLE 4.5 – MECHANICAL PROPERTIES USED FOR THE REJUVENATED STATE IN THE MODEL	151
TABLE 4.6 – MECHANICAL PROPERTIES USED FOR THE PHYSICALLY AGED AND SEAWATER SATURATED STATE IN THE MODEL.....	163
TABLE 4.7 – COMPARISON BETWEEN THE EXPERIMENTAL AND PREDICTED DELAMINATION (STANDARD AND ORIENTED MESHES) FOR AGED COUPONS IMPACTED FROM 5J TO 35J	167
CHAPTER 5 – TOWARDS MORE REPRESENTATIVE TESTS FOR COMPOSITE PROPELLERS.....	170
TABLE 5.1 – ELASTIC COMPRESSION MODULUS AFTER IMPACT, INFLUENCE OF SEAWATER AGING VERSUS REFERENCE	174
TABLE 5.2 – CHANGE OF THE COMPRESSION MATERIAL STRENGTH WITH THE AGING (ASTM 6641)	178
TABLE 5.3 – EXPERIMENTAL IMPACT TESTS ON CURVED PANELS PERFORMED.....	181
TABLE 5.4 – COMPARISON OF THE CONTACT DURATIONS [MS] FOR IMPACTS ON CURVED COUPONS IMPACTED FROM 7J TO 17J.....	183
TABLE 5.5 – COMPARISON OF THE ENERGY BALANCE MEASURED FOR IMPACTS ON LEADING-EDGES	192
TABLE 5.6 – STRAIN-RATES MEASURED FOR IMPACTS AT 35J, 50J AND 70J.....	193
APPENDIX 5 – EXTENDED FRENCH ABSTRACT	218
TABLE A.1 – PROPRIETES ULTIMES DU COMPOSITE EN COMPRESSION	220

Appendix 1 – C-Scans of aged C/Epoxy coupon impacted from 5J to 80J

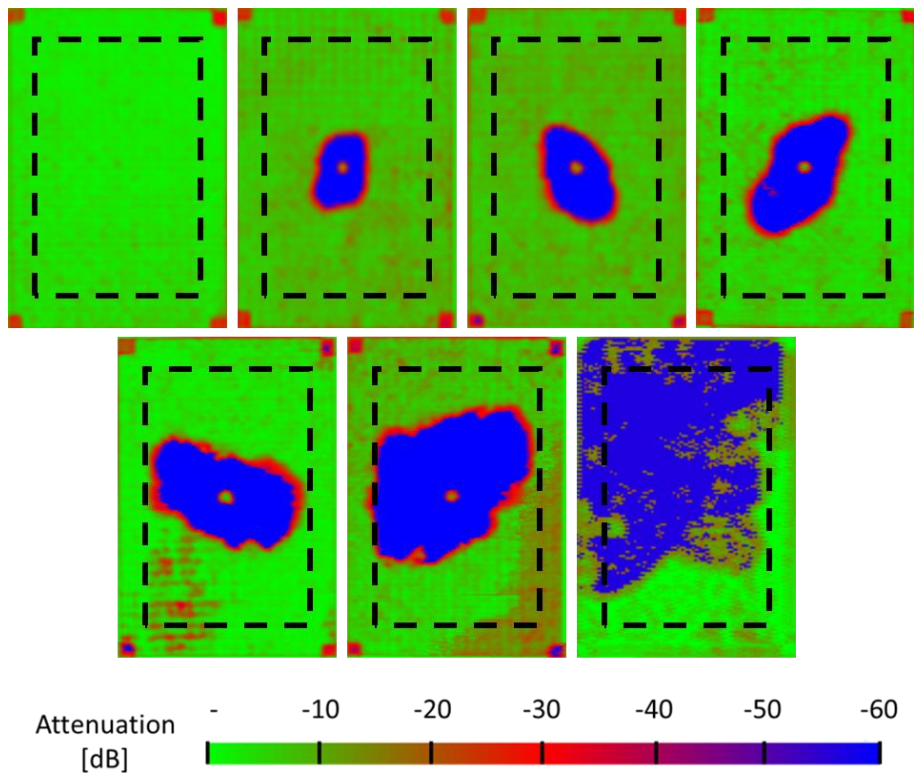


Figure A.1 – C-Scans of physically aged coupons impacted (from left to right) : (Top) 5J, 15J, 25J, 35J (Bottom) 45J, 60J and 80J

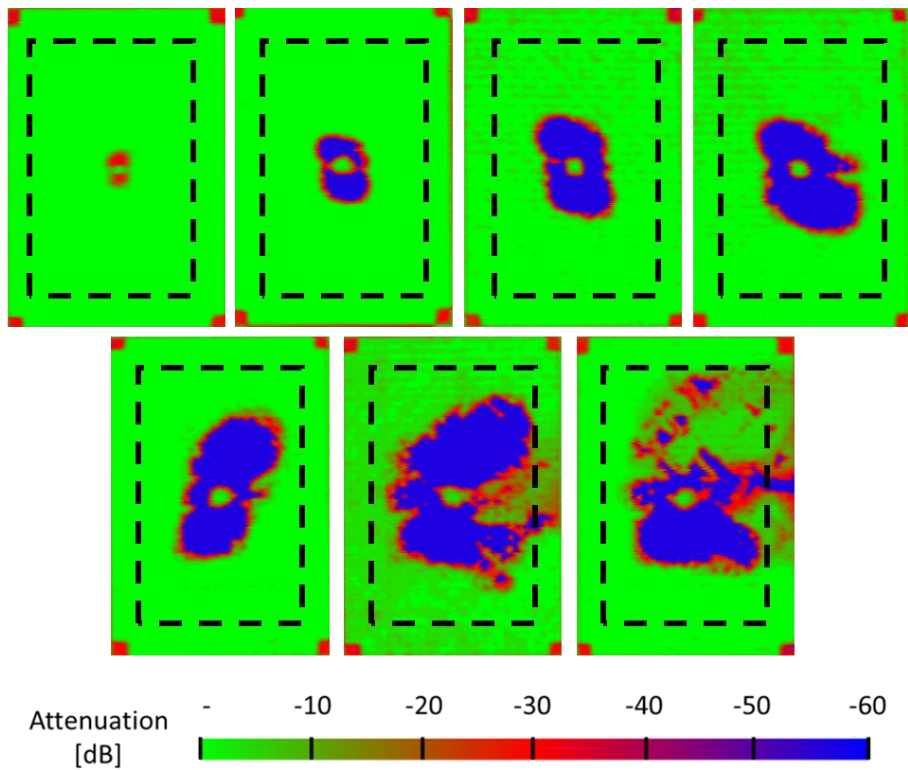
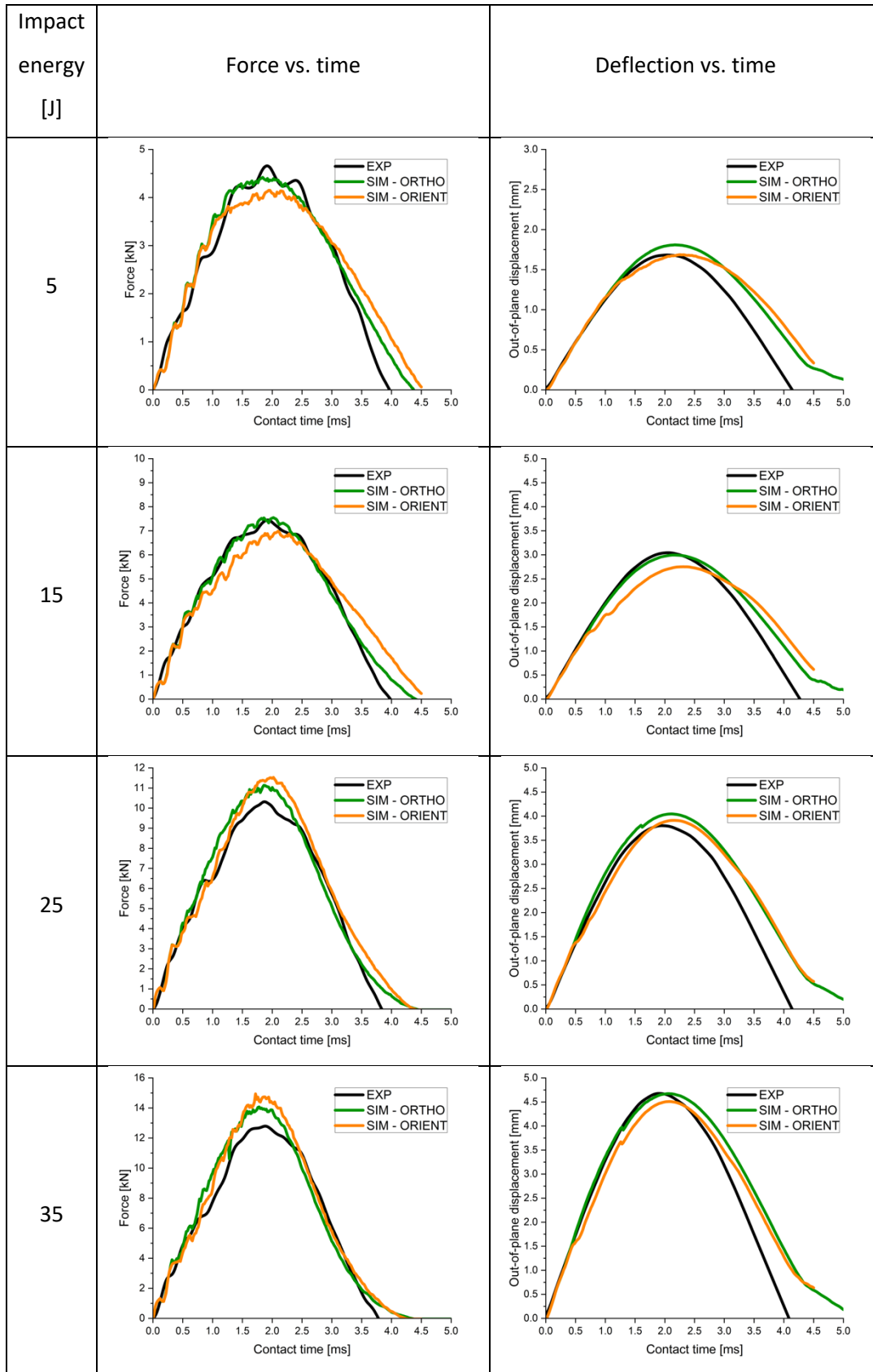
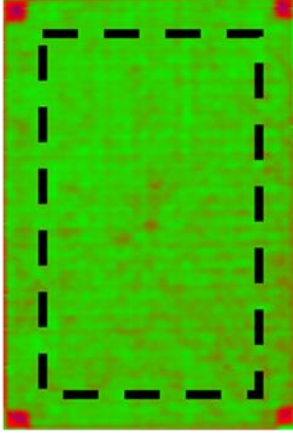
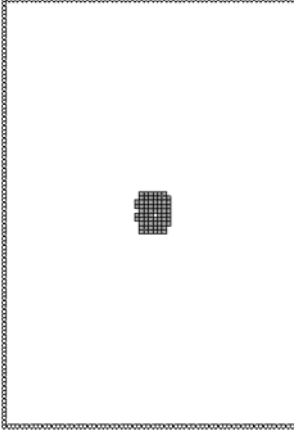
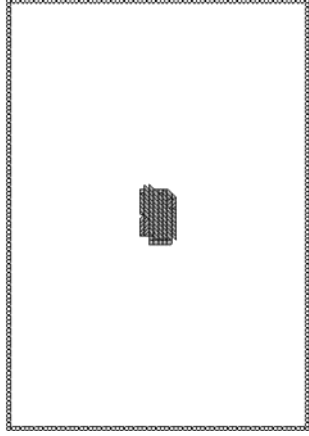
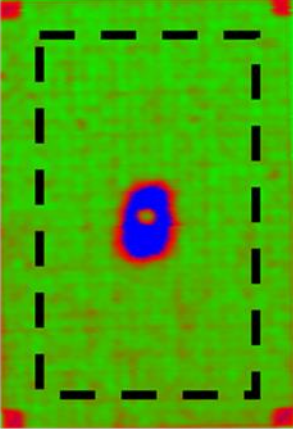
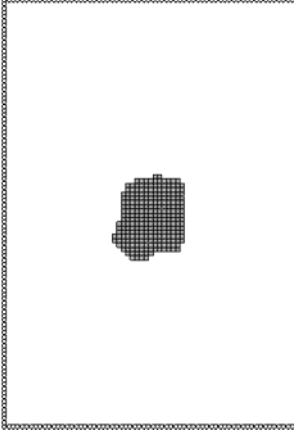
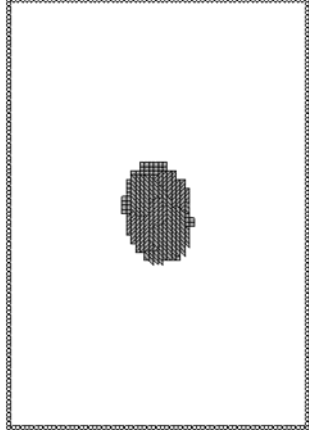
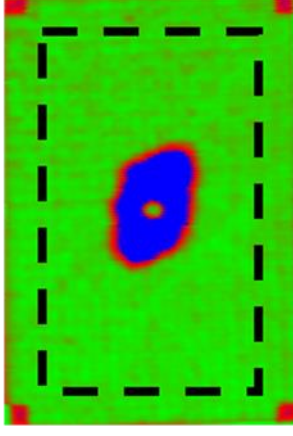
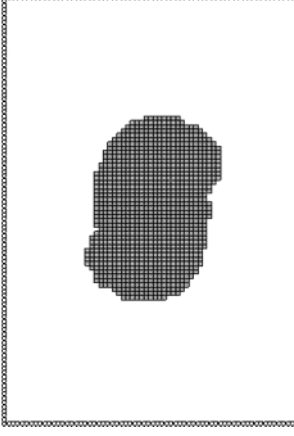
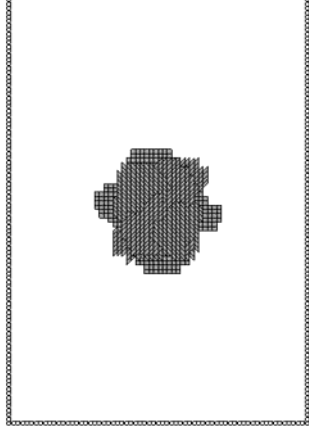
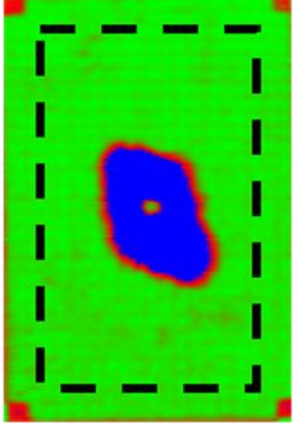
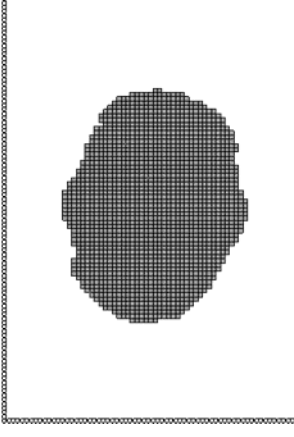
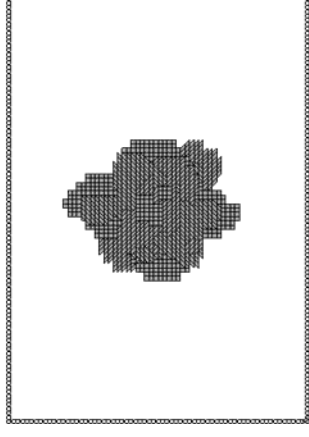


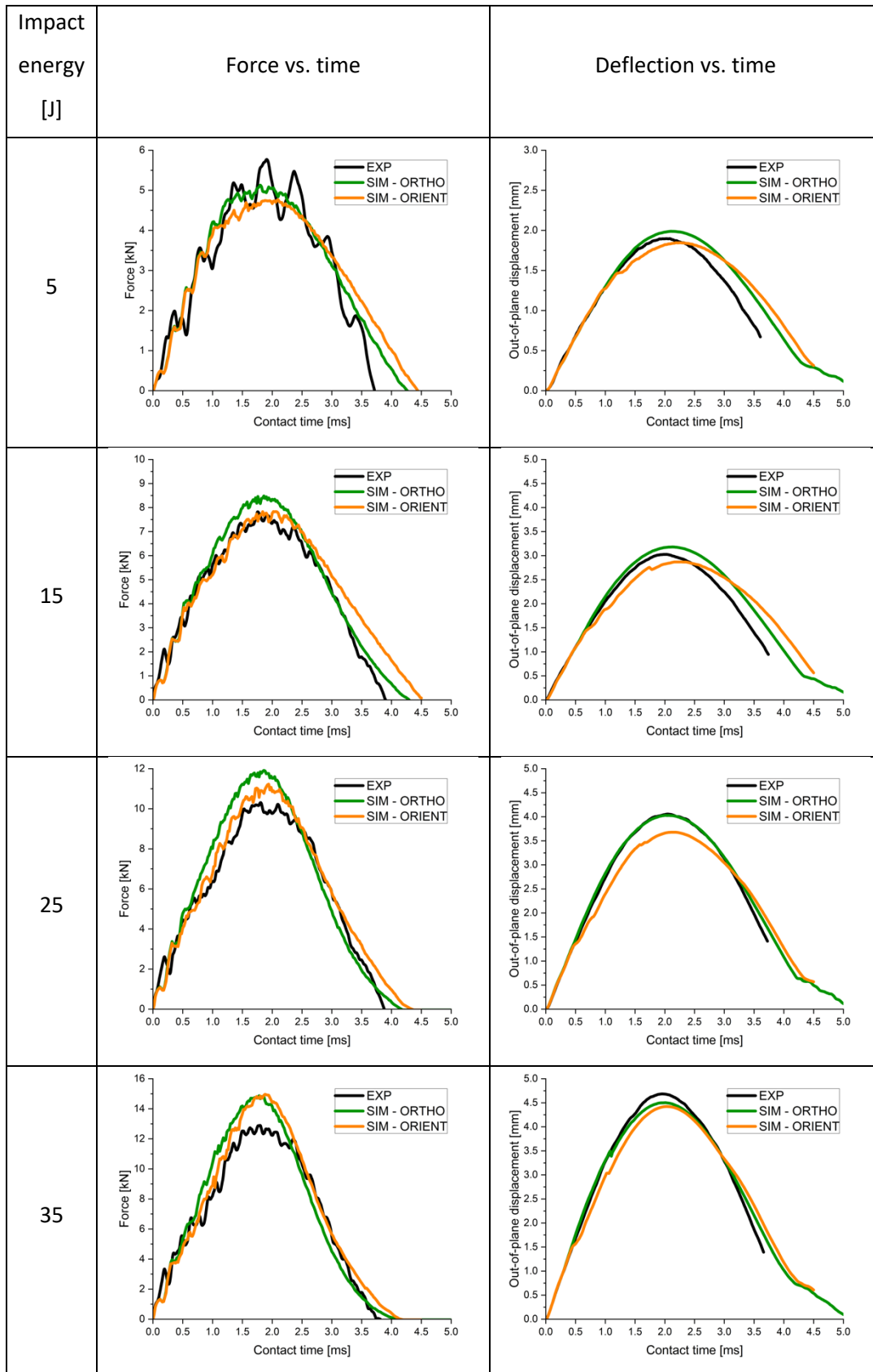
Figure A.2 – C-Scans of seawater saturated coupons impacted (from left to right) : (Top) 5J, 15J, 25J, 35J (Bottom) 45J, 60J and 80J

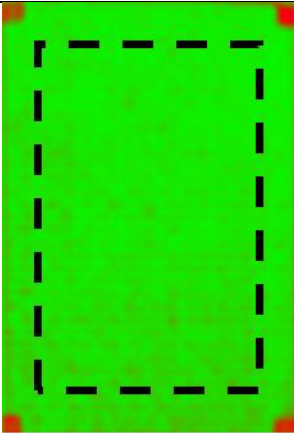
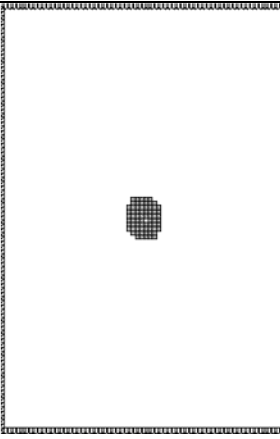
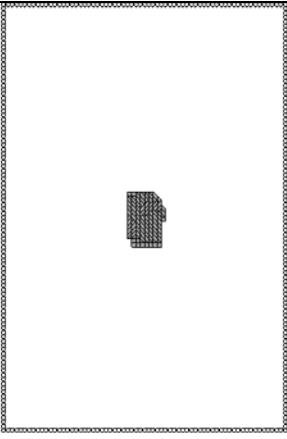
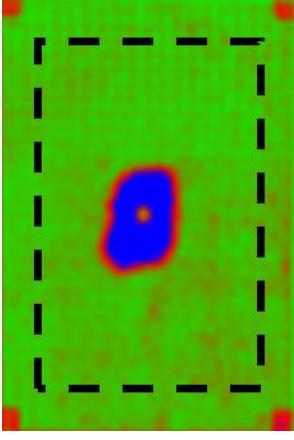
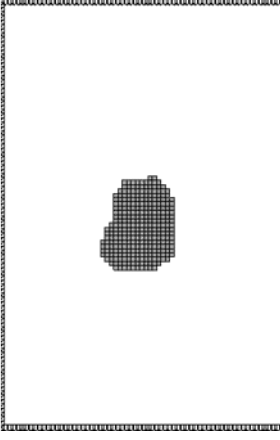
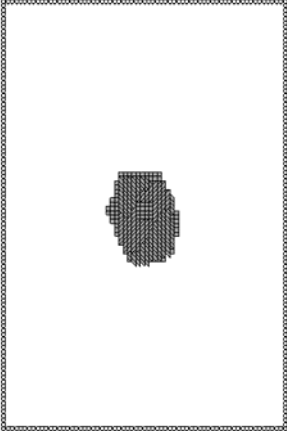
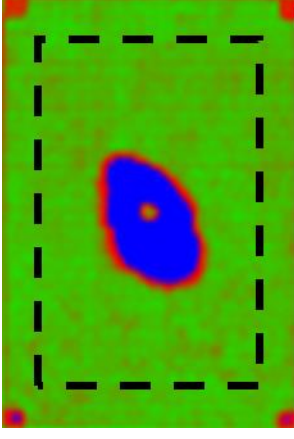
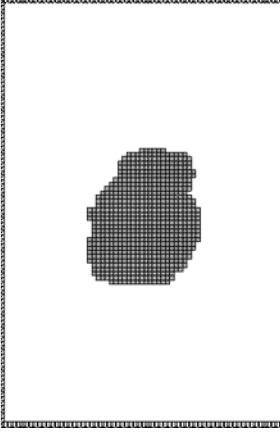
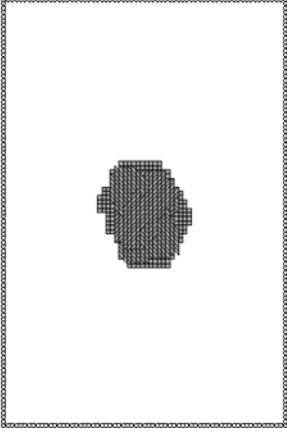
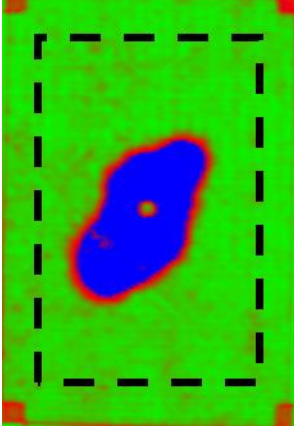
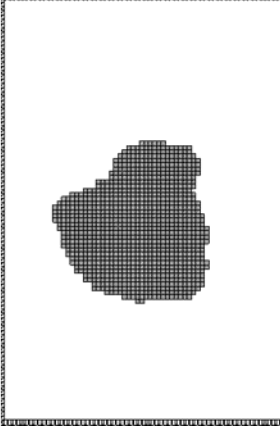
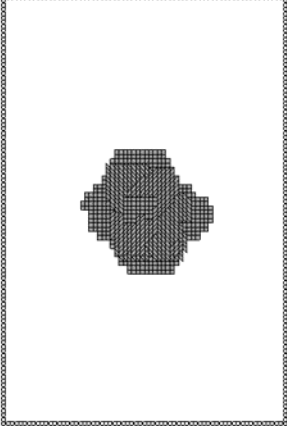
Appendix 2 – Comparison EXP/SIM for unaged coupons



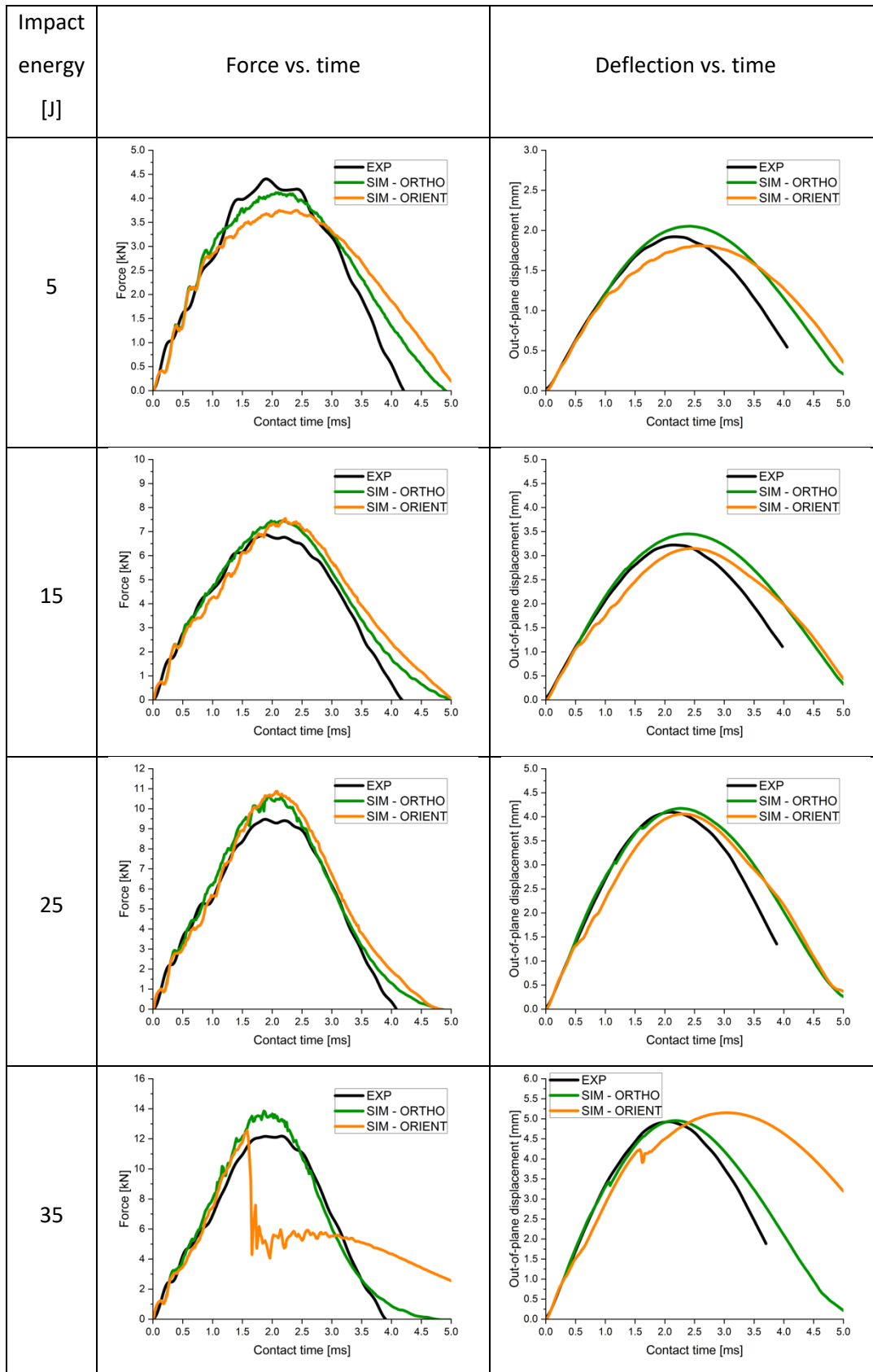
Impact energy [J]	Comparison of the delamination (Exp / Sim_Ortho / Sim_Orient)		
5			
15			
25			
35			

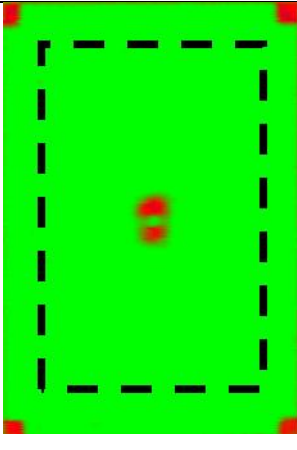
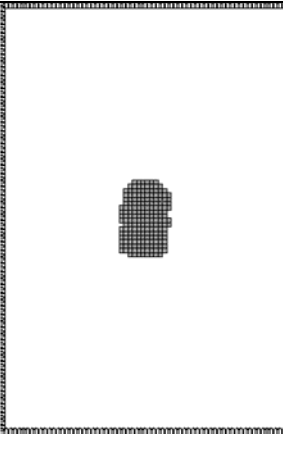
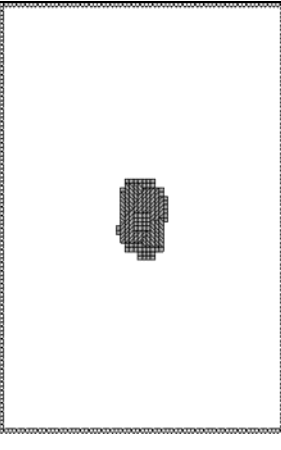
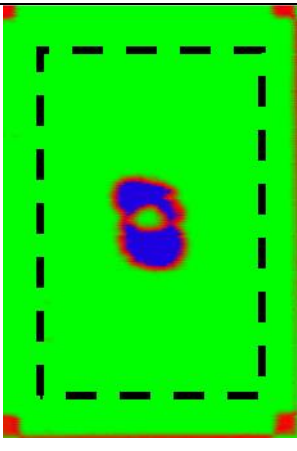
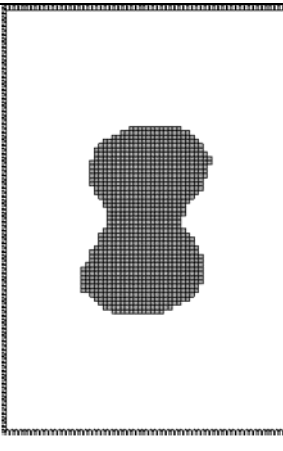
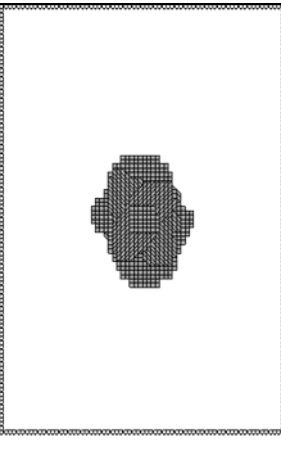
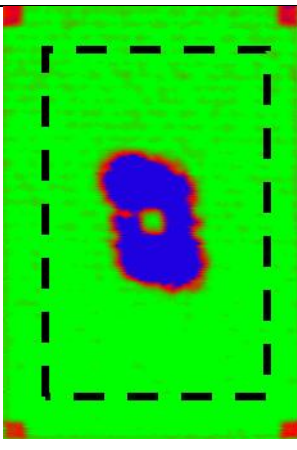
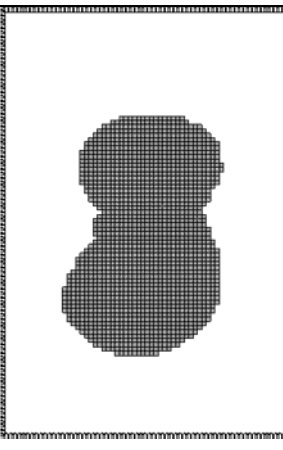
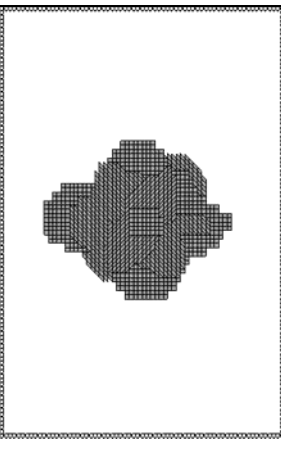
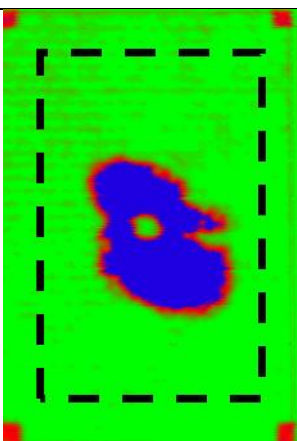
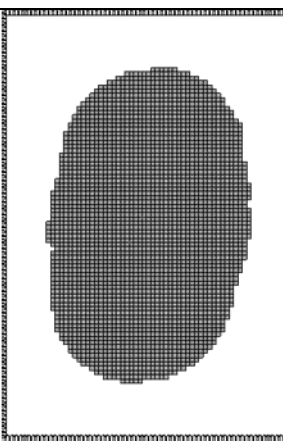
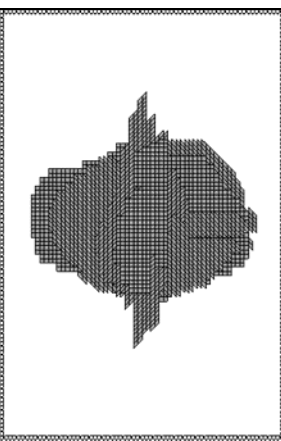
Appendix 3 – Comparison EXP/SIM for physically aged coupons



Impact energy [J]	Comparison of the delamination (Exp / Sim_Ortho / Sim_Orient)		
5			
15			
25			
35			

Appendix 4 – Comparison EXP/SIM for Seawater saturated coupons



Impact energy [J]	Comparison of the delamination (Exp / Sim_Ortho / Sim_Orient)		
5			
15			
25			
35			

Appendix 5 – Extended French abstract

De par leurs propriétés mécaniques spécifiques, les matériaux composites sont de plus en plus utilisés dans l'industrie du transport. Pour l'industrie navale, les matériaux métalliques historiques sont peu à peu remplacés par des composites hautes performances. Ces matériaux ont comme renfort des fibres de carbone et comme matrice des résines thermodurcissables, telles les résines Epoxy, ou des résines thermoplastiques, comme le PEEK. De nombreuses pièces ont déjà été fabriquées et sont actuellement utilisées : coques, foils, radomes, superstructures, ... Une application récente est l'hélice de propulsion en composite, qui a déjà fait ses preuves dans le domaine aéronautique (Ratier-Figeac NP2000). Néanmoins, l'utilisation de structures tournantes en milieu marin génère des efforts plus importants du fait de la densité du fluide, mais aussi un vieillissement du matériau lié à son contact permanent avec l'eau de mer.

Cette thèse s'est intéressée à l'influence de vieillissements sur les propriétés mécaniques du matériau. Un état réjuvené et séché a d'abord été étudié. Cet état correspond à un matériau sec et dénué de vieillissement physique. Ensuite, un état vieilli physiquement sous vide à 60°C pendant 30 jours a été étudié. Finalement, un état vieilli en eau de mer jusqu'à saturation a été étudié. Ces vieillissements sont basés sur des travaux antécédents qui ont apporté une première compréhension du comportement du matériau sur le long terme [170].

A.1. Vieillissement en eau de mer

La première étape de ce travail a consisté à immerger des éprouvettes de C/Epoxy de 40x40x4.4 mm³ en eau de mer à différentes températures. Le vieillissement étant accéléré par la température, plus la température est élevée, plus le temps d'immersion nécessaire pour obtenir la saturation sera court. La T_g initiale du matériau étant de 82°C, les températures de 4°C, 15°C, 25°C, 40°C et une température maximale de 60°C ont été choisies. Cette dernière est supposée ne pas engendrer de dégradation chimique irréversible au matériau.

Au cours de leur immersion, les échantillons sont pesés. Une comparaison entre les données expérimentales et le modèle de Fick 1D est présentée Figure A.3. A 60°C, le modèle suit les données expérimentales jusqu'à 7 mois d'immersion. Ensuite, le modèle diverge. Une cause probable est l'endommagement du réseau macromoléculaire à cette température qui engendre une plus grande absorption d'eau. A plus basse température, le modèle est cohérent avec les données expérimentales. Néanmoins, après plus de deux années d'immersion à 40°C, le matériau n'est pas saturé, d'où la nécessité d'un vieillissement à 60°C.

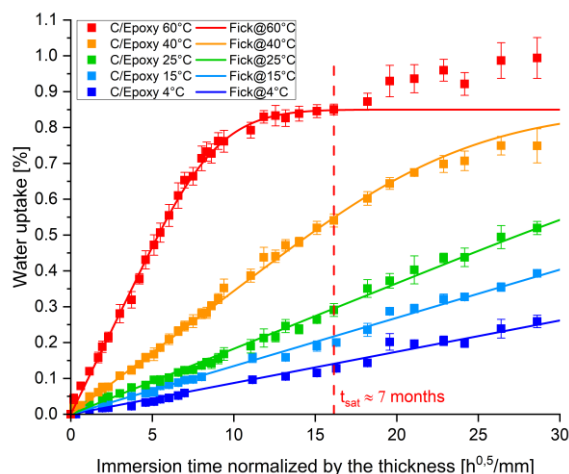


Figure A.3 – Prise en eau en fonction du temps d'immersion normalisé par l'épaisseur des échantillons : comparaison expérimental/modèle de Fick

Le modèle de Fick a été utilisé pour comparer les données expérimentales. Deux propriétés matériaux ont été optimisées pour que le modèle corrèle les données expérimentales : le coefficient de diffusion isotrope D ainsi que la masse à saturation. Ces données ont ensuite été utilisées dans Abaqus™ pour prédire la diffusion d'eau dans un bord d'attaque. Connaissant le drapage initial de la section, il a été possible de définir plis par plis la concentration moyenne en eau. Celles-ci sont présentées en Figure A.4 pour différents temps de vieillissements.

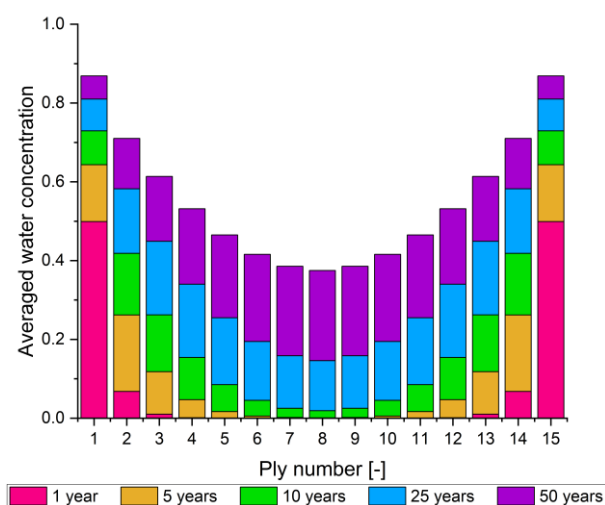


Figure A.4 – Concentration moyenne en eau de plis de composites d'une section de 15mm vieillie à 15°C

Il est à noter que pour cette section, aucun pli n'est saturé en eau, mais qu'après 10 ans d'immersion, tous les plis ont absorbé de l'humidité. Une modélisation du comportement mécanique au plus près des conditions opérationnelles pourrait se faire à partir de données d'essais mécaniques réalisés sur des éprouvettes vieilles et saturées en humidité ($0 < RH < 1$). Néanmoins, ces essais n'ont pas été réalisés durant cette thèse du fait de la multiplication des essais mécaniques et du nombre d'éprouvettes à fabriquer.

A.2. Influence du vieillissement sur les propriétés quasi-statiques

Ce travail de thèse s'est intéressé à l'influence du vieillissement sur les propriétés mécaniques du composite. Pour cela, une importante campagne expérimentale a été réalisée. Des essais de caractérisation du pli ainsi que de l'interface ont permis de mettre en avant le caractère nocif du vieillissement en eau de mer, et dans une moindre mesure celui amélioratif du vieillissement physique.

Tout d'abord, des essais ont été réalisés pour définir l'influence des vieillissements sur la matrice de raideur. Une comparaison des modules de cisaillement en fonction du vieillissement est présentée en Figure A.5. Le vieillissement en eau de mer réduit les modules alors que le vieillissement physique les augmente, excepté pour le G_{23} .

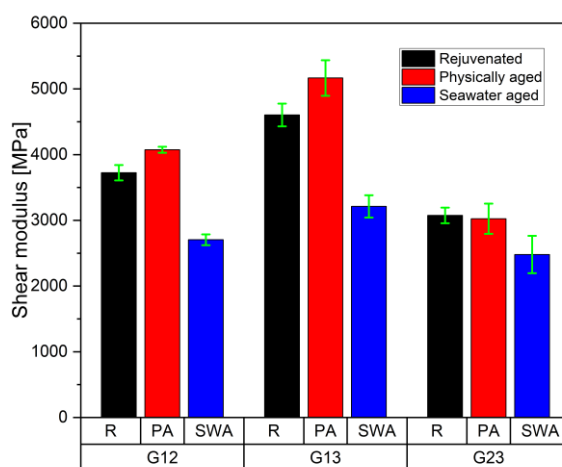


Figure A.5 – Evolution des modules de cisaillement en fonction du vieillissement

Concernant les propriétés ultimes, la Table A.1 présente l'évolution de la contrainte en compression longitudinale et transverse à rupture en fonction du vieillissement. Les données sur l'UD montrent une diminution drastique de 35% de la contrainte de compression à rupture après saturation en eau. Cette baisse est attribuée à la trame en PET dont le but est de maintenir les fibres alignées durant le process de mise en œuvre, mais qui a pour défaut d'onduler les fibres de carbone de chaque pli, menant à une rupture prématurée du matériau. La perte de propriétés avec le vieillissement en eau de mer peut s'expliquer par une détérioration de l'interface fibre/matrice, qui aurait des conséquences néfastes lors d'essais de compression.

Table A.1 – Propriétés ultimes du composite en compression

	Rejuvéné	Vieilli physiquement	Vieilli en eau de mer et saturé
X^C [MPa]	933.6 ± 50.1	949.9 ± 76.1	607 ± 33
Y^C [MPa]	123.5 ± 4.2	134.2 ± 2.6	94.1 ± 3.4

Les propriétés obtenues expérimentalement par les essais quasi-statiques ont été utilisées pour simuler un essai expérimental de flexion 4 points ($l/t=12$), entre un essai de flexion sur poutre courte ($l/t=4$), avec une réponse dominée par le cisaillement interlaminaire, et un essai de flexion sur poutre longue ($l/t=24$), avec une réponse plus proche d'un essai de flexion. La simulation numérique réalisée avec le logiciel commercial de Dassault Systemes Abaqus™ a montré des résultats cohérents (Figure A.6) même s'il a été trouvé que les propriétés de fissurations translaminaires, non obtenus expérimentalement du fait d'une rupture hors de la zone d'intérêt, étaient critiques pour corrélérer au plus proche les résultats expérimentaux. Les résultats de simulation ont montré une surprédiction moyenne de 5,3% pour la raideur, et de 8,9% pour la contrainte à rupture. Ces résultats pourraient être améliorés si des éléments volumiques, qui donnent un état de contrainte tridimensionnel malgré une augmentation du temps de calcul, étaient utilisés.

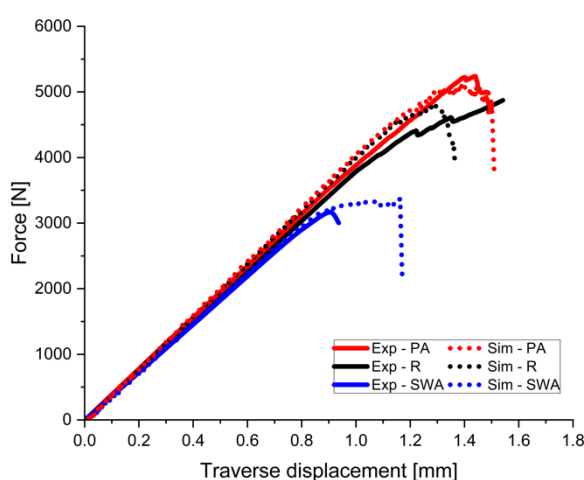


Figure A.6 – Comparaison Exp/Sim pour l'essai de flexion 4 points

A.3. Influence du vieillissement sur le comportement à l'impact hors-plan

La validation des propriétés mécaniques obtenues expérimentalement en chargement quasi-statique étant faite, une campagne d'essais de caractérisation du comportement à l'impact de plaques composites vieilles et non vieilles a été réalisée. Cette campagne a suivi la norme ASTM D7136. Un banc d'impact a été développé pour augmenter le nombre de mesures et rigidifier l'ensemble. Des essais d'impact hors-plan de 5J à 80J ont été réalisés, suivi par des essais de compression après impact (ASTM D7137). Ces derniers ont pour objectifs de caractériser les propriétés résiduelles en compression d'une plaque impactée et endommagée.

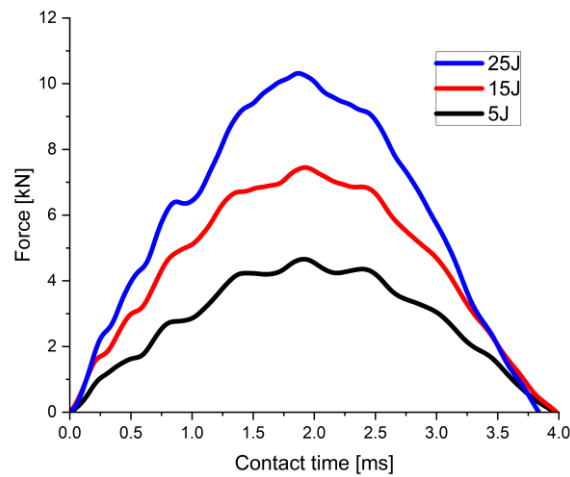


Figure A.7 – Comparaison Force–Temps pour des essais d’impact hors–plan de 5J à 25J

Tout d’abord, les essais d’impact ont été réalisés sur le matériau non vieilli. Les courbes Force–Temps ont montré des temps de contact aux alentours de 4ms (Figure A.7). En termes d’endommagement, des contrôles US ont montré un seuil de délaminage entre 5J et 10J. Plus l’énergie d’impact augmente, plus le délaminage est important (Figure A.8). Au-dessus de 35J, la propagation du délaminage est bloquée par le montage d’essai. L’essai est donc valide jusqu’à ce niveau d’énergie. Des tomographies aux niveaux d’énergie de 5J (non délaminé) et 30J ont été réalisées. Les sections montrent un délaminage entre les surfaces –45/45 et 45/0 vers le centre de l’éprouvette. Aucune rupture de fibre n’a été observée, à l’inverse de ruptures matricielles et de délaminages autour des torons de fibres de carbone.

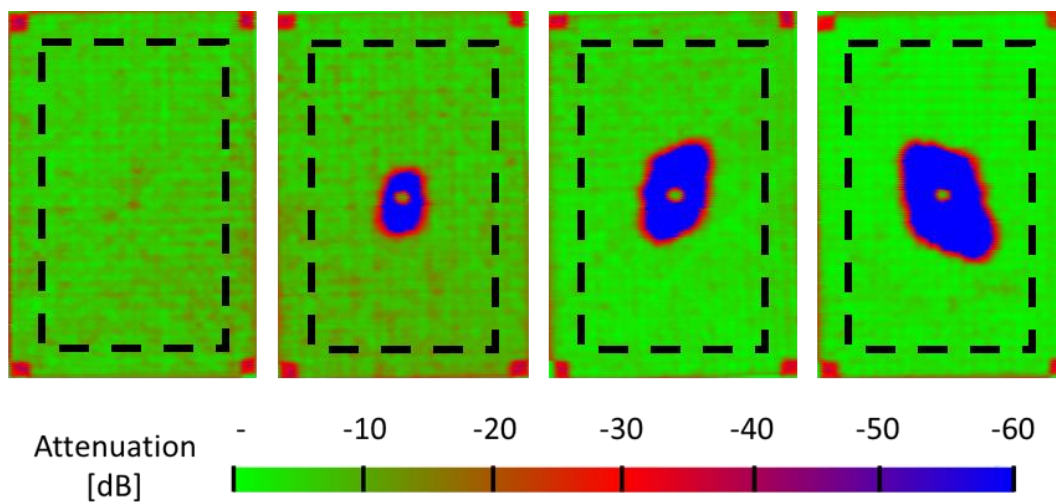


Figure A.8 – Contrôles US réalisés sur des éprouvettes non vieilles impactées à 5J, 15J, 25J et 35J (de gauche à droite)

Ensuite, ces mêmes essais ont été réalisés sur les matériaux vieillis physiquement et saturés en eau de mer. La principale conclusion du vieillissement physique est que celui-ci n’apporte pas grand intérêt sur des problématiques dynamiques de type impact hors–plan. A l’inverse, le vieillissement en eau de mer a montré une diminution du seuil d’endommagement interlaminaire inférieur à 5J (Figure A.9).

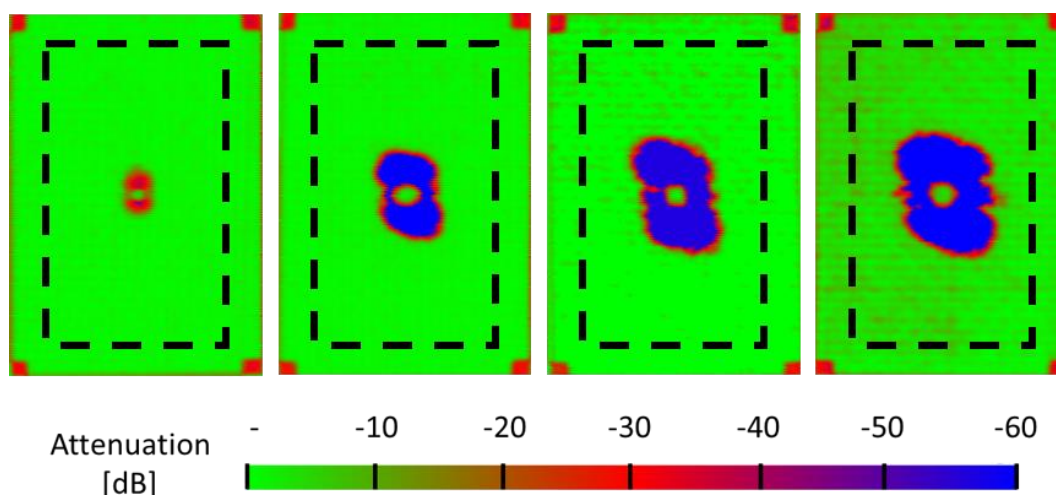


Figure A.9 – Contrôles US réalisés sur des éprouvettes vieilles et saturées en eau de mer impactées à 5J, 15J, 25J et 35J (de gauche à droite)

Des analyses par tomographie ont permis d'identifier les surfaces délaminées d'éprouvettes vieilles, saturées et impactées à 5J et 35J. A 5J, il est possible d'observer des délaminages sur des surfaces 0/45 et –45/45. A 35J, ces délaminages sont plus visibles (Figure A.10). De plus, il a été observé des délaminages 0/0 (Figure A.11), du fait du stitching (couture) utilisé pour maintenir les fibres alignées durant le process de mise en œuvre. Ce stitching fait office de défaut artificiel dans le matériau, favorisant l'initiation de délaminage à ses abords.

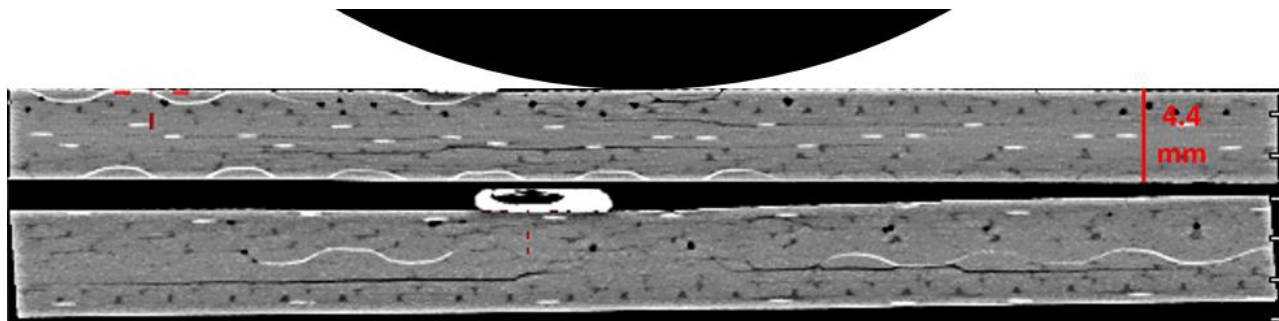


Figure A.10 – Vue de côté d'une éprouvette vieillie en eau de mer impactée à 30J

Un modèle sous Abaqus Explicit™ a été développé pour simuler numériquement ces essais d'impact. Deux types de maillages avec des éléments de type coque (SC8R) ont été utilisés. Cet élément a l'avantage d'avoir le critère de rupture d'Hashin en 2D déjà implémenté, ainsi qu'un critère énergétique pour la prédiction de la propagation de l'endommagement. Le premier maillage suit une approche standard, où les mailles de base carrée sont empilées les unes sur les autres. En vue d'améliorer la prédiction du délaminage, un autre maillage orienté a été utilisé. Dans cette approche, les mailles sont orientées dans la direction des fibres. La génération d'un tel maillage nécessite d'écrire le fichier d'entrée d'Abaqus™ avec un code externe, Python dans notre cas. Les plis sont en contact les uns avec les autres avec des surfaces cohésives, moins précises que les éléments cohésifs, mais permettant la réduction du temps de calcul. Ces surfaces permettent une

prédiction du délaminage. Les données d'entrée sont celles obtenues expérimentalement par les essais quasi-statiques.

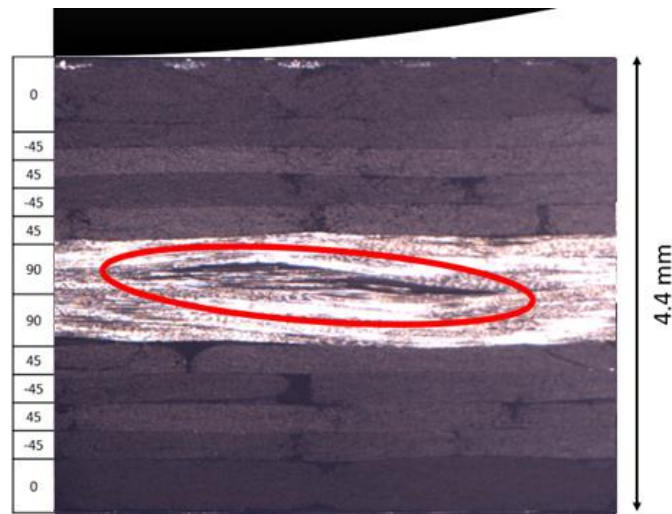


Figure A.11 – 0/0 delamination in the mid-thickness of a coupon saturated and impacted at 15J

Le modèle permet de comparer les mesures effectuées expérimentalement ainsi que la prédiction du délaminage, pour les différentes conditions de vieillissement et aux niveaux d'énergie de 5J, 15J, 25J et 35J. Au-delà, les données expérimentales ont montré que la propagation du délaminage était bloquée par le montage d'essai, favorisant d'autres endommagements pouvant ne pas être prédictibles par le modèle.

Pour un essai d'impact à 15J sur une éprouvette non vieillie, et comme le montrent les Figure A.12 et Figure A.13, les deux modèles prédisent correctement la raideur initiale de l'éprouvette non vieillie. Néanmoins, le modèle avec un maillage standard ne présente pas la rupture prématurée telle que prédite par le maillage orienté. En termes de délaminage, à ce niveau d'énergie, la prédiction du délaminage est cohérente avec celle expérimentale (Figure A.14). Sous le point de contact, la zone purement en compression est observée comme non délaminee expérimentalement mais celle-ci est prédite comme délaminee dans les simulations numériques. L'augmentation des coefficients de friction pour éviter des déplacements latéraux de la plaque sur le montage pourrait être une solution pour améliorer la prédiction du modèle.

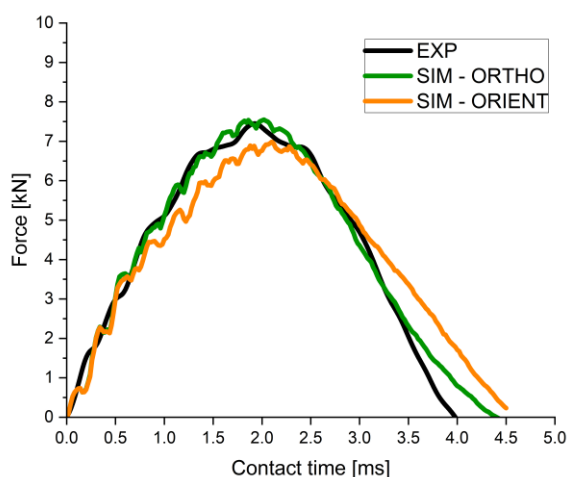


Figure A.12 – Comparaison Exp/Sim des courbes Force–Temps d’un matériau non vieilli impacté à 15J

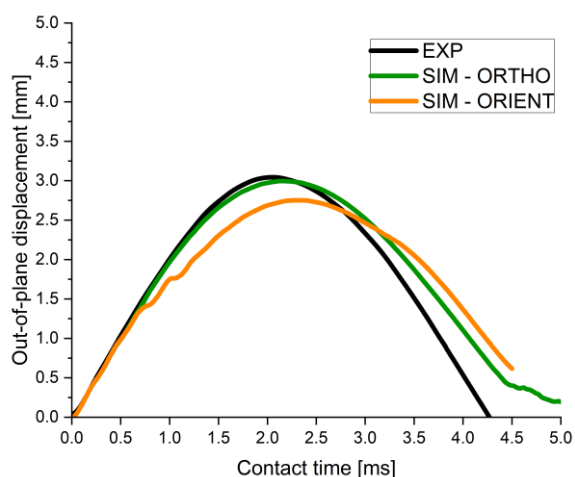


Figure A.13 – Comparaison Exp/Sim des courbes Déflexion–Temps d’un matériau non vieilli impacté à 15J

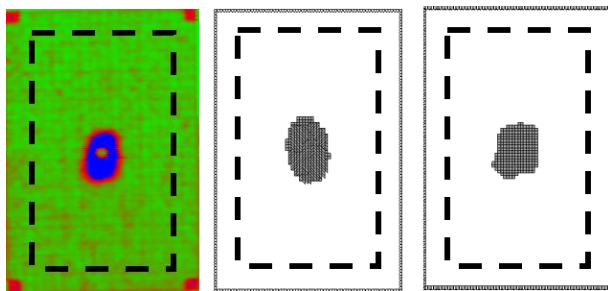


Figure A.14 – Comparaison du délaminage expérimental (gauche) aux délaminages prédits par le maillage orienté (centre) et standard (droite) pour un impact de 15J sur une éprouvette non vieilli

A 35J, une surprédiction de la force maximale est observée (Figure A.15), alors que le déplacement hors-plan semble correctement prédit (Figure A.16). Aussi, une surprédiction de la surface du délaminage est observée (Figure A.17), celle-ci dépendant du type de maillage utilisé. Ces deux observations peuvent trouver leur origine dans le type d’élément utilisé. Contrairement aux éléments volumiques (C3D8) qui permettent le calcul des composantes tridimensionnelles des contraintes, les éléments de type coque ici utilisés (SC8R) se limitent aux contraintes dans le plan. Pour des problématiques de type impact, la contrainte de cisaillement σ_{23} est importante car celle-ci permet la prédiction des fissures matricielles. Avec le modèle développé dans le cadre de cette thèse, la prédiction de σ_{23} n’est pas possible. En pratique, les conséquences directes sur la simulation numérique sont une surprédiction de la réponse mécanique de l’éprouvette, car chaque endommagement prédit aura tendance à diminuer localement la raideur des éléments. De plus, chaque rupture d’élément est associée à une perte d’énergie, qui diminue donc l’énergie distribuée au matériau et réduit donc le délaminage prédit.

L’évolution du modèle vers un modèle avec des éléments volumiques prend son sens aussi du fait des fissures matricielles observées. Néanmoins, il est à noter qu’un tel modèle augmenterait drastiquement le temps de calcul, ce qui n’était pas souhaité dans le cadre de ce projet.

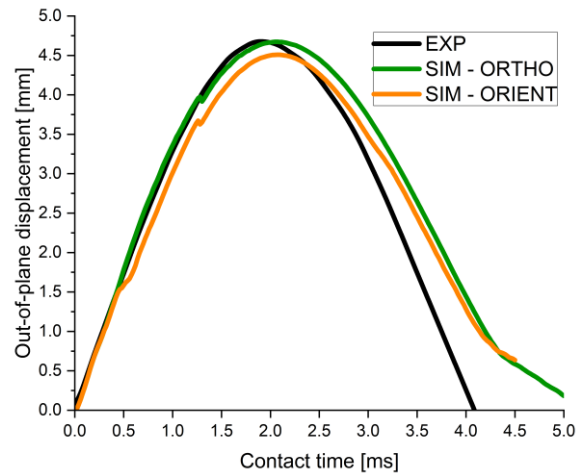
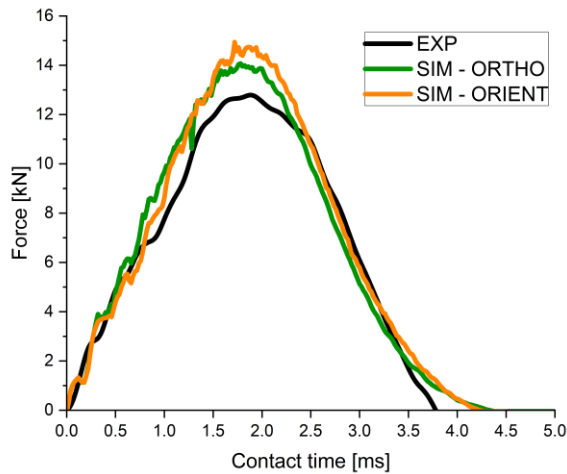


Figure A.15 – Comparaison Exp/Sim des courbes Force–Temps d’un matériau non vieilli impacté à 35J

Figure A.16 – Comparaison Exp/Sim des courbes Déflexion–Temps d’un matériau non vieilli impacté à 35J

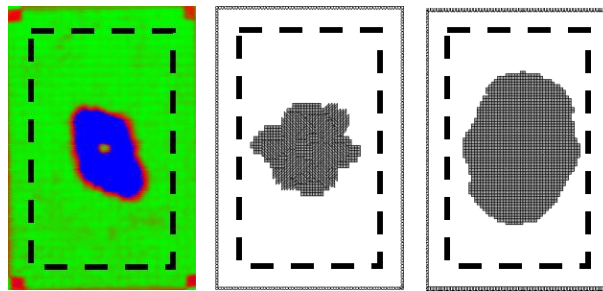


Figure A.17 – Comparaison du délaminage expérimental (gauche) aux délaminages prédits par le maillage orienté (centre) et standard (droite) pour un impact de 35J sur une éprouvette non vieillie

A.4. Vers des essais mécaniques plus représentatifs pour des hélices de propulsion navales

Des essais complémentaires de caractérisation des propriétés résiduelles en compression ont été réalisés. Ces essais suivaient la norme ASTM D7137. Cet essai a le principal avantage de tester une éprouvette impactée sans travail de découpe, mais a pour inconvénient des ruptures parfois prématurées au niveau des plateaux de compression, du fait de défauts de parallélisme.

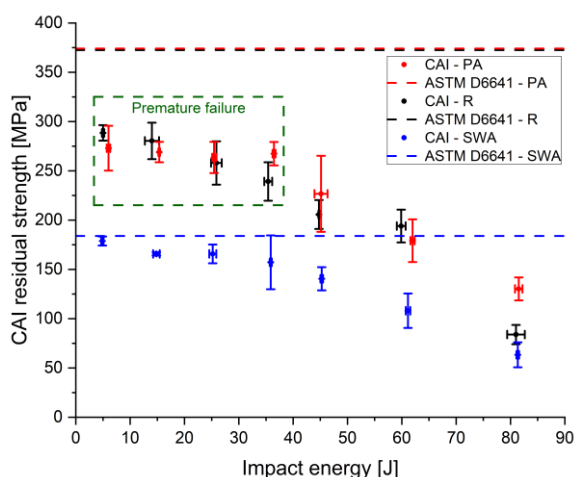


Figure A.18 – Comparaison entre la contrainte résiduelle post-impact et la contrainte maximale donnée par un essai de compression uniaxiale

La Figure A.18 présente les résultats de compression après impact aux différents niveaux d'énergie d'impact, et pour les trois conditions de vieillissement. Alors que le vieillissement physique n'a aucune influence sur les propriétés résiduelles, les effets du vieillissement en eau de mer sont clairement visibles. Néanmoins, ces essais ont présenté des ruptures en dehors de la zone d'intérêt à certains niveaux d'énergie, encadrées en vert. Un essai de compression uniaxiale (ASTM D6641) a donc été réalisé sur des éprouvettes non impactées. Par rapport à l'essai de CAI qui est structurel, l'essai uniaxial apporte des réponses quant à la contrainte matériau admissible. Pour les essais valides, la rupture a toujours été obtenue du fait du stitching. Celui-ci est intéressant lors de la mise en œuvre du matériau puisqu'il maintient les fibres alignées, mais ondule les fibres de carbone ce qui a des conséquences néfastes en compression. Après vieillissement en eau de mer, ces conséquences sont empirées du fait d'une dégradation de l'interface entre le stitching et la résine. D'autres essais d'impact de caractérisation ont été réalisés. Ces essais exploratoires avaient pour but d'identifier des essais qui seraient plus proches d'impacts susceptibles d'être rencontrés par des hélices. Tout d'abord, l'influence de la courbure sur le comportement à l'impact a été étudié. Des plaques courbées non vieilles de rayon de courbure de 15mm, 25mm et 35mm ont été fabriquées puis impactées avec un impacteur hémicylindrique de rayon 25mm. Des mesures d'effort et de déplacement hors plan ont été effectuées mais les essais préliminaires ne permettent pas de conclure quant à l'effet du rayon de courbure sur le pic de force ou sur la déflexion maximale. Néanmoins, au plus bas niveau d'énergie de 5J, un délaminage est observé (Figure A.19) ce qui n'était pas le cas sur les éprouvettes planes impactées hors plan. Cet essai semble donc plus critique que les essais d'impacts hors plan, même si des essais de reproductibilité sont nécessaires.

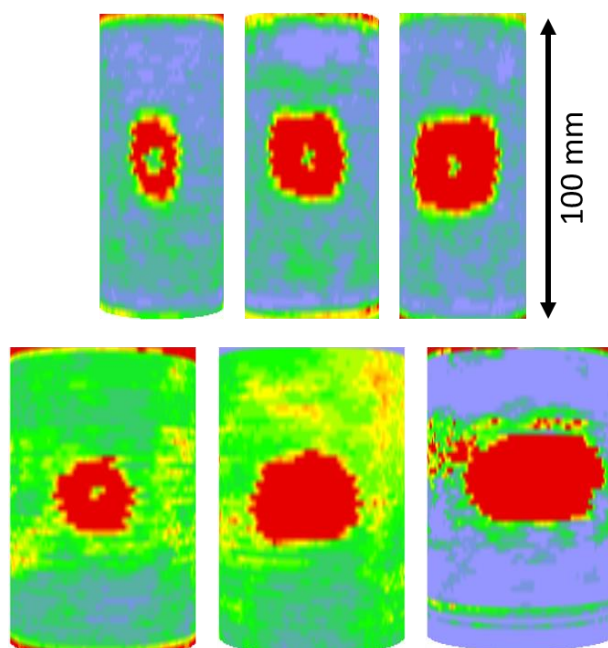


Figure A.19 – Contrôles US réalisés sur les éprouvettes courbées de $\Phi 50\text{mm}$ (haut) et $\Phi 70\text{mm}$ (bas) impactées (de gauche à droite) à 5J, 10J et 15J

Deuxièmement, des essais d’impact sur chant ont été effectués. Ceux-ci visaient à caractériser l’influence du vieillissement sur le comportement dynamique du matériau dans le plan. Des éprouvettes non vieilles et vieilles en eau de mer ont été testées à l’aide d’un impacteur hémicylindrique. Un exemple de rupture est proposé en Figure A.20. La force maximale mesurée pour ces essais est diminuée après vieillissement en eau de mer (Figure A.21). La conséquence est un crush du matériau sous l’impacteur qui aura lieu à plus basse charge. Des contrôles ultrasons ont été réalisés et montrent que l’endommagement reste local, le délaminage ne se propageant par hors de la zone d’impact.



Figure A.20 – Epreuve impactée dans le plan à 330J

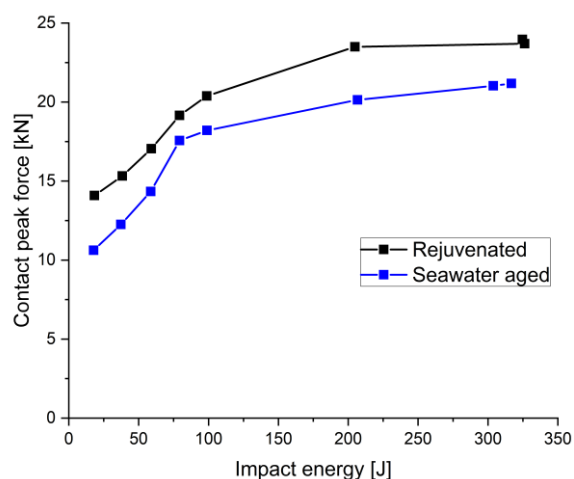


Figure A.21 – Evolution de la force maximale mesurées en fonction de l’énergie d’impact

Enfin, des essais d’impact sur des bords d’attaque ont été réalisés avec un impacteur métallique hémicylindrique de diamètre 50mm. La géométrie de l’éprouvette est issue du programme *Fabheli*. Ces essais

ont été réalisés pour des énergies d'impact de 24J à 160J. A la différence des essais sur chant, ces essais sont plus représentatifs puisque la section de l'éprouvette n'est pas constante : plus épaisse au niveau du pied de pale et plus mince au niveau du bord d'attaque. Les courbes force–temps (Figure A.22) montrent un temps de contact de l'ordre de 4.5ms, mais pour l'impact à 160J, la pénétration est plus importante et le temps de contact est mesuré à 6ms. Concernant l'endommagement, la Figure A.23 présente le bout du bord d'attaque après les impacts. Plus l'énergie d'impact est élevée, et plus la pénétration dans l'éprouvette est importante, ce qui augmente la zone de crush.

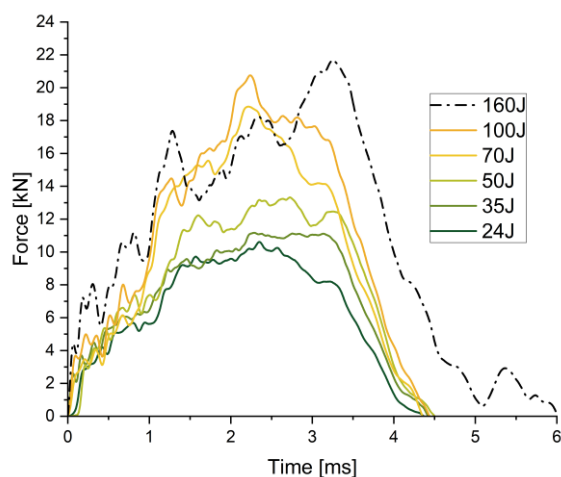


Figure A.22 – Comparaison des courbes Force–Temps pour des impacts sur bords d'attaque pour des énergies de 24J à 160J

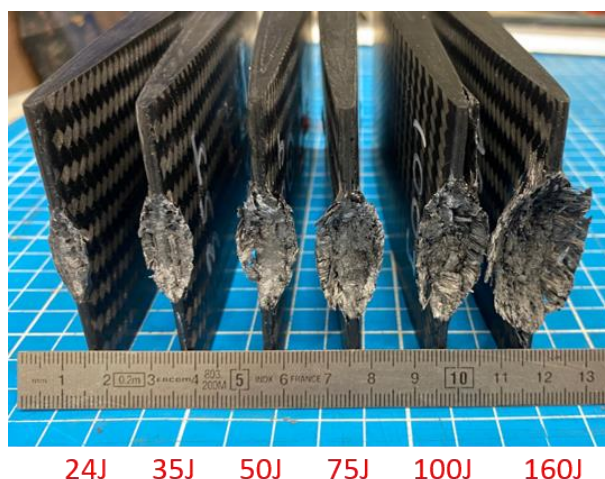


Figure A.23 – Comparaison du bord d'attaque impacté de 24J à 160J

A.5. Conclusion est perspectives

Cette étude a permis de contribuer à l'évaluation et la prédiction des propriétés mécaniques sur le long–terme d'un composite qui pourrait être utilisé pour le domaine naval. Un état non vieilli et deux états vieillis physiquement et vieillis en eau de mer ont été étudiés.

La première partie expérimentale a permis de mettre en avant un abattement des propriétés mécaniques du composite après vieillissement en eau de mer de l'ordre de 30%, alors qu'une augmentation de l'ordre de

5% a été observée grâce au vieillissement physique. Néanmoins, ce dernier est surtout lié au process de mise en œuvre, puisqu'en pratique, l'eau de mer est à basse température et que ce vieillissement se révèle lent. Les propriétés mécaniques obtenues ont permis de simuler et valider la simulation d'un essai de flexion complexe.

Dans la seconde partie, des essais d'impact ont été réalisés expérimentalement puis simulés numériquement. Les données d'entrée de la simulation numérique sont les propriétés quasi-statiques obtenues dans la première partie expérimentale. Le modèle numérique, à base d'éléments de type coque, est concluant pour la prédiction de la raideur, mais sous évalue les endommagements.

Enfin, la troisième partie expérimentale a permis la caractérisation des propriétés résiduelles post-impact du composite. L'apport du vieillissement physique n'a pas été observé par rapport à un état non vieilli. Le vieillissement en eau de mer a des conséquences néfastes sur la tenue du composite, avec des ruptures toujours observées au niveau du stitching. Des essais d'impact sur tubes pour juger de l'influence de la courbure sur le comportement du composite non vieilli ont été réalisés, de 5J à 15J, pour des rayons de courbure de 15mm, 25mm et 35mm. A 5J, des délaminages ont été observés sur toutes les éprouvettes, alors que les impacts hors-plan à ce niveau d'énergie n'avaient pas généré de délaminage. Enfin des essais de caractérisation d'impact sur chant et d'impact sur bord d'attaque ont été réalisés. Pour les premiers, le vieillissement en eau de mer diminue la force maximale lors des essais. La conclusion est qu'en comparaison à un état non vieilli, l'écrasement du matériau vieilli en eau de mer aura lieu à une charge inférieure. Concernant les essais sur bord d'attaque, les éprouvettes ont été endommagées pour tous les niveaux d'énergie. Le temps de contact d'est révélé identique jusqu'à 100J.

Concernant les perspectives, la caractérisation de composites saturés à différents niveaux d'humidité permettrait de simuler au plus près l'influence du vieillissement sur l'évolution des propriétés d'une structure immergée en régime transitoire. Une loi de comportement qui serait fonction de la quantité d'eau apporterait des réponses même si les simulations numériques deviendraient plus longues. Un autre point est l'effet de la vitesse de déformation. Les essais de caractérisation réalisés dans cette thèse se sont limités aux des vitesses de déformation de l'ordre de $0.1s^{-1}$, alors que les jauges extensométriques ont mesuré des vitesses de l'ordre de $2 s^{-1}$ pour un impact à 4m/s. Suivant la littérature pour ce type d'impacts [114], les vitesses maximales annoncées sont de l'ordre de 40m/s, donc à minima les essais devraient être réalisés à des vitesses de déformation de $20 s^{-1}$. Des essais de caractérisation quasi-statiques pourraient aussi être réalisés pour mettre en avant le rôle de l'eau dans la propagation des fissures translaminaires.

En termes d'impacts hors-plan, des améliorations sont possibles au niveau du modèle numérique développé. L'utilisation d'éléments volumiques permettrait le calcul tridimensionnel des contraintes, et l'utilisation d'un modèle matériau prenant en compte les endommagements hors plan devrait permettre d'améliorer les résultats du modèle. Néanmoins, cette approche mènera à une augmentation drastique du temps de calcul.

Finalement, concernant la partie exploratoire, des essais d'impacts sur une gamme plus étendue de rayons de courbure et la simulation associée devrait permettre de conclure quant au rôle de la courbure sur le comportement structurel. Pour les essais sur chant, une simulation numérique de l'essai devrait mettre en avant l'influence du vieillissement en eau de mer sur la ténacité à rupture des fibres de carbone.

Finalement, pour un cas de chargement au plus près de la réalité, le vieillissement de bords d'attaque pendant une durée suivie d'un impact apporterait des réponses quant à l'influence d'une diffusion d'eau transitoire sur les propriétés de la structure.

Des essais ont été réalisés en partenariat avec l'UNSW pour la thèse de Rowan Caldwell. Les composites thermoplastiques doivent être comparés aux thermodurcissables. De plus, le rôle de l'eau dans le cas d'un impact sous-marin doit aussi être caractérisé et une simulation numérique de type interaction fluide-structure pourrait apporter des réponses.

Appendix 6 – Scientific contributions

➤ **Papers published:**

- A. ROBIN, P. DAVIES, M. ARHANT, S. LE JEUNE, N. LACOTTE, E. MORINEAU, F. IOOS, R. CAIRO, “Sandwich materials with reduced environmental impact for marine structures”, accepted for publication in *Journal of Sandwich Structures & Materials*, September 2022
- A. ROBIN, M. ARHANT, P. DAVIES, S. LEJEUNE, E. LOLIVE, T. BONNEMAINS and B. HABERT, “Effect of aging on the in-plane and out-of-plane mechanical properties of composites for design of marine structures”, accepted for publication in *Composites Part C*, March 2023

➤ **Conference - oral contributions:**

- A. ROBIN, M. ARHANT, P. DAVIES and B. HABERT, “Development of tests to investigate impact behavior of marine composites for propellers”, presented at CompTest–2021, online, May 2021
- A. ROBIN, M. ARHANT, P. DAVIES and B. HABERT, “Effets du vieillissement en eau de mer sur le comportement à l’impact de composites marins pour des hélices de navires”, presented at JNC22 – 22^{èmes} Journées Nationales sur les Composites, online, June 2021
- A. ROBIN, M. ARHANT, P. DAVIES and B. HABERT, “Effect of seawater aging on fracture behavior of a C/Epoxy composite”, presented at EMMC18 – 18th European Mechanics of Materials Conference, online, April 2022
- A. ROBIN, M. ARHANT, P. DAVIES and B. HABERT, “Influence du vieillissement en eau de mer sur le comportement mécanique d’un composite C/Epoxy pour des hélices de propulsion navale”, presented at Conférence VIP – Vieillissement des Polymères, ENSAM Paris, June 2022
- A. ROBIN, P. DAVIES, M. ARHANT, E. MORINEAU and R. CAIRO, “Sandwich materials with reduced environmental impact for marine structures”, ICSS13 – 13th International Conference on Sandwich Structures, Knoxville, October 2022
- A. ROBIN, M. ARHANT, P. DAVIES and B. HABERT, “Effect of seawater aging on the in-plane and out-of-plane impact of C/Epoxy composites”, ECCCS2 – 2nd European Conference on Crashworthiness of Composite Structures, Toulouse, November 2022

References

- [1] V. Bertram, "Propellers", in *Practical Ship Hydrodynamics*, Elsevier, 2012, pp. 41–72.
- [2] S. Gudmundsson, "Chapter 14 - The anatomy of the propeller", in *General Aviation Aircraft Design*, S. Gudmundsson, Ed. Boston: Butterworth-Heinemann, 2014, pp. 581–659.
- [3] J. S. Carlton, "Chapter 1 - The early development of the screw propeller", in *Marine Propellers and Propulsion (Third Edition)*, J. S. Carlton, Ed. Oxford: Butterworth-Heinemann, 2012, pp. 1–9.
- [4] J. Dubranna, "An overview of marine renewable energy - Paris Innovation Review", 2017.
- [5] L. Mishnaevsky, K. Branner, H. Petersen, J. Beauson, M. McGugan, and B. Sørensen, "Materials for wind turbine blades: an overview", *Materials*, vol. 10, no. 11, p. 1285, Nov. 2017.
- [6] H. Boye, E. Caquot, P. Clement, L. de La Cochetiere, J.-M. Nataf, and P. Sergent, "Rapport de la mission d'étude sur les energies marines renouvelables", Mar. 2013.
- [7] S. E. B. Elghali, M. E. H. Benbouzid, and J. F. Charpentier, "Marine tidal current electric power generation technology: state of the art and current status", in *2007 IEEE International Electric Machines & Drives Conference*, Antalya, May 2007, pp. 1407–1412.
- [8] Z. Zhou, M. Benbouzid, J.-F. Charpentier, F. Sculler, and T. Tang, "Developments in large marine current turbine technologies – A review", *Renewable and Sustainable Energy Reviews*, vol. 71, pp. 852–858, May 2017.
- [9] R. Pelc and R. M. Fujita, "Renewable energy from the ocean", *Marine Policy*, vol. 26, no. 6, pp. 471–479, Nov. 2002.
- [10] A. Roberts, B. Thomas, P. Sewell, Z. Khan, S. Balmain, and J. Gillman, "Current tidal power technologies and their suitability for applications in coastal and marine areas", *J. Ocean Eng. Mar. Energy*, vol. 2, no. 2, pp. 227–245, May 2016.
- [11] Ocean Energy Systems, "Annual report - An overview of ocean energy activities in 2022", Mar. 2023.
- [12] A. G. L. Borthwick, "Marine renewable energy seascape", *Engineering*, vol. 2, no. 1, pp. 69–78, Mar. 2016.
- [13] T. Flanagan, J. Maguire, C. Ó. Brádaigh, P. Mayorga, and A. Doyle, "Smart affordable composite blades for tidal energy", presented at the 11th European Wave and Tidal Energy Conference, 2015.
- [14] C.-C. Lin, Y.-J. Lee, and C.-S. Hung, "Optimization and experiment of composite marine propellers", *Composite Structures*, vol. 89, no. 2, pp. 206–215, Jun. 2009.
- [15] R. Balasubramanian, "A case history on the phenomenal corrosion of marine propellers in fishing boats", *Fishery Technology*, vol. 10, 1973.
- [16] T. S. Koko, K. O. Shahin, U. O. Akpan, and M. E. Norwood, "Review of composite propeller developments and strategy for modeling composite propellers using PVASt", R&D Canada - Atlantic, Sep. 2012.
- [17] J. S. Carlton, "Chapter 2 - Propulsion systems", in *Marine Propellers and Propulsion (Fourth Edition)*, J. S. Carlton, Ed. Butterworth-Heinemann, 2019, pp. 11–28.
- [18] A. F. Molland, Ed., "Chapter 6 - Marine engines and auxiliary machinery", in *The Maritime Engineering Reference Book*, Oxford: Butterworth-Heinemann, 2008, pp. 344–482.
- [19] J. S. Carlton, "Propeller materials", in *Marine Propellers and Propulsion*, Elsevier, 2012, pp. 385–396.
- [20] A. Drach, I. Tsukrov, J. DeCew, J. Aufrecht, A. Grohbauer, and U. Hofmann, "Field studies of corrosion behaviour of copper alloys in natural seawater", *Corrosion Science*, vol. 76, pp. 453–464, Nov. 2013.
- [21] C. D. Wozniak, "Analysis, fabrication, and testing of a composite bladed propeller for a naval academy yard patrol (YP) craft", Defense Technical Information Center, Fort Belvoir, VA, May 2005.
- [22] A. P. Mouritz, E. Gellert, P. Burchill, and K. Challis, "Review of advanced composite structures for naval ships and submarines", *Composite Structures*, vol. 53, no. 1, pp. 21–42, Jul. 2001.
- [23] G. Marsh, "A new start for marine propellers ?", *Reinforced Plastics*, vol. 48, no. 11, pp. 34–38, Dec. 2004.
- [24] T. J. Searle, J. Chudley, and D. Short, "Composites offer advantages for propellers", *Reinforced Plastics*, vol. 37, no. 12, pp. 24–26, Dec. 1993.
- [25] T. Yamatogi, H. Murayama, K. Uzawa, K. Kageyama, and N. Watanabe, "Study on Cavitation Erosion of Composite Materials for Marine Propeller", presented at the ICCM17, 2009.
- [26] "About Propulse", *Propulse website*. <https://propulse.se/en/about-propulse/about-propulse/>
- [27] "History of Piranha Propellers – Piranha Propellers". <https://piranha.com/about/>

- [28] B. Stahl, "United States Patent: 4930987 - Marine propeller and hub assembly of plastic", 4930987, Jun. 05. 1990
- [29] "Composite marine propellers, Inc.". <http://comprop.com/>
- [30] "Composite propeller for warship propulsion - Construction and advantages of the composite propeller", *AZoM.com*. <https://www.azom.com/article.aspx?ArticleID=2126>
- [31] K. Kim *et al.*, "The Propulsion Committee: final report and recommendations to the 25th ITTC", in *25th ITTC (International Towing Tank Conference)*, 2008.
- [32] S. Black, "Composite propeller for Royal Navy minehunter", *CompositeWorld*, Jan. 09. 2011. [https://www.compositesworld.com/articles/composite-propeller-for-royal-navy-minehunter\(2\)](https://www.compositesworld.com/articles/composite-propeller-for-royal-navy-minehunter(2))
- [33] Katsudou, "Benefits of carbon composite marine propeller", 2015. https://www.classnk.or.jp/classnk-rd/assets/pdf/katsudou201511_D.pdf
- [34] G. Dolo, S. Durand, F. Boursier, P. Muller, and F. Le Lay, "Composite propeller in marine industry: first steps toward a technological breakthrough", in *OCEANS 2019 - Marseille*, Jun. 2019, pp. 1–6.
- [35] C. E. Kane and J. R. Smith, "Composite blades in marine propulsors", presented at the International conference on advanced marine materials: techniques and applications, The royal institution of naval architects, London, 2003.
- [36] K. O. Stromberg, "Deformation-controlled composite CP propeller blades", Maritime defence, 1991.
- [37] C. Dai, J. Fraser, P. Coffin, H. Garala, and G. Rappl, "Hydrodynamic simulation of a passive blade control for tip vortex cavitation control", presented at the PROPCAV'95, 1995.
- [38] S. Gowing, P. Coffin, and C. Dai, "Hydrofoil cavitation improvements with elastically coupled composite materials", presented at the 25th American Towing Tank Conference, Iowa City, Iowa, Sep. 1998.
- [39] J. S. Carlton, "Chapter 22 - Propeller design", in *Marine Propellers and Propulsion (Fourth Edition)*, J. S. Carlton, Ed. Butterworth-Heinemann, 2019, pp. 469–497.
- [40] C.-S. Lee, "Prediction of steady and unsteady performance of marine propellers with or without cavitation by numerical lifting-surface theory", Thesis, Massachusetts Institute of Technology, 1979.
- [41] G.-F. Lin, "Comparative Stress/Deflection Analyses of a Thick-Shell Composite Propeller Blade", David Taylor Research Center, Bethesda, DTRC/SHD-1373-01, Dec. 1991.
- [42] H.-J. Lin and J.-J. Lin, "Nonlinear hydroelastic behavior of propellers using a finite-element method and lifting surface theory", *J Mar Sci Technol*, vol. 1, no. 2, p. 114, Apr. 1996.
- [43] Y.-J. Lee and C.-C. Lin, "Optimized design of composite propeller", *Mechanics of Advanced Materials and Structures*, vol. 11, no. 1, pp. 17–30, Jan. 2004.
- [44] Z. Hashin, "Failure criteria for unidirectional fiber composites", *Journal of Applied Mechanics*, vol. 47, no. 2, pp. 329–334, Jun. 1980.
- [45] H. J. Lin, J. J. Lin, and T. J. Chuang, "Strength evaluation of a composite marine propeller blade", *Journal of Reinforced Plastics and Composites*, vol. 24, no. 17, pp. 1791–1807, Nov. 2005.
- [46] H. J. Lin and J. F. Tsai, "Analysis of underwater free vibrations of a composite propeller blade", *Journal of Reinforced Plastics and Composites*, vol. 27, no. 5, pp. 447–458, Mar. 2008.
- [47] R. L. Taylor, P. J. Beresford, and E. L. Wilson, "A non-conforming element for stress analysis", *International Journal for Numerical Methods in Engineering*, vol. 10, no. 6, pp. 1211–1219, 1976.
- [48] J. P. van Doormaal and G. D. Raithby, "Enhancements of the simple method for predicting incompressible fluid flows", *NHTA*, vol. 7, no. 2, pp. 147–163, Apr. 1984.
- [49] Y. L. Young, "Dynamic hydroelastic scaling of self-adaptive composite marine rotors", *Composite Structures*, vol. 92, no. 1, pp. 97–106, Jan. 2010.
- [50] X. D. He, Y. Hong, and R. G. Wang, "Hydroelastic optimisation of a composite marine propeller in a non-uniform wake", *Ocean Engineering*, vol. 39, pp. 14–23, Jan. 2012.
- [51] M. T. Herath, S. Natarajan, B. G. Prusty, and N. St. John, "Isogeometric analysis and genetic algorithm for shape-adaptive composite marine propellers", *Computer Methods in Applied Mechanics and Engineering*, vol. 284, pp. 835–860, Feb. 2015.
- [52] M. T. Herath, B. G. Prusty, A. W. Phillips, and N. St. John, "Structural strength and laminate optimization of self-twisting composite hydrofoils using a genetic algorithm", *Composite Structures*, vol. 176, pp. 359–378, Sep. 2017.

- [53] M. T. Herath, S. Natarajan, B. G. Prusty, and N. St. John, "Smoothed finite element and genetic algorithm based optimization for shape adaptive composite marine propellers", *Composite Structures*, vol. 109, pp. 189–197, Mar. 2014.
- [54] A. F. Molland and S. R. Turnock, "The design and construction of model ship propeller blades in hybrid composite materials", *Composites Manufacturing*, vol. 2, no. 1, pp. 39–47, Mar. 1991.
- [55] D. Buchler, R. Schult, A. I. R. Fertigung-Technologie, and H. Luckow, "Design, fabrication and testing of pitch-adapting (flexible) composite propellers", presented at the Propeller & shafting symposium, 2006.
- [56] K. Beng Yeo, W. J. Leow, W. H. Choong, and F. Mohd Tamir, "Hand lay-up GFRP composite marine propeller blade", *J. of Applied Sciences*, vol. 14, no. 22, pp. 3077–3082, Dec. 2014.
- [57] B.-G. Paik *et al.*, "Investigation on the performance characteristics of the flexible propellers", *Ocean Engineering*, vol. 73, pp. 139–148, Nov. 2013.
- [58] P. Maung, B. G. Prusty, J. M. White, M. David, A. W. Phillips, and N. A. St John, "Structural performance of a shape-adaptive composite hydrofoil using automated fibre placement", *Engineering Structures*, vol. 183, pp. 351–365, Mar. 2019.
- [59] J. M. White, P. Maung, M. David, A. W. Phillips, N. A. St John, and B. G. Prusty, "Hydrofoil manufacture with automated fibre placement", *9th Australasian Congress on Applied Mechanics (ACAM9)*, p. 773, 2017.
- [60] D. Griffin and T. Ashwill, "Alternative composite materials for megawatt-scale wind turbine blades: design considerations and recommended testing", in *41st Aerospace Sciences Meeting and Exhibit*, American Institute of Aeronautics and Astronautics, 2003.
- [61] M. H. Flanagan *et al.*, "Large scale structural testing of wind turbine blades manufactured using a one-shot out-of-autoclave process", presented at the CERI Conferences, 2016.
- [62] G.-J. Zondervan, N. Grasso, and W. Lafeber, "Hydrodynamic design and model testing techniques for composite ship propellers", Espoo, Finland, Jun. 2017.
- [63] E. M. Fagan, M. Flanagan, S. B. Leen, T. Flanagan, A. Doyle, and J. Goggins, "Physical experimental static testing and structural design optimisation for a composite wind turbine blade", *Composite Structures*, vol. 164, pp. 90–103, Mar. 2017.
- [64] J. Yang *et al.*, "Structural investigation of composite wind turbine blade considering structural collapse in full-scale static tests", *Composite Structures*, vol. 97, pp. 15–29, Mar. 2013.
- [65] E. J. Premont and K. R. Stubenrauch, "Impact resistance of composite fan blades", NASA-CR-134515, 1973.
- [66] I. Tawk *et al.*, "Study of impact on helicopter blade", *Engineering Failure Analysis*, vol. 24, pp. 38–45, Sep. 2012.
- [67] C. Baley, P. Davies, Y. Grohens, and G. Dolto, "Application of interlaminar tests to marine composites. A literature review", *Applied Composite Materials*, vol. 11, no. 2, pp. 99–126, Mar. 2004.
- [68] U. K. Vaidya, "Impact response of laminated and sandwich composites", in *Impact Engineering of Composite Structures*, S. Abrate, Ed. Vienna: Springer, 2011, pp. 97–191.
- [69] P. O. Sjoblom, J. T. Hartness, and T. M. Cordell, "On low-velocity impact testing of composite materials", *Journal of Composite Materials*, vol. 22, no. 1, pp. 30–52, Jan. 1988.
- [70] K. N. Shivakumar, W. Elber, and W. Illg, "Prediction of low-velocity impact damage in thin circular laminates", *AIAA Journal*, vol. 23, no. 3, pp. 442–449, 1985.
- [71] W. J. Cantwell and J. Morton, "The impact resistance of composite materials — a review", *Composites*, vol. 22, no. 5, pp. 347–362, Sep. 1991.
- [72] S. Abrate, "Impact on laminated composite materials", *Appl. Mech. Rev.*, vol. 44, no. 4, pp. 155–190, Apr. 1991.
- [73] D. Zheng, "Low velocity impact analysis of composite laminated plates", PhD Thesis, University of Akron, 2007.
- [74] R. Olsson, "Mass criterion for wave controlled impact response of composite plates", *Composites Part A: Applied Science and Manufacturing*, vol. 31, no. 8, pp. 879–887, Aug. 2000.
- [75] L. S. Sutherland, "A review of impact testing on marine composite materials: Part I – Marine impacts on marine composites", *Composite Structures*, vol. 188, pp. 197–208, Mar. 2018.

- [76] M. O. W. Richardson and M. J. Wisheart, "Review of low-velocity impact properties of composite materials", *Composites Part A: Applied Science and Manufacturing*, vol. 27, no. 12, pp. 1123–1131, Jan. 1996.
- [77] A. A. A. Alghamdi, "Collapsible impact energy absorbers: an overview", *Thin-Walled Structures*, vol. 39, no. 2, pp. 189–213, Feb. 2001.
- [78] M. Guida, F. Marulo, M. Bruno, B. Montesarchio, and S. Orlando, "Design validation of a composite crash absorber energy to an emergency landing", *Advances in aircraft and spacecraft science*, vol. 5, no. 3, pp. 319–334, May 2018.
- [79] D. Guillon, "Étude des mécanismes d'absorption d'énergie lors de l'écrasement progressif de structures composites à base de fibre de carbone", PhD Thesis, Université de Toulouse, 2008.
- [80] S. Z. H. Shah, S. Karuppanan, P. S. M. Megat-Yusoff, and Z. Sajid, "Impact resistance and damage tolerance of fiber reinforced composites: A review", *Composite Structures*, vol. 217, pp. 100–121, Jun. 2019.
- [81] I. Ivañez, M. M. Moure, S. K. Garcia-Castillo, and S. Sanchez-Saez, "The oblique impact response of composite sandwich plates", *Composite Structures*, vol. 133, pp. 1127–1136, Dec. 2015.
- [82] P. Navarro, J. Aubry, S. Marguet, J.-F. Ferrero, S. Lemaire, and P. Rauch, "Experimental and numerical study of oblique impact on woven composite sandwich structure: Influence of the firing axis orientation", *Composite Structures*, vol. 94, no. 6, pp. 1967–1972, May 2012.
- [83] G. Zhou and G. A. O. Davies, "Impact response of thick glass fibre reinforced polyester laminates", *International Journal of Impact Engineering*, vol. 16, no. 3, pp. 357–374, Jun. 1995.
- [84] L. S. Sutherland, "A review of impact testing on marine composite materials: Part IV – Scaling, strain rate and marine-type laminates", *Composite Structures*, vol. 200, pp. 929–938, Sep. 2018.
- [85] L. S. Sutherland, R. A. Shenoi, and S. M. Lewis, "Size and scale effects in composites: I. Literature review", *Composites Science and Technology*, vol. 59, no. 2, pp. 209–220, Feb. 1999.
- [86] L. S. Sutherland and C. Guedes Soares, "Scaling of impact on low fibre-volume glass–polyester laminates", *Composites Part A: Applied Science and Manufacturing*, vol. 38, no. 2, pp. 307–317, Feb. 2007.
- [87] H. E. Johnson, L. A. Louca, and S. E. Mouring, "Current research into modelling of shock damage to large scale composite panels", *J Mater Sci*, vol. 41, no. 20, pp. 6655–6672, Oct. 2006.
- [88] J. Summerscales, "1 - Materials selection for marine composites", in *Marine Composites*, R. Pemberton, J. Summerscales, and J. Graham-Jones, Eds. Woodhead Publishing, 2019, pp. 3–30.
- [89] M. Arhant and P. Davies, "2 - Thermoplastic matrix composites for marine applications", in *Marine Composites*, R. Pemberton, J. Summerscales, and J. Graham-Jones, Eds. Woodhead Publishing, pp. 31–53.
- [90] D. Choqueuse, R. Baizeau, and P. Davies, "Experimental studies of Impact on Marine Composites", presented at the ICCM12, Jul. 1999.
- [91] R. Trask, B. Cripps, and A. Shenoi, "Damage Tolerance Assessment of Repaired Composite Sandwich Structures", in *Sandwich Structures 7: Advancing with Sandwich Structures and Materials*, Dordrecht, 2005, pp. 507–516.
- [92] A. T. Echtermeyer, "Advanced composite hull structures for high speed craft", in *Proceedings of the International European Chapter Conference of the Society for the Advancement of Material and Process Engineering*, Toulouse, 1994.
- [93] S. Madjidi, W. S. Arnold, and I. H. Marshall, "Damage tolerance of CSM laminates subject to low velocity oblique impacts", *Composite Structures*, vol. 34, no. 1, pp. 101–116, Jan. 1996.
- [94] N. O. Niclasen, "Light weight marine vessels operating in brash ice", Royal Institute of Technology, 2015.
- [95] R. Tan, J. Xu, W. Sun, Z. Liu, Z. Guan, and X. Guo, "Relationship between matrix cracking and delamination in CFRP cross-ply laminates subjected to low velocity impact", *Materials*, vol. 12, no. 23, p. 3990, Jan. 2019.
- [96] C. J. Jih and C. T. Sun, "Prediction of delamination in composite laminates subjected to low velocity impact", *Journal of Composite Materials*, vol. 27, no. 7, pp. 684–701, Jul. 1993.
- [97] S.-W. R. Lee and C. T. Sun, "A quasi-static penetration model for composite laminates", *Journal of Composite Materials*, vol. 27, no. 3, pp. 251–271, Mar. 1993.

- [98] F.-K. Chang, H. Y. Choi, and S.-T. Jeng, "Study on impact damage in laminated composites", *Mechanics of Materials*, vol. 10, no. 1, pp. 83–95, Nov. 1990.
- [99] D. Liu, "Impact-induced delamination — A view of bending stiffness mismatching", *Journal of Composite Materials*, vol. 22, no. 7, pp. 674–692, Jul. 1988.
- [100] R. Craven, P. Sztetek, and R. Olsson, "Investigation of impact damage in multi-directional tape laminates and its effect on local tensile stiffness", *Composites Science and Technology*, vol. 68, no. 12, pp. 2518–2525, Sep. 2008.
- [101] G. D. Sims and W. R. Broughton, "2.05 - Glass Fiber Reinforced Plastics—Properties", in *Comprehensive Composite Materials*, vol. 2 : Polymer matrix composites, A. Kelly and C. Zweben, Eds. Oxford: Pergamon, 2000, pp. 151–197.
- [102] T. Mitrevski, I. H. Marshall, R. Thomson, R. Jones, and B. Whittingham, "The effect of impactor shape on the impact response of composite laminates", *Composite Structures*, vol. 67, no. 2, pp. 139–148, Feb. 2005.
- [103] E. Sevkat, B. Liaw, and F. Delale, "Drop-weight impact response of hybrid composites impacted by impactor of various geometries", *Materials & Design (1980-2015)*, vol. 52, pp. 67–77, Dec. 2013.
- [104] B. M. Icten, B. G. Kiral, and M. E. Deniz, "Impactor diameter effect on low velocity impact response of woven glass epoxy composite plates", *Composites Part B: Engineering*, vol. 50, pp. 325–332, Jul. 2013.
- [105] C. Evci, "Thickness-dependent energy dissipation characteristics of laminated composites subjected to low velocity impact", *Composite Structures*, vol. 133, pp. 508–521, Dec. 2015.
- [106] R. Park and J. Jang, "Effect of laminate thickness on impact behavior of aramid fiber/vinylester composites", *Polymer Testing*, vol. 22, no. 8, pp. 939–946, Dec. 2003.
- [107] V. Lopresto and G. Caprino, "Damage mechanisms and energy absorption in composite laminates under low velocity impact loads", in *Dynamic Failure of Composite and Sandwich Structures*, S. Abrate, B. Castanié, and Y. D. S. Rajapakse, Eds. Dordrecht: Springer Netherlands, 2013, pp. 209–289.
- [108] A. D. Resnyansky, "The impact response of composite materials involved in helicopter vulnerability assessment: Literature review - Part 2", Defence science and technology organisation Edinburgh (Australia) weapons systems div, DSTO-TR-1842, Apr. 2006.
- [109] M. Quaresimin, M. Ricotta, L. Martello, and S. Mian, "Energy absorption in composite laminates under impact loading", *Composites Part B: Engineering*, vol. 44, no. 1, pp. 133–140, Jan. 2013.
- [110] C. Cho and G. Zhao, "Effects of geometric and material factors on mechanical response of laminated composites due to low velocity impact", *Journal of Composite Materials*, vol. 36, no. 12, pp. 1403–1428, Jun. 2002.
- [111] L. S. Kistler and A. M. Waas, "Experiment and analysis on the response of curved laminated composite panels subjected to low velocity impact", *International Journal of Impact Engineering*, vol. 21, no. 9, pp. 711–736, Oct. 1998.
- [112] L. Ballère, P. Viot, J.-L. Lataillade, L. Guillaumat, and S. Cloutet, "Damage tolerance of impacted curved panels", *International Journal of Impact Engineering*, vol. 36, no. 2, pp. 243–253, Feb. 2009.
- [113] H. Saghafi, G. Minak, and A. Zucchelli, "Effect of preload on the impact response of curved composite panels", *Composites Part B: Engineering*, vol. 60, pp. 74–81, Apr. 2014.
- [114] A. Phillips, M. Pantelidi, J. Salloum, F. Solano, and A. Orifici, "Low velocity impact of thick maritime composites", presented at the ICCM 22, Melbourne, Australia, Apr. 2018.
- [115] G. Dorey, G. R. Sidey, and J. Hutchings, "Impact properties of carbon fibre/Kevlar 49 fibre hybrid composites", *Composites*, vol. 9, no. 1, pp. 25–32, Jan. 1978.
- [116] B. Z. Jang, L. C. Chen, L. R. Hwang, J. E. Hawkes, and R. H. Zee, "The response of fibrous composites to impact loading", *Polym. Compos.*, vol. 11, no. 3, pp. 144–157, Jun. 1990.
- [117] L. Greve and A. K. Pickett, "Delamination testing and modelling for composite crash simulation", *Composites Science and Technology*, vol. 66, no. 6, pp. 816–826, May 2006.
- [118] A. P. Mouritz, "Ballistic impact and explosive blast resistance of stitched composites", *Composites Part B: Engineering*, vol. 32, no. 5, pp. 431–439, Jan. 2001.
- [119] K. T. Tan, N. Watanabe, and Y. Iwahori, "Experimental investigation of bridging law for single stitch fibre using Interlaminar tension test", *Composite Structures*, vol. 92, no. 6, pp. 1399–1409, May 2010.
- [120] M. D. K. Wood, X. Sun, L. Tong, Q. Luo, A. Katzos, and A. Rispler, "A new ENF test specimen for the mode II delamination toughness testing of stitched woven CFRP laminates", *Journal of Composite Materials*, vol. 41, no. 14, pp. 1743–1772, Jul. 2007.

- [121] K. A. Dransfield, L. K. Jain, and Y.-W. Mai, "On the effects of stitching in CFRPs — I. mode I delamination toughness", *Composites Science and Technology*, vol. 58, no. 6, pp. 815–827, Jan. 1998.
- [122] M. Yasaei, L. Bigg, G. Mohamed, and S. R. Hallett, "Influence of Z-pin embedded length on the interlaminar traction response of multi-directional composite laminates", *Materials & Design*, vol. 115, pp. 26–36, Feb. 2017.
- [123] R. Seltzer, C. González, R. Muñoz, J. Llorca, and T. Blanco-Varela, "X-ray microtomography analysis of the damage micromechanisms in 3D woven composites under low-velocity impact", *Composites Part A: Applied Science and Manufacturing*, vol. 45, pp. 49–60, Feb. 2013.
- [124] A. K. Bandaru, Y. Sachan, S. Ahmad, R. Alagirusamy, and N. Bhatnagar, "On the mechanical response of 2D plain woven and 3D angle-interlock fabrics", *Composites Part B: Engineering*, vol. 118, pp. 135–148, Jun. 2017.
- [125] L. H. Strait, M. L. Karasek, and M. F. Amateau, "Effects of seawater immersion on the impact resistance of glass fiber reinforced epoxy composites", *Journal of Composite Materials*, vol. 26, no. 14, pp. 2118–2133, Dec. 1992.
- [126] M. de Freitas, A. Silva, and L. Reis, "Numerical evaluation of failure mechanisms on composite specimens subjected to impact loading", *Composites Part B: Engineering*, vol. 31, no. 3, pp. 199–207, Apr. 2000.
- [127] N. Baker, R. Butler, and C. B. York, "Damage tolerance of fully orthotropic laminates in compression", *Composites Science and Technology*, vol. 72, no. 10, pp. 1083–1089, Jun. 2012.
- [128] C. B. York, "Unified approach to the characterization of coupled composite laminates: benchmark configurations and special cases", *J. Aerosp. Eng.*, vol. 23, no. 4, pp. 219–242, Oct. 2010.
- [129] S. Samborski, "Numerical analysis of the DCB test configuration applicability to mechanically coupled fiber reinforced laminated composite beams", *Composite Structures*, vol. 152, pp. 477–487, Sep. 2016.
- [130] S. Samborski, "Analysis of the end-notched flexure test configuration applicability for mechanically coupled fiber reinforced composite laminates", *Composite Structures*, vol. 163, pp. 342–349, Mar. 2017.
- [131] L. S. Sutherland, "A review of impact testing on marine composite materials: Part II – Impact event and material parameters", *Composite Structures*, vol. 188, pp. 503–511, Mar. 2018.
- [132] J. J. Andrew, S. M. Srinivasan, A. Arockiarajan, and H. N. Dhakal, "Parameters influencing the impact response of fiber-reinforced polymer matrix composite materials: A critical review", *Composite Structures*, vol. 224, no. 111007, Sep. 2019.
- [133] V. Tita, J. de Carvalho, and D. Vandepitte, "Failure analysis of low velocity impact on thin composite laminates: Experimental and numerical approaches", *Composite Structures*, vol. 83, no. 4, pp. 413–428, Jun. 2008.
- [134] S. Li, S. R. Reid, and Z. Zou, "Modelling damage of multiple delaminations and transverse matrix cracking in laminated composites due to low velocity lateral impact", *Composites Science and Technology*, vol. 66, no. 6, pp. 827–836, May 2006.
- [135] W. Tan, B. G. Falzon, M. Price, and H. Liu, "The role of material characterisation in the crush modelling of thermoplastic composite structures", *Composite Structures*, vol. 153, pp. 914–927, Oct. 2016.
- [136] M. J. Laffan, "Testing the toughness of polymer matrix composites", in *Failure Mechanisms in Polymer Matrix Composites*, Elsevier, 2012, pp. 110–128.
- [137] I. De Baere, S. Jacques, W. Van Paepegem, and J. Degrieck, "Study of the mode I and mode II interlaminar behaviour of a carbon fabric reinforced thermoplastic", *Polymer Testing*, vol. 31, no. 2, pp. 322–332, Apr. 2012.
- [138] K. Friedrich, T. Gogeva, and S. Fakirov, "Thermoplastic impregnated fiber bundles: Manufacturing of laminates and fracture mechanics characterization", *Composites Science and Technology*, vol. 33, no. 2, pp. 97–120, Jan. 1988.
- [139] J. A. Hinkley, "Interface effects in interlaminar fracture of thermoplastic composites", *Journal of Reinforced Plastics and Composites*, vol. 9, no. 5, pp. 470–476, Sep. 1990.
- [140] S.-L. Gao and J.-K. Kim, "Cooling rate influences in carbon fibre/PEEK composites. Part III: impact damage performance", *Composites Part A: Applied Science and Manufacturing*, vol. 32, no. 6, pp. 775–785, Jun. 2001.
- [141] M. A. Umarfarooq, P. S. Shivakumar Gouda, G. B. Veeresh kumar, N. R. Banapurmath, and A. Edacherian, "Impact of process induced residual stresses on interlaminar fracture toughness in carbon

- epoxy composites", *Composites Part A: Applied Science and Manufacturing*, vol. 127, p. 105652, Dec. 2019.
- [142] W. Harris, C. Soutis, and C. Atkin, "Impact Response of Curved Composite Laminates: Effect of Radius and Thickness", *Appl Compos Mater*, vol. 27, no. 5, pp. 555–573, Oct. 2020.
- [143] C. Bouvet, J. Serra, and P. G. Perez, "Strain rate effect of mode II interlaminar fracture toughness on the impact response of a thermoplastic PEEK composite", *Composites Part C: Open Access*, vol. 2, p. 100031, Oct. 2020.
- [144] S. CHAIBI, "Prediction of low-velocity/low-energy impact damages in the latest generation of carbon-epoxy laminated composites", ISAE SUPAERO, 2022.
- [145] C. Maierhofer, P. Myrach, M. Reischel, H. Steinfurth, M. Röllig, and M. Kunert, "Characterizing damage in CFRP structures using flash thermography in reflection and transmission configurations", *Composites Part B: Engineering*, vol. 57, pp. 35–46, Feb. 2014.
- [146] A. Fahr and A. Y. Kamdeil, "Ultrasonic C-Scan Inspection Of Composite Materials", *Engineering Journal of Qatar University*, vol. 5, 1992.
- [147] K. T. Tan, N. Watanabe, and Y. Iwahori, "Impact damage resistance, response, and mechanisms of laminated composites reinforced by through-thickness stitching", *International Journal of Damage Mechanics*, vol. 21, no. 1, pp. 51–80, Jan. 2012.
- [148] E. Oterkus, C. Diyaroglu, D. De Meo, and G. Allegri, "Fracture modes, damage tolerance and failure mitigation in marine composites", in *Marine Applications of Advanced Fibre-Reinforced Composites*, Elsevier, 2016, pp. 79–102.
- [149] G. A. O. Davies, D. Hitchings, and G. Zhou, "Impact damage and residual strengths of woven fabric glass/polyester laminates", *Composites Part A: Applied Science and Manufacturing*, vol. 27, no. 12, pp. 1147–1156, Jan. 1996.
- [150] G. Zhou and L. J. Greaves, "Damage resistance and tolerance of thick laminated woven roving GFRP plates subjected to low-velocity impact", in *Impact Behaviour of Fibre-Reinforced Composite Materials and Structures*, Elsevier, 2000, pp. 133–185.
- [151] A. P. Mouritz, J. Gallagher, and A. A. Goodwin, "Flexural strength and interlaminar shear strength of stitched GRP laminates following repeated impacts", *Composites Science and Technology*, vol. 57, no. 5, pp. 509–522, Jan. 1997.
- [152] C. Santiuste, S. Sanchez-Saez, and E. Barbero, "Residual flexural strength after low-velocity impact in glass/polyester composite beams", *Composite Structures*, vol. 92, no. 1, pp. 25–30, Jan. 2010.
- [153] P. B. Gning, M. Tarfaoui, F. Collombet, L. Riou, and P. Davies, "Damage development in thick composite tubes under impact loading and influence on implosion pressure: experimental observations", *Composites Part B: Engineering*, vol. 36, no. 4, pp. 306–318, Jun. 2005.
- [154] I. Kimpara and H. Saito, "Post-Impact Fatigue Behavior of Woven and Knitted Fabric CFRP Laminates for Marine Use", in *Major Accomplishments in Composite Materials and Sandwich Structures*, I. M. Daniel, E. E. Gdoutos, and Y. D. S. Rajapakse, Eds. Dordrecht: Springer Netherlands, 2009, pp. 113–132.
- [155] R. Bogenfeld, J. Kreikemeier, and T. Wille, "Review and benchmark study on the analysis of low-velocity impact on composite laminates", *Engineering Failure Analysis*, vol. 86, pp. 72–99, Apr. 2018.
- [156] S. I. Thorsson, A. M. Waas, and M. Rassaian, "Low-velocity impact predictions of composite laminates using a continuum shell based modeling approach part A: Impact study", *International Journal of Solids and Structures*, vol. 155, pp. 185–200, Dec. 2018.
- [157] M. R. Abir, T. E. Tay, M. Ridha, and H. P. Lee, "Modelling damage growth in composites subjected to impact and compression after impact", *Composite Structures*, vol. 168, pp. 13–25, May 2017.
- [158] N. Hongkarnjanakul, C. Bouvet, and S. Rivallant, "Validation of low velocity impact modelling on different stacking sequences of CFRP laminates and influence of fibre failure", *Composite Structures*, vol. 106, pp. 549–559, Dec. 2013.
- [159] F. Pascal, P. Navarro, S. Marguet, and J.-F. Ferrero, "5 - Study of medium velocity impacts on the lower surface of helicopter blades", in *Dynamic Response and Failure of Composite Materials and Structures*, V. Lopresto, A. Langella, and S. Abrate, Eds. Woodhead Publishing, 2017, pp. 159–181.
- [160] J. I. Bech, C. B. Hasager, and C. Bak, "Extending the life of wind turbine blade leading edges by reducing the tip speed during extreme precipitation events", *Wind Energy Science*, vol. 3, no. 2, pp. 729–748, Oct. 2018.

- [161] O. Dorival *et al.*, "Experimental results of medium velocity impact tests for reinforced foam core braided composite structures", *Jnl of Sandwich Structures & Materials*, vol. 20, no. 1, pp. 106–129, Jan. 2018.
- [162] P. Navarro, F. Pascal, S. Marguet, J.-F. Ferrero, J. Aubry, and S. Lemaire, "Experimental and numerical study of oblique impact on helicopter blades – Influence of the curvature", Seville, Spain, Jun. 2014.
- [163] P. Robinson and G. A. O. Davies, "Impactor mass and specimen geometry effects in low velocity impact of laminated composites", *International Journal of Impact Engineering*, vol. 12, no. 2, pp. 189–207, Jan. 1992.
- [164] A. S. Verma, N. P. Vedvik, P. U. Haselbach, Z. Gao, and Z. Jiang, "Comparison of numerical modelling techniques for impact investigation on a wind turbine blade", *Composite Structures*, vol. 209, pp. 856–878, Feb. 2019.
- [165] P. Navarro, J. Aubry, S. Marguet, J.-F. Ferrero, S. Lemaire, and P. Rauch, "Semi-continuous approach for the modeling of thin woven composite panels applied to oblique impacts on helicopter blades", *Composites Part A: Applied Science and Manufacturing*, vol. 43, no. 6, pp. 871–879, Jun. 2012.
- [166] N. Nanami and O. O. Ochoa, "Bird impact study of a preloaded composite wind turbine blade", presented at the ICCM19, Montreal, Canada.
- [167] B. Ostré, C. Bouvet, C. Minot, and J. Aboissière, "Edge impact modeling on stiffened composite structures", *Composite Structures*, vol. 126, pp. 314–328, Aug. 2015.
- [168] C. Bouvet, N. Hongkarnjanakul, S. Rivallant, and J.-J. Barrau, "Discrete Impact Modeling of Inter- and Intra-laminar Failure in Composites", in *Dynamic Failure of Composite and Sandwich Structures*, S. Abrate, B. Castanié, and Y. D. S. Rajapakse, Eds. Dordrecht: Springer Netherlands, 2013, pp. 339–392.
- [169] S. I. Thorsson, S. P. Sringeri, A. M. Waas, B. P. Justusson, and M. Rassaian, "Experimental investigation of composite laminates subject to low-velocity edge-on impact and compression after impact", *Composite Structures*, vol. 186, pp. 335–346, Feb. 2018.
- [170] A. Le Guen-Geffroy, "Marine ageing and fatigue of carbon/epoxy composite propeller blades", PhD Thesis, Université de Bretagne Occidentale, 2019.
- [171] A. Le Guen-Geffroy, P.-Y. Le Gac, B. Habert, and P. Davies, "Physical ageing of epoxy in a wet environment: Coupling between plasticization and physical ageing", *Polymer Degradation and Stability*, vol. 168, p. 108947, Oct. 2019.
- [172] B. Fayolle and J. Verdu, "Vieillissement physique des matériaux polymères". *Techniques de l'ingénieur*, Jan. 2005.
- [173] J. Heijboer, "Secondary loss peaks in glassy amorphous polymers", *International Journal of Polymeric Materials*, vol. 6, no. 1–2, pp. 11–37, Dec. 1977.
- [174] E. S.-W. Kong, "Physical aging in epoxy matrices and composites", in *Epoxy Resins and Composites IV*, Berlin, Heidelberg, 1986, pp. 125–171.
- [175] G. M. Odegard and A. Bandyopadhyay, "Physical aging of epoxy polymers and their composites", *Journal of Polymer Science Part B: Polymer Physics*, vol. 49, no. 24, pp. 1695–1716, 2011.
- [176] Y. G. Lin, H. Sautereau, and J. P. Pascault, "Epoxy network structure effect on physical aging behavior", *Journal of Applied Polymer Science*, vol. 32, no. 4, pp. 4595–4605, 1986.
- [177] D. Lévêque, A. Schieffer, A. Mavel, and J.-F. Maire, "Analysis of how thermal aging affects the long-term mechanical behavior and strength of polymer–matrix composites", *Composites Science and Technology*, vol. 65, no. 3, pp. 395–401, Mar. 2005.
- [178] J. M. G. Cowie and R. Ferguson, "Physical aging studies in poly(vinylmethyl ether). I. Enthalpy relaxation as a function of aging temperature", *Macromolecules*, vol. 22, no. 5, pp. 2307–2312, Sep. 1989.
- [179] J. K. Lee and J. Y. Hwang, "Erasure behavior of isothermal physical aging effect below glass transition temperature in a fully cured epoxy resin: Differential scanning calorimetry measurement", *Polym J*, vol. 35, no. 2, pp. 191–196, Feb. 2003.
- [180] X.-G. Li, M.-R. Huang, R.-F. Chen, Y. Jin, and Y.-L. Yang, "Preparation and characterization of poly(p-phenylenediamine-co-xylidine)", *Journal of Applied Polymer Science*, vol. 81, no. 13, pp. 3107–3116, 2001.
- [181] G. Wisanrakkit and J. K. Gillham, "Continuous heating transformation (CHT) cure diagram of an aromatic amine/epoxy system at constant heating rates", *Journal of Applied Polymer Science*, vol. 42, no. 9, pp. 2453–2463, 1991.

- [182] W. D. Cook, M. Mehrabi, and G. H. Edward, "Ageing and yielding in model epoxy thermosets", *Polymer*, vol. 40, no. 5, pp. 1209–1218, Mar. 1999.
- [183] C. G. Sell and G. B. McKenna, "Influence of physical ageing on the yield response of model DGEBA/poly(propylene oxide) epoxy glasses", *Polymer*, vol. 33, no. 10, pp. 2103–2113, Jan. 1992.
- [184] T. D. Chang and J. O. Brittain, "Studies of epoxy resin systems: Part D: Fracture toughness of an epoxy resin: a study of the effect of crosslinking and sub-Tg aging", *Polym. Eng. Sci.*, vol. 22, no. 18, pp. 1228–1236, Dec. 1982.
- [185] V.-T. Truong and B. C. Ennis, "Effect of physical aging on the fracture behavior of crosslinked epoxies", *Polymer Engineering & Science*, vol. 31, no. 8, pp. 548–557, 1991.
- [186] I. García-Moreno, M. Caminero, G. Rodríguez, and J. López-Cela, "Effect of thermal ageing on the impact and flexural damage behaviour of carbon fibre-reinforced epoxy laminates", *Polymers*, vol. 11, no. 1, p. 80, Jan. 2019.
- [187] Y. J. Weitsman, *Fluid effects in polymers and polymeric composites*. Springer US, 2012.
- [188] P. Davies and Y. D. S. Rajapakse, Eds., *Durability of Composites in a Marine Environment*, vol. 208. Dordrecht: Springer Netherlands, 2014.
- [189] P. Davies and Y. D. S. Rajapakse, Eds., *Durability of Composites in a Marine Environment 2*, vol. 245. Cham: Springer International Publishing, 2018.
- [190] A. Kootsookos and A. P. Mouritz, "Seawater durability of glass- and carbon-polymer composites", *Composites Science and Technology*, vol. 64, no. 10, pp. 1503–1511, Aug. 2004.
- [191] A. C. Loos and G. S. Springer, "Moisture absorption of graphite-epoxy composites immersed in liquids and in humid air", *Journal of Composite Materials*, vol. 13, no. 2, pp. 131–147, Apr. 1979.
- [192] A. F. Abdelkader and J. R. White, "Water absorption in epoxy resins: the effects of the crosslinking agent and curing temperature", *J. Appl. Polym. Sci.*, vol. 98, no. 6, pp. 2544–2549, Dec. 2005.
- [193] B. F. Boukhoulda, E. Adda-Bedia, and K. Madani, "The effect of fiber orientation angle in composite materials on moisture absorption and material degradation after hygrothermal ageing", *Composite Structures*, vol. 74, no. 4, pp. 406–418, Aug. 2006.
- [194] C. Humeau, "Contribution to the study of coupling between moisture diffusion and mechanical stress, in high performance marine materials", Université de Nantes, 2017.
- [195] J. Crank, *The mathematics of diffusion*, 2. ed., Reprinted. Oxford: Oxford Univ. Press, 1979.
- [196] N. Tual, N. Carrere, P. Davies, T. Bonnemains, and E. Lolive, "Characterization of sea water ageing effects on mechanical properties of carbon/epoxy composites for tidal turbine blades", *Composites Part A: Applied Science and Manufacturing*, pp. 380–389, Nov. 01. 2015.
- [197] Y. Weitsman, "Moisture in composites: sorption and damage", in *Composite Materials Series*, vol. 4, Elsevier, 1991, pp. 385–429.
- [198] R. F. Boyer, "Physical properties of molecular crystals, liquids and glasses", *J. Polym. Sci. A-1 Polym. Chem.*, vol. 7, no. 8, pp. 2466–2466, Aug. 1969.
- [199] E. L. McKague, J. D. Reynolds, and J. E. Halkias, "Swelling and glass transition relations for epoxy matrix material in humid environments", *J. Appl. Polym. Sci.*, vol. 22, no. 6, pp. 1643–1654, Jun. 1978.
- [200] R. Simha and R. F. Boyer, "On a general relation involving the glass temperature and coefficients of expansion of polymers", *The Journal of Chemical Physics*, vol. 37, no. 5, pp. 1003–1007, Sep. 1962.
- [201] R. P. Kambour, "Correlations of the dry crazing resistance of glassy polymers with other physical properties", *Polym. commun*, vol. 24, no. 10, pp. 292–296, 1983.
- [202] P. J. Flory and J. Rehner, "Statistical mechanics of cross-linked polymer networks I. Rubberlike elasticity", *The Journal of Chemical Physics*, vol. 11, no. 11, pp. 512–520, Nov. 1943.
- [203] N. A. St John, L. Booth, and J. W. Heath, "Dimensional stability of composite materials", presented at the Advanced Composites Innovation Conference, Gold Coast, Australia, Mar. 2017.
- [204] M. Assarar, D. Scida, A. El Mahi, C. Poilâne, and R. Ayad, "Influence of water ageing on mechanical properties and damage events of two reinforced composite materials: flax-fibres and glass-fibres", *Materials & Design*, vol. 32, no. 2, pp. 788–795, Feb. 2011.
- [205] J. D. Garcia-Espinel, D. Castro-Fresno, P. Parbole Gayo, and F. Ballester-Muñoz, "Effects of sea water environment on glass fiber reinforced plastic materials used for marine civil engineering constructions", *Materials & Design (1980-2015)*, vol. 66, pp. 46–50, Feb. 2015.

- [206] K. Imielińska and L. Guillaumat, "The effect of water immersion ageing on low-velocity impact behaviour of woven aramid–glass fibre/epoxy composites", *Composites Science and Technology*, vol. 64, no. 13, pp. 2271–2278, Oct. 2004.
- [207] A. Le Guen-Geffroy, P. Davies, P.-Y. Le Gac, and B. Habert, "Influence of Seawater Ageing on Fracture of Carbon Fiber Reinforced Epoxy Composites for Ocean Engineering", *Oceans*, vol. 1, no. 4, pp. 198–214, Sep. 2020.
- [208] L. S. Sutherland, "A review of impact testing on marine composite materials: Part III - Damage tolerance and durability", *Composite Structures*, vol. 188, pp. 512–518, Mar. 2018.
- [209] K. Berketis and P. J. Hogg, "Impact response of composites after long-term water immersion", *Journal of Materials Science*, vol. 42, no. 16, pp. 6642–6650, 2007.
- [210] M. Dale, B. A. Acha, and L. A. Carlsson, "Low velocity impact and compression after impact characterization of woven carbon/vinylester at dry and water saturated conditions", *Composite Structures*, vol. 94, no. 5, pp. 1582–1589, Apr. 2012.
- [211] Sicomin Epoxy Systems, "SR8100 : Epoxy systems for injection and infusion, SR 8100 / SR 882x2 SD477x E 1616". Technical datasheet, 2017.
- [212] A. F. Johnson, R. S. Thomson, M. David, M. W. Joosten, and M. Waimer, "13 - Design and testing of crashworthy aerospace composite components", in *Polymer Composites in the Aerospace Industry (Second Edition)*, P. Irving and C. Soutis, Eds. Woodhead Publishing, 2020, pp. 371–414.
- [213] R. H. Rigby, M. Al-Khalil, and M. R. C. Fouinneteau, "Tire debris impact modeling on a composite wing structure", presented at the Simulia Community Conference, 2013.
- [214] M. Bruyneel, P. Jetteur, J. P. Delsemme, S. Siavoshani, and A. Cheruet, "Modeling and Simulating Progressive Failure in Composite Structures for Automotive Applications", presented at the SAE 2014 World Congress & Exhibition, Apr. 2014, pp. 2014-01–0962.
- [215] P. Davies, "Introduction to delamination fracture of continuous fibre composites", in *European Structural Integrity Society*, vol. 28, Elsevier, 2001, pp. 271–275.
- [216] A. J. Brunner, B. R. K. Blackman, and P. Davies, "Mode I delamination", in *European Structural Integrity Society*, vol. 28, Elsevier, 2001, pp. 277–305.
- [217] P. Davies, B. R. K. Blackman, and A. J. Brunner, "Mode II delamination", in *European Structural Integrity Society*, vol. 28, Elsevier, 2001, pp. 307–333.
- [218] B. R. K. Blackman, A. J. Brunner, and P. Davies, "Delamination fracture of continuous fibre composites: Mixed-mode fracture", in *European Structural Integrity Society*, vol. 28, Elsevier, 2001, pp. 335–359.
- [219] M. Kenane and M. L. Benzeggagh, "Mixed-mode delamination fracture toughness of unidirectional glass/epoxy composites under fatigue loading", *Composites Science and Technology*, vol. 57, no. 5, pp. 597–605, 1997.
- [220] Dassault Systemes, "Abaqus Documentation". 2022.
- [221] M. L. Benzeggagh and M. Kenane, "Measurement of mixed-mode delamination fracture toughness of unidirectional glass/epoxy composites with mixed-mode bending apparatus", *Composites Science and Technology*, vol. 56, no. 4, pp. 439–449, Jan. 1996.
- [222] Kropka J., Arechederra G., Wilson K., McCoy J., Tenney C., and Long K., "Chemical and physical aging of Epoxies", presented at the 32nd CASS Working Group, Livermore, CA, October 2018.
- [223] C.-C. M. Ma, C.-L. Lee, M.-J. Chang, and N.-H. Tai, "Effect of physical aging on the toughness of carbon fiber-reinforced poly(ether ether ketone) and poly(phenylene sulfide) composites. I", *Polym. Compos.*, vol. 13, no. 6, pp. 441–447, Dec. 1992.
- [224] E. José-Trujillo, C. Rubio-González, and J. Rodríguez-González, "Seawater ageing effect on the mechanical properties of composites with different fiber and matrix types", *Journal of Composite Materials*, vol. 53, no. 23, pp. 3229–3241, Sep. 2019.
- [225] W. H. Choong, K. B. Yeo, M. T. Fadzlit, Y. Y. Farm, and M. Azlan Ismail, "GFRP Composite Material Degradation Under Seawater and Weathering Effect", in *Developments in Sustainable Chemical and Bioprocess Technology*, R. Pogaku, A. Bono, and C. Chu, Eds. Boston, MA: Springer US, 2013, pp. 395–399.
- [226] H. Li, K. Zhang, X. Fan, H. Cheng, G. Xu, and H. Suo, "Effect of seawater ageing with different temperatures and concentrations on static/dynamic mechanical properties of carbon fiber reinforced polymer composites", *Composites Part B: Engineering*, vol. 173, p. 106910, Sep. 2019.

- [227] M. A. Abanilla, Y. Li, and V. M. Karbhari, "Durability characterization of wet layup graphite/epoxy composites used in external strengthening", *Composites Part B: Engineering*, vol. 37, no. 2–3, pp. 200–212, Apr. 2005.
- [228] B. De'Nève and M. E. R. Shanahan, "Water absorption by an epoxy resin and its effect on the mechanical properties and infra-red spectra", *Polymer*, vol. 34, no. 24, pp. 5099–5105, Dec. 1993.
- [229] C.-H. Shen and G. S. Springer, "Moisture Absorption and Desorption of Composite Materials", *Journal of Composite Materials*, vol. 10, no. 1, pp. 2–20, Jan. 1976.
- [230] N. Tual, "Durabilité des composites carbone/époxy pour applications pales d'hydroliennes", PhD Thesis, Université de Bretagne occidentale - Brest, 2015.
- [231] J. Germain, "Evaluation des capacités prédictives d'un modèle avancé pour la prévision de la tenue de plaques stratifiées perforées", Université Paris-Saclay, 2020.
- [232] L. Xu, Y. He, S. Ma, L. Hui, Y. Jia, and Y. Tu, "Effects of aging process and testing temperature on the open-hole compressive properties of a carbon fiber composite", *High Performance Polymers*, vol. 32, no. 6, pp. 693–701, Aug. 2020.
- [233] J. R. Reeder, "Stitching vs. a Toughened Matrix: Compression Strength Effects", *Journal of Composite Materials*, vol. 29, no. 18, pp. 2464–2487, Dec. 1995.
- [234] M. J. Laffan, S. T. Pinho, P. Robinson, and A. J. McMillan, "Translaminar fracture toughness testing of composites: A review", *Polymer Testing*, vol. 31, no. 3, pp. 481–489, May 2012.
- [235] Y. Saadati, G. Lebrun, C. Bouvet, J.-F. Chatelain, and Y. Beauchamp, "Study of translaminar fracture toughness of unidirectional flax/epoxy composite", *Composites Part C: Open Access*, vol. 1, p. 100008, Aug. 2020.
- [236] J. D. Pujols Gonzalez, B. Vieille, and C. Bouvet, "High temperature translaminar fracture of woven-ply thermoplastic laminates in tension and in compression", *Engineering Fracture Mechanics*, vol. 246, p. 107616, Apr. 2021.
- [237] N. Blanco, D. Trias, S. T. Pinho, and P. Robinson, "Intralaminar fracture toughness characterisation of woven composite laminates. Part II: Experimental characterisation", *Engineering Fracture Mechanics*, vol. 131, pp. 361–370, Nov. 2014.
- [238] B. M. Lempriere, "Poisson's ratio in orthotropic materials.", *AIAA Journal*, vol. 6, no. 11, pp. 2226–2227, Nov. 1968.
- [239] R. M. Jones, *Mechanics of Composite Materials*, 2nd ed. CRC Press, 2018.
- [240] Reeder J. R., "An Evaluation of Mixed-Mode Delamination Failure Criteria". NASA Tech Memo 104210, 1992.
- [241] T. O'Brien, "Composite Interlaminar Shear Fracture Toughness GIIC: shear toughness or sheer myth?". ASTM International, Jan. 01. 1998.
- [242] S. T. Pinho, P. Robinson, and L. Iannucci, "Developing a four point bend specimen to measure the mode I intralaminar fracture toughness of unidirectional laminated composites", *Composites Science and Technology*, vol. 69, no. 7–8, pp. 1303–1309, Jun. 2009.
- [243] L. F. Varandas, D. Dalli, G. Catalanotti, and B. G. Falzon, "Estimating the mode I through-thickness intralaminar R -curve of unidirectional carbon fibre-reinforced polymers using a micromechanics framework combined with the size effect method", *Composites Part A: Applied Science and Manufacturing*, vol. 162, p. 107141, Nov. 2022.
- [244] J. V. BLITTERSWYK, L. FLETCHER, and F. PIERRON, "Characterisation of the Interlaminar Properties of Composites at High Strain Rates: A Review". The Japanese Society for Experimental Mechanics, 2017.
- [245] C. T. Sun and C. Han, "A method for testing interlaminar dynamic fracture toughness of polymeric composites", *Composites Part B: Engineering*, vol. 35, no. 6–8, pp. 647–655, Sep. 2004.
- [246] A. Aliyu and I. Daniel, "Effects of Strain Rate on Delamination Fracture Toughness of Graphite/Epoxy", in *Delamination and Debonding of Materials*, W. Johnson, Ed. 100 Barr Harbor Drive, PO Box C700, West Conshohocken, PA 19428-2959: ASTM International, 1985, pp. 336-336–13.
- [247] G. Yaniv and I. Daniel, "Height-Tapered Double Cantilever Beam Specimen for Study of Rate Effects on Fracture Toughness of Composites", in *Composite Materials: Testing and Design (Eighth Conference)*, J. Whitcomb, Ed. 100 Barr Harbor Drive, PO Box C700, West Conshohocken, PA 19428-2959: ASTM International, 1988, pp. 241-241–18.
- [248] A. J. Smiley and R. B. Pipes, "Rate Effects on Mode I Interlaminar Fracture Toughness in Composite Materials", *Journal of Composite Materials*, vol. 21, no. 7, pp. 670–687, Jul. 1987.

- [249] I. M. Daniel, G. Yaniv, and J. W. Auser, "Rate Effects on Delamination Fracture Toughness of Graphite/Epoxy Composites", in *Composite Structures 4*, I. H. Marshall, Ed. Dordrecht: Springer Netherlands, 1987, pp. 258–272.
- [250] T. Kusaka, M. Hojo, Y.-W. Mai, T. Kurokawa, T. Nojima, and S. Ochiai, "Rate dependence of mode I fracture behaviour in carbon-fibre/epoxy composite laminates", *Composites Science and Technology*, vol. 58, no. 3–4, pp. 591–602, Mar. 1998.
- [251] B. R. K. Blackman *et al.*, "The failure of fibre composites and adhesively bonded fibre composites under high rates of test: Part I Mode I loading-experimental studies", *J Mater Sci*, vol. 30, no. 23, pp. 5885–5900, Dec. 1995.
- [252] C. Guo and C. T. Sun, "Dynamic Mode-I crack-propagation in a carbon/epoxy composite", *Composites Science and Technology*, vol. 58, no. 9, pp. 1405–1410, Sep. 1998.
- [253] R. Eqra and M. H. Moghim, "Effect of strain rate on the fracture behaviour of epoxy–graphene nanocomposite", *Bull Mater Sci*, vol. 39, no. 5, pp. 1197–1204, Sep. 2016.
- [254] A. Gilat, R. K. Goldberg, and G. D. Roberts, "Strain Rate Sensitivity of Epoxy Resin in Tensile and Shear Loading", *J. Aerosp. Eng.*, vol. 20, no. 2, pp. 75–89, Apr. 2007.
- [255] Dassault Systèmes, "Analysis of composite materials with Abaqus". 2021.
- [256] L. Manseri, P. Navarro, O. Dorival, S. Marguet, B. Mahmoud, and J.-F. Ferrero, "Development of a hybrid element to model intralaminar damage in thick composite plates under impact loading", *Composites Part B: Engineering*, vol. 222, p. 109024, Oct. 2021.
- [257] A. Bajpai, P. Saxena, and K. Kunze, "Tribo-Mechanical Characterization of Carbon Fiber-Reinforced Cyanate Ester Resins Modified With Fillers", *Polymers*, vol. 12, no. 8, p. 1725, Jul. 2020.
- [258] E. V. González, P. Maimí, P. P. Camanho, A. Turon, and J. A. Mayugo, "Simulation of drop-weight impact and compression after impact tests on composite laminates", *Composite Structures*, vol. 94, no. 11, pp. 3364–3378, Nov. 2012.
- [259] D. A. Drake, R. W. Sullivan, A. E. Lovejoy, S. B. Clay, and D. C. Jegley, "Influence of stitching on the out-of-plane behavior of composite materials – A mechanistic review", *Journal of Composite Materials*, vol. 55, no. 23, pp. 3307–3321, Sep. 2021.
- [260] N. B. Bektaş and İ. Ađır, "Impact response of composite plates manufactured with stitch-bonded non-crimp glass fiber fabrics", *Science and Engineering of Composite Materials*, vol. 21, no. 1, pp. 111–120, Jan. 2014.
- [261] L. R. Xu, A. Krishnan, H. Ning, and U. Vaidya, "A seawater tank approach to evaluate the dynamic failure and durability of E-glass/vinyl ester marine composites", *Composites Part B: Engineering*, vol. 43, no. 5, pp. 2480–2486, Jul. 2012.
- [262] E. V. González *et al.*, "Simulating drop-weight impact and compression after impact tests on composite laminates using conventional shell finite elements", *International Journal of Solids and Structures*, vol. 144–145, pp. 230–247, Jul. 2018.
- [263] K. L. Alderson and K. E. Evans, "Low velocity transverse impact of filament-wound pipes: Part 1. Damage due to static and impact loads", *Composite Structures*, vol. 20, no. 1, pp. 37–45, Jan. 1992.
- [264] M. E. Deniz, O. Ozdemir, M. Ozen, and R. Karakuzu, "Failure pressure and impact response of glass–epoxy pipes exposed to seawater", *Composites Part B: Engineering*, vol. 53, pp. 355–361, Oct. 2013.
- [265] F. Islam, C. Wanigasekara, G. Rajan, A. Swain, and B. G. Prusty, "An approach for process optimisation of the Automated Fibre Placement (AFP) based thermoplastic composites manufacturing using Machine Learning, photonic sensing and thermo-mechanics modelling", *Manufacturing Letters*, vol. 32, pp. 10–14, Apr. 2022.
- [266] Shafaq, M. J. Donough, A. L. Farnsworth, A. W. Phillips, N. A. St John, and B. Gangadhara Prusty, "Influence of deposition rates on the mode I fracture toughness of in-situ consolidated thermoplastic composites", *Composites Part B: Engineering*, vol. 251, p. 110474, Feb. 2023.
- [267] W. Zuo, Q. Luo, Q. Li, and G. Sun, "Effect of thermal and hydrothermal aging on the crashworthiness of carbon fiber reinforced plastic composite tubes", *Composite Structures*, vol. 303, p. 116136, Jan. 2023.
- [268] Quentin Dezulier, "Etude du couplage entre diffusion d'eau et comportement mécanique de matériaux composites en milieu marin", Université de Nantes, 2022.

- [269] Q. Dezulier, A. Clement, P. Davies, F. Jacquemin, M. Arhant, and B. Flageul, "Characterization and modelling of the hygro-viscoelastic behaviour of polymer-based composites used in marine environment", *Phil. Trans. R. Soc. A.*, vol. 381, no. 2240, p. 20210221, Jan. 2023.

Titre : Compréhension du comportement au choc et durabilité sur le long terme d'un composite pour des hélices de propulsion navale

Mots clés : Composite, Durabilité, Eau de mer, Vieillesse, Impact

Résumé : De par leurs propriétés mécaniques spécifiques, les matériaux composites sont de plus en plus utilisés en milieu marin. Une application nouvelle est l'hélice de propulsion. Comparés aux matériaux métalliques historiques, les composites permettent d'optimiser les formes et raideurs des pales, pour optimiser leurs performances hydrodynamiques.

Dans ce travail de thèse, la durabilité d'un composite C/Epoxy a été étudiée. Cette étude vise à prédire le comportement sur le long-terme du composite selon un état non vieilli, un état vieilli physiquement et un état saturé en eau de mer.

Tout d'abord, les propriétés quasi-statiques du composite ont été caractérisées. Les données obtenues ont permis de simuler numériquement le comportement d'une éprouvette soumise à un chargement complexe.

Ensuite, des essais d'impacts hors-plan ont été réalisés. Les mesures effectuées ont été comparées à un modèle éléments finis développé avec des éléments de type coque, ainsi qu'avec le critère d'Hashin pour prédire la rupture des plis. Ce modèle a été alimenté par les propriétés mécaniques du matériau, obtenues à partir des essais quasi-statiques.

Enfin, des essais d'impacts non normés ont été réalisés dans le but de réaliser des essais sur des éprouvettes plus proches d'une géométrie d'hélice. Ces essais, préliminaires, ont permis de mettre en avant le caractère nocif de l'eau de mer sur le comportement à l'impact, ainsi que la perte de propriétés résiduelles post-impact.

Title : Understanding the impact behavior and long-term durability of marine composites for propellers

Keywords : Composite, Durability, Seawater, Aging, Impact

Abstract : Because of their specific mechanical properties, composite materials are increasingly used in marine environment. A recent application is the propeller blade. Compared to historical materials, composites allow the optimization of shapes and local stiffnesses of the blades, in order to optimize their hydrodynamic performance.

In this PhD work, the durability of a Carbon/Epoxy composite has been studied, with the aim to predict the long-term behavior of the composite. Three conditions were examined; unaged, physically aged and seawater saturated.

First, quasi-static mechanical properties have been characterized during an extensive campaign of experiments. Mechanical properties obtained were used to simulate the mechanical behavior of a coupon submitted to a complex loading.

Then, out-of-plane impact tests have been performed. Measurements obtained have been compared to a finite element model. The model was based on shell elements, with the Hashin criterion to predict the ply failure. The dataset obtained experimentally during the quasi-static campaign was used as input data.

Finally, non-standard impact tests have been performed. The aim was to perform impact tests on coupon geometries that are closer to a real blade. These preliminary tests allowed the effect of seawater aging on both the impact behavior and also the post-impact strength to be quantified.